High-speed diagnostics for the study of flame stabilization and transient behaviour in a swirled burner with variable liquid-fuel distribution

Antoine Renaud

NNT : 2015SACLC003

THESE DE DOCTORAT
DE
L'UNIVERSITE PARIS-SACLAY
PREPAREE A
CENTRALESUPELEC

ECOLE DOCTORALE N° 579
Sciences Mécaniques et Energétiques, Matériaux et Géosciences

Spécialité Combustion

Par

M. Antoine RENAUD

Etude de la stabilisation des flammes et des comportements transitoires dans un brûleur étagé à combustible liquide à l'aide de diagnostics rapides.

Thèse présentée et soutenue à Châtenay-Malabry, le 07 décembre 2015:

Composition du Jury :

Mme Rousselle, Christine	Professeure, Université d'Orléans	Présidente
M. Grisch, Frédéric	Professeur, INSA de Rouen	Rapporteur
M. Guibert, Philippe	Professeur, UPMC	Rapporteur
M. Hardalupas, Yannis	Professor, Imperial College	Examinateur
M. Méry, Yoann	Design Engineer , Snecma	Examinateur
M. Ducruix, Sébastien	Directeur de Recherche, CNRS	Directeur de thèse
M. Zimmer, Laurent	Chargé de Recherche, CNRS	Co-Directeur de thèse

Remerciements

Mes remerciements vont tout d'abord aux personnes qui ont supervisé mon travail. Tout d'abord Laurent Zimmer pour m'avoir suivi de près durant le stage de master et l'ensemble de la thèse, m'avoir initié à d'innombrables techniques expérimentales et m'avoir toujours poussé à aller au delà de ce qui était déjà obtenu. Ensuite Sébastien Ducruix pour son recul permettant de remettre en question les choix effectués et les théories proposées pour leur assurer des bases solides. Le plus grand remerciement que j'ai à leur faire est toutefois de m'avoir suffisamment fait confiance pour me laisser explorer des chemins qui n'étaient pas forcément prévus au départ et m'avoir par là offert une liberté que j'ai fortement appréciée.
J'en profite ici pour adresser un remerciement particulier à Philippe Scouflaire pour sa disponibilité pour la mise en place des diagnostics expérimentaux et surtout pour son soutien et sa réactivité face aux problèmes de laser.

Je souhaiterais ensuite remercier Christine Rousselle pour avoir accepté la présidence de mon jury. De grands remerciements sont également destinés aux deux rapporteurs de mon travail, Frédéric Grisch et Philippe Guibert, pour le temps qu'ils y ont consacré. Enfin, je remercie Yannis Hardalupas pour ses commentaires approfondis ainsi que Yoann Méry pour son point de vue plus industriel.

Il me faut également absolument remercier l'ensemble des personnels administratifs et techniques du laboratoire. Il va sans dire qu'aucune thèse, en particulier expérimentale, ne pourrait voir le jour sans leur aide pour les fabrications et dépannages de toutes sortes ainsi que les commandes. Leur réactivité et leur expertise m'ont permis d'éviter bon nombre de problèmes potentiellement bloquants.

En restant dans le domaine du laboratoire, il me faut remercier l'ensemble des chercheurs y travaillant pour la bonne ambiance qui y règne. Les discussions informelles mais cependant instructives avec les permanents et la bonne humeur apportée par les thésards sont de vrais points bénéfiques pour la réussite d'une thèse. Quelques mentions spéciales aux "devenus permanents" que sont Aymeric, Bene et Clément ainsi qu'aux thésards avec qui j'ai pu partager notre

grand bureau : les "old school" (Aless, Fred, Tapish), les "normaux" (Raph, PEB, Wenjie, Ayane, Meng, Benjamin) et les "new school" (Pedro, Mathieu, Robin, Milan). Merci également à tous les motivés avec qui j'ai pu faire du sport et surtout aux super-motivés du Raid (Wenjie, Marek, Nico, Théa, Matthieu, Adam, Aymeric).

Un grand merci à tous mes proches. Ma famille tout d'abord, notamment pour m'avoir permis de faire des études aussi longues sans aucun souci matériel et de m'avoir laissé faire mes choix tout en me conseillant du mieux possible. Mes amis ensuite, qui ne veulent toujours pas me lâcher même après plus de 15 ans pour les plus anciens. Je ne comprends toujours pas mais ça me va très bien. Enfin une mention particulière pour Céline qui a su me soutenir tout au long de cette période particulière qu'est la thèse.

Pour finir, merci à tous ceux que j'ai pu oublier de citer : je vous aime quand même.

Résumé

Les émissions polluantes des moteurs d'avions, en particulier les oxydes d'azote, sont soumises à des normes de plus en plus sévères. En conséquence, il faut faire appel à des stratégies innovantes pour continuer à les réduire. L'une d'entre elle, correspondant à un vrai changement de paradigme, consiste à se diriger vers un mode de combustion dit prévaporisé prémélangé pauvre au lieu de la méthode traditionnelle faisant appel à des flammes de diffusion. Cela consiste à assurer un bon mélange et une évaporation des gouttes de combustible avant la réaction de combustion réalisée avec de l'air en excès. Il est ainsi possible de réduire la température de flamme et d'éviter les points chaud ce qui diminue la production d'oxydes d'azote, dommageables pour la qualité de l'air aux abords des aéroports. Toute médaille ayant son revers, il faut noter que ce nouveau régime de combustion rend les flammes susceptibles de déclencher des instabilités thermo-acoustiques caractérisées par la mise en résonance du brûleur et de la flamme. Parce qu'elles créent d'importantes fluctuations de pression, de vitesse et de température, elles induisent de fortes contraintes sur le système, pouvant conduire à son endommagement.
Dans le but, entre autres, d'éviter ce genre de phénomènes, on peut avoir recours à une stratégie d'étagement du combustible qui consiste à contrôler sa répartition spatiale en utilisant plusieurs zones d'injection pilotables séparément. Le degré de liberté ainsi ajouté permet de mieux maîtriser la flamme mais s'accompagne d'une complexité pouvant déboucher sur des phénomènes inattendus, tels que des cas de bistabilité rendant impossible la prédiction a priori des propriétés de la flamme. Pour ces raisons, l'étude expérimentale des mécanismes pilotant la stabilisation des flammes dans de tels brûleurs est nécessaire.

L'étude présentée ici utilise un brûleur de laboratoire fonctionnant à l'aide de dodécane liquide. Le système est équipé d'une injection de combustible à deux étages indépendants : un injecteur central de type simplex (le pilote) et une couronne multipoint distribuant le combustible sur 10 trous. La disposition de ces éléments donne à l'injecteur une géométrie relativement complexe, à rapprocher des systèmes industriels. La combustion s'effectue en revanche à relativement faible puissance ($<$100 kW) dans une chambre à pression atmosphérique.
La modification de la distribution spatiale du combustible, en jouant sur le poids

relatif de chaque étage d'injection, permet d'observer nombre de phénomènes intéressants. En effet, la forme de flamme peut subir d'importants changements induisant des modifications sensibles de son comportement. En particulier, certains points de fonctionnement sont particulièrement actifs d'un point de vue acoustique tandis que d'autres restent calmes. Un autre effet notable est l'existence potentielle de deux flammes très différentes pour les mêmes conditions opératoires en fonction de la manière dont le point de fonctionnement a été atteint.

L'analyse de ces phénomènes, dans le but de comprendre les mécanismes de stabilisation sous-jacents, fait appel à des diagnostics optiques à haute cadence couplés à des méthodes de post-traitement avancées, notamment la Décomposition en Modes Dynamiques (DMD). Une attention particulière est portée au signal issu de la diffusion de Mie de la lumière par les gouttes de combustible. En effet, en réalisant une tranche laser traversant la chambre, il est possible d'observer la forme générale du spray ainsi que de réaliser des mesures de vitesse par la méthode de vélocimétrie par images de particules (PIV). Des mesures par anémométrie laser Doppler permettent de combiner ces résultats avec une mesure de la taille des gouttes. L'enregistrement du signal de Mie venant des gouttes situées à l'intérieur de l'injecteur permet également de déceler la présence d'une structure cohérente, le PVC (Precessing Vortex Core), prenant racine autour de l'injecteur pilote. En dépit de la difficulté d'accès optique, d'importants éléments sur l'état de l'écoulement d'air à cet endroit peuvent ainsi être obtenus. L'utilisation de ces diagnostics est complétée par une observation précise de la flamme grâce à une caméra intensifiée à haute cadence enregistrant l'émission spontanée du radical CH^*.

La comparaison des données ainsi obtenues ainsi que l'étude des informations provenant des différents capteurs placés sur le système permettent de proposer des mécanismes de stabilisation pour chacune des flammes rencontrées. Ceux-ci mettent en évidence de fortes interactions entre l'écoulement gazeux, les gouttes de combustible et la flamme elle-même, contribuant à la complexité des phénomènes obervés. Deux effets particuliers dus à l'utilisation de combustible liquide peuvent notamment être mis en évidence. En premier lieu, il apparaît que les plus grosses gouttes du spray peuvent être éjectées vers l'extérieur de celui-ci par effet centrifuge, générant ainsi une inhomogénéité dans la répartition du combustible qui peut être la cause d'une forme particulière de la flamme. Le second effet notable provient de la possibilité de maintenir des flammes de très faible richesse lorsque le combustible est injecté à l'état liquide. Ce phénomène est probablement responsable d'un phénomène d'hystérésis observé au cours des expériences. Les résultats obtenus mettent ainsi en évidence l'importance des effets associés à la phase liquide et, par voie de conséquence, l'importance qui doit être accordée à son analyse et sa description lors d'expériences réelles ou numériques.

Abstract

Because of increasingly stringent regulations on jet engines pollutant emissions, new ways of reducing them are needed. A promising way is the use of Lean Premixed Prevaporized (LPP) combustion where the liquid fuel is vaporized and mixed with air in excess before burning. By reducing the flame temperature and avoiding hot spots, this enables to curb the production of nitrogen oxides. This kind of flames tend however to trigger thermo-acoustic instabilities that correspond to a resonance between the flame and the burner and lead to very high amplitude limit cycles. To improve the stability of these flames, a procedure called staging consists in splitting the fuel injection to control its spatial distribution. This however leads to an increased complexity and unexpected phenomena such as bistability can occur. For this reason, experimental studies of the mechanisms leading to flame stabilization in this kind of burner are needed.

In the present work, a model gas turbine combustor fed with liquid dodecane is used. It is equipped with two fuel injection stages: a pressurized nozzle called the pilot and a multipoint device. These elements create an injection system with an intricate geometry that is close to industrial cases. The burner remains however operated at a relatively low power ($<$100 kW) and the combustion chamber is at atmospheric pressure.

When the distribution of the fuel injection is changed, several phenomena can be observed. The flame shapes can change drastically and present different behaviours, some of them showing a strong acoustic activity. In some particular cases, two different flame shapes can be obtained for the same operating conditions depending on the burner history.

To analyse these phenomena and gain insight on the stabilizing mechanisms at stake, high speed diagnostics coupled with advanced post processing techniques such as Dynamic Mode Decomposition are used. The fuel droplets Mie scattering signal is recorded at two different locations in the burner. With a laser sheet crossing the combustion chamber, the general shape of the spray can be observed and PIV post-processing is performed. PDA measurements at the same location allow to monitor the fuel droplet sizes. The second location from which the droplets Mie scattering signal is obtained is just after their exit of the pilot injector thanks to a volumetric illumination there. This enables to monitor the frequency of a Precessing Vortex Core that takes root inside the

injector and impacts the spray. This information provides insight on the state of the air flow inside the injector that is not optically accessible. On top of these diagnostics, the spontaneous emission of the flame in the band corresponding to CH^* is also recorded with a intensified high-speed camera.
By comparing the data provided by all these advanced diagnostic techniques and also analysing the information coming from different sensors all along the experimental setup, it is possible to propose stabilization mechanisms for all the encountered flame shapes. They highlight a strong interplay between the gaseous flow, the liquid fuel spray and the flame itself, leading to the observed complex phenomena. In particular, a fuel segregation effect due to the centrifugation of the biggest droplets is emphasized and can be related to a particular shape to the flame. Similarly, the capability of liquid-fuel to maintain a flame even for very low equivalence ratios is probably associated to a hysteresis phenomenon in the burner by shaping the air flow. The importance of a good monitoring of the liquid phase when dealing with spray combustion is thus emphasized as well as the need for its precise description in numerical simulations.

Contents

List of Tables

List of Figures

Introduction

Environmental and industrial context

Since the beginning of its control by early humans about half a million years ago, fire has been widely used for its propensity to quickly generate heat and light. It is only in the 19th century that its properties have enable to massively produce mechanical work, first through steam generation and then with piston engines and, more recently (beginning of the 20th century), gas turbines. In 2012, around 90% of the worldwide primary energy demand was supplied through combustion (International Energy Agency 2014) and, because it is a complex field involving numerous interactions between thermodynamics, fluid mechanics and chemistry, it remains a strong research topic, especially with the growing environmental concerns.

Even though air transportation contributes to only 2.5% of worldwide CO_2 emissions (DGAC 2012), it is rapidly growing and, more importantly, it also generates pollutant species that can impact local air quality. Aircraft engine emissions are thus strictly monitored and increasingly stringent regulations are set up by the International Civil Aviation Organization (International Civil Aviation Organization 2011). These norms especially target unburned hydrocarbons (UHC), carbon monoxide (CO), nitrogen oxides (NO_x) and smoke (soot).

Pollutants formation and effect

A perfect, complete hydrocarbon combustion reaction would only generate water (H_2O) and carbon dioxide (CO_2). Although these two species have an impact on global climate change, they are generally not considered as pollutant species in the combustion field. The only way to curb their production is to reduce the amount of burnt fuel and thus act on the overall efficiency of the system. Optimizing the combustion reaction can however help to tackle the emissions of other pollutant species.

Unburned hydrocarbons come from an incomplete combustion process. They have an impact on human health and on the environment as well. For example, benzene (C_6H_6) is toxic and carcinogenic. UHC in general can also react with

UV light from the sun to generate ozone (O_3) which is toxic for humans and animals and also a component of photochemical smog.

Particulate matter composed mainly of carbon (soot) can also be produced by a combustion reaction. It is the reason for the black smoke from a candle but also why it can produce a lot of light. Soot is generally produced in rich regions and, although its formation process remains a research topic, the aggregation of polycyclic aromatic hydrocarbon (PAH) plays a key role in its existence. Particles are harmful for human health, especially when they are small enough to enter the respiratory system. Soot can lead to respiratory diseases such as asthma and is a known human carcinogen (IARC 1985). From an environmental point of view, soot is suspected to be a strong contributor to global warming (Bond et al. 2013).

Carbon monoxide is a toxic gas for humans since it reduces the capacity of blood to absorb oxygen and can lead to death by asphyxiation in high concentration. Its production mainly comes from an incomplete combustion reaction when CO is not oxidized into CO_2. In the case of a rich combustion regime, it is the lack of oxygen that prevents the complete formation of CO_2 whereas, in really lean regimes, the low flame temperature is detrimental to the oxidation rate of CO (Rink and Lefebvre 1986). When the temperature increases (namely over 1800 K), it is to be noted that chemical dissociation of CO_2 can happen:

$$CO_2 = CO + \frac{1}{2}O_2$$

and generate more carbon monoxide. There is thus an optimal region for CO emissions in the lean regimes.

Nitrogen oxides regroup both NO and NO_2 because even though NO is predominantly produced, it can be quickly oxidized into NO_2 (leading to the typical brownish color of heavily polluted city air). NO_x are toxic, lead to the formation of ozone and contribute to acid rains. They are currently the major concern about aircraft emissions and three main production mechanisms can be identified. Except in the rare cases when the fuel contains it, the source of nitrogen is N_2 which composes 80% of the air used for combustion. The main contributor is generally the thermal NO mechanism although it can be drastically curbed for temperatures under 1800 K (Lefebvre 1995). It is the oxidation of atmospheric N_2, following the Zeldovich mechanism (Zeldovich et al. 1947):

$$N_2 + O = NO + N$$
$$N + O_2 = NO + O$$
$$N + OH = NO + H$$

Another mechanism for NO production goes from air N_2 to nitrous oxide (N_2O) which is then oxidized into NO (Nicol et al. 1994). Finally, NO can be produced through the prompt-NO mechanism (Fenimore 1971). In this case where NO is found early in the flame, its production involves several reactions which are initiated by the dissociation of N_2 by the CH radical:

$$N_2 + CH = HCN + N$$

UHC and soot emissions can be reduced respectively by ensuring that the combustion is complete (which is also required to achieve high efficiency) and by avoiding fuel-rich conditions. For CO and NO_x however, the problem is more complex and flame temperature plays a great role, as shown in Fig.1.

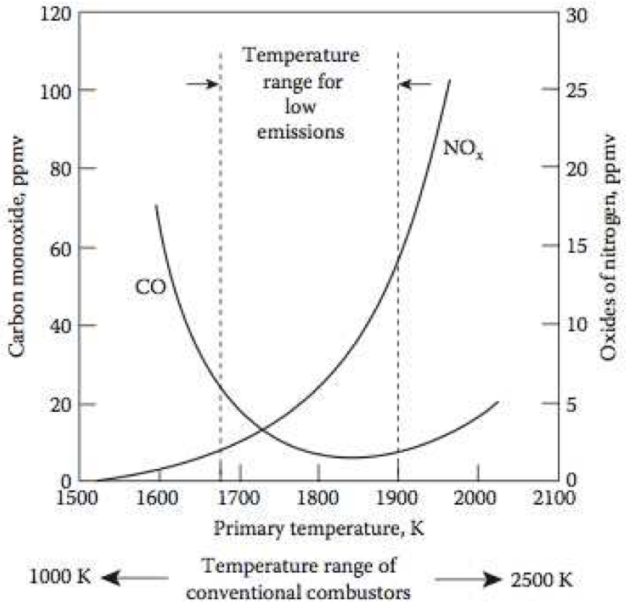

Figure 1 – *Effect of the combustion temperature on the CO and NO_x emissions (Lefebvre 2010)*

Technological solutions

To reduce the amount of produced pollutants, especially NO_x, several technological solutions are studied and implemented. For stationary gas turbines, where weight is not a concern, post treatment techniques can be used. Commonly, steam or water injection in the combustion chamber is used to dilute the burnt gases with interesting performances but a high cost (Mellor 2000). Catalytic reduction can also be used but is still extremely expensive. For aeronautical engines, changing the combustion regime is the preferred way.

Traditionally, combustion in jet engines relies on diffusion flames for stability and safety issues. This combustion mode yields high temperatures, rich regions and poor mixing between fuel and air. As a consequence, the amount of produced pollutant species is high, as explained previously. New injection concepts have thus been developed (Tacina 1990).

The RQL concept (Rich burn, Quick quench, Lean burn) consists in splitting the combustion reaction in two steps (Novick and Troth 1981). First, the combustion process begins in a rich regime just after the fuel injection. It is then quickly diluted by air and continues in lean conditions. The goal here is to avoid hot regions in the chamber coming from burning near the stoichiometry. The key feature for the efficiency of this technique lies in the capability of the injection system to provide a fast and uniform dilution (Rizk and Mongia 1991).

As shown in Fig.1, an optimum in terms of CO and NO_x emissions lies in the lean region for a moderate flame temperature. This condition has to be realised everywhere in the chamber and thus requires an excellent mixing between the reactants. Lean Direct Injection (LDI), where small amounts of fuel are directly injected in the combustion chamber, is generally not optimal because of mixing and vaporization times. The ideal situation is provided by Lean Premixed Prevaporized (LPP) injections but they raise other concerns (Correa 1998), namely in terms of flame stabilization issues (Fritz et al. 2004; Sommerer et al. 2004; Galley et al. 2011) and sensitivity to thermo-acoustic instabilities (Candel 2002; Lieuwen and Yang 2005).

For practical applications, staged fuel injection is often used to try and provide a compromise between LDI and LPP systems with a stabilizing pilot region and a well-mixed main injection. This choice is effective in reducing combustion instabilities (Barbosa et al. 2009) and enhancing flame anchoring (Sengissen et al. 2007). The experimental setup used in this work is equipped with a staged injection for liquid fuel which leads to a complex injection and flame behaviour with key features highlighted in the next section.

Two-phase lean premixed flames

In aeroengines, and by extension in this work, flames are liquid fueled and stabilized by swirling flows. Because of pollutant emission concerns, they also tend towards lean premixed regimes which can lead to stability issues such as flashback or thermo-acoustic oscillations. They are thus the result of an interplay of several complex phenomena, some of which will now be described.

Swirling flows

Swirling flows are used in a wide variety of industrial devices for different purposes from flame stabilization to particle separation. These flow are not only rotating but also have an axial component: the general motion of a fluid particle is thus of helical shape. In order to characterize these kinds of flows, a way of comparing the axial and rotating components is needed. The swirl number is used for this purpose (Chigier and Beér 1964) and represents a ratio between the axial thrust and the axial flux of angular momentum. Assuming the axial flow direction is along the z direction, the swirl number S is defined by the following expression:

$$S = \frac{G_\theta}{RG_z} \tag{1}$$

where R is the radial dimension of the flow and G_θ and G_z are respectively the axial flux of angular momentum and the axial thrust of the flow, defined by the following expressions:

$$G_\theta = \int_0^R \rho u_\theta u_z 2\pi r^2 dr \tag{2}$$

$$G_z = \int_0^R (\rho u_z^2 + p) 2\pi r dr \tag{3}$$

In the previous definitions, ρ represents the density, u_θ and u_z the velocity components in the azimuthal and axial directions respectively and finally p stands for the pressure. When $S = 0$, no rotational component exist and the jet is purely axial. Similarly, an increase of S means that the rotational component becomes more and more dominant and, when the swirl number is high enough (usually over 0.6), the stability of the swirling flow is impacted and vortex breakdown occurs.

Research on vortex breakdown started when this phenomenon was observed in flows around delta wings at high incidence angles, leading to sudden changes in the aircraft behaviour (Hall 1972). Vortex breakdown corresponds to a sudden change in the topology of the flow, when the core of the vortex abruptly widens and the downstream flows becomes highly turbulent. Several studies have been performed with water at moderate Reynolds numbers (Sarpkaya 1971; Leibovich 1978; Escudier 1984) and, although no consensus seems to exist regarding a global theory, some common properties can be extracted (Lucca-Negro and O'Doherty 2001). When the rotation of the flow is dominant over its axial velocity, a stagnation point is created and a low pressure central region is created because of centrifugal effects. As the tangential velocity decays axially, the pressure in the center increases and an axial pressure gradient is created, leading to a reverse flow in this region, as shown in Fig.2. It is called the Inner Recirculation Zone (IRZ) or Center Recirculation Zone (CRZ) and is a key feature of vortex breakdown.

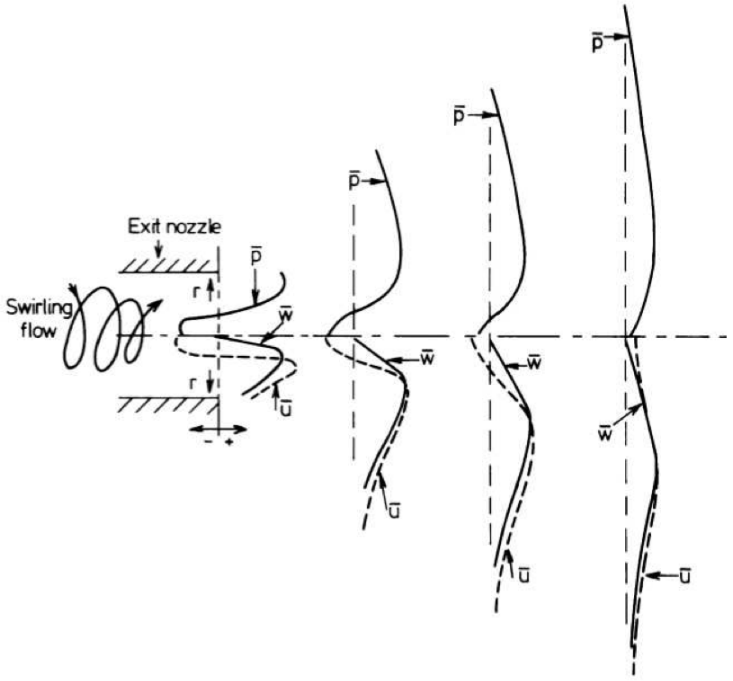

Figure 2 – *Schematic diagram of the IRZ formation from the axial decay of tangential velocity (Syred 2006).*

In some cases, vortex breakdown shows a helical shape which is supposed to come from an instability in the shear layer separating the IRZ from the rest of the flow. This helical structure, shown in Fig.3, is generally quickly damped and is often referred to as the Precessing Vortex Core (PVC). It appears for highly swirling flows (Liang and Maxworthy 2005) and is wrapped around the IRZ. It rotates at a frequency which is a function of swirl number and burner configuration and increases linearly with flowrate.

In practical combustion systems, the whole situation becomes even more complex. First, the velocities are such that the flow is highly turbulent and that compressibility effects can play a role in the formation of vortex breakdown. The swirling flow also comes from a small section and is expanded as it enters the combustion chamber, creating another recirculation region because of its interaction with the corners of the chamber, the Outer Recirculation Zone (ORZ). The intricate geometry induced by fuel feeding systems and the temperature gradients from the flame increase even more the complexity of the problem. Fortunately, the phenomena remain qualitatively similar to what was exposed before which gives swirling flows interesting properties for flame stabilization (Syred et al. 1997).

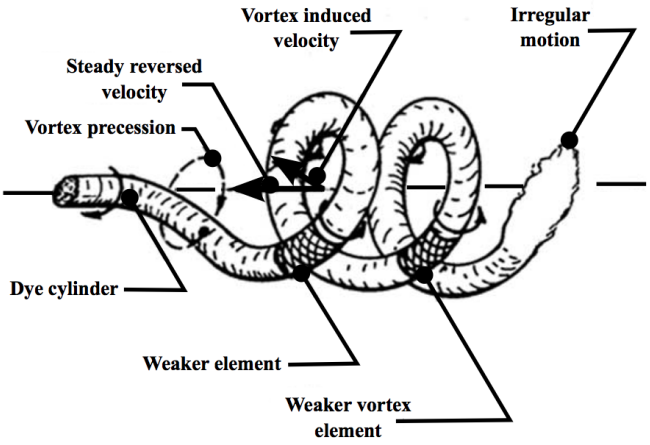

Figure 3 – *Schematics of a vortex breakdown with a helical structure (Chanaud 1965).*

Stabilizing a flame in a high speed flow requires the creation of lower velocity regions and recirculation zones in order to provide fresh reactants with the heat from burnt gases and permanently relight the flame. Such a recirculation zone can be created by a bluff body which may be subjected to strong thermal stress because the flame is anchored on it. A swirling flow provides an interesting alternative because the IRZ can lead to a fully aerodynamic flame stabilization by heating the fresh reactant and creating a high shear region at its border. This shear layer is indeed subjected to strong turbulence levels which increase the mixing between the reactants. These phenomena lead to compact and quite stable flames, two critical features for aero-engines.

The interactions between the Precessing Vortex Core and the flame remain however unclear. The PVC can be either damped or strengthened by the combustion, even in the same burner with different operating points (Oberleithner et al. 2015). The effect of the PVC on flame stabilization and thermo-acoustic instabilities remains an open research topic (Galley et al. 2011; Moeck et al. 2012).

Flashback

In premixed system, a major concern is that the flame can travel upstream as long as it encounters a flammable mixture instead of staying where it is expected to: it is the flashback phenomenon. By inducing thermal stress where parts are not designed for it, flashback can lead to the destruction of the burner (Bernier 2001). Several types of flashback can be identified, with different causes leading to different countermeasures. A typical occurrence of flashback where the flame stabilizes in the mixing tube can be seen in Fig.4.

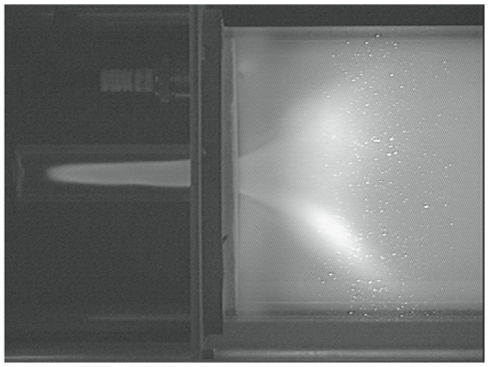

Figure 4 – *Flashback in the premixing tube of a propane-fuelled burner (Galley et al. 2011)*

Four major types of flashback are generally described (Fritz et al. 2004):

- Wall boundary layer flashback
  Primarily in low turbulence flows, the flame can propagate upstream in the boundary layers, where the velocity is lower than the bulk flow velocity. This phenomenon is counterbalanced by the heat loss at the wall which can quench the flame. For this reason, in turbulent conditions where the velocity gradient near the wall is high, this mode of flashback is not commonly observed.
- Turbulent flame propagation
  In turbulent conditions, flame speed is increased because of the wrinkling of the flame front (Poinsot and Veynante 2005). In some cases, the turbulent flame speed can exceed the local axial velocity of the flow and flashback can occur in the core of the flow.
- Flashback due to combustion instabilities
  When combustion instabilities occur and no strong damping mechanism takes place, high amplitude pressure, velocity and heat release fluctuations can be created. Flame can thus be transported upstream by such oscillations and flashback happens. Such extremely high amplitude combustion instabilities are anyway unacceptable in practical combustion systems and rarely occur, except in transient cases.
- Combustion-Induced Vortex Breakdown (CIVB)
  Finally, flashback can be induced by a vortex breakdown creating a recirculation zone that helps the flame travelling upstream. It is referred to as Combustion-Induced Vortex Breakdown (CIVB). This flashback type seems to be dominant in Lean Premixed systems (Sommerer et al. 2004) although the possible interactions between vortex breakdown and flame front are still under scrutiny.

Although, it is not a flashback phenomenon by itself because the flame does not propagate upstream, auto-ignition can also lead to the presence of a flame where it is not supposed to be. Because auto-ignition delay is reduced when temperature and pressure increase, this phenomenon has to be taken into account, especially for industrial applications (Guin and Trichet 2004).

Thermo-acoustic instabilities

Lean premixed flames are especially responsive to flow perturbations (Lieuwen and Yang 2005) and thus have a high dynamic sensitivity. A detrimental consequence of this are thermo-acoustic instabilities which arise when combustion and acoustic waves couple to reach high amplitude limit cycles. They can lead to severe failures, for example in liquid rocket engines (Culick 2006).

In the end of the 19th century, Rayleigh (1878) showed that flames could amplify acoustical oscillations if what is now known as the Rayleigh criterion is met:

$$\int_0^T p'(t)q'(t)dt > 0 \tag{4}$$

where T is the period of an oscillation, p' stands for the pressure fluctuations and q' for the heat release rate fluctuations. Roughly speaking, it means that the phenomenon is amplified when heat release and pressure oscillations are in phase. Pressure fluctuations come from the acoustic behaviour of the combustor and heat release rate fluctuations from changes in the flame position or reaction rate. There thus needs to be a feedback mechanism to couple pressure and heat release rate fluctuations.

Changes in the heat released by the flame can happen due to modulations of the reaction rate coming from oscillations of the equivalence ratio (Lieuwen and Zinn 1998). A sound wave travelling in the combustor can indeed modify the fuel flow rate of the injector. Large coherent structures can also be excited by acoustic waves and create deformations of the flame front or small flame pockets leading to heat release fluctuations (Paschereit et al. 1999). A feedback of the acoustic waves on the flame can thus have several sources and it has been shown that the delay between the fuel injection and the reaction zone is a key parameter for the onset of thermo-acoustic instabilities (Poinsot et al. 1987).

Because of the dramatic impact they can have on industrial systems (Mirat 2015), thermo-acoustic instabilities are a strong current research topic, even on simple configurations to extract tools for prediction and control (Noiray 2007; Boudy 2012). For industrial configurations, three main ways of tackling the issue exist. First passive control consists in modifying the geometry or flow field in the chamber by using acoustic dampers for example. Although this

solution may not be ideal for low frequencies (Delabroy et al. 1998), promising results have recently been obtained with perforated plates (Scarpato 2014). Active control uses an active element (such as an electrovalve or a siren) to generate modulations of parameters in open or closed loop and avoid the onset of thermo-acoustic instabilities (Candel 1992). Finally, it is possible to change the operating point for a more stable one when instabilities start to appear. This kind of control requires a constant monitoring of the system as well as the knowledge of its stability regions. Staged injection are natural candidates for such a control because fuel flow rate (and thus power output) can be kept constant while spatial fuel distribution is changed.

Flame topology

In perfectly premixed conditions, the flame position can be described by level set approaches such as the G-equation. A simple averaged version of this equation yields (Palies et al. 2011):

$$\frac{\partial \overline{G}}{\partial t} + \overline{v}.\nabla \overline{G} = S_T |\nabla \overline{G}| \tag{5}$$

where $\overline{v}$ is the averaged flow velocity and S_T the turbulent flame speed. It can be seen from this equation that when the turbulent burning velocity is opposed and equal to the flow velocity, the flame position does not change. This very rough analysis shows that the flame will stabilize itself in regions where the flow velocity corresponds to the turbulent burning velocity, and because the latter cannot generally reach extremely high values, it corresponds to relatively low velocity regions. In confined swirling flames, these regions are the shear layers created at the boundaries between the swirling jet and the inner and outer recirculation zones, as shown in Fig.5. This explains why V-shaped and M-shaped flames are often encountered in such burners.

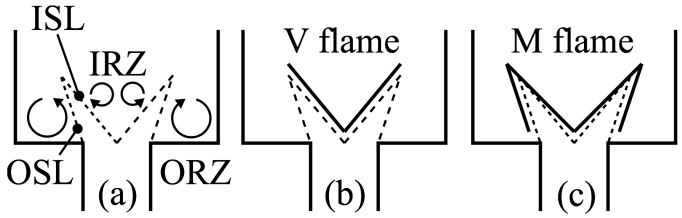

Figure 5 – *(a) Schematic of a swirling flow with vortex breakdown in a combustion chamber showing its inner (ISL) and outer (OSL) shear layers and the inner (IRZ) and outer (ORZ) recirculation zones. (b) Stabilization of V-shaped flames. (c) Stabilization of M-shaped flames. From Guiberti (2015).*

As shown by the previous consideration of the G-equation, changing the flame position can happen because of a change in the flow velocity or the turbulent

burning velocity. S_T depends on the flame front stretching and wrinkling due to turbulence and on the reaction rate. At the combustor level, different means of changing the flame position can thus be used. Acting on the flow obviously changes the velocity but also the turbulence level and the reaction rate can be changed by acting on the chemistry (with a different fuel or equivalence ratio for example) or the temperature.

Changing the flow field is the simplest way of changing the flame topology. For example, by modifying the swirl number thanks to a variable blade angle swirler, Durox et al. (2013) observed drastic changes in the flame position. Results can be seen in Fig.6.

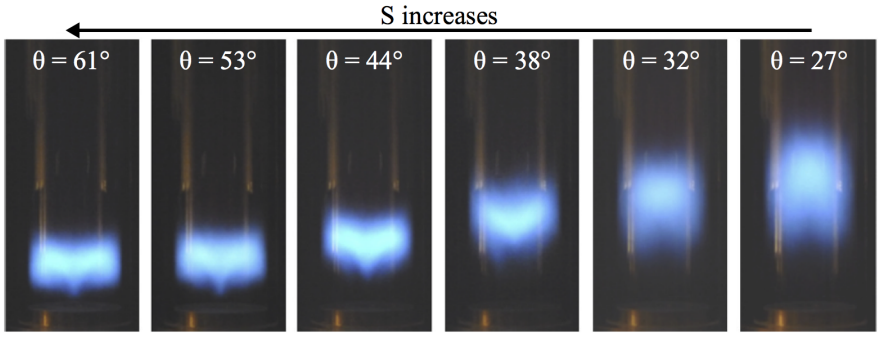

Figure 6 – *Images of premixed CH4/air flames in an atmospheric laboratory scale burner for different swirler blade angles. From Durox et al. (2013).*

Changing the combustible mixture can also lead to modifications of the flame shape. Kim et al. (2010) found that an increase of the proportion of hydrogen (H_2) in a CH_4/H_2/air promotes the existence of M-shaped flames because of the increase in flame speed that enables the flame to stabilize in the outer shear layer.

In a pressurized model combustor, Seo (1999) observed that an increase in the injection temperature of the reactant mixture leads to a bifurcation from a V-shaped to a M-shaped flame. Results of 2D large eddy simulation on the same problem by Huang and Yang (2004) can be seen in Fig.7. They show that the flame shape transition is triggered by a flashback in the boundary layer along the wall. By increasing the reaction rate and thus the turbulent flame speed, the increase in fresh gases temperature enables this flashback to happen.

Flame topology and stabilization is thus a complex subject because it involves numerous interactions between the flow field and the combustion reaction zone. Furthermore, the flame itself has an effect on the flow field and can drastically change it. It has been shown that different flame shapes could lead

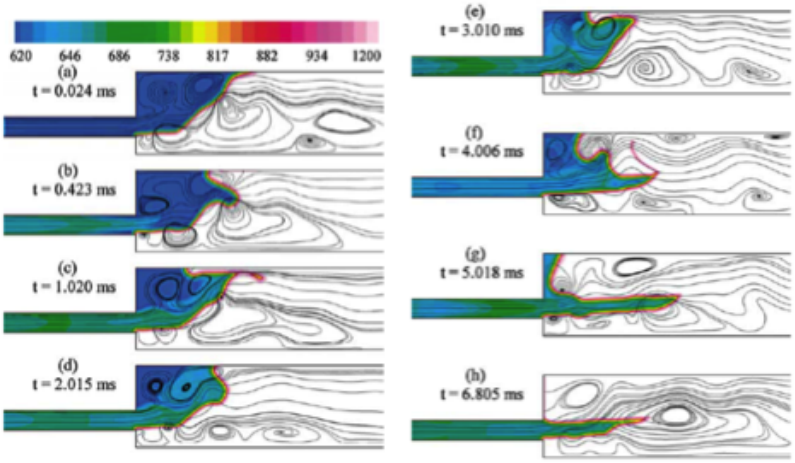

Figure 7 – *Change in flame topology triggered by a flashback in the boundary layer along a combustion chamber wall. From Huang and Yang (2004).*

to completely different properties, in terms of resistance to thermo-acoustic instabilities or pollutant emissions for example (Schmitt et al. 2007). When the flow is not perfectly premixed, the complexity of the problem is even higher because reactants availability is an added factor to all the previously exposed phenomena.

Liquid fuel combustion specificity

Because of their high energy density, the use of liquid fuel is mandatory for aircrafts. This however yields added complexity to the combustion process. The fuel indeed needs to be atomized in order to be transported to the reaction zone and to vaporize before the combustion itself can take place.

The first step for liquid fuel combustion consists in creating droplets small enough to vaporize quickly. Two main ways of atomizing fuel for gas turbines exist. Pressurized nozzles (sometimes referred to as simplex atomizers) rely on the injection of high pressure liquid into a gaseous atmosphere at a lower pressure. With the help of a proper geometrical design (by imparting swirl before the injection for example), a cone of droplets is created. The second family uses air assistance to create shear stress on the liquid and atomize it (for example by injecting the liquid in a gaseous crossflow).

Two non-dimensional numbers are to be considered for liquid atomization in a gaseous medium: the Ohnesorge number Oh (Ohnesorge 1936) and the Weber

number We which are defined by the following formulas:

$$Oh = \frac{\mu_l}{\sqrt{\rho_l \sigma L}} \tag{6}$$

$$We = \frac{\rho_g v_{l-g}^2 L}{\sigma} \tag{7}$$

where μ_l is the liquid viscosity, ρ_l the liquid density, σ the liquid surface tension and L a characteristic length scale (typically a droplet diameter). In the Weber number formula, ρ_g is the gas phase density and v_{l-g} the relative velocity between the fuel droplet and the gaseous medium. Oh depends only on the geometry and on the fuel properties. It characterizes the propensity of a liquid to form droplets by comparing the viscous dissipation of energy which prevents breakup to the inertia and surface tension. A high Ohnesorge number means the liquid is too viscous to properly break up whereas a low value corresponds to a potential multiple atomization (McKinley and Renardy 2011). The Weber number We is used to compare an external stress on the droplet (here created by the inertia of the surrounding flow) to the stability of the droplet provided by the surface tension. It is generally accepted that a droplet breaks up if its Weber number is over a critical value (Hinze 1955). No universal value for this critical Weber number can however be extracted from the literature because it depends among other things on the value of Oh (Tarnogrodzki 1993). When the Ohnesorge number is low (under 0.1), it can however be noted that a critical value of 12 for We is generally retained (Pilch and Erdman 1987).

The atomization of the liquid fuel in practical systems never provides only one size of droplet but rather a polydisperse spray where droplets have different behaviours depending on their size. It is thus necessary to characterize the quantity of droplets of each size, by using a diameter distribution based either on the number of droplets or on their mass. Commonly, for aeroengine injectors, these distributions can be fitted to classical probability laws such as the log-normal distribution or the Rosin-Rammler (or Weibull) distribution (Mugele and Evans 1951). In order to quickly compare different fuel injectors or injection conditions, a particular average diameter is used: the Sauter Mean Diameter (SMD or D_{32}). It is defined as the diameter of an individual droplet with the same ratio between the volume and the surface area as the entire spray. It is of practical interest in fuel sprays because volume can be related to the mass of injected fuel and surface area represents the exchange capacity with the environment, namely for vaporization purposes.

Atomizing the liquid fuel is not enough because the droplets have to mix with the air and be transported to the reaction zone. The propensity of the droplets to follow the gaseous flow is given by the Stokes number St defined as follow:

$$St = \frac{\tau_d}{\tau_f} \tag{8}$$

where τ_d is a characteristic relaxation time for the droplet and τ_f a characteristic time for the flow. St is roughly a comparison between a droplet inertia and its drag, meaning that for large Stokes numbers, droplets show a ballistic behaviour. This means that they will not follow the underlying gaseous flow but will be driven by their own momentum. On the contrary, for low Stokes numbers, droplets will be perfect tracers of the gaseous flow. Because of the wide range of droplet diameters in a typical spray, the different Stokes numbers can lead to the segregation of droplets (Zimmer et al. 2003), changing the local mixture fraction and evaporation rate (Reveillon and Demoulin 2007).

Because combustion is a chemical reaction happening between gaseous species, the liquid fuel needs to vaporize before reacting. A simple evaporation model is given by the d^2-law (Spalding 1953) which states, under very strong assumptions, that the squared diameter of an evaporating droplet decreases linearly with time. Empirical values for the evaporation rate can be found in the literature (Ghassemi et al. 2006). This model however considers an isolated spherical stationary droplet at a constant temperature in a stable environment and is therefore not suitable for the turbulent combustion cases (Law 1982). Still, it can provide interesting orders of magnitude.

All the previously described phenomena (atomization, transport and vaporization) generally occur simultaneously in a gas turbine environment, leading to a more or less dense droplet cloud with or without fuel vapour. As a consequence, the combustion reaction can yield very different behaviours. A classification of the two-phase combustion regimes, proposed by several authors (Chiu and Liu 1977; Chiu et al. 1982; Candel et al. 1999), is based on the group combustion number G which takes into account the number of droplets and the distance between them. As shown on Fig.8, for large values of G, the cloud of droplets is very dense and its core presents non-vaporizing droplets because heat diffusion inside the cloud is prevented. The flame only stabilizes outside the cloud once fuel vapour has mixed with the surrounding air. As G decreases, the core droplets can vaporize but are still too close to each other to allow the fuel vapour to mix with the air and the flame thus remains outside of the cloud. A further decrease in the group combustion number shows some droplets surrounded by a flame until finally, when the cloud is dilute enough ($G \ll 1$), all the droplets burn individually. Further information can be found in Chigier (1983).

The classification based on G is quite static and does not take into account the convection of the droplets relatively to their vaporization time. It has been shown (Borghi 1996; Reveillon and Vervisch 2005) that the droplets can, if their vaporization time is large, cross the flame front and create fuel inhomogeneities. On the contrary, a short vaporization time leads to a flame behaviour similar

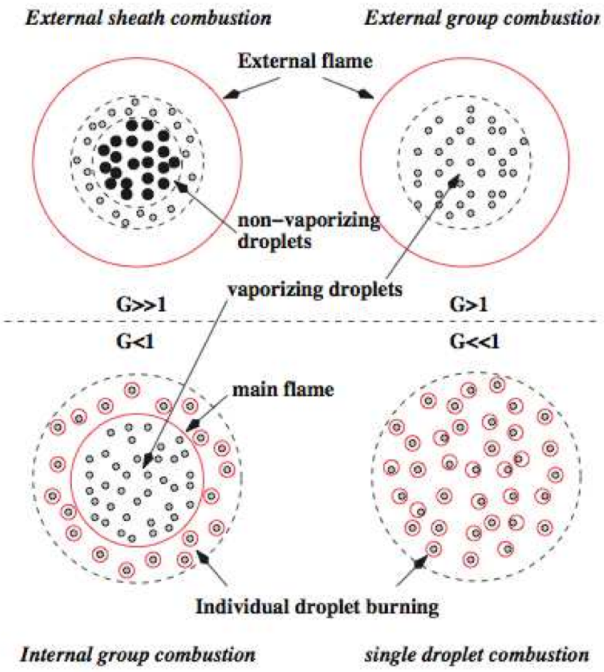

Figure 8 – *Morphological classification of two-phase combustion regimes. From Chiu and Liu (1977).*

to a gaseous flame.

Thesis objective and content

This introductory part shows that, because of increasing environmental concerns, aircraft pollutant emissions need to be curbed. From a combustion point of view, this means moving towards lean premixed combustion which can provide the adequate flame temperature. Such conditions need to be achieved with proper mixing and vaporization of the liquid fuel but perfectly premixed flames can become unstable. Multipoint injection systems, which distribute the fuel at several locations, are good candidates for the mixing part but they need to be coupled with a pilot injection in order to ensure stability. Such added complexity in an already harsh environment requires a proper understanding of the physical processes leading to flame stabilization.

This thesis follows the work of Barbosa (2008) who studied a staged multipoint injector with propane as a gaseous fuel and showed that changing the fuel staging led to different flame behaviours that can trigger thermo-acoustic instabilities. Providakis (2013) then converted the experimental setup to liquid fuel adding the complexity of atomization and vaporization to an already intricate

geometry. He highlighted a hysteresis phenomenon with fuel staging leading to different flame shapes with a competition between a coherent aerodynamical structure (the Precessing Vortex Core) and a thermo-acoustic instability based on the quarter-wave mode of the chamber. The goal of the present work is to provide data on the flame stabilization processes depending on the fuel staging by focusing on the bistable regions and on the transient phenomena. The general aim is to provide an insight on the interplay between the airflow, the spray and the flame happening in this kind of multipoint staged burner.

The first of the three parts of this document presents the tools used in this study. In the first chapter, the laboratory-scale experimental setup is exposed. Chapter 2 focuses on the diagnostics, with a tendency towards time-resolved optical methods. The third chapter presents the methods used to obtain and post-process the data. The second part, divided into two chapters, focuses on the burner behaviour when the fuel staging is fixed. Chapter 4 describes an operating point with a pilot-only injection which presents a characteristic flame shape and is also used to perform an analysis of the sensitivity of the PVC to air flow rate modulations. The following chapter highlights a multipoint-dominated fuel injection which can present two different flame topologies with different properties. The last part focuses on the hysteresis phenomenon and the transition between flame shapes happening when the fuel staging is changed while keeping the power constant. Chapter 6 presents the hysteresis phenomenon and studies the effect of slight changes in the operating conditions on the cycle. The last chapter then highlights a particular transition event which has the particularity of showing a metastable flame shape. Finally, a summary of the main findings ends the document together with potential perspectives to go further in the exploration of this field.

Part I

Experimental setup and processing methods

Chapter 1

Staged burner

This chapter presents the experimental setup BIMER (Banc à Injection Multiple pour les Ecoulements Réactifs). The injection system consists in two stages, each of them including fuel and co-rotating swirled air injections, in order to deliver a maximum power of 150 kW. The combustor features a water-cooled combustion chamber and an automated control software to allow repeatable operation for extended durations. The most recent addition is a siren-type device to perform modulations of the air flow rate.

1.1 Injection system

The injection system geometry is a simplified version of a SNECMA prototype. Details on the design choices for the injector and its similarities with the industrial device can be found in Barbosa (2008) and Providakis (2013).

1.1.1 Geometrical description

The injection device, which can be seen in Fig. 1.1, is composed of two stages: the pilot stage (upstream) and the take-off stage (downstream). Each stage consists in one swirler and one liquid fuel injection device.

The pilot stage fuel injection system is a pressurized nozzle with a flow number of 1.4 $\mathrm{l{\cdot}h^{-1} \cdot bar^{-1/2}}$. Provided by the MMP company (Micro-Mécanique Pyrénéenne), it generates a hollow cone of fuel droplets. Air is injected through an 18 vane swirler with inner and outer diameters of 30 mm and 45 mm respectively. The channels are equally spaced and have a width of 6 mm and an angle of 42° so that the geometrical swirl number is close to 0.6.

The take-off stage uses a multipoint fuel injection device made of a hollow ring supplied with fuel. From this ring, the fuel is injected through 10 holes of 0.3 mm in diameter equally spaced over a circle on the frontal face of the ring.

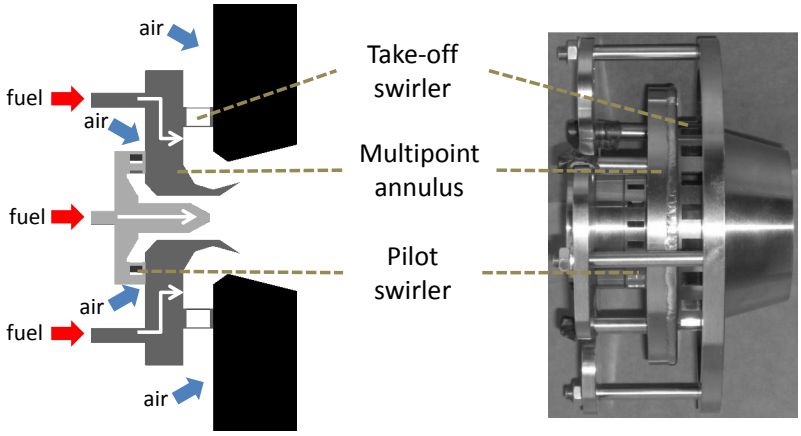

Figure 1.1 – *Radial cut and picture of the injector showing the pilot stage (light grey) and the take-off stage (dark grey).*

The air injection is made through a swirler with inner and outer diameters of respectively 55 mm and 75 mm. Twenty 10 mm-wide vanes inclined with a 35° angle create the swirl motion to obtain a geometrical swirl number close to 1. The swirler is placed so that each fuel injection hole is aligned with the center of a vane and that the pilot and take-off swirls are co-rotating.

The injection system is installed in a plenum to provide clean upstream air conditions and comes out in the combustion chamber.

1.1.2 Air staging

In Barbosa (2008), the pilot and take-off swirlers were designed to provide a fixed air mass flow rate split of 20% in the pilot stage and 80% in the take-off stage. However, adding the pressurized nozzle for liquid fuel changed the geometry of the injector and thus the air split which has to be measured again.

To compute this air split, three measurements with a differential manometer (Kimo CP100 with an accuracy of 1.5% of the measured value) were performed. First, the pressure drop between the plenum and the beginning of the combustion chamber is measured for different air flows. Each swirler is then alternatively plugged and corresponding pressure drops are recorded. The results are plotted on Fig. 1.2.

Using the Bernoulli theorem, an analogy with electricity can be drawn. Indeed, a generic link between pressure drop (ΔP) and flow rate (Q_{air}) can be made using the following equation, where R_H represents a hydraulic resistance:

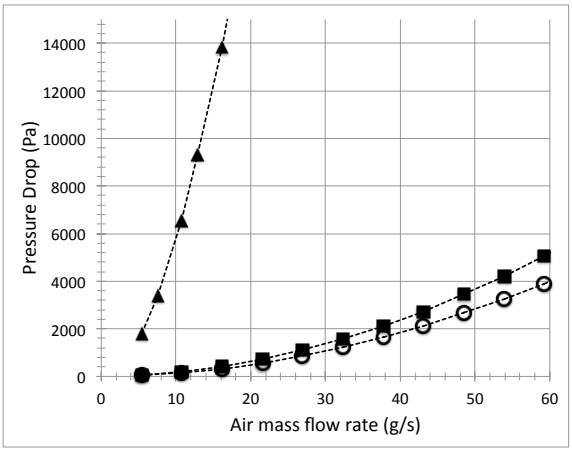

Figure 1.2 – *Pressure loss between the plenum and the chamber versus air flow rate for the complete injector (circles), the pilot stage only (triangles) and the take-off stage only (squares).*

$$\Delta P = R_H Q_{air}^2 \tag{1.1}$$

From the data on Fig. 1.2, values of R_H can easily be obtained for the three cases and are shown in table 1.1 with $R_{H,i}$, $R_{H,po}$ and $R_{H,to}$ respectively standing for the complete injector, the pilot-only and the take-off-only measurements.

Table 1.1 – *Hydraulic resistances for the three cases measured with the differential manometer.*

$R_{H,i}$	$R_{H,po}$	$R_{H,to}$
$(Pa \cdot s^2 \cdot g^{-2})$	$(Pa \cdot s^2 \cdot g^{-2})$	$(Pa \cdot s^2 \cdot g^{-2})$
1.09 ± 0.02	51.36 ± 0.77	1.41 ± 0.02

The values of $R_{H,i}$, $R_{H,po}$ and $R_{H,to}$ cannot however be used directly to compute the air split between the stages. Indeed, the pressure ports of the differential manometer cannot be placed just before and after the stages and common pressure drops have occurred for the three measurements. To take into account this phenomenon, an electrical analogy for the complete system can be found on Fig. 1.3, where $R_{H,p}$ represents the hydraulic resistance of the pilot stage, $R_{H,t}$ the hydraulic resistance of the take-off stage and $R_{H,c}$ the hydraulic resistance of the common parts which is expected to be way lower than the two other.

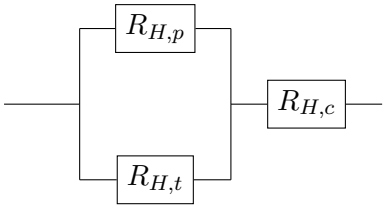

Figure 1.3 – *Electrical analogy for the pressure drop through the injector.*

From Fig. 1.3 and the definition of the hydraulic resistance in equation (1.1), it is then possible to obtain the system of equations (1.2) linking the measured resistances $R_{H,i}$, $R_{H,po}$ and $R_{H,to}$ to the desired values of $R_{H,p}$, $R_{H,t}$ and $R_{H,c}$.

$$\begin{aligned} R_{H,po} &= R_{H,p} + R_{H,c} \\ R_{H,to} &= R_{H,t} + R_{H,c} \\ R_{H,i} &= R_{H,eq} + R_{H,c} \\ \text{with } R_{H,eq} &= \frac{R_{H,p}R_{H,t}}{(\sqrt{R_{H,p}} + \sqrt{R_{H,t}})^2} \\ &\text{from the parallel association of } R_{H,p} \text{ and } R_{H,t}. \end{aligned} \tag{1.2}$$

The values of $R_{H,p}$, $R_{H,t}$ and $R_{H,c}$ obtained by solving the system are shown in table 1.2. As expected, the value of the common hydraulic resistance, $R_{H,c}$, is lower than the other hydraulic resistances.

Table 1.2 – *Hydraulic resistances of the injector parts computed from the system of equations (1.2).*

$R_{H,p}$	$R_{H,t}$	$R_{H,c}$
$(Pa \cdot s^2 \cdot g^{-2})$	$(Pa \cdot s^2 \cdot g^{-2})$	$(Pa \cdot s^2 \cdot g^{-2})$
51.21 ± 0.86	1.26 ± 0.11	0.15 ± 0.09

From these values, it is now possible to compute the air split, that is the proportion of air which went through the pilot stage, from the following equation:

$$\frac{Q_{air,p}}{Q_{air}} = \sqrt{\frac{R_{H,eq}}{R_{H,p}}} \tag{1.3}$$

where $Q_{air,p}$ represents the mass flow rate of air in the pilot stage and Q_{air} the mass flow rate of air through the whole injector. The numerical value of the air flow proportion in the pilot stage is thus $13.5 \pm 0.6\%$ which is, as expected, lower than the previous 20% used in Barbosa (2008) because the pressurized fuel nozzle disturbs the path of air through the pilot stage.

1.2 Burner setup

A 3D rendering of the experimental burner is presented in Fig. 1.4. It shows the entire air feeding line as well as the combustion chamber which will now be described.

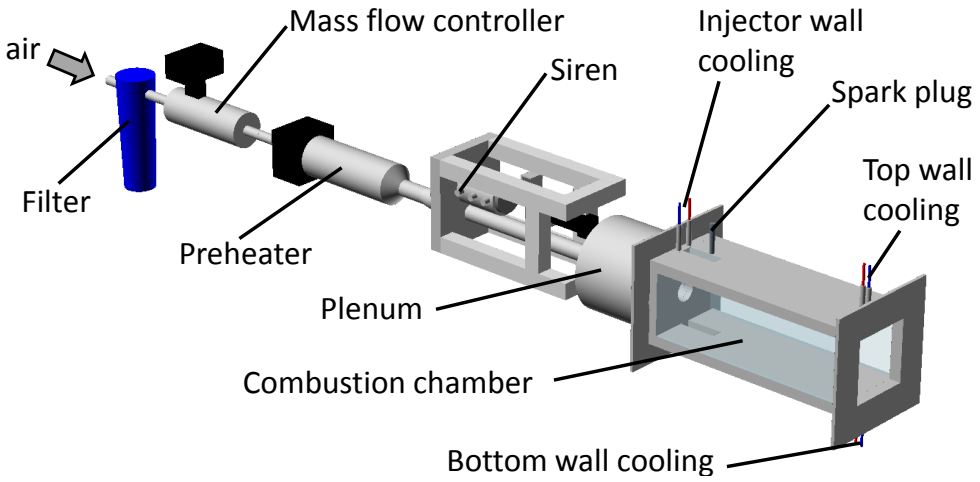

Figure 1.4 – *3D rendering of the burner with its air feeding line.*

1.2.1 Combustion chamber

The cylindrical plenum in which the injection system previously described is placed is coupled to a water-cooled, optically-accessible combustion chamber. The chamber has a square section (150×150 mm^2) with a length of 500 mm and its outlet is fully open which means it remains at the atmospheric pressure. To enable prolonged operation, the walls on the top, bottom and beginning of the chamber are water-cooled. Three thermocouples measure the exit temperature of the cooling water of each wall for safety reasons. Because optical diagnostics are extensively used with this setup, the two side walls are made with long silica windows and slits in the top and bottom walls, near the injection system, enable the use of a vertical laser sheet on the axis of the chamber. To ignite the mixture at the beginning of an experiment, an aeronautical spark plug (Eyquem HEP-502) is placed through the top wall, near the laser slit, at an axial distance of 60 mm from the injector wall, following a careful optimisation process described in Providakis (2013).

1.2.2 Fluids distribution

From the Fig. 1.4, the path of air can be described from left to right. First, dry, compressed air at 0.6 MPa comes from the laboratory compressor. It is filtered before reaching the mass flow controller (Bronkhorst In-Flow F-206-BI

with a precision of ±1% of the full scale which corresponds to 107.75 g/s). The air is then preheated with an electric heating system (Sylvania SureHeat Max, 18 kW) in order to ease the vaporization of the liquid fuel. Modulations of the flow rate can then be performed with the siren which will be described in the dedicated section. The air can finally flow in the plenum to reach the injector and be split between the two stages (13.5% in the pilot and 86.5% in the take-off) as described before. K-type thermocouples are placed along the air feeding line to monitor the air inlet temperature, the preheater temperature and the temperature inside the plenum.

A schematic view of the fuel feeding system from the tanks to the injector is shown in Fig. 1.5. Two completely separated lines are used for the pilot and take-off fuel injections which enables to precisely control the fuel staging in the injector.

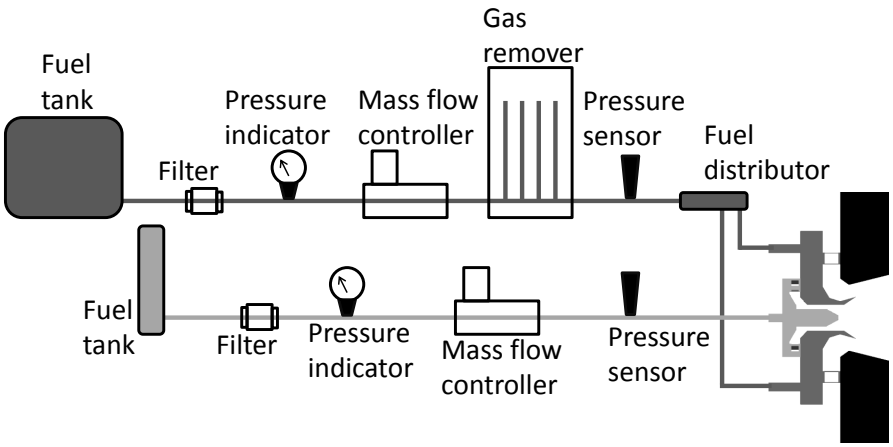

Figure 1.5 – *Schematic view of the fuel seeding system.*

Since the pilot stage of the injector uses a pressurized nozzle for the fuel injection, high pressure is needed in the corresponding feeding line. For this purpose, a 3.6 l tank is pressurized with nitrogen at 2.7 MPa. The fuel is filtered before flowing into a mass flow rate controller (Bronkhorst Mini Cori-Flow M14-AAD with an accuracy of 0.2% of the rate) coupled with an air assisted vane (because of the high pressure in the line). It then directly reaches the center of the injector.

For the take-off injection, the multipoint device creates much less pressure drop than the pressurized nozzle of the pilot stage. The associated 15 l tank is thus also pressurized with nitrogen but only at 0.4 MPa. After the filter, the fuel reaches the mass flow rate controller (Bronkhorst Cori-Flow M54C with an accuracy of 0.2% of the rate). It then goes through a gas removing device

because bubbles of previously dissolved nitrogen may appear after the pressure drop created by the flow rate controller. After being split in two secondary lines in a distributor, the fuel finally reaches the back of the multipoint annulus to be injected. Pressure sensors are placed before and after the mass flow controllers in both the pilot and take-off feeding lines in order to detect any incorrect operation of the system.

1.2.3 Automated control

To ensure the repeatability of the experiments, especially during transient operation, a LabView routine has been developed to control the mass flow rates. The built-in PID feedback loops of the mass flow controllers remain in use but the setpoints are automatically defined and changed by the program at a lower rate (about 10 Hz). Because the air mass flow controller is faster to react than the liquid mass flow controllers, two different automated control modes can be used. The first one, mainly used for increasing power from the ignition point to the measurement point, sets a target to be reached in an adjustable number of steps for the fuel flow rates. The air flow rate setpoint is then adjusted on the fly to keep the global equivalence ratio as stable as possible from the fuel flowmeters readings. The second operating mode decouples the air flow rate from the fuel flow rates and enables to perform variations of the fuel staging at a stable fixed air flow rate. An emergency mode is used to quickly stop the fuel flow while keeping a fixed air flow rate. This mode can be manually triggered but can also be automatically launched if some sensors reach preset thresholds (too hot cooling water for example). Finally, a manual mode enables to set each flowmeter setpoint separately just like with the regular hardware system.

This routine is also used to gather information on the system and create a log of the experiments performed with the burner. Indeed, every tenth of a second, data from several sensors are recorded in a text file saved on the control computer. One can then analyse after the experiment the values of the flow rates, of several temperatures all along the setup (for air and cooling water) and of the pressures in the fuel feeding lines. These values are also displayed live and used to compute useful instantaneous information such as power, equivalence ratio or the amount of remaining fuel in the tanks.

1.3 Siren device

The most recent addition to the experimental setup is a siren device placed between the preheater and the plenum. This device, created by the company Combustion Bay One (CBOne, Graz, Austria), enables to perform air flow rate modulations with independently controlled frequency and amplitude (Giuliani et al. 2002).

1.3.1 Principle

The main idea behind this siren device is a rotating toothed wheel in front of a nozzle through which the air flows. As they alternatively cover and uncover the nozzle surface, the teeth of the wheel modulate the air flow at a frequency depending on its rotational speed. By varying the position of the toothed wheel relatively to the nozzle, the surface covered by the teeth also varies, meaning that the amplitude of the modulation can be chosen (Giuliani et al. 2012).

The diameter of the nozzle and the number of teeth on the wheel can be changed depending on the setup on which the siren is mounted and on the goals of the experiment. For its use with the BIMER burner, the siren is equipped with a 12 mm diameter nozzle and a wheel with ten 9 mm-high teeth. Because the relative position of the nozzle and the wheel can be varied to change the amplitude of the flow rate modulations, a way to measure this change is needed. From geometrical considerations, the Covered Surface Ratio (CSR) is defined as the ratio between the maximum area of the nozzle covered by the tooth and the nozzle area when the tooth is not in front of it. For example, a CSR of 55% means that 55% of the nozzle area is alternatively covered and uncovered by the teeth of the wheel while the remaining 45% undergo no modulation. The relative positions of the nozzle and toothed wheel for different CSR can be seen in Fig. 1.6.

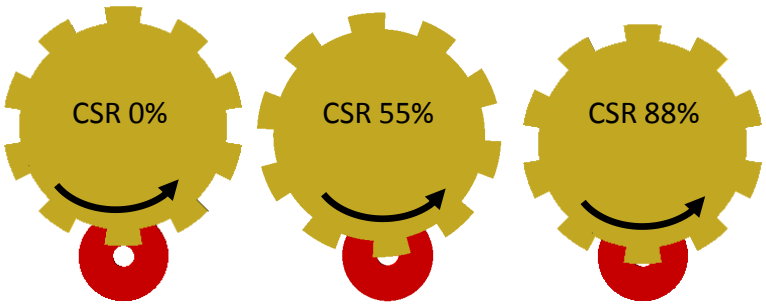

Figure 1.6 – *Relative positions of the toothed wheel and siren nozzle for different CSR.*

1.3.2 Harware description

A 3D rendering of the siren can be seen in Fig. 1.7. To ease the visualization of the different parts, the supports have been made transparent.

The toothed wheel and the nozzle are integrated in a carter that prevents any leak. The wheel is linked to its motor (frequency motor) with a shaft and a

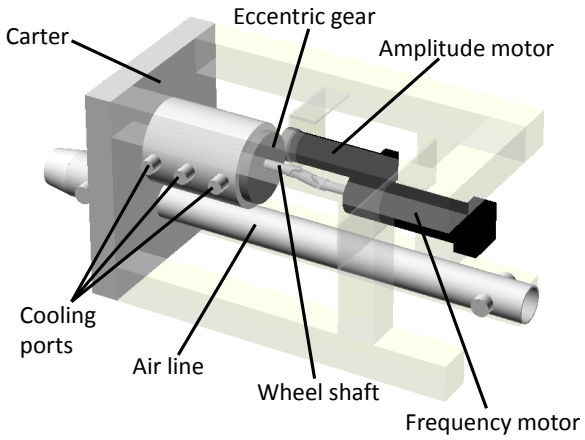

Figure 1.7 – *External appearance of the siren device when the wheel is retracted (CSR 0%).*

joint coupling to allow for rotation and translation relative to the nozzle. This latter motion is made possible by an eccentric gear linked with another gear to the amplitude motor. One rotation of the amplitude motor thus creates a half rotation of the eccentric gear, effectively moving the shaft of the toothed wheel from the top position (as shown in Fig. 1.7) to the bottom position (CSR 88%, when the wheel is fully in front of the nozzle). Because the siren is rated to work at elevated pressure and temperature, the shaft and the bearings are cooled with air at ambient temperature through the cooling ports. To monitor the air flow before and after the siren, ports are placed on each side of the air line and enable the use of different sensors (pressure sensor, thermocouple, hot wire...) if needed.

1.4 Operating conditions

In a lab scale experiment, the use of kerosene as a fuel has several drawbacks. The composition of kerosene is indeed complex and includes several species and, especially considering the multipoint injection in this burner, it can clog small holes with impurities or coking. Because of close physical properties (reported in table 1.3), dodecane has been chosen as a surrogate in Providakis (2013) and is also used in this study. The equation of its complete combustion in air is as follows:

$$C_{12}H_{26} + 18.5(O_2 + 3.76N_2) \rightarrow 12CO_2 + 13H_2O + 69.56N_2 \tag{1.4}$$

Table 1.3 – *Comparison of some physical properties of kerosene and dodecane. From Providakis (2013).*

Fuel	Kerosene	Dodecane
Density (kg.m^{-3} - 293 K)	720	750
Evaporation Temperature (K)	477	490
Lower Heating Value (kJ.kg^{-1})	43100	44150

Because the combustion in the burner is premixed to some degree, it is possible to define a global equivalence ratio to analyse the combustion regime relatively to stoichiometry. It is computed from the mass flows of air and fuel, using the following equation:

$$\Phi = \frac{(\frac{\dot{m}_{fuel}}{\dot{m}_{air}})}{(\frac{\dot{m}_{fuel}}{\dot{m}_{air}})_{stoich}} \tag{1.5}$$

where $(\frac{\dot{m}_{fuel}}{\dot{m}_{air}})_{stoich}$ is obtained from equation 1.4.

As described before, the fuel injection can be made through the two different stages. A parameter is thus needed to define how much fuel goes in each stage. This is the role of the staging parameter α defined from the pilot fuel flow rate and the global fuel flow rate (Barbosa 2008):

$$\alpha = \frac{\dot{m}_{fuel,pilot}}{\dot{m}_{fuel,global}}(\times 100\%) \tag{1.6}$$

A value of 0% means that all the fuel is injected through the take-off stage by the multipoint device while $\alpha = 100\%$ stands for a pilot-only injection. From equation 1.5, local equivalence ratios for each stage can be defined using the value of α and the air staging ratio computed previously. These equivalence ratios however have to be used with care since the two stages are not fully separated.

The power produced by the burner is computed from the fuel mass flow rate and the lower heating value of dodecane (44147 kJ.kg^{-1}). It can be used to characterize the operating point of the burner along with other parameters. Indeed, an operating point is fully characterized by the four values to set: the air flow rate, the air temperature, the pilot fuel flow rate and the take-off fuel flow rate. For simplification reasons, the flow rates can be combined to calculate the values of equivalence ratio, power or α.

Chapter 2

Experimental diagnostics

In order to analyse the combustion process in the BIMER burner, the experimental setup can be equipped with several kinds of diagnostics. They can be used to monitor the fuel spray or the flame with different spatial and temporal resolutions. Most of them are based on optical processes but small sensors can also be used to determine the pressure fluctuations or the temperature at different positions in the burner.

2.1 Mie scattering setup

2.1.1 Mie theory

When light encounters particles, it is scattered in a way that depends on the size of the particle relatively to the light wavelength. Indeed, when the particle size is small compared to the incident light wavelength, the dominant scattering phenomenon is called Rayleigh scattering (it is, for example, responsible for the blue color of the sky). When the light wavelength and the particle size are comparable, the theory of choice for light scattering is Mie scattering which is a particular solution to Maxwell's equations. It describes an elastic scattering of incident light which means that the frequency of the scattered photon is the same as the one of the incident photon.

In the BIMER test bench, the liquid fuel droplets scatter incident light as described in Mie scattering theory. An example of how light is scattered by a droplet can be seen in Fig. 2.1.

When applied to a spray of droplets, one can obtain a signal from each droplet to get its position. The overall signal is thus dependent on the number of droplets (the spray density) and the size of each droplet. In particular, for a big enough droplet, it is proportional to its squared diameter (Domann and Hardalupas 2003).

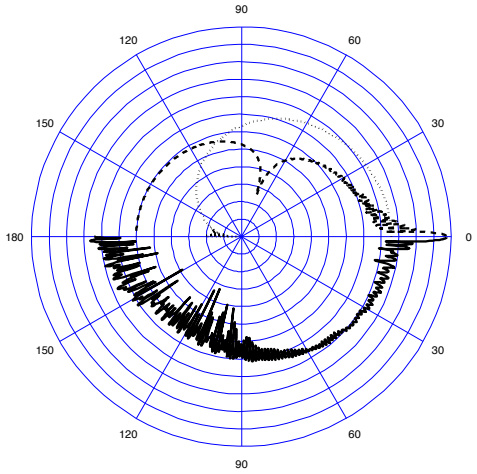

Figure 2.1 – *Scattered light intensity from a 20µm dodecane droplet in 200° C air as a function of the scattering angle. The solid line on the bottom is the intensity according to Mie theory. The top lines represent the contributions of the reflection (dashed line) and the first order refraction (dotted line) from the Debye series. Each circle represents an order of magnitude.*

2.1.2 Tomographic Mie scattering

The scattered light by the fuel droplets can be used to perform several analyses, depending on the illumination method and the light collection system. By creating a laser sheet and using a camera, one can probe the intersection between the fuel spray and the plane of light. This method is used here to obtain images on the axial-vertical plane in the beginning of the combustion chamber, as shown in Fig. 2.2.

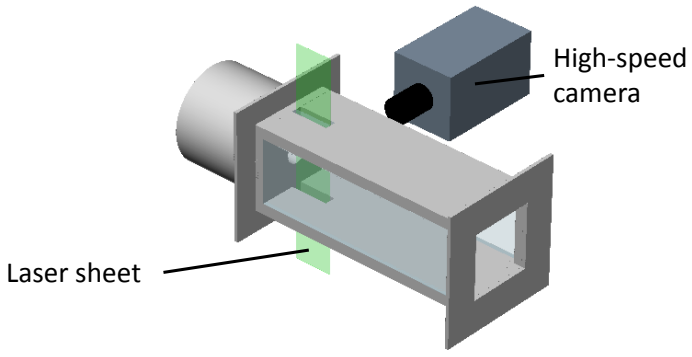

Figure 2.2 – *Setup used for tomographic Mie-scattering imaging. The resulting image is the intersection of the spray and the laser sheet.*

Two high-speed Nd:YAG lasers (Quantronix Condor with a 10 kHz repetition rate) are used to create the laser sheet for illumination. The beams go through a laser-sheet generation device (Melles Griot) where they are compressed into a plane which is eventually directed through the silica slit in the bottom wall of the chamber to illuminate the region of interest. To record the scattered light, a high-speed camera recording at 20000 frames per second (Photron SA-5) is placed perpendicularly to the plane.

Each laser creates a 120 ns pulse and the delay between the pulses can be modified at will. This way, two successive exposures from the camera can be used to perform a Particle Image Velocimetry (PIV) post-processing and obtain a velocity field for the spray in the analysis plane.

2.1.3 Volumetric Mie scattering

Mie scattering signal can also be obtained with volumetric illumination, in order to obtain information on the fuel spray behaviour just after its injection. Visualizations inside fuel injectors are not widespread due to limited optical access. They can lead to valuable insight on the behaviour of the fuel injection but, because of the volumetric illumination, only limited quantitative information can be obtained. The associated setup is described in Fig. 2.3.

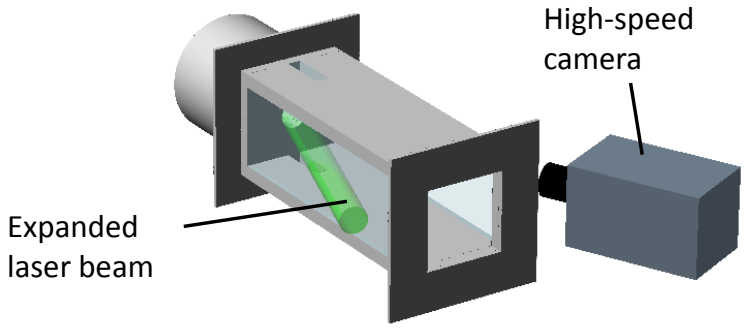

Figure 2.3 – *Setup used for internal Mie-scattering imaging. The resulting image enables to monitor the fuel injection by the pilot nozzle.*

Only one Nd:YAG laser is used here and its beam is expanded with a diverging lens (f=-75 mm) in order to be wide enough to illuminate the inlet hole in the injector wall. The light scattered by the fuel spray is recorded by a high-speed camera (Photron SA-5) at 10000 frames per second.

2.2 Chemiluminescence diagnostic

2.2.1 Spontaneous emission

Because of their traditional use for centuries, flames are associated with two keywords: heat and light. The light emission from a flame can come from two distinct physical mechanisms. The first one, mainly in diffusion flames, comes from the heating of soot that then radiate as black bodies. This light emission mechanism gives the orange color of a candle or of a fireplace. When the flame is premixed, its color changes with a dominance of the blue color, as seen in stove flames. The process for this kind of light emission is quite different from soot thermal radiation and is called chemiluminescence. Indeed, since the flame is a highly reactive medium, intermediate species are created in excited states and emit photons when they return to their ground state. Three main contributors for this emission can be identified in usual hydrocarbon flames: OH^* (around 310 nm), CH^* (around 431 nm) and C_2^* (around 516 nm). C_2^* is produced when the combustion goes towards rich regimes and gives the flame a greenish color while CH^* is responsible for the blue color of the flame. In perfectly premixed conditions, the chemiluminescence signal is proportional to the heat release from the flame (Higgins et al. 2001; Schuller et al. 2002). In the present work, the premixing is not perfect but good enough to assume a qualitative relationship between chemiluminescence and heat release.

2.2.2 Chemiluminescence setup

Recording the light emitted by the flame is a quite common diagnostic and often the first monitored phenomenon when the combustion chamber is optically accessible. The easiest way to perform this is to simply use a camera that collects all the light from the flame. In the BIMER setup, a monitoring consumer-grade video-camera performs this operation and helps analyze the evolution of the experiments. For more precise information, a high-speed camera (Photron SA-5) can be used at a frequency of 5000 frames per second which represents a compromise between signal-to-noise ratio in the images and time resolution. This camera is placed at 90° relatively to the flow direction, at the same position as the camera shown in Fig. 2.2 except when both diagnostics need to be used simultaneously in which case the chemiluminescence camera is placed in a symetrical fashion on the other side of the chamber.

For a more precise analysis, the light emitted from the flame can be filtered at particular wavelengths to record only the emission from specific radicals. In this work, a 431±10 nm filter is used to monitor the chemiluminescence from CH^* but it reduces the amount of light that reaches the camera. The exposure time would thus need to be increased, leading to a lower sampling frequency which would have prevented the detection of interesting high frequency phenomena. To avoid this, a light intensifier (Hamamatsu C10880-03C), is mounted

on a high speed camera (Photron SA-X) and this setup enables to record CH* chemiluminescence at a sampling rate as high as 20000 frames per second.

2.3 Phase Doppler Anemometry

When a liquid fuel spray is used, the size of the droplets is a key information because it has a strong impact on the droplets trajectories and evaporation behaviours. Several techniques have been developed for this purpose from planar, like Interferometric Laser Imaging for Droplet Sizing (Mounaïm-Rousselle and Pajot 1999; Sahu et al. 2014) or Planar Droplet Sizing (Domann and Hardalupas 2003), to pointwise measurements like Phase Doppler Anemometry (PDA).

2.3.1 Principle

The purpose of PDA is to measure the size and velocity of individual particles. This is achieved with a laser technique using the Mie scattering from the droplets as shown in Fig 2.4.

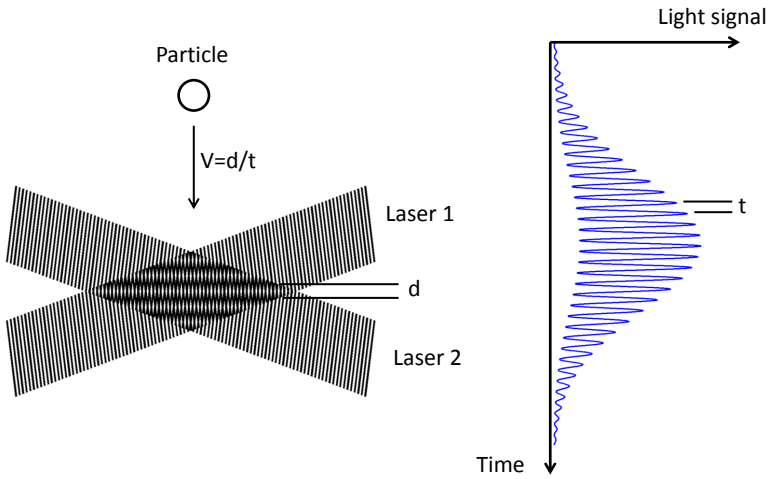

Figure 2.4 – *Simplified working principle of Laser Doppler Velocimetry: when a particle crosses the probe volume, it scatters the light from the interference pattern created by the lasers. The collected signal from the scattered light can be used to obtain the particle velocity.*

A laser beam is divided in two and an optical path difference is applied to one of the beams. The two lasers are directed to the same point and thus create interference fringes when they cross each other. When a fuel droplet crosses this interference pattern, it scatters light and emits a signal called a doppler burst whose frequency depends on the velocity of the particle in an orthogonal

direction to the fringes. A drawback of this technique is that only the magnitude of the velocity is obtained but the direction remains unknown.

To overcome this issue, instead of using a fixed optical path difference, one of the beams is sent through a Bragg cell which creates a continuously varying phase shift. The interference fringes thus continuously move in one direction. The frequency of the Doppler burst now represents the velocity of the particle relatively to the movement of the fringes and thus the travelling direction of the particle orthogonally to the fringes can be obtained too.

This setup can also be used to obtain the particle size by looking at how the scattered light is collected. Since the size of the particle is not negligible compared to the spacing of the interference fringes, light detectors placed at different positions around the measurement volume receive the scattered signal with different phase shifts. Knowing the geometrical configuration of the detectors and the dominant mode of light scattering, this phase shift can be linked to the particle diameter D_p, for example by using the following equation for the first order refraction (Albrecht et al. 2013):

$$\Phi = -\frac{2\pi}{\lambda} D_p \frac{n_{rel} \sin\theta \sin\psi}{\sqrt{2(1+\cos\theta\cos\psi\cos\phi)(1+n_{rel}^2 - n_{rel}\sqrt{2(1+\cos\theta\cos\psi\cos\phi)})}} \tag{2.1}$$

where λ is the wavelength of the laser, n_{rel} is the relative refraction index defined by $n_{rel} = \frac{n_{dodecane}}{n_{air}}$, θ is the angle between the laser beam paths, ψ the elevation angle between the scattering plane and the considered photodetector and ϕ the scattering angle between the laser direction and the receiving head (set here to 30° to ensure that first order refraction is predominant, as shown in Fig. 2.1).

Phase Doppler Anemometry is thus a powerful tool to retrieve fuel droplet size and velocity distributions in the BIMER setup. It does not need any calibration and it is a robust technique. Its main drawback is that it is a pointwise measurement and thus requires prolonged experiments in order to perform a spatial analysis.

2.3.2 PDA setup and parameters

In this study, an integrated system provided by Dantec Dynamics is used as shown in Fig.2.5.

The PDA setup is composed of two lasers with different wavelengths (532 and 561 nm) placed orthogonally in order to obtain two components of the

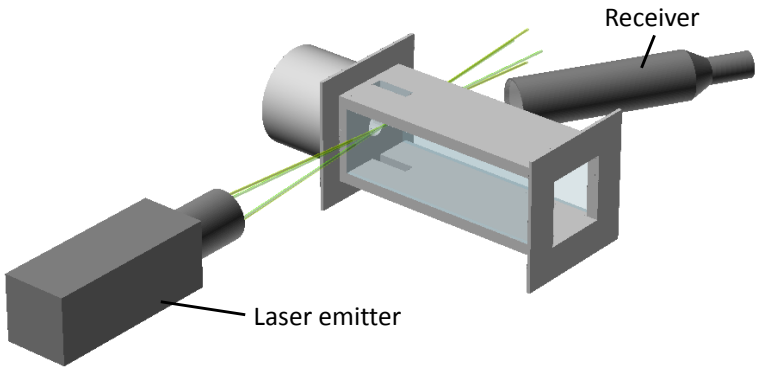

Figure 2.5 – *PDA in the BIMER setup. The position of the laser emitter is such that the beams cross in the center of the chamber and the receiver is placed with a 30° angle in the horizontal plane.*

droplet velocity. The focal length for the emission is 500 mm and the emitter is placed so that the laser beams cross in the middle of the chamber. This creates a $140\times140\times400$ μm^3 measurement volume that can be moved on the same axial-vertical plane as the one used for the tomographic Mie scattering measurements. The axial and vertical components of the droplets velocity can thus be obtained at different probing points. The receiver (Dantec FiberPDA) is placed with a 30° angle to ensure a predominant first order refraction for diameter measurements while remaining as far as possible from the chamber since its focal length is only 300 mm. From there, three optical fibers collect the signal and send it to four photomultipliers placed in a separate device (Dantec BSA signal processor). One of these PM is used to measure the axial velocity components while the other three are processed to obtain the vertical velocity component and the droplet size from their phase difference. The main advantage in using three detectors for the droplet size measurement comes from the fact that phase is a quantity defined with a 2π uncertainty. The phase difference between the two closest detectors is thus first used to obtain a value of the droplet diameter with a relatively poor precision which will be corrected by looking at the phase difference between the two furthest detectors. Using only the two furthest detectors is not possible because their phase difference is affected by 2π jumps.

All these calculations are performed by the Dantec BSA Flow software which then provides a list of arrival times, velocity components and diameters. A start signal can be sent to other devices in order to synchronise the measurements. Finally, since the PDA setup is placed on a motorised table allowing for controlled movements in the axial and vertical directions, measurements can be taken at different locations in the combustion chamber.

2.4 Pressure, heat release and temperature sensors

The previously described diagnostics require strong experimental means and a dedicated computer. In order to analyse the combustion process and also monitor the evolution of the experiments, smaller sensors are also used and their signals are acquired through a LabView interface. The positions of some of them can be seen in Fig. 2.6.

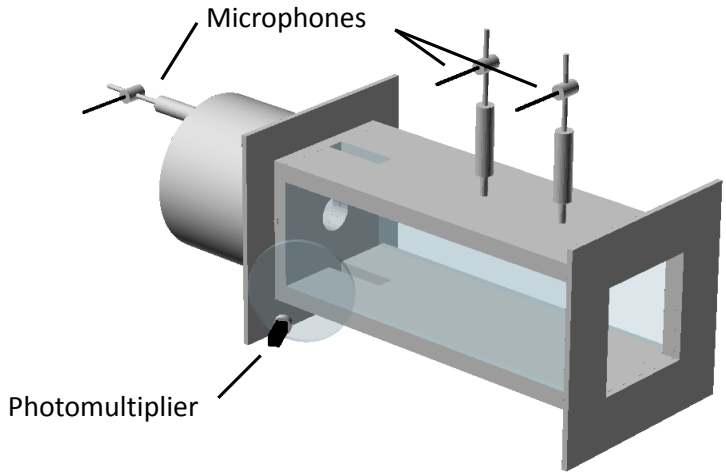

Figure 2.6 – *Positions of the microphones in their water-cooled waveguides and of the photosensor and its collection lens.*

Pressure fluctuations measurements are often used to analyse the combustion process, especially when thermo-acoustic instabilities occur. Another common diagnostic is to record the integrated chemiluminescence signal from the flame with a photomultiplier, for example when flame transfer function measurements are performed. Finally, since combustion is a highly exothermic chemical reaction and vaporisation is a key element when using liquid fuels, temperature measurements are performed with thermocouples at several positions in the burner.

2.4.1 Microphones

Pressure fluctuations in the burner are recorded with three Bruel & Kjaer (B&K) microphones composed of a pressure-sensing capacitor (B&K type 4938) and a preamplifier (B&K type 2670). The signal is sent to a conditioning amplifier (B&K NEXUS type 2690) which outputs a usable signal between -5 and +5 V with a sensitivity of 1 mV/Pa. This device also filters the signal with a bandpass filter with cutoff frequencies of 0.1 Hz and 20 kHz. Because of the high temperature encountered in the chamber, the microphones are placed in semi-

infinite water-cooled waveguides. One of them is placed in the plenum while the other two record the pressure fluctuations inside the combustion chamber, respectively at the half and at the three fourth of its length.

2.4.2 Photomultiplier

In order to analyse the heat release fluctuations, a high-speed recording of the chemiluminescence fluctuations is needed. This is performed by collecting a part of the light emitted by the flame and focusing it with a converging lens (f=300 mm) onto a photosensor module (Hamamatsu H10722). This device is composed of a photo-multiplier tube which enables to amplify the signal from a photocathode impacted by the incident light through a cascade of dynodes and then uses an amplifier to generate a tension signal. It requires a power supply (Hamamatsu C107009) and provides a dynamic signal with high sensitivity to incident light fluctuations. In this study, the photosensor module is coupled with a filter (431±10 nm) to record mainly the CH^* spontaneous emission.

2.4.3 Thermocouples

Thermocouples are common temperature sensors used in a wide range of applications. Their use is based on the Seebeck effect when a junction of two different materials produce an electric potential depending on the temperature difference with the other side of the circuit. The thermocouples used in the BIMER setup are of type K which means they use a couple of chromel and alumel to create this potential. These thermocouples are inexpensive and can be used for a wide range of temperature (up to 1350°C). They are however intrusive and yield a relatively poor precision, this is why they are mainly used for monitoring purposes.

In the BIMER setup, several thermocouples are used. Starting from upstream, two thermocouples measure the air temperature before and inside the preheater. Another one is placed inside the plenum to monitor the air temperature just before the injector. This thermocouple is used as a reference to characterize the operating points. A fourth thermocouple sits on the lip of the injection device, originally to be used as a flashback detector. Finally, two post-injection thermocouples are used, one placed in the corner of the chamber and one at the exit of the burner. They can be used to determine the operating conditions of the burner. Four more of these sensors are used to monitor the water cooling of the chamber and avoid overheating.

Chapter 3

Processing methods

The purpose of this chapter is to describe the processing methods used in the present work. First statistical and time-series analysis methods are presented. They are used to extract information from complex sets of data and experimental conditions. Then particular post-processing methods for raw data obtained from specific diagnostics are explained. Their main purpose is to obtain reliable information on spray velocity. Finally, a recent post-processing technique, the Dynamic Mode Decomposition, is introduced and thoroughly described.

3.1 Experimental design and statistical analysis

The BIMER setup aims at remaining relatively close to industrial applications while allowing the use of laboratory scale investigation techniques. This dual requirement imposes highly turbulent flows to be representative of the practical situation while retaining several control parameters to conduct in-depth analysis. This leads to a complexity that requires specific analysis tools that are described in what follows.

3.1.1 Experimental design

As stated in the first chapter, an operating point is fully characterized by four parameters (air flow rate, air preheating temperature, fuel flow rate and fuel split ratio). A key information is the effect of a fuel split ratio change while keeping the other parameters constant. Furthermore, the effect of the value at which the other three parameters are fixed on the response of the flame to changes in fuel split ratio should be investigated. The effect of these three parameters is studied around a given operating point and each of them can either take the operating value (0), a higher value (+1) or a lower value (-1). Giving each value to each parameter, which is called a factorial design, results in performing at least $3^3 = 27$ experimental campaigns. Adding a few more to test for repeatability will also be necessary. Since each campaign requires to test for changes in

the fuel split ratio, conducting so many of them becomes time-consuming and expensive. However, because the factorial design has some inner redundancy, it is possible to gather information on the effects of the parameters while limiting the amount of experiments to perform. Indeed, different experimental designs can be chosen based on the amount of required information and the specificity of the experiment.

The choice of an adequate experimental design firstly depends on how much information on the effect of the parameters must be gathered. For example, if one wants to study the impact of each parameter separately, a star-shaped experimental matrix can be chosen. In this case, only one parameter is changed while the others retain the design values. With three values for each parameter, only 7 experiments are required but interactions between the parameters cannot be highlighted. Moreover, if one wants to fit a quadratic model on the results, no information on the variability can be obtained. In the framework of this study, a quadratic model with the first interaction terms is sought for which means that 10 coefficients must be determined (leading to at least ten separate experiments with two varying parameters), as shown in the following equation:

$$\begin{aligned} result = {} & k_0 \\ & + k_1 * air + k_2 * fuel + k_3 * temperature \\ & + k_4 * air^2 + k_5 * fuel^2 + k_6 * temperature^2 \\ & + k_7 * air * fuel + k_8 * air * temperature + k_9 * fuel * temperature \end{aligned} \tag{3.1}$$

Once the desired model is defined, one has to look at the limits of the experiments relatively to the chosen factors. Some experimental designs require to set the parameters beyond the chosen values, which can lead to safety problem or plain impossibilities in some cases. In this study, a Box-Behnken design is chosen, mainly for safety and practical reasons first. This kind of design gives an experimental matrix where only two parameters are changed at a time while the third one keeps the design value, leading to 13 different experimental conditions as shown in Fig. 3.1. This means that the three parameters cannot get their extreme values at the same time which is of paramount importance in the present case. Indeed, when a large amount of fuel is injected with a small amount of air (high equivalence ratio) and a high preheating temperature (enhanced vaporization), the flame can become quite reactive and raise safety concerns. On the contrary, when a small amount of fuel is injected with a large amount of cold air, lean blow-off happens and no measurement can be performed. In order to be more confident in the results and account for the variability in the experiments, the central point is performed three times instead of one. This leads to a total of 15 experiments to determine the 10 parameters of the quadratic

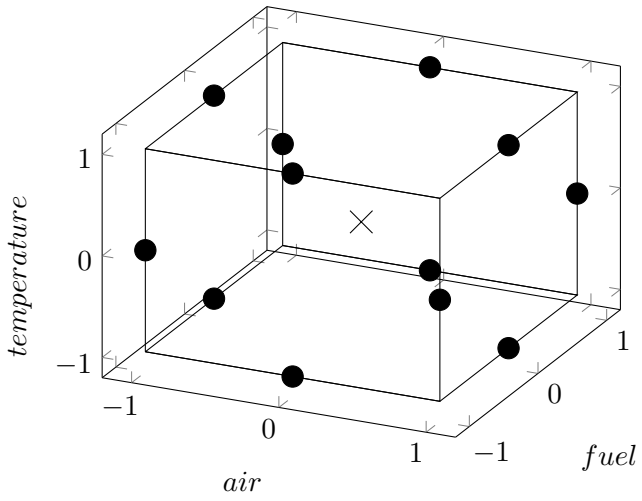

Figure 3.1 – *Position of the experimental points in the control variables space for a Box-Behnken design. The cross represents the operating point around which information is needed.*

model including the interaction terms.

3.1.2 Statistical estimation

Because of turbulence, experimental uncertainty and measurement noise, the results of experiments always contain a random component and can be considered as random variables. From this point of view, measuring a quantity is similar to drawing a sample from a random process. However, because science requires generalizations and comparisons, what is expected from an experiment is not information on the sample itself but on the underlying process. Inferring information on the whole population from a sample of it is called statistical estimation and requires great care because some effects and properties of this operation are not necessarily intuitive.

In general, one wants to obtain the statistical expectation and the variance of the complete population. In flows, this corresponds for example to getting a mean velocity and its fluctuations. This operation is performed by analyzing the sample obtained by measurement. Let's now assume that X corresponds to a quantity of interest (velocity, pressure, etc) with an unknown distribution of expectation μ and variance σ^2. Each of the N measurements of this quantity gives a random variable X_i and the goal is to estimate the values of μ and σ^2 from the values of X_i.

The first quantity one wants to compute after measurements is the mean value of the N samples $\overline{X}$ through the following formula:

$$\overline{X} = \frac{1}{N}\sum_{i=1}^{N} X_i \tag{3.2}$$

Since, it is a combination of random variables, $\overline{X}$ can be considered as a random variable itself with interesting properties: its expectation is μ and its variance tends to zero when N increases. These characteristics make of $\overline{X}$ an unbiased and convergent estimator of μ and this is the reason why sample mean and population expectation can be sometimes confused.

Another commonly computed quantity is the sample variance with the following equation:

$$S_X^2 = \frac{1}{N}\sum_{i=1}^{N}(X_i - \overline{X})^2 \tag{3.3}$$

Because $\overline{X}$ is not μ but an estimator of it obtained from the sample data, the expectation of S_X^2 is not σ^2 as one would intuitively believe but $\frac{N}{N-1}\sigma^2$. This makes S_X^2 a biased estimator of the variance of the population and to correct this effect, an unbiased estimator S_X^{*2} needs to be computed with the following formula:

$$S_X^{*2} = \frac{1}{N-1}\sum_{i=1}^{N}(X_i - \overline{X})^2 \tag{3.4}$$

The $N-1$ as the denominator can be seen as the effect of having computed $\overline{X}$ from the sample which leaves only $N-1$ remaining degrees of freedom: knowing $N-1$ values and $\overline{X}$ is enough to fully characterize the sample. It is to be noted here that the bias decreases quickly when the sample size increases and, for large samples, S_X^2 and S_X^{*2} can be used indifferently without a real impact on the result.

Because $\overline{X}$ and S_X^{*2} are only estimators (for μ and σ^2 respectively) and random variables themselves, a measure of the trust that can be put in the estimations needs to be obtained. For this purpose, one can compute confidence intervals within which the values for the population can be found for a given amount of trust. Such a computation however requires to know the probability distribution of the estimators which is not necessarily straightforward.

When the sample size is large, the central limit theorem can be used. It states that the result of a sum of independent random variables tends to a normal

distribution when the summation size is large enough. Looking at the formula of $\overline{X}$, it can be seen that it is indeed a sum of N random variables. So, when N increases, the distribution of $\overline{X}$ tends to a normal distribution of expectation μ and standard deviation $\frac{\sigma}{\sqrt{N}}$, whose probability density function is described by the following equation:

$$f(x) = \frac{1}{\frac{\sigma}{\sqrt{N}}\sqrt{2\pi}} e^{-\frac{(x-\mu)^2}{2(\frac{\sigma}{\sqrt{N}})^2}} \tag{3.5}$$

Because the quantiles of the normal distribution are well known, it is then easy to then compute a confidence interval for μ based on the computed values of $\overline{X}$ and S_X^{*2}. For example, the 95% confidence interval for the mean in this case is:

$$CI_{95\%} = \left[\overline{X} - 1.96\sqrt{\frac{S_X^{*2}}{N}}; \overline{X} + 1.96\sqrt{\frac{S_X^{*2}}{N}}\right] \tag{3.6}$$

Unfortunately, a similar simple operation cannot be performed for the variance estimator S_X^{*2} because its own variance is not easily obtained and computing its confidence interval thus requires further calculations.

When N is not considered as large enough (namely when $N < 30$), the central limit theorem cannot be applied and no general method for computing confidence intervals exists. However, if it is assumed that X follows a normal distribution, interesting results can be obtained. In such a case, the estimator $\overline{X}$ follows a specific distribution called Student's t-distribution. This distribution is well studied and tabulated depending on a parameter which represents the number of degrees of freedom ($N-1$ in our case) and allows to quickly determine the confidence interval for μ. Similarly, the probability distribution of S_X^{*2} when X is normally distributed has been studied and tabulated. It is called the χ^2-law and it can be used to compute confidence intervals for the estimation of the variance σ^2 of the population from the sample data.

When the distribution of X is too far from a normal distribution, confidence intervals can still be obtained using the bootstrap method. It consists in drawing N times a random value in the sample to create a new sample from which μ and σ^2 can be estimated using $\overline{X}$ and S_X^{*2}. When this operation is repeated a large number of times (namely 1000), one obtains an empirical distribution of estimations of μ and σ^2 from which it is possible to extract quantiles to determine a confidence interval. Although it can be used without any pre-requisite, this method can be computationally expensive.

3.1.3 Principal Component Analysis

The experimental setup being equipped with several diagnostics, it is possible to obtain several variables for the same event. This unfortunately does not

mean that all these variables are relevant nor that they are independent from each other. Ways of reducing the information to a few interesting values is thus needed and Principal Component Analysis (PCA) is one of them (Pearson 1901). PCA, also known as Karhunen-Loève transform or Hotelling transform, is a statistical analysis tool that allows to extract a set of orthogonal variables which maximizes the variance of a set of observations, giving access to the dominant parameters of a phenomenon. This method can also be used for data reduction. As an illustration, a visual bi-dimensional representation of the PCA can be seen in Fig. 3.2.

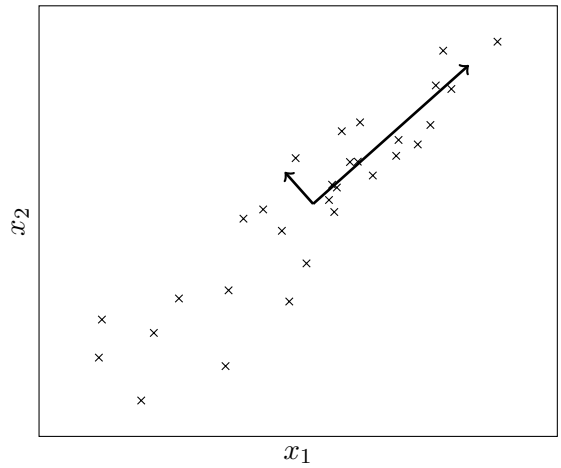

Figure 3.2 – *Visual representation of the PCA process. The analysis determines the two principal directions (arrows) of the data cloud. Here, the first principal direction (the longest arrow) can be used to explain most of the variability of the data.*

Mathematically speaking, the PCA corresponds to an eigenvalue decomposition of the covariance matrix of the data. Practically, if X is a data matrix with each row representing an observation and each column a different variable, the PCA consists in taking the singular value decomposition of X. Each squared singular value corresponds to how much variance is explained by the corresponding principal component. The right singular vectors represent the coordinates of the original variables in the principal component basis.

In the fluid mechanics field, a particular version of the PCA is widely used for turbulent flow analysis under the name Proper Orthogonal Decomposition (POD). This corresponds to applying the PCA on a spatio-temporal dataset where each time step is considered as an observation and each spatial coordinate is a variable. The principal components are then called POD modes and they represent the most energetic structures in the flow (Berkooz et al. 1993). This technique can be used for turbulent flow analysis (Roudnitzky et al. 2006)

as well as for spatial or temporal interpolation of missing data (Everson and Sirovich 1995; Druault et al. 2005).

3.2 Time series analysis

In the framework of this study, measurements are often performed at a high sampling rate, yielding a large amount of data. Extracting features from time series is however very complex and transformation techniques to obtain frequency domain representations prove extremely useful.

3.2.1 Power spectral density

To obtain the frequency content of a signal, the Fourier transform is the tool of choice and is defined for a temporal signal x(t) by:

$$X(\omega) = \int_{-\infty}^{+\infty} x(t) e^{-i\omega t} dt \tag{3.7}$$

This integral is not always convergent for stochastic signals (a white noise for example), so the Fourier transform is not necessarily defined. A workaround is to compute the Fourier transform of the autocorrelation function of the signal instead: this is the Power Spectral Density (PSD) which is an extremely widespread signal processing technique. It is the representation of the signal power by frequency.

In reality, recorded signals are discrete and of finite length and can thus be seen as a sample extracted from an infinite signal from which the power spectral density is required. A simple technique to estimate the PSD from a discrete signal x_n of length N is to compute a periodogram which is the squared modulus of the discrete Fourier transform of the signal:

$$P(\omega) = \frac{1}{2\pi N} \left| \sum_{n=0}^{N-1} x_n e^{-i\omega n} \right|^2 \tag{3.8}$$

The periodogram is however a poor estimator of the PSD because it is not convergent and can be biased. A modified method, proposed by Welch (1967), computes a windowed version of several overlapping periodograms from the signal which are then averaged to yield a better and less noisy estimate of the PSD with the price of reduced spectral resolution. This technique is used with a Hamming window in the present work.

3.2.2 Time-frequency analysis

A spectral analysis of a signal is sometimes not sufficient, especially when the studied process is not stationary but transient. One thus wants to keep tem-

poral information while remaining in the easy to interpret spectral representation. An ideal representation would be similar to a musical score, showing which frequency is played at which instant. Unfortunately, the Heisenberg-Gabor uncertainty principle states that a signal cannot simultaneously have an arbitrarily small support in time and frequency. Roughly speaking, each gain in frequency localisation is paid by a loss in time localisation and vice versa; the two extreme cases being the temporal representation (where no frequency information is present) and the spectrum (which is not localized in time). The goal of time-frequency representations is thus not to extract information but to present it in a more intelligible way by choosing a middle-ground.

The trade-off between time and frequency resolution can be treated by several methods. Short-term Fourier transform is the most widespread of them and yields a fixed temporal resolution and fixed frequency resolution while respecting the uncertainty principle (*ie* the product of time resolution and frequency resolution is lower bounded). Wavelet transform, by working with scales instead of frequencies, gives a better time precision when the frequency is higher.

In the framework of this study, the spectrogram is used. This method can roughly be seen as computing a windowed periodogram over a finite duration for each time step. The result is a distribution of the energy of the signal on the time-frequency plane. Although it yields a quite poor resolution, it is relatively immune to cross-terms that appear in time-frequency energy representations. The precision of the spectrogram can be improved by the reassignment method which shifts the time-frequency positions of previously computed spectrogram values to locations closer to their actual positions by taking advantage of the phase information contained in the short-term Fourier transform. Further details on time-frequency representations can be found in Auger et al. (1996).

3.3 PDA data post-processing

3.3.1 Sampling bias

In PDA measurements, the probe volume is placed at a fixed position and detects crossing particles. For a given acquisition time, particles with a higher velocity are sampled more often than particles with lower velocities. The results are thus biased towards the properties of these fast particles and this bias must be corrected. This correction can be performed by applying a weighting factor to each sample (Albrecht et al. 2013). An intuitive value for this weighting factor would be the inverse of the particle velocity (McDougall 1980) but this requires to know the three velocity components of each particle. Another option is to use the transit time of the particle in the probe region (obtained by the BSA Flow Software from the duration of the Doppler burst) as a weighting factor (Buchhave et al. 1979). This correction is well suited when the seeding

is uniform (in number of particle per volume unit) and will be used in the present study. This weighting influences the computed statistics, such as the mean value:

$$\overline{X} = \frac{\sum_{i=1}^{N} \tau_i X_i}{\sum_{i=1}^{N} \tau_i}, \tag{3.9}$$

where $\overline{X}$ represents the mean value of a measured quantity X, X_i the i-th value of this quantity and τ_i the associated transit time of the i-th particle.

3.3.2 Channel synchronisation

The Dantec PDA system used for the BIMER setup records two independent channels. The first one measures the droplet size and vertical velocity component while the other channel measures the axial velocity component. Nothing ensures that a particle is detected by the two channels at the same time meaning that, if an association of the three parameters for a particle is needed, the channels must be synchronised. This association is performed by checking the arrival times for the two channels: close enough arrival times mean that the same particle was detected by the two channels. This has to be done by setting a threshold to take into account the fact that the detection might not happen exactly at the same time for the two channels while preventing wrong associations to be made. In this study, the threshold is set as a function of the minimal time difference between two samples of the same channel. In order to avoid too high rejection rates while keeping a sufficient accuracy, five times the previously defined minimal time difference has shown to be an interesting choice for the threshold value. If there are several potential candidates within the threshold, the measurement with the lowest time difference is chosen.

3.3.3 Data resampling and spectral analysis

Because data are obtained only when a particle crosses the probe volume, PDA measurements are characterised by a non-uniform sampling in time. In order to analyze the dynamics of a phenomenon, power spectral density is the tool of choice but the non-constant sampling rate complicates its computation. Three main approaches can be cited: the direct Fourier transform, the slotting technique and the Fast Fourier Transform (FFT) after equidistant resampling (Albrecht et al. 2013). The direct Fourier transform approach is not recommended because of its variability (Benedict et al. 2000). The slotting technique directly computes an autocorrelation estimate from the data whereas the resampling technique generates a uniformly sampled signal from the data before processing it to obtain a PSD estimate from its FFT. In this work, the latter technique is used.

Historically, the sample and hold technique is the most used resampling technique because of its simplicity of implementation and the fact that it can be

used on the fly to provide an analog output signal for example. The principle is to keep the output equal to the value of the last sample obtained until a new one is available. A main drawback however is that this technique may provide a constant output for extended periods of time. A slightly modified technique is thus used here because the complete PDA signal is known before it is processed. To each time step of the uniformly sampled signal is associated the closest value from the original PDA signal. This enables to decrease the duration of constant values while keeping the resampling algorithm simple.

3.4 Particle Image Velocimetry

The objective of Particle Image Velocimetry (PIV) is to calculate the best estimation of the displacement of particles between two instants from their Mie scattering signal recorded on two successive images. If the particles are distant enough from each other, it is possible to follow them individually from one image to another: this is the Particle Tracking Velocimetry (PTV) technique. However, fuel sprays are generally dense and other techniques have to be used, yielding a global displacement field of the droplets.

3.4.1 Principle of PIV

The PIV technique consists in dividing the first image into interrogation windows of sufficient size to contain enough particles, 8 of them being the generally accepted minimal value (Adrian 1991). Each window is then cross-correlated with the second image and the maximum of cross-correlation corresponds to the most likely displacement of the particles within the window. Because cross-correlation is much faster when performed in the Fourier domain (it is reduced to a simple multiplication), the interrogation window and the second image are both subjected to a 2-dimensional Fourier transform which are then multiplied and an inverse Fourier transform follows (Scarano and Riethmuller 1999). The main drawback of this approach is that the particle displacement must not exceed half of the interrogation window size otherwise aliasing occurs (Raffel et al. 1998).

Several methods exist to improve the results of the computation. First, generally by assuming a particular shape of the correlation peak, subpixel precision for the displacement can be obtained. To overcome the aliasing issue while keeping a sufficient spatial resolution, adaptive algorithms can be used. They consist in several passes of the cross-correlation step with smaller and smaller windows. The first passes give a first displacement estimate for the following steps. With this technique, since displacement estimates are already known from the previous steps, it is possible to use deformed windows that can take into account the gradients in the flow.

Once the cross-correlation computation is performed, specific methods can be used to help eliminate spurious vectors. The most common of these techniques is to assess the signal-to-noise ratio of the cross-correlation map by computing the ratio between the highest peak and the second highest one. If the ratio is under a defined value, often set at 1.2 (Keane and Adrian 1992), the corresponding displacement vector is rejected. Another common method is called the range validation where limits on the upper and lower values velocity components can reach is set based on external considerations. Any vector not fulfilling these criteria is thus discarded. Finally, the displacement vectors can be compared to their local neighbourhood when the flow is assumed to be sufficiently uniform spatially.

3.4.2 Cross-correlation on fuel Mie scattering images

In this work, Particle Image Velocimetry algorithms are used on the images of Mie scattering from the fuel spray. The repartition of droplets is thus limited to particular regions and goes against the implicit assumption of uniform seeding which allows the use of fixed interrogation windows. The results will thus have to be taken with care and the choice of the processing method is of paramount importance.

To select an adequate PIV algorithm for this particular use, a comparison between three methods is performed on experimental data for which PDA measurements also exist. The details of this study are reported in appendix A.
The results show that the best suited algorithm for the present study is one using a direct cross-correlation method, implemented in the PIVLab software (Thielicke and Stamhuis 2014). The raw Mie scattering images are thus first pre-processed with a high-pass filter to remove unwanted low spatial frequency components coming from laser reflections. The direct cross-correlation step is then performed on windows whose size depend on the studied case. After this step, a range-validation is performed based on PDA data when they are available or on estimations of the standard deviation when they are not. Finally, a key element to keep in mind in the analysis of the calculated velocity fields is that they represent the spray velocity and behaviour, that can be completely unrelated to the underlying flow.

3.5 Dynamic Mode Decomposition

3.5.1 Principle and algorithm

Dynamic Mode Decomposition is a fairly recent linear analysis technique in the field of fluid mechanics. It has been proposed by Peter Schmid in 2010 to provide a way of analyzing the global dynamical features of a flow (Schmid 2010). Tt consists in extracting, from a set of time-resolved data, spatial features

called modes that oscillate at a fixed frequency. It is thus a very useful tool to spot and analyze coherent structures and oscillations from a flow visualization (Lusseyran et al. 2011).

Let's denote by V_1^N a set of N snapshots of m points which can be composed of any kind of time-resolved data, such as velocity, Mie scattering intensity, dynamic pressure or any mix of them (Richecoeur et al. 2012). Each column of V_1^N corresponds to one snapshot and each line represents the time evolution for a fixed point in space. If a constant linear mapping A is assumed from one time-step to the following, the link between V_1^{N-1} (the matrix of the first to the penultimate snapshots) and V_2^N (the matrix of the second to the last snapshots) is of the following form:

$$V_2^N = AV_1^{N-1} \tag{3.10}$$

Computing the eigenvalues and eigenvectors of A provides the dynamical features of the studied phenomenon. However, A can only be obtained by linearizing the underlying equations which is not achievable when studying experimental data. A companion matrix S can nonetheless be obtained through the following equation:

$$V_2^N = V_1^{N-1}S \tag{3.11}$$

S has interesting properties, namely that its eigenvalues and eigenvectors are approximations of the eigenvalues and eigenvectors of A.

Because S is of size $N-1 \times N-1$ and m (the number of spatial data, *ie* the number of pixels in an image for example) is generally larger than $N-1$ (generally a few hundred), the previous equation is over-constrained and S is in fact computed as its best approximate solution through various algorithms.

The simplest algorithm for S consists in remarking that its role is mainly to shift of one step the columns of V_1^{N-1}. Then, S is almost empty and has the following form:

$$S = \begin{bmatrix} 0 & - & - & - & 0 & c_1 \\ 1 & . & & & | & c_2 \\ 0 & 1 & . & & | & c_3 \\ | & . & 1 & . & | & | \\ | & & . & 1 & 0 & | \\ 0 & - & - & 0 & 1 & c_{N-1} \end{bmatrix} \tag{3.12}$$

where the last column represents the best linear approximation of the last column of V_2^N (the last snapshot) from the columns of V_1^{N-1} (the $N-1$ previous snapshots). Computing S is thus equivalent to solving an over-determined linear equations system.

The matrix S can also be obtained by a QR-decomposition of V_1^{N-1}, that is by transforming it into a product of an orthogonal matrix Q and an upper triangular matrix R (Schmid et al. 2011). The following equation can then be solved to obtain S:

$$Q^t V_2^N = RS \tag{3.13}$$

Because R is triangular, this equation can quickly be solved and it is also more numerically stable than the previous method.

Finally, a third method can be used to obtain an approximation of A. Instead of trying to solve the equation for S in the basis created by the snapshots, a change of basis can be made by performing a Singular Value Decomposition (SVD) on V_1^{N-1}. It somehow corresponds to working in the space of the POD modes of the phenomenon and this property can be used to reduce the dimensionality of the problem by choosing to keep only the most energetic modes. The purpose of this method is to obtain a matrix F which represents the projection of A on the POD modes of V_1^{N-1}. If $U\Sigma V^*$ is the "economy-size" SVD of V_1^{N-1}, the matrix F is defined by $F = U^*AU$ (with * denoting the Hermitian transpose operation). The governing equation of DMD thus becomes:

$$V_2^N = UFU^*V_1^{N-1} \tag{3.14}$$

and replacing V_1^{N-1} by its SVD yields the following expression for F:

$$F = U^*V_2^N V\Sigma^{-1} \tag{3.15}$$

The SVD method is generally more numerically stable than the methods based on the matrix S (Guéniat 2013) and it is used for the results presented in this work. It is however to be noted that when dealing with experimental data (by essence dynamically limited and noisy), the matrices are in general well conditioned and all the algorithms presented previously yield very similar results.

Once the matrices F or S have been computed, their eigendecomposition is performed. One thus obtains a diagonal eigenvalue matrix D coupled with an eigenvector matrix X, the eigenvalues being complex. Their phase angle represents the frequency of the related mode whereas their norm can be linked to the mode growing or decaying behaviour.

3.5.2 Post-processing of the results

From the previous equations, it is possible to generate a reconstruction of V_2^N based on the dynamic mode decomposition:

$$V_2^N \approx M_{dm}DC \tag{3.16}$$

where D is the diagonal matrix of eigenvalues, M_{dm} a m by $N-1$ matrix of spatial modes and C the $N-1$ by $N-1$ matrix of temporal evolutions. Each column of M_{dm} represents the spatial structure of a dynamic mode under the form of complex quantities which associate to each point in space an amplitude and a phase for the given mode. Similarly, each line of C corresponds to the temporal evolution of a mode along the $N-1$ snapshots of the recording and takes the form of a sinusoidal oscillation coupled with an exponential growth or decay, as shown in Fig.3.3. From there, it is possible to perform a DMD-

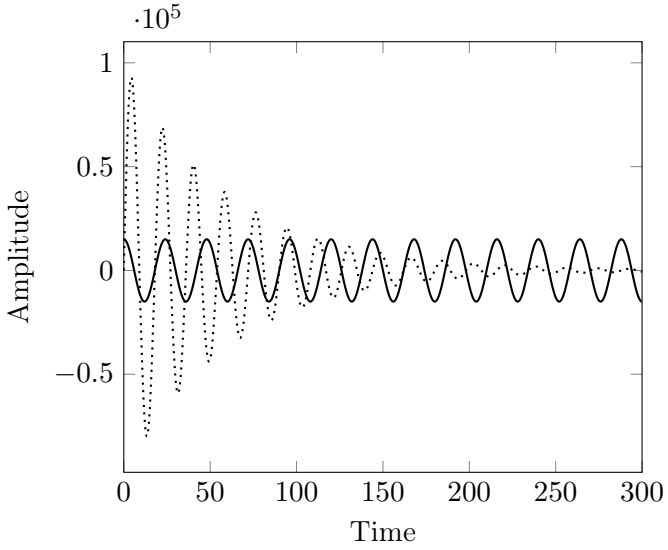

Figure 3.3 – *Typical temporal evolution of DMD modes. Although the dotted curve has a higher amplitude in the beginning, it is quickly damped and the associated mode may not be very relevant for the description of the studied phenomenon.*

filtered reconstruction of the data, simply by setting to 0 the eigenvalues in D corresponding to the unwanted modes. By keeping only one mode, for example, this enables to analyse its shape and influence on the phenomenon that is studied.

In order to quickly compare the respective impacts of the modes on a particular phenomenon, it is often interesting to use a spectrum-like representation. This is well suited because dynamic modes correspond by nature to only one frequency. However, as shown before, they also have a spatial extent and a temporal behaviour. Defining an amplitude for them in the spectrum is thus not straightforward and strongly depends on what is under scrutiny because it requires to reduce the spatial and temporal information from the mode into only one number.

A common way to reduce spatially extended information into one number is to perform an averaging operation. This can be done on the spatial structure

of the dynamic modes, leading to a spatially-averaged oscillation amplitude induced by the mode. On a velocity field, it could for example be used to show that the corresponding coherent structure imparts an average oscillatory motion of 10 m/s over the whole region of interest. For a more robust measurement but with a less straightforward interpretation, the 2-norm can be used. By giving more weight to high values (which often come from coherent structures), it enables to damp the effect of the small oscillations corresponding to noise. It can also be related to a kind of energy content for the mode. Finally, one can also choose to only consider one spatial point to obtain local information from a global DMD decomposition.

Similarly, to deal with the temporal growth or decay of the modes, it is possible to perform a temporal averaging operation. It returns to the average amplitude of the mode along the duration of the studied phenomenon. A main drawback is that, because of exponential decay, some modes have a very high amplitude at the beginning and are then quickly damped (as shown on Fig. 3.3). Since the mean is very sensitive to extreme values, their amplitude from an averaging operation is artificially high even though they may finally be of no interest in the phenomenon. This issue can be tackled by using the median value rather than the mean one to provide more robust but less straightforward results. Because of the monotony of the exponential however, it is easy to show that the median corresponds to the amplitude of the mode at half the duration of the studied recording. It is also possible to choose an arbitrary point in time for the amplitude. The first sample is often implicitly chosen, see Jovanović et al. (2014) for example, where the counterpart of the C matrix is written to have a Vandermonde shape with values of 1 for the first time-step. A DMD spectrum is thus constructed from the choice of a measurement in space and in time. It must however be kept in mind that it is inherently different from a Fourier spectrum, as stressed out by the fact that the spectral resolution is not constant for example.

Empirical considerations tend to show that it is often more interesting to perform several DMDs on a relatively small amount of samples (around a few hundred) than one very long decomposition. Indeed, choosing a large number of snapshots quickly gets computationally expensive and results in a large number of modes for the decomposition. Because of the turbulent and noisy nature of the observed phenomena they never have a precisely fixed frequency and end up spread over several modes, leading to troubles in identifying the relevant ones. A sequential analysis of smaller bits of the same recording is thus more interesting and also helps in assessing the variability of the studied phenomenon.

Part II

Steady conditions

Chapter 4

Pilot-only injection

In this chapter, one operating point where all the fuel injection comes from the pilot stage is chosen. It enables to reduce the complexity of the system in order to analyze several phenomena before adding the staging effect. First, the non-reacting spray is described and dynamical features are emphasized. The effect of the flame is then exposed and changes in the spray structure are highlighted. Finally, air flow rate modulations are performed with the siren device to observe the non-reacting and reacting responses to perturbations.

Pilot-only operations are not uncommon in real jet engines staged combustors, being useful when low power is needed (idle or taxi for example). For the study of such an operating point (power and pressure scaling aside) in the BIMER setup, several criteria must be met. Due to the limited pressure in the pilot dodecane tank, a strong constraint exists on the fuel flow rate. The operating point must also be stable, both in the sense of blow-off avoidance and limited acoustic activity. Finally, because this operating point is the basis for a study of the Precessing Vortex Core, the response to this aerodynamic structure must be high. All these constraints lead to a choice of parameters summed up in table 4.1.

Table 4.1 – *Pilot-only operating point definition.*

Global Parameters				
$\dot{m}_{air}$	T_{air}	$\dot{m}_{fuel}$	P	ϕ
($g.s^{-1}$)	(K)	($g.s^{-1}$)	(kW)	(-)
32.3	473	1.02	45	0.5
Staging				
α	$\dot{m}_{fuel,pilot}$	ϕ_{pilot}	$\dot{m}_{fuel,takeoff}$	$\phi_{takeoff}$
(%)	($g.s^{-1}$)	(-)	($g.s^{-1}$)	(-)
100	1.02	3.70	0	0

4.1 Non-reacting conditions

4.1.1 Study of the spray

The tomographic Mie scattering setup has been presented in chapter 2. In this section, a Photron FastCam SA-5 equipped with a 50 mm lens is used and the experimental parameters are reported in table 4.2.

Table 4.2 – *Acquisition parameters for the tomographic Mie scattering measurements.*

Acquisition frequency (kHz)	2×10
Delay between laser pulses (µs)	25
Image size (pixels)	704×520
Equivalent field of view (mm)	176×130
Number of images	15637
Recording duration (s)	0.78

Because of the laser sheet width, only the first 90 mm are really useful despite the 176 mm-wide image. An instantaneous image of the spray is shown in Fig. 4.1.

From this image, it can be seen that the light scattered by the fuel droplets is quite scarce and very localized. It can thus easily be understood that averaging such images would only result in highlighting the unwanted background features more than the spray shape itself. The useful information from the Mie scattering images indeed lie in the fluctuating part because of the very localized nature of the scattered light, which is why the Root Mean Square (RMS) is more interesting to emphasize the characteristic shape of the spray. A high RMS value for a pixel means that numerous droplets flow at this location, giving alternating black and white levels for this pixel. On the contrary, a pixel where no fuel droplets are found continuously keeps the same value and thus yields a low RMS value. That is why a RMS image of Mie scattering is proposed in Fig. 4.2 to present the average spray shape.

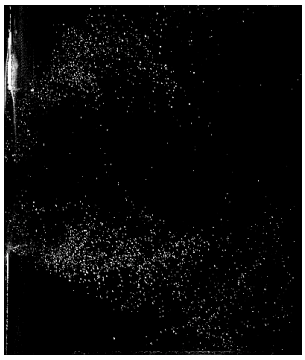

Figure 4.1 – *Instantaneous image of Mie scattering from the dodecane droplets. Flow from left to right.*

The image shows two symmetrical arms diverging from the center of the chamber which is the trace of a hollow-cone distribution of the droplets. This particular shape has to be analyzed with respect to the underlying flow field. Indeed, previous studies on the setup (Barbosa et al. (2009), Providakis (2013))

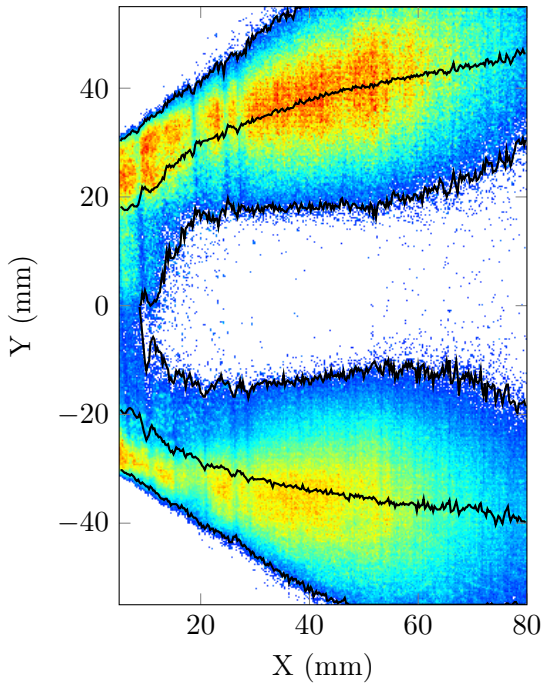

Figure 4.2 – *RMS image of Mie scattering intensity in the non-reacting case. A threshold has been set at 15% of the maximum value to highlight the shape of the spray. The black lines represent the positions of the "center of mass" and the spray limits for each half image.*

have shown that the air flow is characterized by a vortex breakdown structure with an Inner Recirculation Zone (IRZ) and Outer Recirculation Zones (ORZ) in the corners. These regions can be identified in Fig. 4.3 extracted from oil-seeded cold flow PIV measurements.

Because the data in Fig. 4.3 come from cold flow measurements and are averaged, they cannot provide quantitative insight but remain interesting from a qualitative point of view. First, the jet region can be highlighted, with high positive axial velocities and a slightly convergent then divergent trajectory. Around the center of the chamber, a region of reversed flow can be observed: it is the Inner Recirculation Zone. Between this region and the jet, two large scale toroidal structures can be identified, the first one around 15 mm from the injection plane and from the center of the chamber and the second one centered out of the image, probably around 20 mm from the chamber axis. These two structures are probably associated with the fact that the air injection is made of two co-swirling co-annular jets but further evidence for such an assumption needs to be gathered. Finally, on the external part of the jet, a third toroidal structure feeding the ORZ is present. These three structures give the jet its particular trajectory.

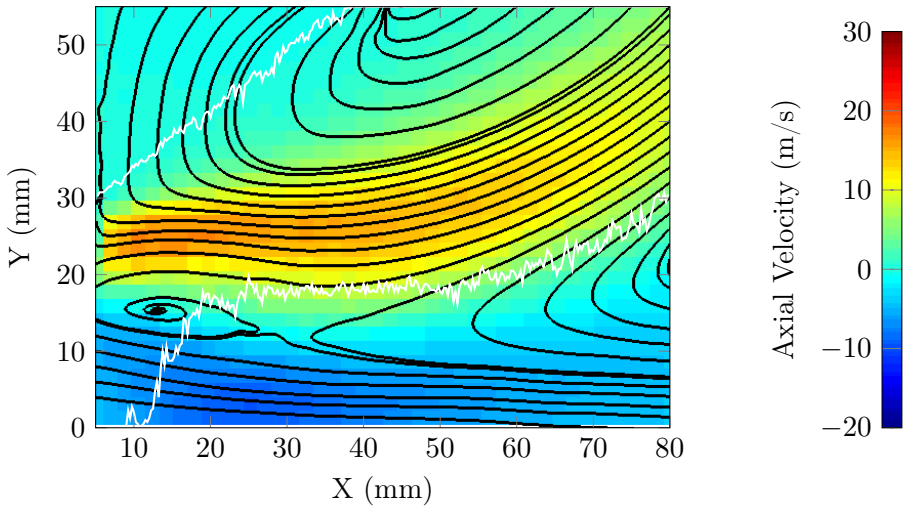

Figure 4.3 – *Mean axial velocity and 2d pseudo-streamlines of the cold air flow seeded with oil droplets. The white lines represent the spray limits from the Mie scattering RMS image (Fig.4.2).*

In Fig. 4.2, the RMS image thus shows that the droplets are mostly located in the jet part of the flow. This is especially noticeable for the inner spray limit which has a very similar convergent then divergent behaviour. Some peculiarities can however be highlighted: the outer spray limit does not seem related to the air flow and some signal is also present in the center of the image for low values of X. Reasons for these will be further discussed with the help of other diagnostics.
A way of obtaining the mean radial position of the spray is to compute its "center of mass": for both half images, the radial position of each pixel is weighted by its intensity and the average is then computed for each axial position. The result of this calculation is shown by the black lines in the center of each spray arm in Fig. 4.2. These lines highlight the fact that the spray is divergent but tends towards a more axial direction as it progresses inside the chamber. It can also be seen that the spray thickness increases with the axial position, which is a consequence of the fact that the fuel droplets are gradually mixing with the surrounding air. The Mie scattering data can also be processed with a PIV algorithm and the resulting spray velocity fields can be seen in Fig.4.4.

The mean PIV fields in Fig. 4.4 are computed using 20×20 pixels windows with 60% overlap to yield a velocity vector every 2 mm. It can be seen that no velocity information is available in the recirculation zones, as expected from the position of the spray limits computed from the RMS images. It seems however that the velocity fields are wider than the spray limits but the use of interrogation windows for the PIV technique and the different thresholding methods must be taken into account.

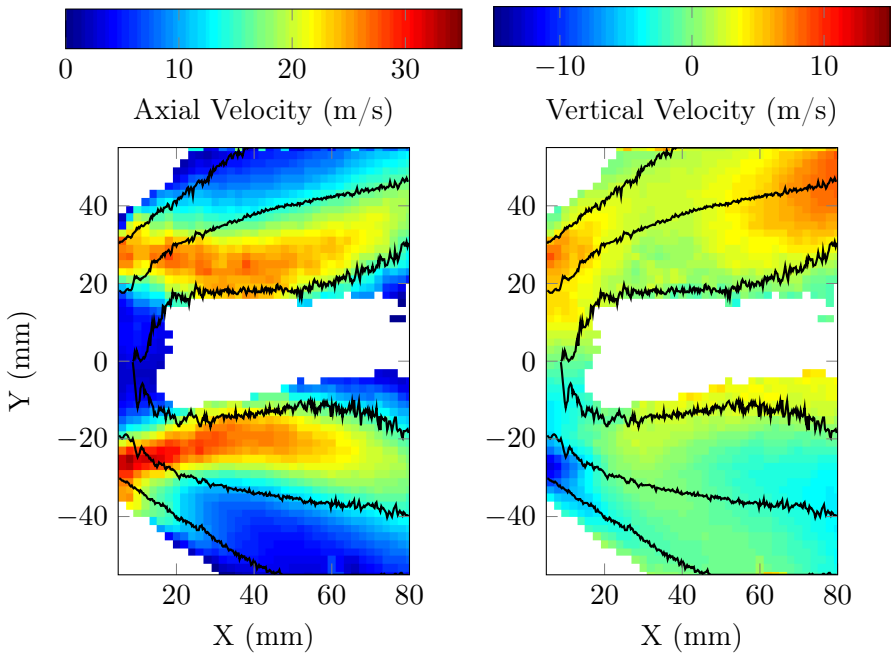

Figure 4.4 – *Mean axial (left) and vertical (right) spray velocities from the PIV treatment of the Mie scattering fields. A threshold has been set at 2% of vector validation explaining the presence of white zones. The black lines represent the spray limits from the Mie scattering RMS image (Fig.4.2).*

In the jet region, the axial velocities are high (about 30 m/s), except in the external parts of the jet after X=25 mm where they remain around 10 m/s. The vertical velocities are globally symmetrical and, in the jet region, an area with much lower values can be highlighted which explains why the spray becomes less divergent with its axial progress. This effect is particularly visible on the inner spray limit. The only data available around the center for low axial positions show low positive axial velocity values although this is supposed to be the location of the Inner Recirculation Zone. Further information can be obtained by comparison with the PDA velocity data, starting with mean velocity interpolated fields shown in Fig. 4.5.

The velocity fields in Fig. 4.5 are obtained from five mean velocity profiles of PDA measurements taken at 10, 15, 20, 25 and 35 mm from the chamber inlet wall. Measurement points are spaced by 3 mm vertically. The data from these profiles are then linearly interpolated in the two dimensions on a 1 mm spaced regular grid. A threshold is set at 2000 detected droplets, which corresponds to a data rate of 200 droplets per second whereas the highest data rate is over 10000 droplets per second in the most dense regions of the spray.
An interesting feature of the images lies in the fact that information can be

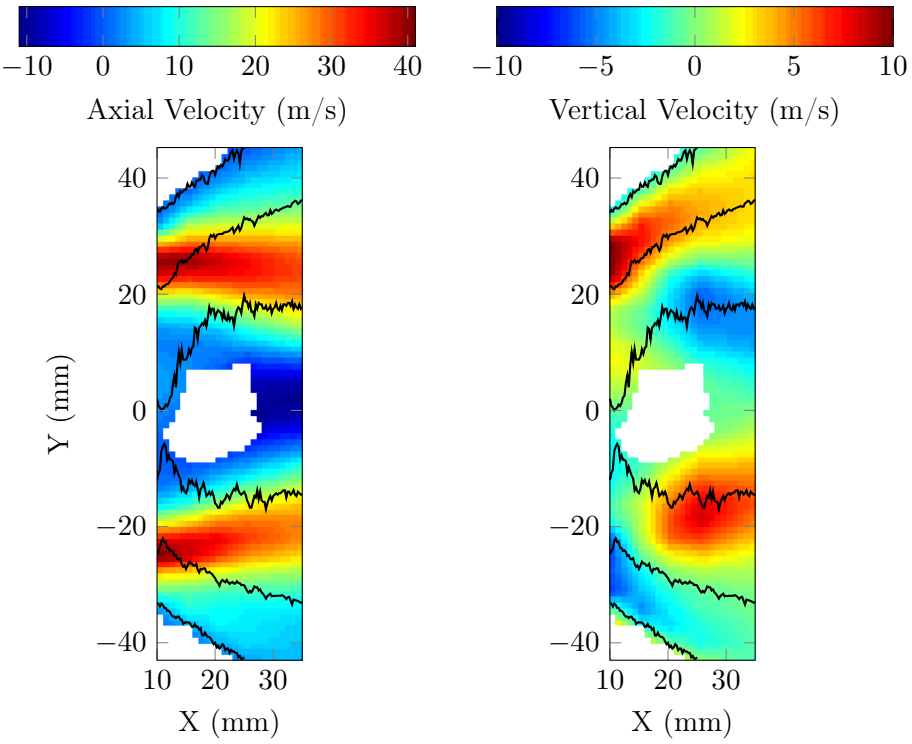

Figure 4.5 – *Interpolated mean axial (left) and vertical (right) spray velocities from PDA measurements. A threshold has been set at 2000 detected droplets explaining the presence of white zones. The black lines represent the spray limits from the Mie scattering RMS image (Fig.4.2).*

obtained even outside of rms-computed spray limits in the center of the chamber. The axial velocity field is very similar to the PIV one with a high axial velocity region in the jet but higher values (up to 40 m/s). The slow positive region in the center is also still present. New information however come from the center of the chamber where negative axial velocities up to 10 m/s can be observed. They are associated with the presence of the IRZ which moves the droplets upstream. In the vertical velocity field, the situation is somewhat different from the PIV. The divergent behaviour of the spray is still present in the beginning of the chamber but, around 30 mm, the vertical velocities are inverted and the droplets seem to converge towards the center of the chamber. This is probably the trace of the first toroidal structure highlighted in Fig. 4.3. The PDA measurements also yield information on the droplets diameters and some phenomena can be highlighted by analyzing the spatial distribution of the diameters in the spray, as shown in Fig. 4.6.

A representative value for the droplets diameter is computed using the Sauter Mean Diameter at each PDA measurement point, the results are interpolated

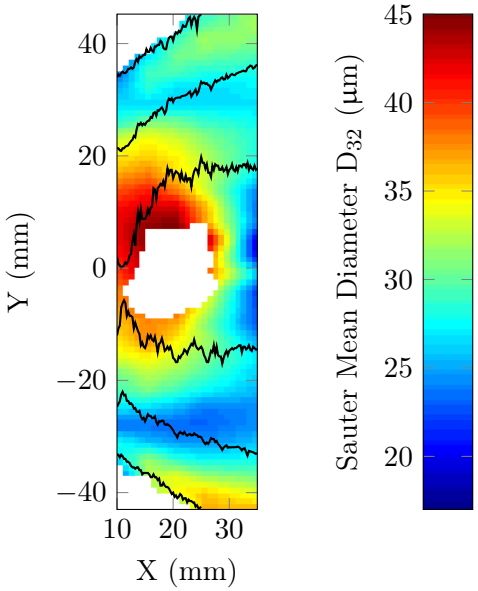

Figure 4.6 – *Interpolated Sauter Mean Diameter from PDA measurements. A threshold has been set at 2000 detected droplets. The black lines represent the spray limits from the Mie scattering RMS image (Fig.4.2).*

similarly as before and plotted in Fig. 4.6. The first striking observation is that the diameter distribution inside the spray is highly inhomogeneous. Three phenomena can be responsible for this.

The first reason may be secondary atomization of the biggest droplets which creates smaller droplets as they progress in the chamber. Such a phenomenon can be associated with a critical Weber number, We, defined in the first chapter. Here, for the maximum measured droplet size of 80 µm and a slip velocity between the air and the droplet of 35 m/s (parameters chosen to provide a high limit for We), the Weber number is around 8. Since the Ohnesorge number for an 80 µm dodecane droplet is around 0.03, the value for the critical Weber number can be taken at 12 which is higher than the computed Weber number for this case. This means that, as the fuel enters the chamber, it is already fully atomized and the spatial variations of diameter seen in Fig. 4.6 cannot arise from secondary atomization.

The second potential reason for the inhomogeneity in diameters can be the fuel vaporization. The d^2-law states that the squared diameter of a droplet decreases linearly with time. In the present case, it would lead to an increase of the D_{32} because the smaller droplets would evaporate faster then the larger ones. Since such an increase with the axial position is not visible in Fig. 4.6, another reason has to be found for the diameter inhomogeneity.

The third potential cause, which remains the only probable one, is an aerodynamical segregation of the droplets because of their different diameters, which

lead to different Stokes numbers. In the external parts of the spray around X=30 mm, an increase in the Sauter Mean Diameter can indeed be observed, which can be linked to the fact that the biggest droplets may remain in the divergent trajectory highlighted in the beginning of the chamber in Fig. 4.5. This phenomenon can also explain why the outer spray limit from Fig. 4.2 is not related to the air flow. Similarly, for X=35 mm in the center of the chamber, small values of D_{32} can be observed and the axial velocity field in Fig. 4.5 shows the IRZ negative axial velocity values for the same region. It can be explained by the fact that the biggest droplets have too much inertia to enter the IRZ. Finally, the low positive axial velocities observed in the center of the chamber close to the inlet can be associated with big droplets that managed to reach this region thanks to their inertia against the negative velocities of the IRZ. Because Fig. 4.5 and 4.6 show that the droplets behaviour changes with their diameters, it is interesting to look at average values conditioned by the droplet size, as shown in Fig.4.7.

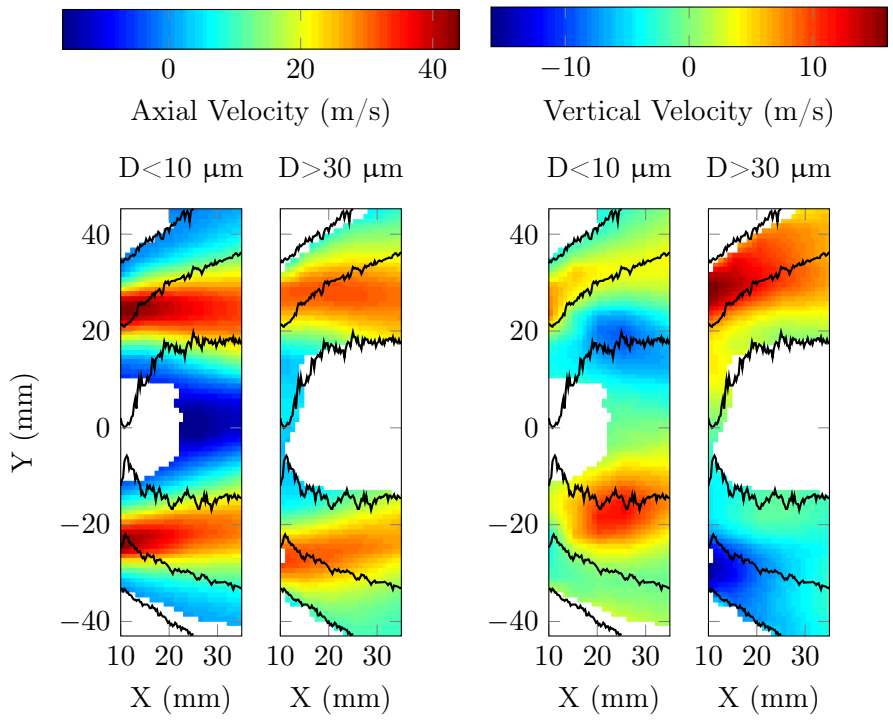

Figure 4.7 – *Interpolated mean axial (left) and vertical (right) spray velocities from PDA measurements conditioned by the droplets diameter. A threshold has been set at 500 detected droplets. The black lines represent the spray limits from the Mie scattering RMS image (Fig. 4.2).*

To obtain the images in Fig. 4.7, the two channels of the PDA are first associated to obtain data triplets gathering droplet axial and vertical velocity and

droplet diameter. By selecting these triplets based on the value of the droplet diameter, it is then possible to compute velocity average values conditioned by the droplet size which can be interpolated over the region of interest similarly to what is done in Fig. 4.5 and 4.6. Two different populations of droplets are studied, the small droplets, with diameters under 10 µm, and the big droplets over 30 µm. Because this conditioning operation reduces the amount of available data, the threshold for the representation in Fig. 4.7 is set at 500 droplets.
A quick analysis of the Stokes number for these two populations show that the small droplets are responsive up to at least 2 kHz fluctuations while the big droplets have a cut-off frequency of about 300 Hz. While the smaller droplets follow the underlying air flow, the bigger ones have a strong ballistic behaviour which explains what can be seen in Fig. 4.7. The small droplets have high axial velocities in the jet region and, as expected, negative values in the IRZ region since they tend to follow the air flow. On the right, the vertical velocity field shows that the small droplets are not really divergent and get captured by the IRZ around X=25 mm since they quickly converge to the center. The absence of small droplets in the center in the beginning of the chamber may be explained by their vaporization inside the IRZ before they have moved far enough upstream. This is supported by a simple d^2-law analysis showing that, in a 200 °C environment, a 10 µm dodecane droplet evaporates in under 0.4 ms leading to only a 4 mm displacement at 10 m/s.
An interesting feature of the big droplets' fields is that their spatial extent is very similar to the spray limits obtained with the Mie scattering data. This comes from the fact that the Mie scattering intensity from a droplet is mainly proportional to the squared diameter of the droplet which leads to a bias towards big droplets in the spray imaging techniques. For these big droplets, the axial and vertical velocity fields show that they are completely absent from the IRZ (as expected from their ballistic behaviour) and that their trajectories are divergent in the jet region, probably because of their high inertia which imparts a strong centrifugal effect on them. Another way of looking at this centrifugal effect is to compute the angle between the droplets velocity and the horizontal direction to analyze the diverging behaviour of the droplets.

To follow the local travelling direction of the droplets in the spray, PDA measurements at vertical positions corresponding to the "center of mass" lines from the RMS spray image are used. For each value of X (10, 15, 20, 25 and 35 mm), the angle between the droplet velocity direction and the horizontal direction is computed for each droplet with positive values meaning a movement away from the center of the chamber. The top and bottom datasets are then gathered and mean values and standard deviations are extracted, depending on the droplet size. Confidence intervals are obtained via the central limit theorem for the mean estimator and with bootstrap resampling for the standard deviation estimator. The results are plotted in Fig. 4.8.
The mean angle plot shows two completely different behaviours for the big and

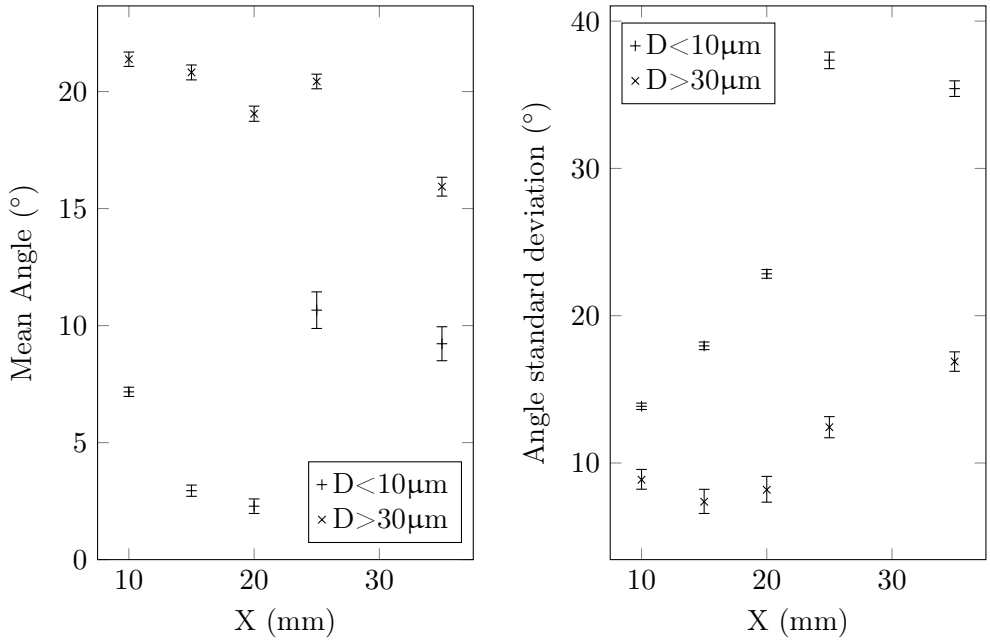

Figure 4.8 – *Mean value (left) and standard deviation (right) of the droplet velocity angle away from the center line. The error bars represent 95% confidence intervals.*

small droplets as expected from the velocity fields in Fig. 4.7. For the small droplets, the velocity angle away from the center line remains very small in the beginning of the chamber and slightly decreases (under 20 mm) to yield an almost purely horizontal velocity. This can be linked to the presence of the convergent regions nearby. The angle however abruptly increases afterwards and the small droplets (*ie* roughly the underlying air flow) are divergent again. However, the increase in the confidence interval shows fluctuating data. The situation for the big droplets is completely different as they have a wide diverging angle which remains roughly stable with the axial position except for X=35 mm where the angle decreases but remains higher than the small droplets angle.
The standard deviation remains low for the big droplets as expected from their high inertia. The values are however increasing because, as they progress inside the chamber, the droplets encounter different situations leading to variable responses compared to the relatively homogeneous conditions they meet before they enter the chamber. The same increasing trend can be observed for the small droplets but with higher values. This increase is a trace of the turbulent behaviour of the flow and higher fluctuations can be observed after 25 mm as some droplets are moving towards the IRZ while others are diverging away from the center.

4.1.2 Dynamic behaviour of the non-reacting spray

From an average point of view, the non-reacting spray for this operating point is characterized by a globally divergent shape where the biggest droplets lie on the outside and where the smallest droplets get sucked into the IRZ, that creates a bubble-like shape in the middle of the chamber. From a dynamic point of view, a particular structure can be observed, which modulates this average behaviour.

From the Mie scattering images, it is possible to analyze the local dynamic behaviour of the spray by selecting a small region of interest and averaging the values inside it at each time-step, yielding a temporal signal that can subsequently be analysed with dicrete Fourier transform. This has been performed on a 30×30 pixels (7.5×7.5 mm) area placed at X=5 mm and Y=-25 mm and the resulting Power Spectral Density (with 0.25 s long Hamming windows and 50% overlap) plot can be seen in Fig. 4.9. It shows a well defined peak around 1580 Hz.

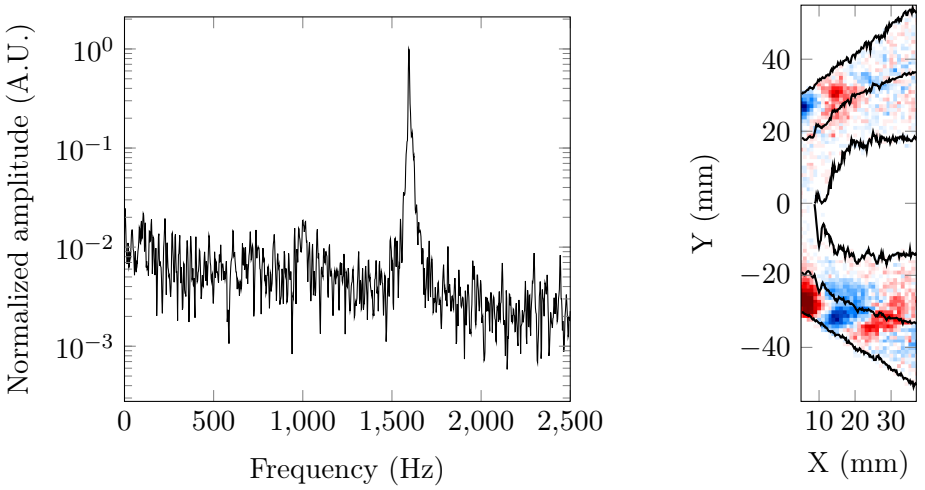

Figure 4.9 – *Power spectral density from a region of interest in the Mie scattering images (left) and DMD mode at the peak frequency (right). Positive Mie scattering fluctuations are in red and negative ones in blue. The black lines represent the spray limits from the Mie scattering RMS image (Fig.4.2).*

PSD cannot however bring information on the spatial extent of the dynamical features so, for this purpose, Dynamic Mode Decomposition is used on 500 Mie scattering images. The mode associated with the peak frequency observed on the PSD plot is presented on the right of Fig. 4.9.
This mode shows alternating and antisymmetric red and blue structures corresponding to Mie scattering fluctuations above average and below average respectively. It seems that only the outer region of the spray is affected by

this modulation. As this mode evolves with time, the structures slowly move downstream as if they were convected away by the flow. This behaviour can be related to the radial cut of a bigger rotating helical structure with a pitch corresponding to the distance between two red spots. Previous studies (Providakis 2013) have shown that the evolution of the frequency of this structure is linear with the air volume flow rate. These clues lead to believe that this structure can be linked to a Precessing Vortex Core (PVC) arising from the vortex breakdown of the swirling flow. To check whether this structure has an effect on the spray velocities, the result of the DMD on PIV data can be seen in Fig. 4.10.

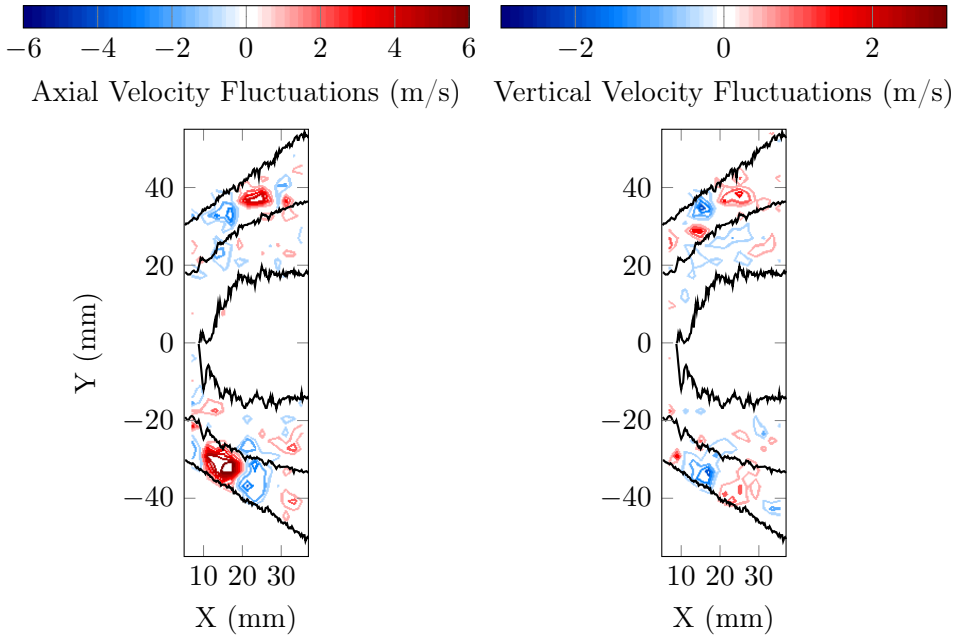

Figure 4.10 – *Contour plot of the DMD mode associated with the PVC for the axial (left) and vertical (right) spray velocities from the PIV treatment of the Mie scattering fields. The black lines represent the spray limits from the Mie scattering RMS image (Fig.4.2).*

The axial and vertical velocity fields computed through PIV treatment are submitted to a Dynamic Mode Decomposition. When a PIV vector is not validated, it is replaced by the temporal mean value computed on all the valid vectors for the same spatial point because DMD cannot handle data with temporal gaps. Each point thus gives two time-resolved datasets (one for each component of the 2D velocity vector) which make the lines of the data matrix. The mode associated to the PVC frequency from a DMD of 500 time samples can be seen in Fig. 4.10. It must be noted that the PVC signal is very hard to extract from the PIV datasets and is very close to the noise level which explains

why the mode is not strongly marked.
The mode, as shown in the axial and vertical velocity fluctuation fields, acts mostly on the outer part of the spray, as already observed for the Mie scattering data in Fig. 4.9. The axial velocity fluctuations show alternate structures with a velocity modulation peaking at ±6 m/s and an antisymmetric behaviour. It means that, as one arm of the spray is faster than average, the opposite arm is slower. The vertical velocity fluctuations also show convected alternating structures but this time they are symmetric. As one arm of the spray moves away from the center, the opposite arm tends to move back towards the center. This tends to give the spray a snake-like motion, compatible with the trace of a helical structure.
To gain more insight on the process, the response of the PDA data to the spray dynamics can be analyzed. However, since no reference signal exists, the data cannot be synchronized and Dynamic Mode Decomposition cannot be used. Only PSD plots are thus displayed in Fig. 4.11 and 4.12.

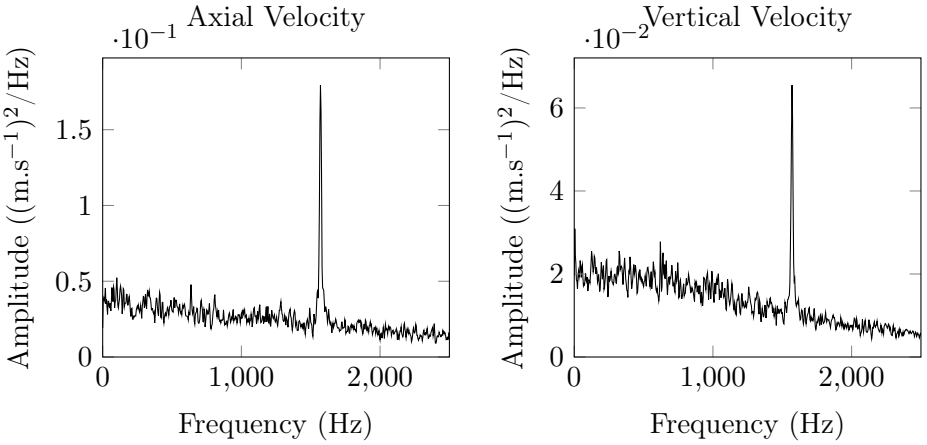

Figure 4.11 – *Power spectral density of the axial and vertical velocity signals from a PDA measurement at X=10 mm and Y=-30 mm.*

At the spatial positions where the PVC mode amplitude is high (see Fig. 4.9), plotting Power Spectral Densities for the PDA data generally shows a strong peak at the PVC frequency, as can be seen in Fig. 4.11 for the point at X=10 mm and Y=-30 mm. To build these graphs, the raw velocity signals were resampled (using the modified sample and hold technique describe in chapter 3) at 8 kHz and Welch's method was used with 50% overlap and 0.2 s long Hamming windows. A clear peak around 1580 Hz can be seen on both the axial and vertical measured velocity components, showing a modulation of these signals at the PVC frequency. The linear y-scale of the plots has nevertheless to be highlighted in comparison to the logarithmic scale in Fig. 4.9. This means that, as already expected from the difficulty to extract velocity fluctuations from the

PIV data, the trace of the PVC in the velocity droplet signal is less detectable than in the Mie scattering data.
The origin of these velocity fluctuations must be identified and, to do so, other types of information extracted from the PDA measurements can be used.

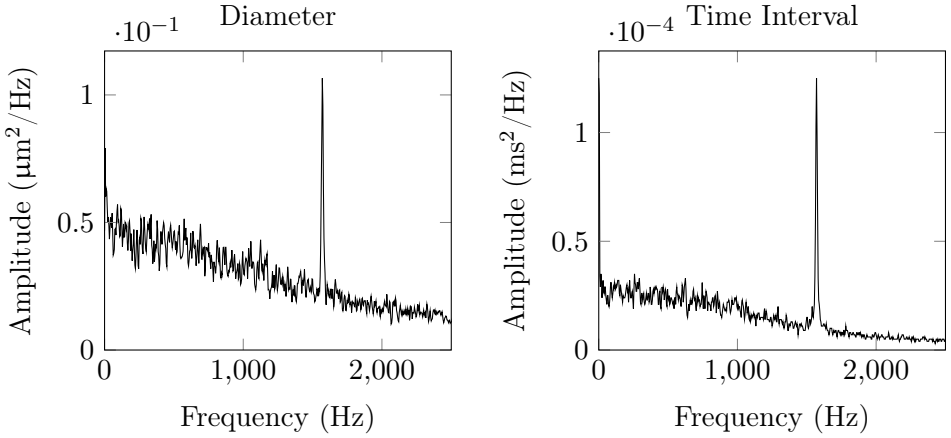

Figure 4.12 – *Power spectral density of the droplet diameter and time interval signals from a PDA measurement at X=10 mm and Y=-30 mm.*

Since the droplet diameter is also measured by the PDA, the associated signal can be processed similarly to the velocity signals in Fig. 4.11. The resulting PSD plot can be seen on the left of Fig. 4.12. Interestingly, it also shows a peak around 1590 Hz meaning that the droplet diameter is also subjected to modulations at the PVC frequency. As explained previously, diameter variations can have three causes: atomization, vaporization or segregation.
The study of the Weber number has shown that atomization can be ruled out as well as vaporization because the non-reacting flow is isothermal. A temporal segregation of the droplets at the PVC frequency must thus exist to generate the diameter fluctuation highlighted in Fig 4.12.
The second plot in Fig. 4.12 is a bit more difficult to analyze. The original signal leading to its creation is the time interval between two droplets, that is the difference between the arrival times of two consecutive measured droplets. A small value of this time interval means that the droplets are temporally close to each other, in other words that the droplet cloud is relatively dense. Similarly, a large time interval can be related to a quite dilute droplet cloud.
On the right of Fig. 4.12, the PSD of the time interval signal shows a peak at the PVC frequency, meaning that the duration between two droplets is modulated. As explained, this can be related to changes in the local droplet cloud density and shows that the PVC generates a non-uniform droplet density.
To continue with the approach used previously, conditioning the signals by the droplet diameters would be the next step but it is not straightforward.

Indeed, conditioning leads to a diminution of the amount of available data. This decrease is too small to bias the statistics but it is unfortunately too high to provide a sufficient data rate for frequency analysis. Another process thus has to be used and a result for big droplets (over 30 µm) at X=10 mm and Y=-30 mm is shown in Fig. 4.13.

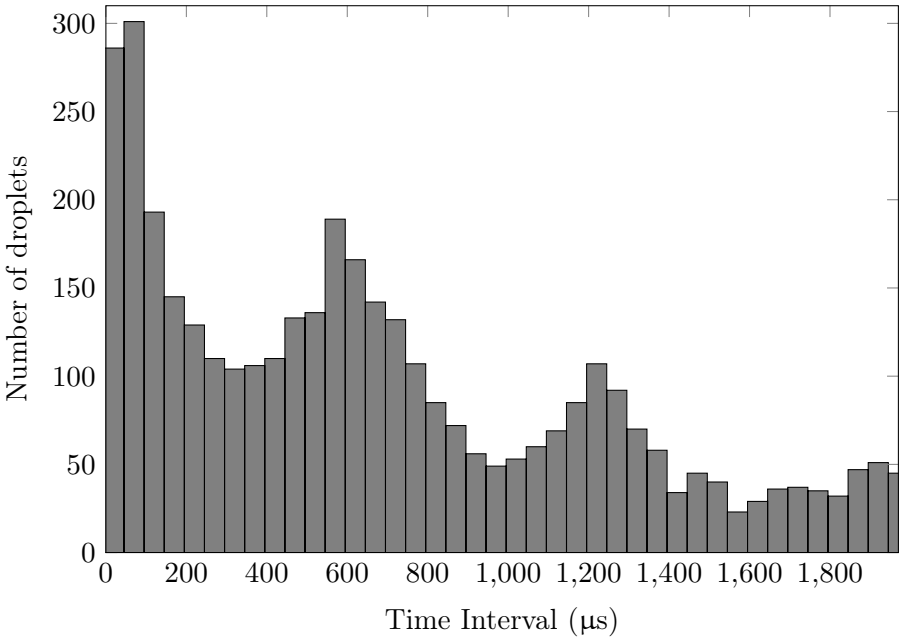

Figure 4.13 – *Histogram of the time intervals for big droplets (D>30 µm) at X=10 mm and Y=-30 mm.*

To generate the histogram in Fig 4.13, the time intervals between the big droplets only are computed and they are grouped into 50 µs-wide bins. The graph shows 3 main peaks, one around zero, one at the 570±25 µs bin and the third one at the 1220±25 µs bin. For comparison purposes, the period of the PVC is 630 µs and, as expected, the time intervals distribution shows peaks a bit under this value and its double. Indeed, a simple simulation of PDA sampling, described in appendix B, shows that a very similar histogram can be obtained when the detection probability of a droplet is modulated by a sine wave at the frequency of the PVC.
Since similar results can also be observed for the small droplets, the variation of the droplet diameter seen in Fig. 4.12 can be explained by the arrival of different droplet populations at the same frequency but with different phases because of different drags leading to different time lags (Lacour et al. (2011)). Since the droplets have different velocities depending on their sizes, such a phenomenon also explains the velocity variations observed in Fig. 4.11. Even though coherent variations of the velocity inside each diameter class cannot be completely ruled

out, no such effect could be detected. It thus seems that most of the effect of the PVC on the spray comes from droplet segregation taking place before the combustion chamber. In order to check this assumption, visualizations of the droplets Mie scattering inside the injector have been recorded and post-processed by DMD in Fig. 4.14 and 4.15.

An instantaneous image of the internal volumetric Mie scattering signal is shown in Fig. 4.14. The chamber backplane can be seen, as well as parts of the injector inside the backplane. The white circle represents the limit of the pilot stage, with a diameter of 24 mm, and some droplets can be distinguished inside this circle as well as the tip of the pilot fuel nozzle. The illumination is performed with an expanded laser beam, as explained in chapter 2. The acquisition frequency is 10 kHz for a duration of 1.09 s. Because of the tilt of the camera and the volumetric illumination, spatial information is difficult to properly retrieve from such images but dynamical phenomena can still be highlighted, as shown by the DMD results in Fig. 4.15.

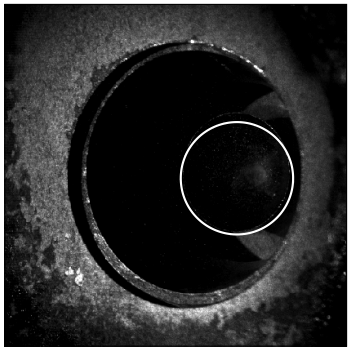

Figure 4.14 – *Instantaneous image of the internal volumetric Mie scattering signal. The white circle highlights the pilot stage limit.*

Five hundred Mie scattering images are processed by DMD and a strong coherent structure at the PVC frequency can be identified. The shape of this mode for different phases of its oscillation cycle is shown in Fig. 4.15. Because of the volumetric illumination, the three spatial dimensions are at play in these pictures. A sense of depth can however be retrieved thanks to the hollow cone shape of the fuel spray: the part of the signal that is radially away from the injection point can be considered downstream from it. Because of the tilt of the camera, it must be noted that the injection point is off-centered to the right, where the signal intensity is the highest.
The structure at the PVC frequency shows a clearly defined yin-and-yang-like structure with a clockwise motion having its roots around the pilot fuel injection point. This is compatible with the trace of a helical structure rotating in the same direction as the swirling flow and, furthermore, recent numerical simulations at a higher air flow rate have highlighted a PVC taking root on the pilot fuel nozzle. It can thus be seen that the PVC starts acting very close to the fuel injection point by creating early variations in the droplet seeding. Such modulations can explain the findings about the spray dynamics obtained with Mie scattering or PDA measurements inside the chamber. The PVC does

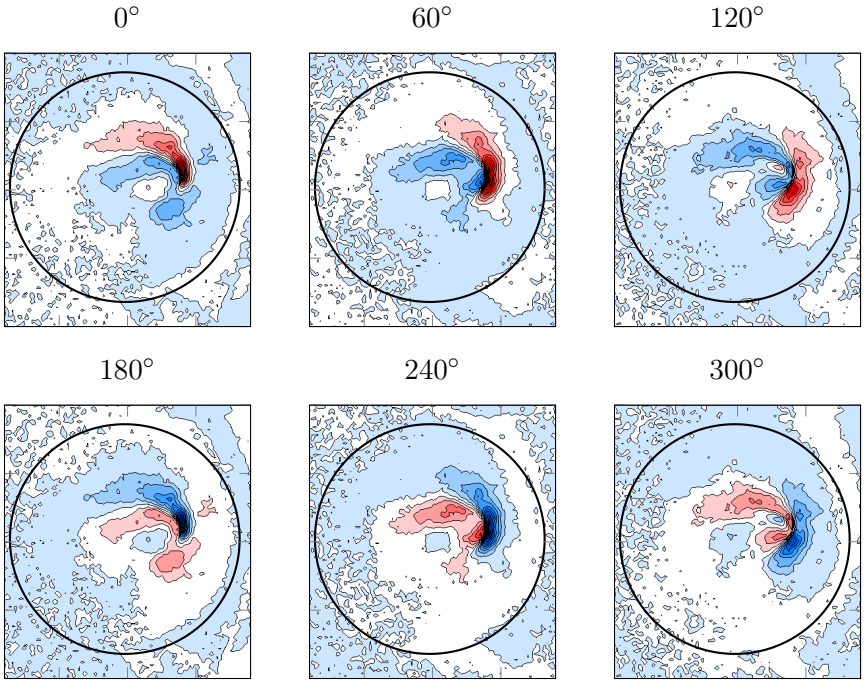

Figure 4.15 – *Evolution of the mode at the PVC frequency from a DMD on the internal Mie scattering visualizations. The blue (resp. red) color represents negative (resp. positive) fluctuations relatively to the mean. The black circle represents the pilot stage limit (Fig. 4.14).*

not necessarily need to exit the injection system to be visible in the chamber because its trace on the spray dynamics is. This would explain why velocity modulations inside any droplet diameter class could not be detected at the PVC frequency.

4.2 Reacting flow and V-flame stabilization

4.2.1 Effect of the combustion

The presence of a flame can strongly disturb a flow, namely by creating sudden changes in the temperature and density fields. The flow also has an obvious impact on the flame by enabling its stabilization. Flame and flow thus work as a couple with feedback mechanisms on each other and the aim of the present section is to analyze some of them. For this pilot-only operating point, the flame takes a V shape often found in swirling burners (Weigand et al. (2006), Galley et al. (2011)), as shown by the photography in Fig. 4.16.
The flame has a strongly diverging conical structure and seems anchored inside the injector upstream of the combustion chamber. After a few centimeters, it apparently interacts slightly with the chamber walls. Its color is mainly blue

(mostly because of the CH* radical), meaning that the combustion happens in a reasonably well mixed regime. The light intensity is also higher near the anchoring point and seems to have a slightly greenish color (trace of the C_2^* radical), probably because of a richer and more intense reaction zone there. From this image of the flame, it seems that the spray can be different compared the non-reacting conditions because none of the previously highlighted features can be observed. This is confirmed by the Mie scattering RMS image shown in Fig. 4.17.

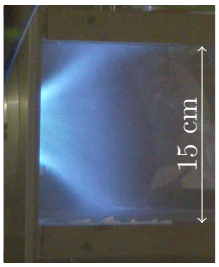

Figure 4.16 – *Photography of the pilot-only flame. Flow from left to right.*

In order to compare the spray in reacting conditions to the previously studied non-reacting spray, the contours of the latter are superimposed to the Mie scattering RMS image in Fig. 4.17.

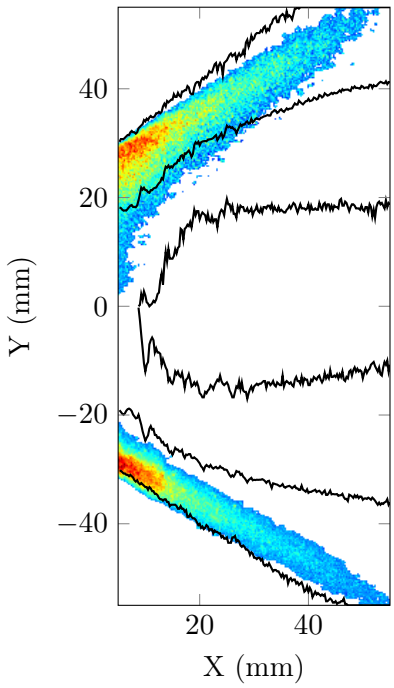

Figure 4.17 – *RMS image of Mie scattering intensity in the reacting case. A threshold has been set at 15% of the maximum value to highlight the shape of the spray. The black lines represent the spray limits from the non-reacting Mie scattering RMS image (Fig.4.2).*

The general shape of the reacting spray seems similar to the flame shape with

a strongly diverging conical structure. Compared to the non-reacting spray, the reacting spray only covers its external parts and does not show the previously highlighted divergent-convergent-divergent structure. No mixing-induced spread of the spray can be observed either, probably because of the combustion process consuming the droplets as they mix with air. For the same reason, the penetration length of the spray is smaller in the reacting case. Finally, the outer limit of the spray is interestingly similar in both conditions which leads to think that the underlying process creating this boundary is the same. In non reacting conditions, the Sauter Mean Diameter spatial distribution in Fig. 4.6 showed that this limit was apparently not related to the air flow but to the ballistic behaviour of the biggest droplets. One thus expects a similar observation in reacting conditions.
A comparison of the spray and flame relative positions can help explain this particular spray shape. This is done in Fig. 4.18 with the help of CH^* chemiluminescence measurements.

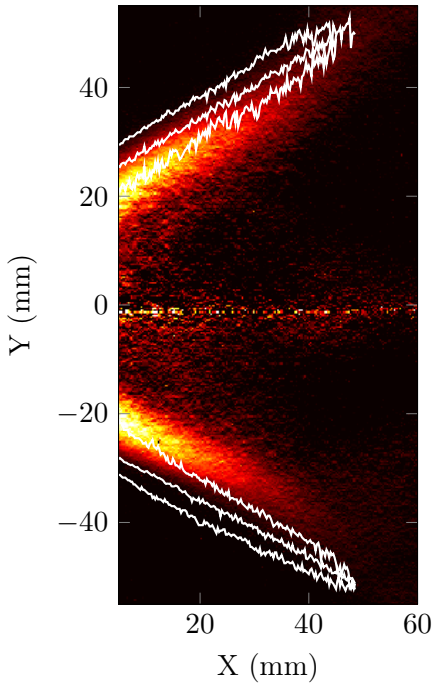

Figure 4.18 – *Abel-inverted mean CH^* chemiluminescence image for the pilot-only condition. The white lines represent the spray limits from the reacting Mie scattering RMS image (Fig.4.17).*

To monitor the position of the flame and its motion, a high-speed Photron FastCam SA-X equipped with an intensifier and a filter (431±10 nm) is used to record the CH^* chemiluminescence signal from the flame. The acquisition parameters are reported in table 4.3.

Table 4.3 – *Acquisition parameters for the CH* chemiluminescence measurements.*

Acquisition frequency (kHz)	10
Image size (pixels)	512×512
Equivalent field of view (mm)	153×153
Number of images	10916
Recording duration (s)	1.09

The background light from the raw CH* images is removed and a pixel-by-pixel average image is computed from the whole dataset. Because the spontaneous emission from the flame is integrated over the line of sight of the camera, the average image is processed by an Abel deconvolution under the assumption of rotational symmetry, proven to be acceptable for a mean image. The resulting picture is shown in Fig. 4.18 with superimposed reacting spray contours computed from the RMS image in Fig.4.17.
As expected, the flame shows a strong V shape, quite similar to the mean spray shape with comparable opening angles. The thickness of the flame image is quite high compared to a real flame brush thickness because of the wrinkling and the motion of the flame which are smeared by the averaging process. The image can thus be seen as a sort of probability map for the position of the instantaneous flame front. The relative positions of the Mie scattering and the chemiluminescence signals show that the reaction actually takes place on the inner side of the spray, with a stabilization process probably involving the inner shear layer between the jet and the IRZ. It could thus be conjectured that the flame just consumes the inner droplets of the non reacting spray, leaving the external ones untouched, which would lead to this particular spray shape. However, the reacting spray velocity data in Fig. 4.19 show that the real flow-spray-flame coupling is much more complex.

The Mie scattering images from the reacting spray have been processed with PIV with 20×20 pixels windows with 60% overlap, as in non-reacting conditions. The mean axial and vertical velocity fields can be seen in Fig. 4.19 with a thresholding highlighting the scarcity of the seeding.
On the contrary to what could be expected, the reacting spray velocity fields are very different from the non-reacting ones. The velocity values are generally higher and, more importantly, the vertical velocities are strongly divergent, which means that the spray does not tend to move back towards the IRZ as before. The presence of the flame has thus a strong impact on the fuel spray velocity. It must nevertheless be noted that the region of positive velocity in the center of the chamber is still present probably because of the previously highlighted ballistic big droplets.
As previously, the PDA data can, among other useful information, help determine the fidelity of the PIV fields to the air flow by providing velocity values

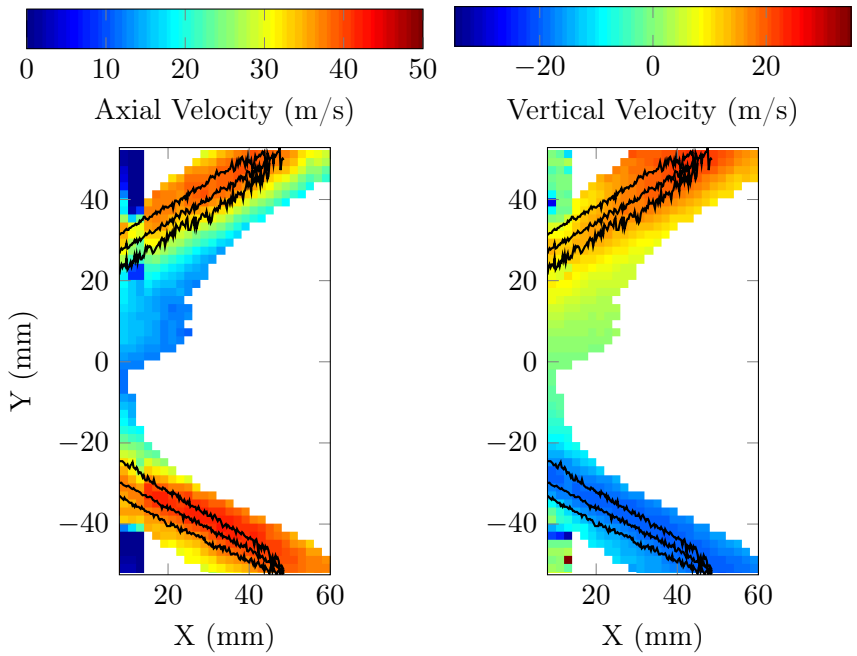

Figure 4.19 – *Mean axial (left) and vertical (right) spray velocities from the PIV treatment of the reacting Mie scattering fields. A threshold has been set at 2% of vector validation. The black lines represent the spray limits from the Mie scattering RMS image (Fig.4.17).*

conditioned by the droplet diameters. Mean interpolated velocity fields for the smallest and biggest droplets can be seen in Fig. 4.20.

The same conditioning technique as in Fig. 4.7 has been used on the PDA data in reacting conditions to obtain the interpolated mean velocity fields of the small (D< 10µm) and big (D>30µm) droplets, displayed in Fig. 4.20.
On the contrary to the non-reacting case, the velocity fields for the two diameters class are not completely different and both show a strong divergent behaviour, as previously expected from the PIV results. The field for the small droplets is particularly interesting because, as stated before, the small droplets can be seen as relatively accurate tracers for the underlying air flow. The notable difference with the non-reacting conditions for the small droplets is thus the proof that the presence of the flame has modified the air flow. Because the small droplets do not show any convergent motion anymore, it can for example be conjectured that the first inner toroidal structure, highlighted in Fig. 4.3, which was responsible for feeding the IRZ with small droplets has drastically changed. Another key observation on the small droplets fields is the increase of the velocity values. For a fixed mass flow rate, the air velocity can only increase by two means: a reduction of the density (leading to a higher volumetric flow

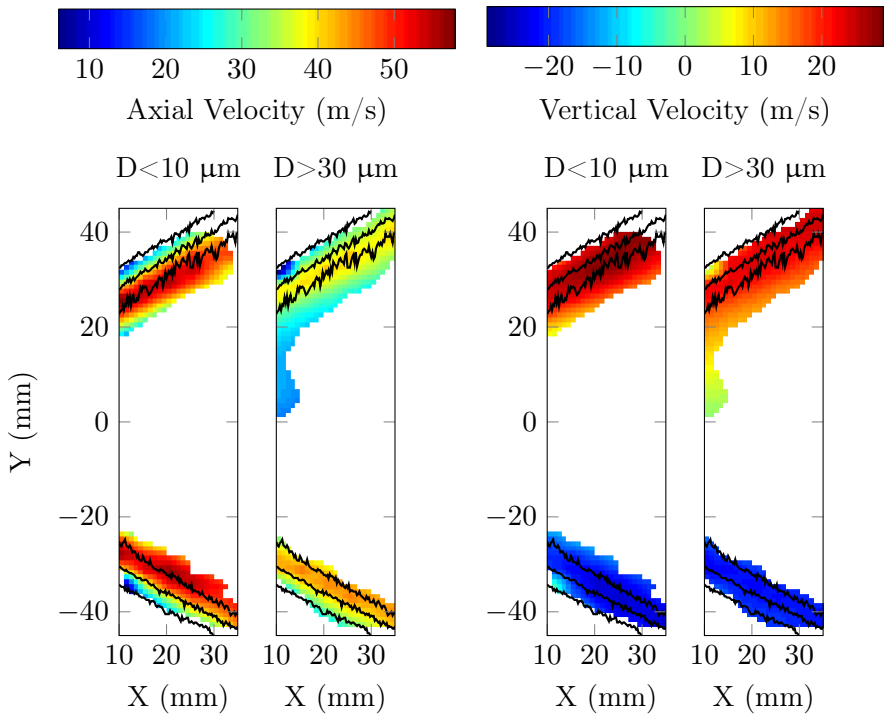

Figure 4.20 – *Interpolated mean axial (left) and vertical (right) spray velocities from PDA measurements conditioned by the droplets diameter. A threshold has been set at 500 detected droplets. The black lines represent the spray limits from the Mie scattering RMS image (Fig. 4.17).*

rate) or a reduction of the passage cross section. In the present case, the flame can induce both phenomena. Because of its heat release, the gas temperature can increase, leading to a decrease in its density. The second effect comes from the fact the flame is anchored inside the injector and can disturb the air flow inside it, leading to an aerodynamical blockage and effectively reducing the injector cross-section.

The big droplets vertical velocity field shows a similar trend as the small droplets one but there is a noticeable discrepancy in the axial velocity fields, with lower velocities for the big droplets. This lower axial velocity for the big droplets can be explained by looking at the response time of these droplets. Indeed, for a slip velocity around 10 m/s (the difference between air flow and big droplets velocity at 10 mm), the response time of a 30 µm droplet is about 0.6 ms, leading to a displacement of the droplet of 24 mm which roughly corresponds to the size of the region of interest. The big droplets have thus no time to get in equilibrium with the air flow, which explains the velocity discrepancy. The differences between the small and big droplets trajectories can be further highlighted by looking at the velocity angles in Fig. 4.21.

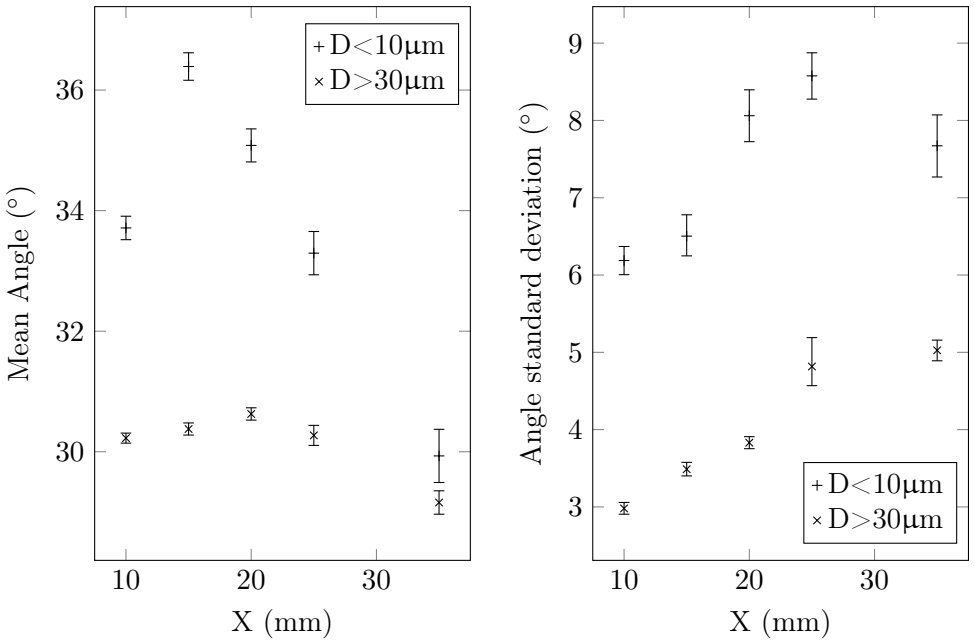

Figure 4.21 – *Mean value (left) and standard deviation (right) of the droplet velocity angle away from the center. The error bars represent 95% confidence intervals.*

The average value and standard deviation of the velocity angle of the droplets are computed at the "center of mass" of the reacting spray based on the RMS Mie scattering image. The results are shown in Fig. 4.21 with confidence intervals computed with the same method as for Fig. 4.8.
The big droplets mean angle is once again quite stable around 30°. This is coherent with their previously highlighted ballistic behaviour. The small droplets have however a different behaviour compared to the non-reacting conditions with a higher angle than the big droplets one. The small variation in the small droplets mean angle shows that the direction of the air flow does not change as much as in the non-reacting conditions.
The standard deviation plot also provides interesting information. As expected, the standard deviation of the big droplets angle is low because of their low response time. Another interesting feature is the low standard deviation of the small droplets angle, showing that their trajectory is less erratic than in non-reacting conditions. This proves that the flame has not only changed the average air flow shape but also its fluctuations level, leading to a much more constrained behaviour.

4.2.2 Flame and spray dynamics

As emphasized previously, the flame has a strong impact on the air flow and some studies have shown that combustion can suppress the PVC. To deter-

mine if a similar phenomenon happens in the present conditions, dynamical informations on the spray can be seen in Fig. 4.22.

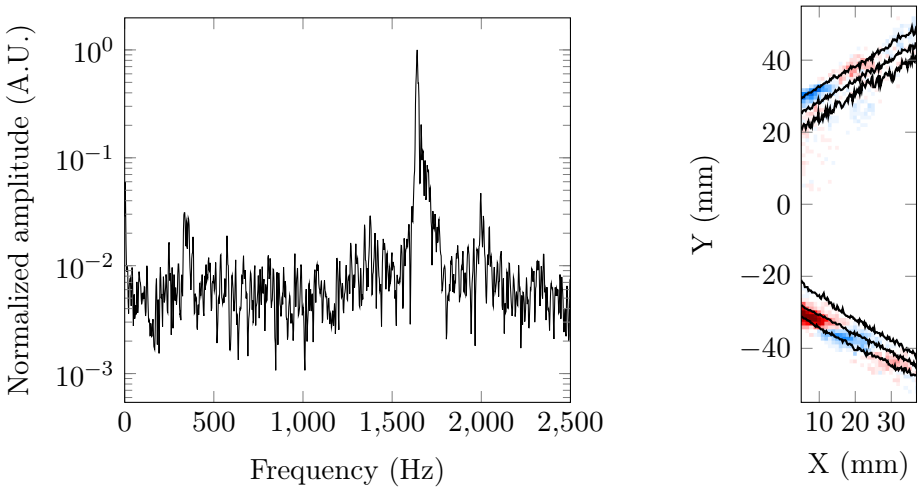

Figure 4.22 – *Power spectral density from a region of interest in the Mie scattering images (left) and DMD mode at the peak frequency (right). Positive Mie scattering fluctuations are in red and negative ones in blue. The black lines represent the spray limits from the Mie scattering RMS image (Fig.4.17).*

As previously done for Fig. 4.9, the Mie scattering signal inside a 30×30 pixels region placed at X=5 mm and Y=-25 mm is averaged and its Power Spectral Density (0.25 s long windows, 50% overlap) is plotted on the left of Fig. 4.22. The spectrum shows a clear peak and the DMD (500 samples) mode at this frequency (shown on the right) shows antisymmetric structures as in the non-reacting conditions, compatible with the variation in the droplet seeding induced by the PVC. These structures are present only in the very external parts of the spray.
The peak frequency is around 1640 Hz which corresponds to an increase of over 3% compared to the non-reacting case. Since the PVC frequency depends on the volumetric flow rate, it is possible that this frequency change comes from the increase in temperature created inside the injector because of the flame.
The PIV treatment on the Mie scattering images does not show any strong dynamical phenomenon, probably because of the scarcity of the data due to the thinness of the reacting spray but it is interesting to look at the spectra for PDA data at X=10 mm and Y=26 mm in Fig. 4.23.

The reacting condition counterparts of the plots in Fig. 4.11 and 4.12 are presented in Fig. 4.23. As previously, the axial and vertical velocity spectra show a peak at the PVC frequency (1640 Hz) meaning that the detected velocity signal is modulated by the PVC. The diameter and time interval spectra also

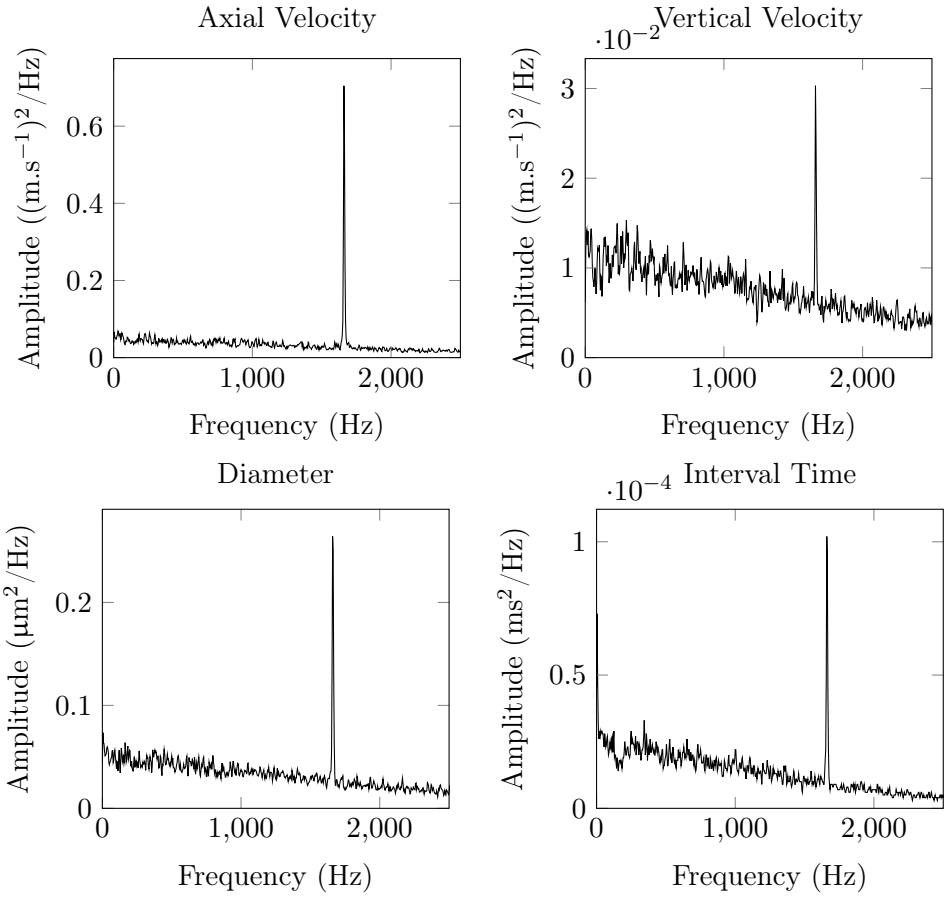

Figure 4.23 – *PSD spectra of four signals (axial velocity, vertical velocity, diameter and time interval) extracted from a PDA measurement at X=10 mm and Y=26 mm.*

still show a response to the PVC frequency. This is of particular interest in reacting conditions because changes in the droplet diameter and in their density mean changes in the local fuel repartition and thus in the equivalence ratio and reaction rate.
It can thus be suspected that the PVC impacts the flame through its effect on the spray. This is confirmed by the dynamical analysis of the CH^* chemiluminescence data in Fig. 4.24.

The spectrum on the left of Fig. 4.24 is computed on a 30×30 pixels region of interest positioned at X=5 mm and Y=20 mm. A peak at the PVC frequency can be seen, meaning that the signal from the flame is modulated at this frequency. The DMD (500 samples) mode at this frequency is shown on the right part of Fig. 4.24.
Looking at the external parts of the modes, alternating antisymmetrical structures similar to that of the spray can be observed. In the middle of the plane,

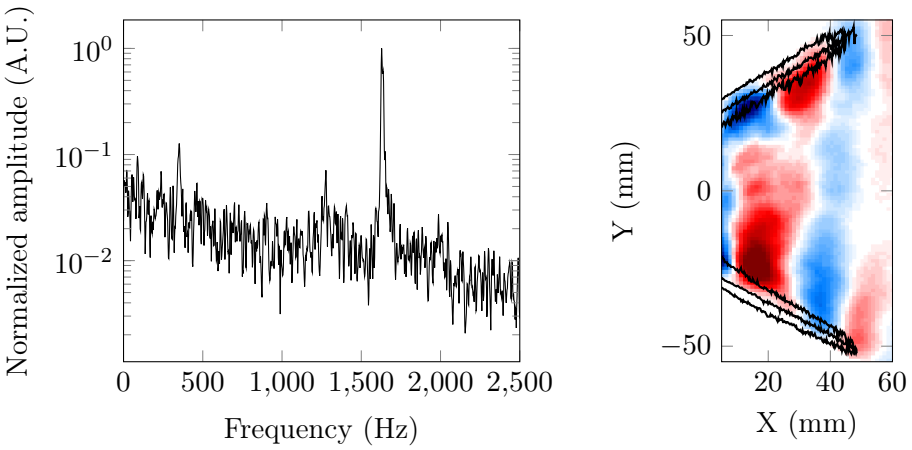

Figure 4.24 – *Power spectral density from a region of interest in the CH* chemiluminescence images (left) and DMD mode at the peak frequency (right). Positive Mie scattering fluctuations are in red and negative ones in blue. The black lines represent the spray limits from the Mie scattering RMS image (Fig.4.17).*

where the signal mostly comes from the part of the flame closest to the camera, links between the structures can be observed with the top being ahead of the bottom. This is once again compatible with modulations rotating in the swirlers direction, as seen in Fig. 4.15.
The PVC has thus a noticeable effect on the local heat release of the flame despite being undetectable from a global heat release point of view because of its antisymmetrical nature Moeck et al. (2013).

4.3 Effect of air flow rate modulations

4.3.1 Siren-induced oscillations

In this section, the previously described non-reacting and reacting conditions are subjected to air flow rate modulations created with the siren introduced in chapter 1. The siren is operated at 290 Hz with varying amplitude setpoints, measured by the Covered Surface Ratio (CSR) of the siren nozzle. This particular frequency is chosen because it is close to the first acoustic longitudinal frequency of the combustion chamber. The CSR is first set at its maximum value of 88% to emphasize the effect of air flow rate modulations on the non-reacting and reacting sprays and eventually on the flame.
Starting with the non-reacting conditions, the DMD (500 samples) mode of the Mie scattering data at the siren frequency is shown in Fig. 4.25.

Air flow rate oscillations seem to have a global effect on the spray with large modulations on the droplets Mie scattering intensity acting on the whole extent

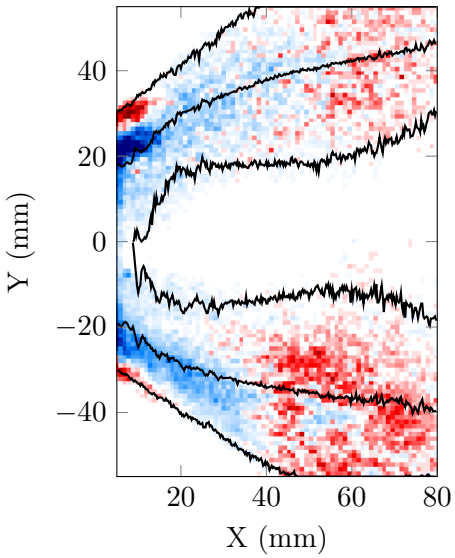

Figure 4.25 – *DMD mode at the siren (CSR 88%) frequency from the non-reacting Mie scattering data. The black lines represent the spray limits from the Mie scattering RMS image (Fig.4.2).*

of the spray. Near the beginning of the measurement region, it can be seen that the oncoming positive fluctuation is outside the previous low signal region, meaning that the spray may also be subjected to radial motion. This can be confirmed by looking at the PIV results in Fig. 4.26.

The axial and vertical velocity data from the PIV treatment are post processed by Dynamic Mode Decomposition on 500 samples and the components of the mode at the siren frequency can be seen in Fig. 4.26.
The axial velocity fluctuations have a symmetrical shape with amplitudes up to 7 m/s which means the droplets are alternatively accelerated and slowed with the air flow rate modulations, as expected. The vertical velocity fluctuations are more interesting to analyze because they have an antisymmetric shape, meaning that the spray is alternatively contracting and expanding. From the beginning of the chamber, it can be seen that the contracting phase corresponds to low axial velocities, that is, a low air flow rate. This effect comes from the fact that the siren is placed before the swirlers. The air flow rate modulations are converted into azimuthal fluctuations which in turn generate radial velocity fluctuations by centrifugal effect.
Because of the low frequency of the siren induced fluctuations (290 Hz), all the droplets present roughly the same response to the modulation so no segregation occurs and PDA data provides no further information about the effect of air flow rate modulations. It has however previously been highlighted that the reacting conditions present a noticeable change in the flow and spray behaviour, it is

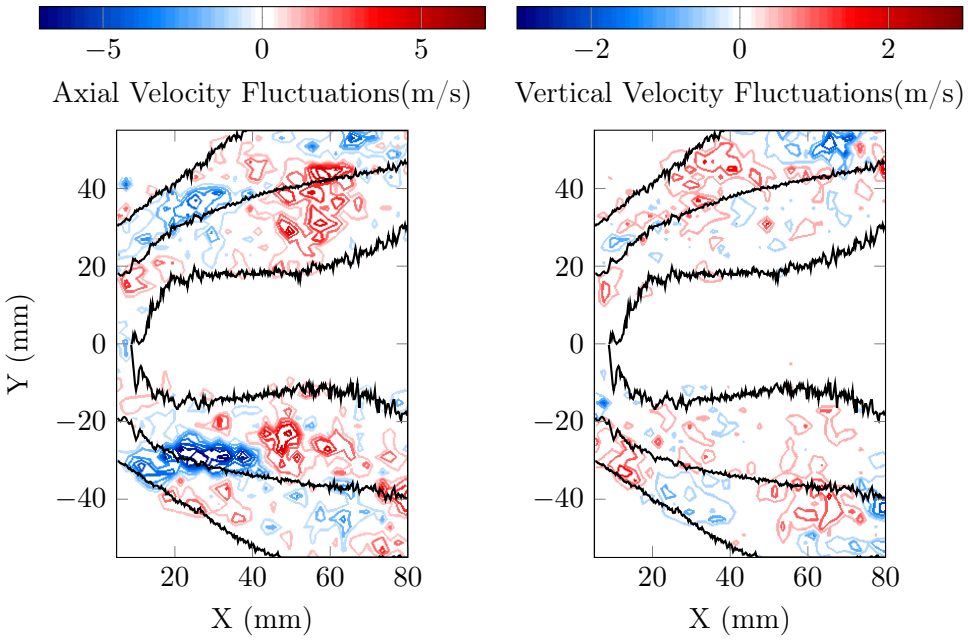

Figure 4.26 – *Contour plot of the DMD mode associated with the siren (CSR 88%) for the axial (left) and vertical (right) spray velocities from the PIV treatment of the non-reacting Mie scattering fields. The black lines represent the spray limits from the Mie scattering RMS image without modulations (Fig.4.2).*

thus needed to observe the effect of the siren on the reacting spray as proposed in Fig. 4.27.

As shown earlier (Fig. 4.17), the reacting spray is much thinner than in the non-reacting conditions because of the confinement created by the flame. The air flow rate modulation in non-reacting conditions showed a global motion of the spray with a contraction and expansion that cannot be seen in Fig. 4.27 for the reacting conditions.
The Mie scattering fluctuations in non-reacting conditions concern the whole spray. They can be seen as alternating high and low density regions convected along the spray arms.
Despite their thinness, these modulations of the fuel spray are expected to have an effect on the flame, which is confirmed by the graph in Fig. 4.28.

The combustion chamber is equipped with a microphone placed at half of its length. Using this microphone, Sound Pressure Level (SPL) values can be computed for 4 s long recordings for each value of the siren amplitude in non-reacting and reacting conditions. The resulting curves can be seen in Fig. 4.28. The non-reacting curve shows, as expected, that the SPL in the chamber increases with the amplitude of the siren-induced modulations. For the maximum

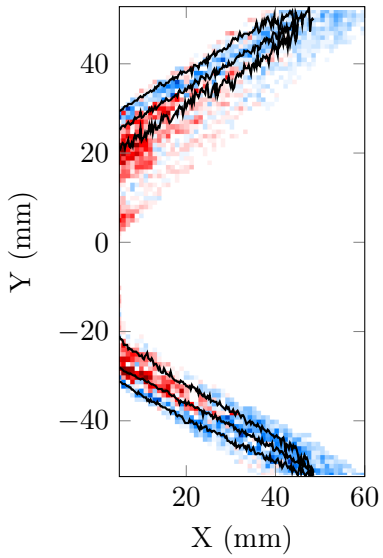

Figure 4.27 – *DMD mode at the siren (CSR 88%) frequency from the reacting Mie scattering data. The black lines represent the spray limits from the Mie scattering RMS image (Fig.4.17).*

CSR (88%), an increase of 14 dB of the SPL in the chamber can be noted. The reacting curve looks like a shift of the non-reacting one. However, because of the decibel graduation of the y axis, the implications of this shift have to be carefully studied with the help of the third curve.
On a linear scale, shifting corresponds to adding a constant value and, here, one would want to apply the same reasoning and see the reacting case curve as the addition of the non-reacting curve and a constant noise from the flame. This simple sound addition in fact corresponds to the middle curve because of the logarithmic scale. The difference between this curve and the reacting one comes from increases in the flame-generated sound, proving that the air flow rate modulations generated by the siren actually affect the flame.
In the absence of flow acceleration, which is necessary for entropy noise production (Motheau et al. 2013; Dowling and Mahmoudi 2015), sound generated from a flame generally directly comes from changes in the reaction rate or motion of the flame brush. To analyze the effect of the air flow rate modulations on the flame spatially, both phenomena can be qualitatively captured by the chemiluminescence intensity, as shown in Fig. 4.29.

The CH^* chemiluminescence data are analyzed with DMD (500 samples) and the mode at 290 Hz is presented in Fig. 4.29. Large scale fluctuations of the chemiluminescence intensity can be observed with almost vertical delimitations which are the trace of a mainly axial motion. It can however be seen near the external limit of the flame that the fluctuations seem ahead compared to the

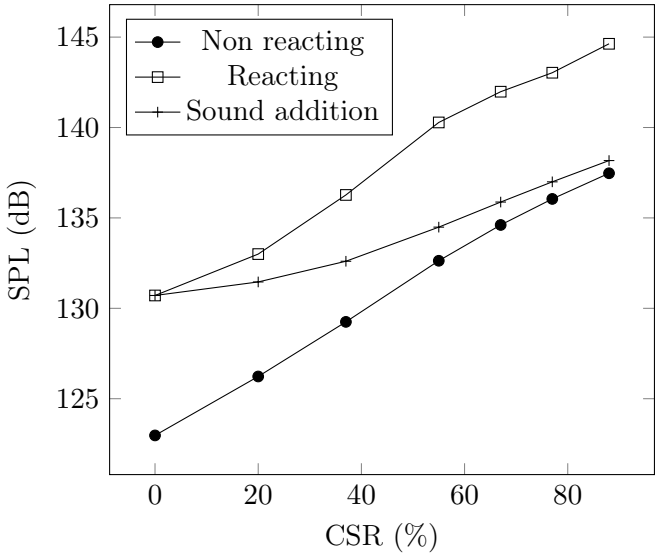

Figure 4.28 – *Evolution of the Sound Pressure Level in the combustion chamber as the siren-induced modulations increase.*

center region. This may indicate a slight radial motion of the flame.
All the previous diagnostics have shown that air flow rate modulations created by the siren affect the fuel spray (in non-reacting and reacting conditions) as well as the flame itself. It has also been highlighted that the PVC impacts them too. There may thus exist interactions between the two phenomena and the next part aims at analyzing them.

4.3.2 Interactions with the PVC

In order to measure the respective impacts of the siren-induced modulation and the PVC, a quantitative value must be associated to both phenomena. PSD spectra can be traced at specific probing points based on the previously studied 30× 30 pixels region of interest for the non-reacting Mie scattering images. The height of the peaks respectively associated with both phenomena could thus be used to measure their relative importance.

On the PSD spectrum presented on the left of Fig. 4.30, two main peaks with roughly the same amplitude are visible, one at the siren frequency of 290 Hz and one at the PVC frequency around 1580 Hz. On each side of the PVC peak, two smaller peaks can be identified with frequencies corresponding respectively to the difference between and the sum of the PVC and siren frequencies. These modes are the trace of non-linear interactions happening between the air flow rate modulations and the PVC and similar traces have been observed in the literature (Boxx et al. (2010), Moeck et al. (2012)).
The problem with using a PSD-based measurement is that it is dependent

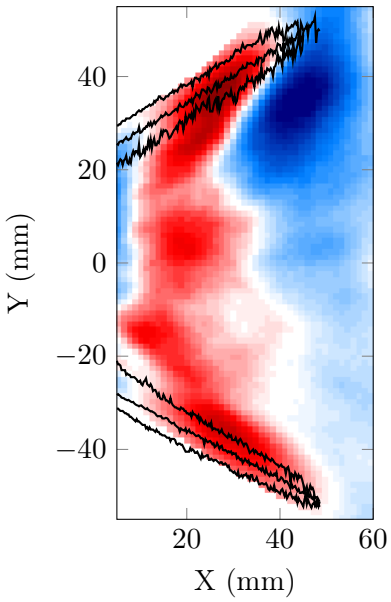

Figure 4.29 – *DMD mode of CH* chemiluminescence measurements at the siren frequency. Positive fluctuations are in red and negative ones in blue. The black lines represent the spray limits from the Mie scattering RMS image (Fig.4.17).*

on a region of interest and can only provide local information which can be deceiving. The other extremity (using the whole image as the averaging region for the signal to be processed by PSD) would be insensitive to antisymmetrical structures, which would prevent the monitoring of the PVC impact for example.
A more relevant way of measuring the intensity of the two studied phenomena is to use a spectrum-like representation based on the DMD and shown on the right of Fig. 4.30. This plot represents the amplitude of the modes (here defined as their L2-norms in space and the median value in time) versus their frequency. In this case, the amplitude of a mode represents a measure of its energy content based on the decomposed data. It is thus a global measurement of the impact of a phenomenon on the whole image and is therefore interesting to compare the respective effects of the siren and the PVC.
On the right of Fig. 4.30, the peaks corresponding to the siren and the PVC can be identified but a lot of other less relevant peaks also seem present. An interesting measure of the intensity of a phenomenon is thus to compute a signal-to-noise ratio (SNR) based on the peak value divided by the median of the values of non-relevant peaks. The use of a median instead of a mean value enables to be more robust to extremely high or extremely low values that can arise from the decomposition of a badly conditioned matrix.
This way of measuring the respective importance of the PVC and the siren-induced modulations on the non-reacting spray is used in Fig. 4.31.

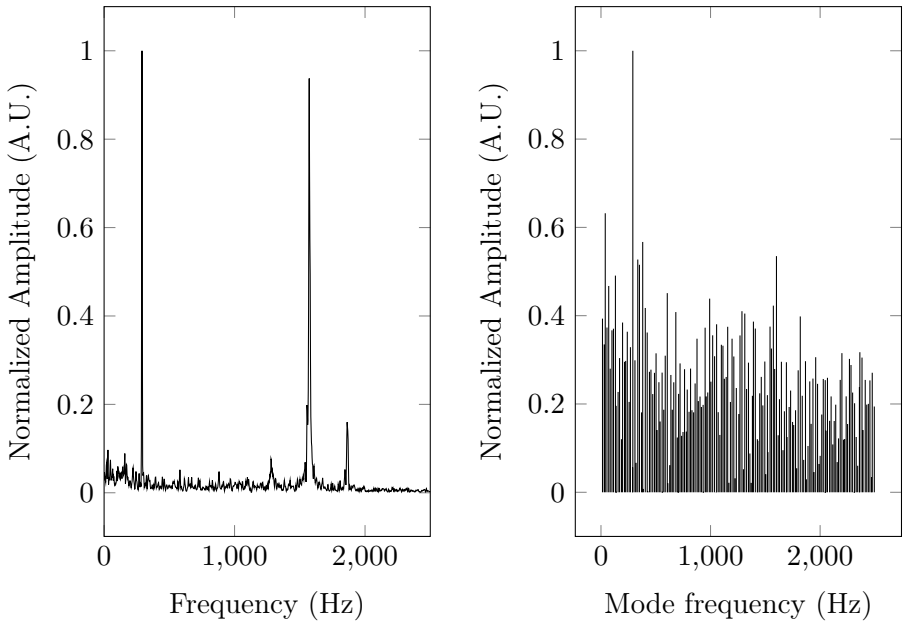

Figure 4.30 – *Region of interest based power spectral density (left) and DMD spectrum (right) of non-reacting Mie scattering measurements for a CSR of 37%.*

Performing a DMD usually requires a relatively small number of time-resolved samples (here 500) and several DMDs can thus be performed on the 15000 images long Mie scattering recordings. In order to gain confidence on the protocole based on the SNR of the mode amplitudes in the DMD spectrum, 30 DMD are performed and the results are averaged. This way, the whole recording length is spanned. A 95% confidence interval is also computed based on the Student's t-distribution under the assumption of a normal distribution of the SNR. This method is applied to seven values of the CSR: 0% (siren turned off), 20%, 37%, 55%, 67%, 77% and 88%. These results are plotted in Fig. 4.31.
First, it can be seen, as expected, that the siren-mode SNR increases with the CSR. Although this result is quite obvious, it is also a proof of the pertinence of this measurement method. It must however be noted that there seems to be a saturation effect for high CSR values but the confidence intervals overlap. It could thus just be a sampling artifact and must not be taken for granted. In general, because only 30 DMD are performed, the confidence intervals are quite large and one must be careful not to over-interpret the data.
The PVC mode SNR shows a clear decreasing tendency as the siren-induced modulation increases until it gets barely detectable for the maximum siren amplitude. One would like to conclude that air flow rate modulations can destroy the PVC but, for the moment, one can only say that they can reduce the trace of the PVC on the non-reacting spray because they could simply act by scattering the droplets or by increasing their vaporization.

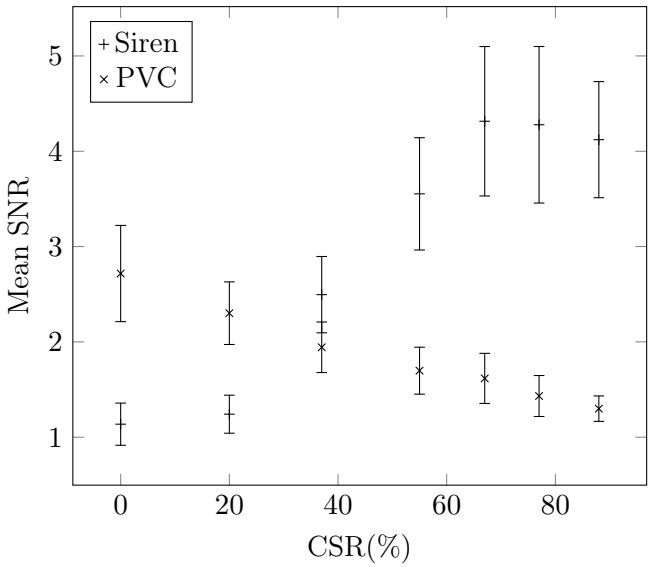

Figure 4.31 – *Mean signal-to-noise ratio (SNR) of the amplitudes of the siren and PVC modes for the non-reacting Mie scattering data as a function of the siren amplitude. The error bars represent the 95% confidence interval for the associated mean value.*

In order to further analyze the diminution of the PVC trace in the spray, it is interesting to look at how things are evolving locally. This is done thanks to the graphs in Fig. 4.32.

With each of the 30 DMD performed on the Mie scattering recordings, a mode associated to the PVC frequency can be extracted. An example of one of them can be seen in Fig. 4.9 when the effect of the PVC on the non-reacting spray was studied. To analyze the local evolution of such a mode, regions of interest of 3×3 mm are used. They are placed on a 33 mm long line along the bottom arm of the spray, starting at X=5 mm and Y=-25 mm and ending at X=35 mm and Y=-40mm. For each of these regions of interest, the oscillation amplitude of the PVC modes is extracted. The plot on the left of Fig. 4.32 shows the evolution of the mean of these oscillation amplitudes versus the position of the regions of interest along the arm of the spray for each CSR.
The first noticeable thing is the decrease of all the curves as the position along the spray arm increases. This represents the fact that the trace of the PVC on the spray is damped as it progresses inside the chamber because of droplet vaporization and mixing. It can also be seen that, as expected from Fig. 4.31, the oscillation amplitude gets lower as the CSR increases.
An interesting information comes from the normalization of these curves based on their initial values, seen on the right of Fig. 4.32. All the data indeed collapse into one curve. This shows that the air flow rate modulations do not noticeably

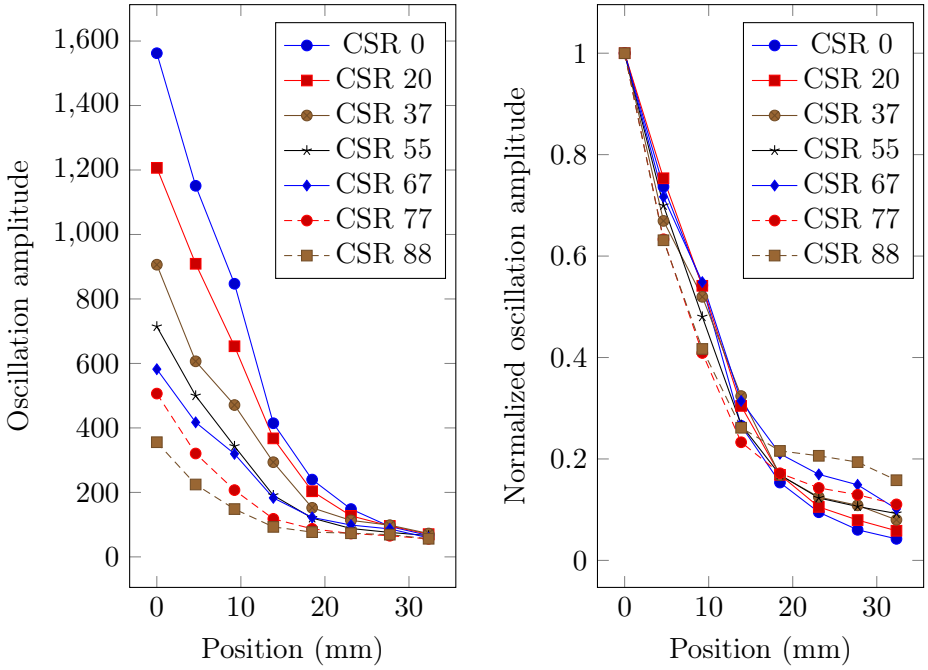

Figure 4.32 – *Evolution of the mean oscillation amplitude of the PVC mode along one arm of the non-reacting spray based on Mie scattering data. The raw values on the left plot are normalized by their initial value and plotted on the right.*

change the damping of the trace of the PVC on the spray due to vaporization and mixing. The change in the intensity of the trace in the spray thus comes from a phenomenon happening before the combustion chamber, out of reach from the Mie scattering recordings.
In reacting conditions, it has been highlighted that the flame induces drastic changes to the air flow and the spray behaviour. The relative impacts of the siren and the PVC on the reacting spray are thus studied in Fig. 4.33.

Figure 4.33 is obtained using the same post-processing methods used in Fig. 4.31 and similar information can be drawn out of it. The siren mode increasing behaviour and PVC mode decreasing behaviour with the increase of the CSR can be retrieved.
There are however major differences between the non-reacting and reacting spray global responses. First, it is needed to deal with the odd point of the PVC mode amplitude at CSR 0%. This point apparently suggests that a low value of air flow rate modulations would be beneficial to the PVC mode amplitude. As for the saturation effect in Fig. 4.31, this assumption needs to be confronted to the size of the confidence interval meaning it could only be a sampling bias. This being said, it can be seen that the two curves do not cross because the PVC mode SNR is higher and the siren mode SNR lower than in non-reacting

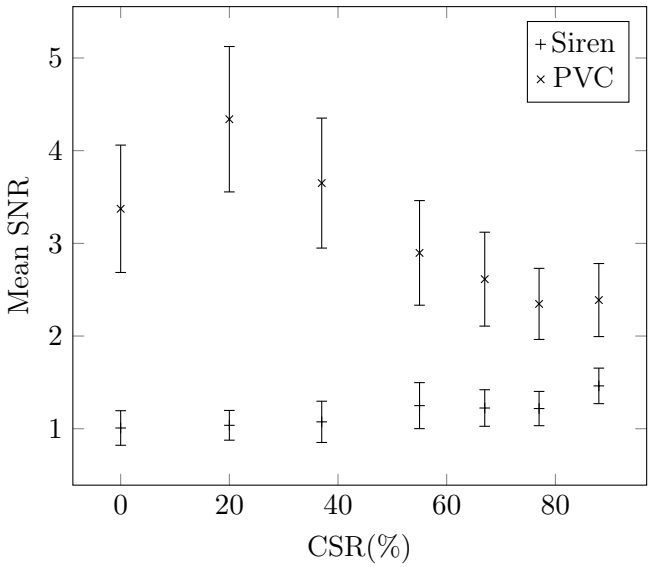

Figure 4.33 – *Mean signal-to-noise ratio of the amplitudes of the siren and PVC modes for the reacting Mie scattering data. The error bars represent the 95% confidence interval for the mean.*

conditions. These information have to be treated in regard with the actual area from where the useful signal comes. In non-reacting conditions, the spray is quite large and it has been seen that the siren induced modulations have a global impact on it (Fig. 4.25) whereas the trace of the PVC is limited to a small external region (Fig. 4.9). This means that, in non-reacting conditions, the siren mode provides signal from the whole image while for the PVC mode, more than half of the spray contributes to the noise level. When the flame is present, the situation for the PVC mode is changed as it impacts the whole reacting spray. On the contrary, because of the flow confinement provided by the flame, the air flow rate oscillations created by the siren cannot generate as much modulation of the spray as in non-reacting conditions since they lack the radial room for their flapping motion. This explains why the siren mode amplitude remains low for the Mie scattering data in reacting conditions.
Because the trace of the PVC on the reacting spray shows a difference with the trace in non-reacting conditions, looking at things more locally can provide useful information on the phenomena involved in this modification. This is the goal of Fig. 4.34.

The plots in Fig. 4.34 are obtained with the same processing performed on the non-reacting Mie scattering data in Fig. 4.32, the same regions of interest placed along the arm of the spray are thus used.
The curves on the left of Fig. 4.34 show the expected decaying behaviour due to vaporization and mixing. The unexpected behaviour observed for CSR 0%

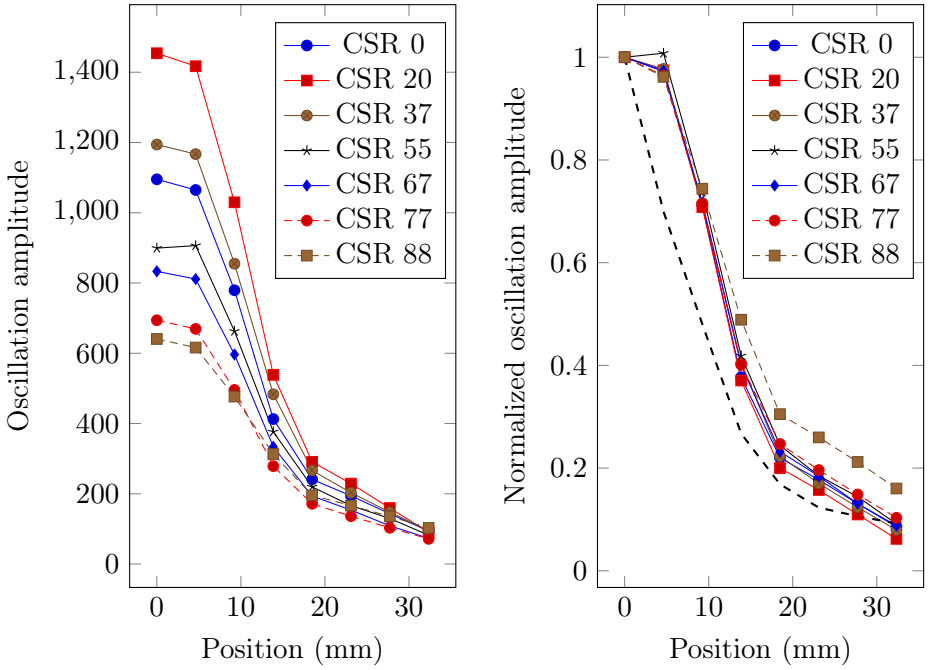

Figure 4.34 – *Evolution of the mean oscillation amplitude of the PVC mode along one arm of the reacting spray. The raw values on the left plot are normalized by their initial value and plotted on the right. The dashed thick black line on the right plot represents the mean non-reacting conditions curve.*

is still visible here but, for the reasons previously given, it can probably be overlooked.

A collapse of the curves can also be observed when they are normalized by their initial value, meaning that, in reacting conditions, the siren still does not change the damping of the PVC trace on the spray but rather acts upstream on the generation of this trace.

Interestingly, when adding the average curve for the same plot in non-reacting conditions (the dashed thick black line), the comparison between the curves shows that, in reacting conditions, the trace of the PVC seems to propagate a bit further before being damped. This information may be analyzed in regard with the droplets velocity angles in Fig. 4.8 and 4.21. In non-reacting conditions, the high standard deviation of the small droplets angles showed that turbulence and mixing are apparently higher than in reacting conditions where the fuel spray is much more constrained by the flame. The reduction of the mixing in reacting conditions can explain the better propagation of the PVC trace. This phenomenon is however competing with an enhanced fuel vaporization due to the flame heat release.

It is clear that the siren has a direct effect on the reacting spray (even though it seems a bit faint) and also reduces the trace of the PVC on it. These effects

have an impact on the flame, as shown in Fig. 4.35.

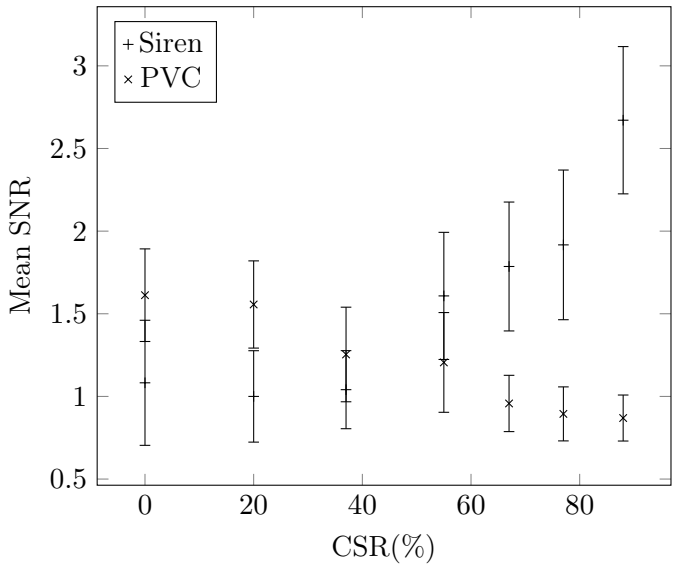

Figure 4.35 – *Mean signal-to-noise ratio of the amplitudes of the siren and PVC modes for the CH* chemiluminescence data. The error bars represent the 95% confidence interval for the mean.*

Using the same post-processing work flow as for Fig. 4.31 and 4.33, the mean SNR values in Fig. 4.35 can be obtained from 30 DMD performed on the CH* chemiluminescence recordings for each CSR.
The typical behaviour of these plots is retrieved with an increasing siren mode and a decreasing PVC mode. However, despite what is shown in Fig. 4.33, the two curves cross and the siren mode reaches relatively high SNR. This is again an effect of the relative dimensions between the modulations and the image size because, as it can be seen in Fig. 4.29, the siren induced modulations act on the whole flame size.
All the previous analyses have shown that, in non-reacting as well as reacting conditions, air flow rate modulations induce a diminution of the trace of the PVC on the spray and the flame. Since the damping of this trace because of droplet mixing and vaporization is not changed by the amplitude of the air flow rate modulations, the effect actually happens upstream, inside the injector. The internal Mie scattering visualization signals are thus used in Fig. 4.36 to provide further insight on this question.

As shown in Fig. 4.15, the internal Mie scattering visualizations are very sensitive to the early spray rotating motion induced by the PVC. A region of interest of 30×30 pixels, placed inside the circle representing the limit of the pilot stage, is used to monitor the PVC frequency. Here, the reacting internal Mie

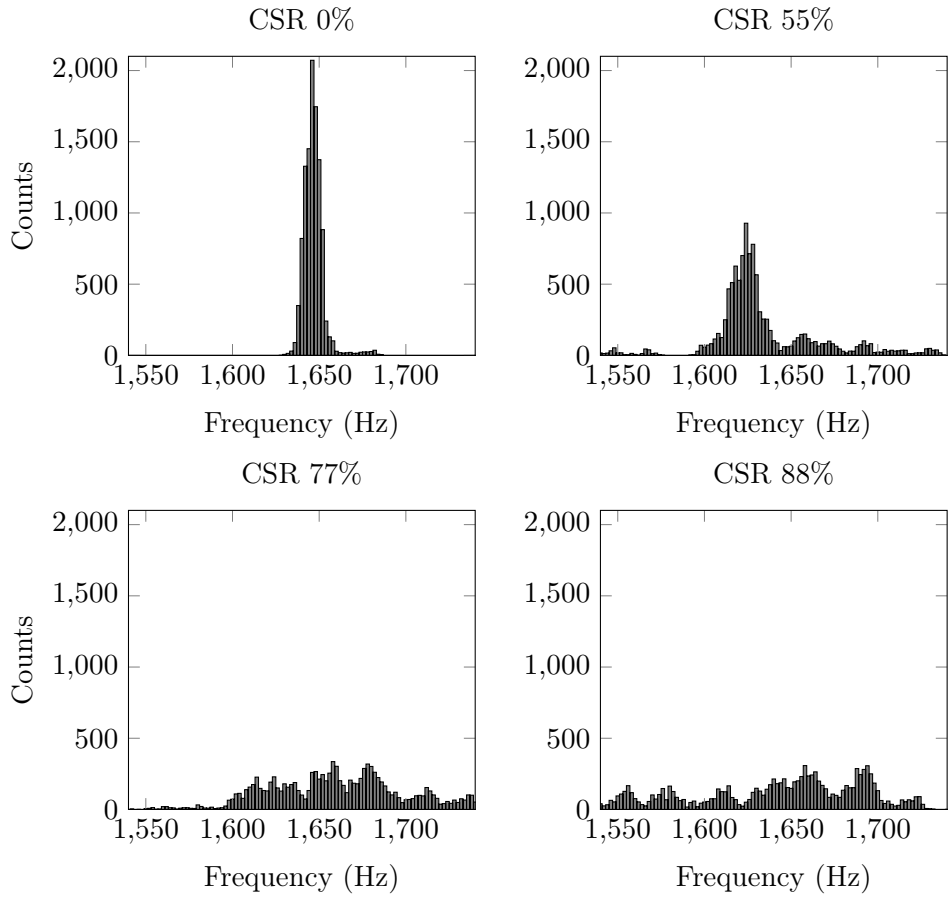

Figure 4.36 – *Histograms of the PVC frequency in reacting conditions for different air flow rate modulation amplitudes.*

scattering data is averaged over this region of interest and provides a temporal signal at a rate of 10 kHz. This signal is processed with a continuous wavelet transform to obtain histograms of the PVC frequency.
A complex Morlet wavelet (center frequency=6; bandwidth parameter=10) is chosen as the mother wavelet for the analysis after a preliminary study showing its adequacy with the present signal. The scales for the analysis are chosen so that the associated frequencies span the interval between 1540 and 1740 Hz with 2 Hz steps. At each time step, the PVC frequency is defined as the frequency associated with the highest scalogram coefficient. This gives 10918 values for the PVC frequency which are then plotted as histograms in Fig. 4.36.
Without any air flow rate modulation (CSR 0%), the detected frequency for the PVC is really stable and centered around 1645 Hz. When the CSR increases, it can be seen that the PVC frequency is spread and the histograms become wider. This means that the structure becomes less coherent as air flow rate modulations increase. Indeed, because the PVC frequency is dependent on

the air flow rate, modulating it with an increasing amplitude leads to a frequency modulation of the PVC which results in the frequency spread observed in Fig.4.36.
Because internal visualizations show the response of the spray to the PVC at the moment when the spray is generated, they can be considered as a relatively accurate monitoring of the PVC since no perturbing phenomena such as vaporization or mixing have happened yet. The histograms in Fig. 4.36 thus prove that siren-generated air flow rate modulations can effectively disturb the PVC to the point where it becomes almost undetectable. This disappearance of the PVC in the presence of acoustic waves has also been highlighted in other experiments as well as in numerical simulations (Iudiciani and Duwig (2011), Alekseenko et al. (2012)).

Summary of the chapter

This study, performed on a pilot-only operating point chosen to avoid the complexity of the stage injection, provides useful information on the interactions between the air flow, the fuel spray and the flame from an average as well as dynamical point of view.

In non reacting conditions, the air flow is characterized by a strong Inner Recirculation Zone fed by two toroidal structures taking place between it and the swirling jet. An outer recirculation zone due to the expansion created by the combustion chamber can also be observed. In these conditions, different fuel droplet behaviours can be highlighted depending on their sizes. The bigger droplets have their own ballistic behaviour, with a clear diverging trajectory, but the smaller ones follow the airflow well and can enter the IRZ thanks to the first toroidal structure. These smaller droplets are characterized by high velocity fluctuations showing a turbulent flow that enhances mixing. From a dynamical point of view, the helical trace of a Precessing Vortex Core can be identified in the spray. The PVC changes the fuel droplets repartition by acting at the pilot fuel injection point but seems quickly damped while its trace remains.

When a flame is present, a visible change in the spray can be observed. The bigger droplets keep their ballistic behaviour but the smaller ones show a strong modification of the air flow, with a more confined diverging jet and less fluctuations. The flame takes a V shape and stabilizes on the inner limit of the fuel spray with roots inside the injector. Despite the strong flow change, the PVC is still present but at a higher frequency than in non-reacting conditions, probably because of the presence of the flame inside the injector. Its effect is visible on the fuel spray as well as on the flame itself due to the non-uniform fuel repartition.

Air flow rate modulations, performed with a siren placed before the swirlers induce an axial and radial perturbation on the air flow. This modulation acts on the fuel spray and on the flame. Increasing the air flow rate modulations leads to a decrease of the PVC trace on the spray despite unchanged vaporization and mixing properties. This is explained by the action of air flow rate modulations on the PVC frequency. As they increasingly destroy the coherence of the structure, its trace becomes less distinguishable within the combustion chamber and for the proposed set of diagnostics.

Chapter 5

Multipoint-dominated injection

This chapter presents an operating regime where the fuel injection is split between the two stages with 85% through the multipoint and 15% through the pilot nozzle. The non-reacting conditions are first described to provide a ground for the reactive study. In reacting conditions, the operating point can lead to two different flames. Both of these flames are studied from an average as well as a dynamical point of view.

In staged jet engines, high power is provided with as much fuel as possible injected through the well-mixed stage (here the take-off stage with the multipoint injection) to reduce pollutant emissions. The operating point chosen here has the peculiarity of presenting two potential stable flames depending on the operation history, which makes it an interesting study material. The set of operating parameters, visible in table 5.1, is chosen so that changing only the fuel staging leads to a closed hysteresis cycle of flame shape and behaviour which will be studied in chapter 6.

Table 5.1 – *Multipoint-dominated operating point definition.*

Global Parameters				
$\dot{m}_{air}$	T_{air}	$\dot{m}_{fuel}$	P	ϕ
($g.s^{-1}$)	(K)	($g.s^{-1}$)	(kW)	(-)
43.1	433	1.64	72	0.6
Staging				
α	$\dot{m}_{fuel,pilot}$	ϕ_{pilot}	$\dot{m}_{fuel,takeoff}$	$\phi_{takeoff}$
(%)	($g.s^{-1}$)	(-)	($g.s^{-1}$)	(-)
15	0.25	0.67	1.39	0.59

5.1 Non-reacting conditions

5.1.1 Average spray behaviour

The tomographic setup presented in chapter 2 and already used in chapter 4 is used in the present study with slightly different parameters, reported in table 5.2.

Table 5.2 – *Experimental parameters for the tomographic Mie scattering measurements.*

Acquisition frequency (kHz)	2×10
Delay between laser pulses (µs)	20
Image size (pixels)	704×520
Equivalent field of view (mm)	176×130
Number of images	31274
Recording length (s)	1.56

The useful size of the image is here again reduced because of the 90 mm wide laser sheet but this value is still more than enough to observe the whole extent of the reacting spray, as shown by the Mie scattering RMS image in Fig. 5.1.

As explained in chapter 4, the RMS image of Mie scattering is best suited to provide a global image of the spray spatial extent. Mie scattering intensity is roughly dependent on the squared diameter of the droplets and the resulting image is thus biased towards the bigger droplets. This drawback is not as deterrent as it seems since the mass of fuel (*ie* what really burns) is dependent on the cube diameter of the droplets. The fuel mass spatial distribution is thus even more biased towards the bigger droplets and Mie scattering then becomes a better trace of it than a basic count of the droplets detected by PDA for example.
To provide a comparison basis, the spray limits computed for the non-reacting pilot-only conditions (chapter 4, Fig. 4.2) are superimposed on the Mie scattering RMS image in Fig. 5.1.
Visible differences can be observed, starting with the spray penetration length in the chamber. Indeed, for the multipoint-dominated operating point, the spray signal disappears after X=70 mm whereas it was still visible at the end of the image for the pilot-only condition. It must also be noted that the spray seems to spread more, yielding a probably better mixing.
The multipoint-dominated operating point is characterized by a higher flow rate and a slightly lower preheating temperature compared to the previously studied pilot-only conditions. Assuming the same droplet size distribution, it would mean a higher penetration length for the spray instead of a lower one.

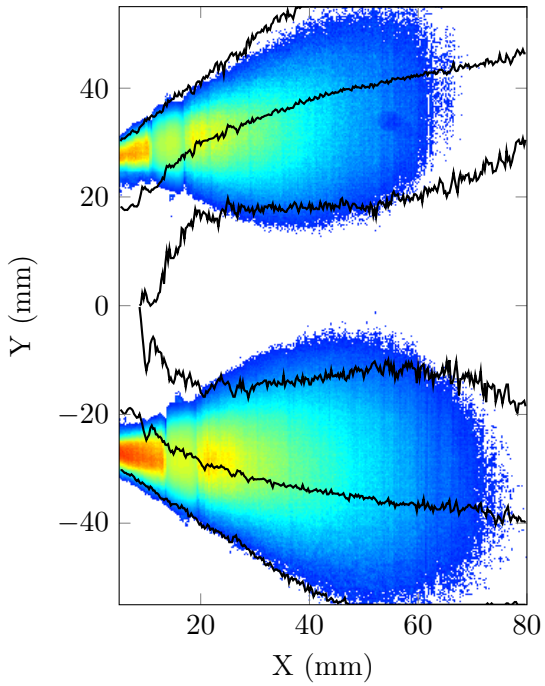

Figure 5.1 – *RMS image of Mie scattering intensity in the non-reacting case. A threshold has been set at 15% of the maximum value to highlight the shape of the spray. The black lines represents the spray limits for the non-reacting pilot-only case studied in chapter 4, Fig. 4.2.*

From this image it can thus already be inferred that the fuel droplets are smaller in the present conditions, which will be confirmed later (Fig. 5.4).
Following the workflow established in the previous chapter, it is possible to look at the average velocity fields, obtained by PIV on the Mie scattering images, in Fig. 5.2.

The PIV treatment of the 31274 non-reacting Mie scattering images with 20×20 pixels windows with 60% overlap yields 15637 velocity fields which are then averaged to give the fields shown in Fig. 5.2. A range validation is performed prior to the averaging operation, based on the extreme velocity values obtained with the PDA ([-41;98] m/s for the axial velocity and [-45;45] m/s for the vertical one). The limits of the non reacting spray based on the Mie scattering RMS image are superimposed on the fields.
A first observation is that PIV data with more than 2% of valid vectors can be found outside of the spray limits computed with Mie scattering. The size of the interrogation windows (5×5 mm) can explain the spread over the outer spray limits but not the inner region. This can be explained by the higher sensitivity of Mie scattering to the bigger droplets. It means that smaller droplets do not contribute much to the Mie signal while their signal is still intense enough for

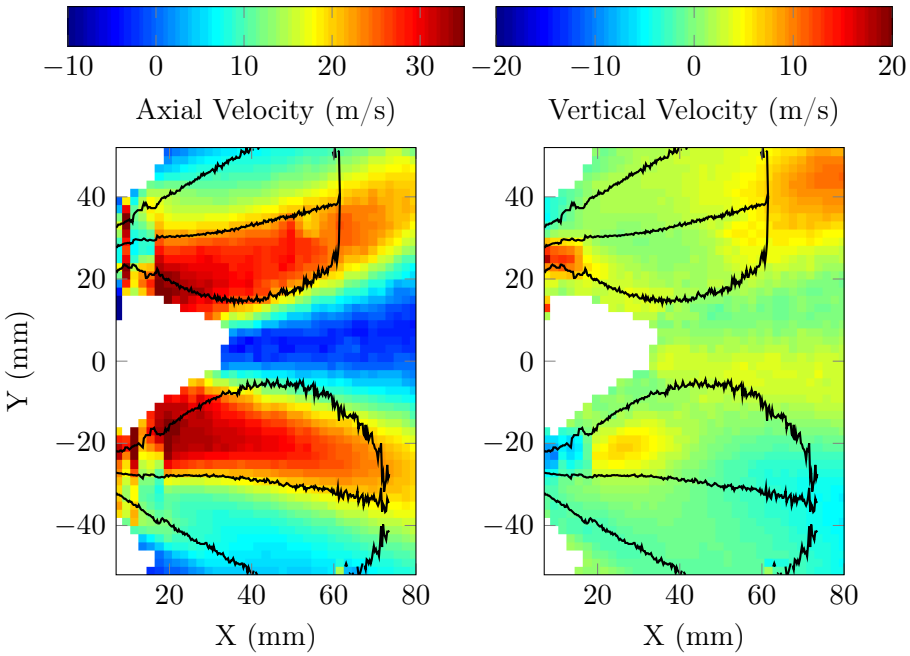

Figure 5.2 – *Mean axial (left) and vertical (right) spray velocities from the PIV treatment of the non-reacting Mie scattering fields. A threshold has been set at 2% of vector validation. The black lines represent the spray limits from the Mie scattering RMS image (Fig.5.1).*

the cross-correlation operation to work.
The general shape of the PIV fields corresponds to the results obtained in cold flow conditions (chapter 4, Fig. 4.3). Indeed, the annular swirling jet and the IRZ are clearly defined. The regions where the first toroidal structure ends and where the flow becomes convergent are also well identified (X≈30 mm). Such a result is expected from the suspected small droplet average size.
For more local information, average velocity fields obtained from the PDA measurements are presented in Fig. 5.3.

Five PDA profiles with 3 mm vertical spacing between the probing points and placed at 10, 15, 20, 25 and 35 mm axially are used to obtain the linearly interpolated fields in Fig. 5.3.
An interesting fit exists between the outer spray limit computed from the Mie scattering images and the PDA thresholding, meaning that the outer spray limit is probably strongly marked. Such a good correspondence can also be found in the pilot-only conditions studied in chapter 4. It had then been highlighted that this limit is formed by the ballistic behaviour of the biggest droplets, independently of the air flow. A similar phenomenon must thus probably be at stake here.

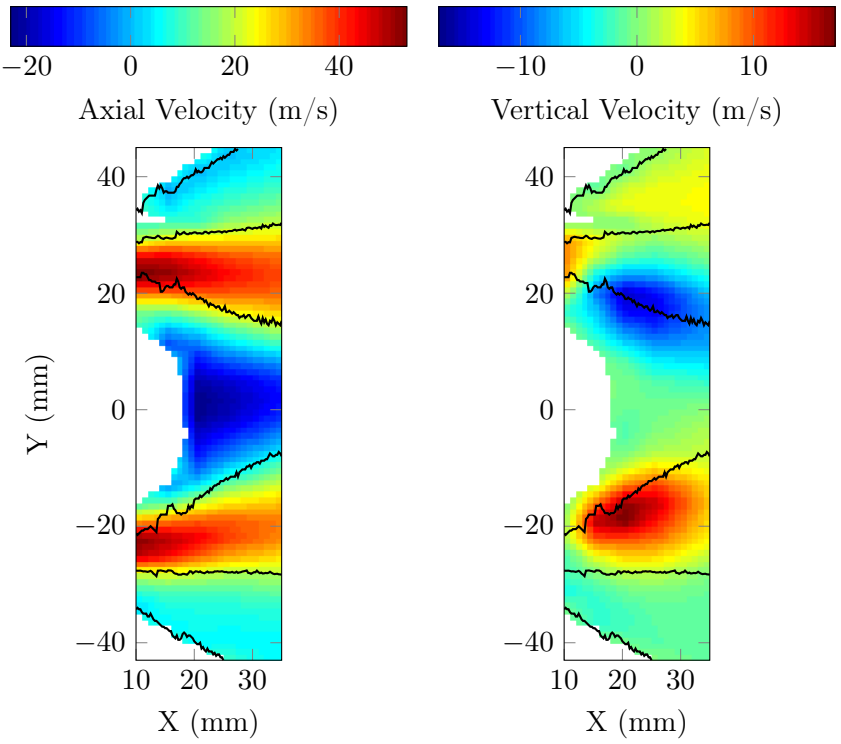

Figure 5.3 – *Interpolated mean axial (left) and vertical (right) spray velocities from PDA measurements. A threshold has been set at 2000 detected droplets. The black lines represent the spray limits from the Mie scattering RMS image (Fig.5.1).*

The shape of the velocity fields is here again very close to the air flow. The axial velocities peak around 53 m/s and the velocity in the IRZ reaches -20 m/s. An interesting comparison can be drawn with the measurement for the pilot-only conditions, conditioned by the small droplet size (chapter 4, Fig. 4.7). Indeed, for that case, the velocity reaches 44 m/s in the jet and -16 m/s in the IRZ. In the present case, the mass flow rate is multiplied by 4/3 and the density is increased by 473/433 (the inverse of the preheating temperatures ratio, assuming a perfect gas law for the air). Applying such a correction on the velocity to the pilot-only conditions air flow (based on the conditioned PDA velocity) provides an almost perfect fit with the present velocity fields in Fig. 5.3. This again leads to think that the spray in the present conditions is mostly composed of small droplets, following the air flow well. This is confirmed by the diameter spatial distribution in Fig. 5.4.

The same PDA measurement points used to obtain Fig. 5.3 are used to compute an interpolated map of the Sauter Mean Diameters (SMD) obtained at each probing point. The result can be seen in Fig. 5.4.
While the previous results yielded some similarity with the pilot-only operating

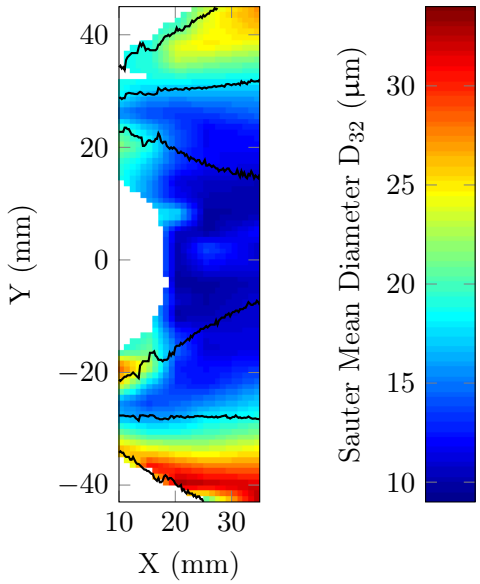

Figure 5.4 – *Interpolated Sauter Mean Diameter from PDA measurements. A threshold has been set at 2000 detected droplets. The black lines represent the spray limits from the Mie scattering RMS image (Fig.4.2).*

point, the SMD distribution here is completely different. The SMD range from 9 to 34 µm and most of the region yields low values, under 20 µm. This is coherent with the previous estimation obtained from the lack of spray penetration and the similarity of the droplets velocity fields with the air flow one. The biggest SMD are however here again obtained at the external parts of the spray, along the outer limit because of their ballistic behaviour.
The present operating point is thus characterized by a predominance of small droplets. This is due to the multipoint injection device which aims at creating the best possible mixing by finely atomizing the fuel. This way, the combustion regime can become closer to perfectly premixed conditions.
Because of the low discrepancy in droplet diameters, conditioned measurements do not provide more information and this is why they will not be not presented here. In chapter 4, the pilot-only injection conditions are characterized by a strong trace of the Precessing Vortex Core on the spray. It is interesting to check whether a trace of the PVC can still be detected in the present conditions.

5.1.2 Dynamical features of the non-reacting spray

As mentioned before, the PVC has a strong impact on the spray in pilot-only injection conditions. The reason for this is the presence of the PVC itself at the exit of the pilot nozzle, generating a non-uniform fuel seeding. In the present conditions, 85% of the fuel is injected through the multipoint injector so the pilot injection is suspected to have only a small influence on the spray. The

PVC trace seems however still detectable, as shown in Fig. 5.5.

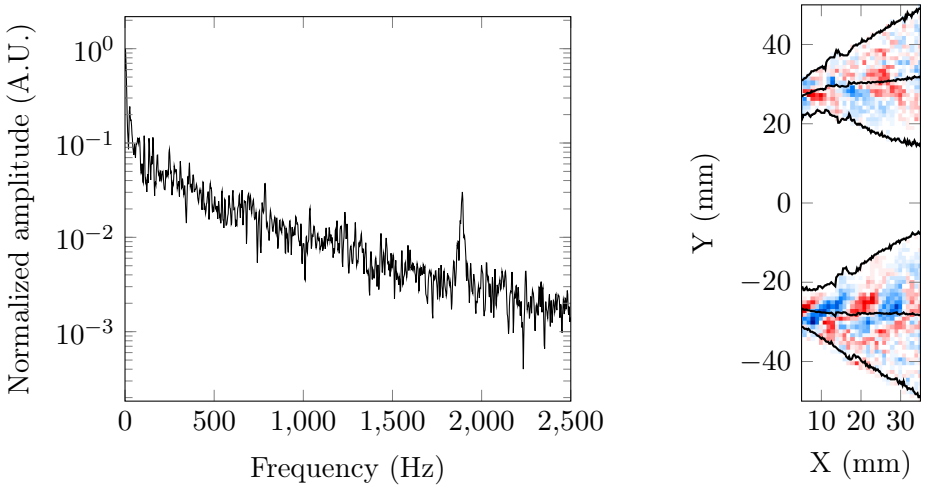

Figure 5.5 – *Power spectral density from a region of interest in the Mie scattering images (left) and DMD mode at the peak frequency (right). Positive Mie scattering fluctuations are in red and negative ones in blue. The black lines represent the spray limits from the Mie scattering RMS image (Fig.5.1).*

A 30×30 pixels region of interest, as defined in chapter 4, is here again used to detect the trace of the PVC on the non-reacting spray. A spectrum of the signal is shown in Fig. 5.5. Comparing this graph with the one obtained for pilot-only conditions in Fig. 4.9, it can be seen that the peak is higher in frequency and much lower in amplitude in the present case. The reduction of amplitude can be explained by the fact that the PVC disturbs the pilot fuel injection while the present operating point is characterized by a dominating multipoint injection. This can explain why a coherent signal can still be found but is not dominant compared to the noise levels.
In terms of frequency, the peak is here around 1920 Hz while it was at 1590 Hz in non-reacting conditions for the pilot-only case. Since the PVC frequency is proportional to the air volume flow rate, a simple correction, similar to what has been done in the analysis of the PDA data in Fig. 5.3, can be performed here to account for the change in mass flow rate and preheating temperature. The theoretical value based on the pilot-only frequency would be 1940 Hz which is very close to the frequency detected here.
From the Mie scattering fields, a DMD can be performed on 500 samples to yield a mode associated to the PVC frequency, shown on the right of Fig. 5.5. It is possible to detect the characteristic antisymmetrical structures of the PVC trace. They are however unexpectedly placed, in the middle of the spray instead of the external parts as highlighted in pilot-only conditions. This can be explained by the fact that the pilot injection is probably too low to generate

a sufficient amount of big and fast droplets (*ie* with a high momentum) so the trace of its injection somewhat follows the air flow while still keeping the non-uniform seeding. Indeed, computations based on simplex atomizers empirical models found in the literature (Lefebvre 1989a; Lefebvre 1989b) yield an injection velocity around 40 m/s in the pilot-only case but only 10 m/s in the present case. Despite the questionable validity of these models in the complex present case, their tendencies provide a ground for the proposed mechanism to explain the change in position of the PVC trace.

Because of its low intensity, no interesting information on the PVC can be found in the PIV or the PDA results. A further study on its frequency and intensity in non-reacting and reacting cases can however be found in the last section of the present chapter.

5.2 sV flame stabilization

To ignite the burner, the same procedure is always used. An aeronautical spark plug is fired at a low power operating point with pilot-only injection. A study on the staging for the ignition of the burner can be found in Providakis (2013). In complement, the use of a laser ignition technique was also analyzed (Agarwal and Zimmer 2012).

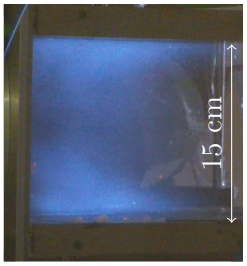

Figure 5.6 – *Photography of the sV flame. Flow from left to right.*

From the pilot-only ignition point, which gives a V-shaped flame completely similar to the one studied in chapter 4, the power is then progressively increased to reach the nominal power of the presently studied operating point while keeping the staging parameter high, over 80%. The power is then kept constant and the staging parameter is reduced until the present operating point is reached. This constant power step is thoroughly described in chapter 6.

A photography of the flame obtained in this case is visible in Fig. 5.6. The flame seems located close to the walls of the chamber and does not have a definite shape. It can however be seen that the flame is globally diverging and that no reaction seems to occur around the centerline of the chamber. For these reasons, and several others that will be highlighted in the following, this flame can be related to the V flame studied in chapter 4. It is referred to as the spread-V (sV) flame.

5.2.1 General behaviour of the spray and flame

First, following the workflow established earlier, Mie scattering images are used to study the shape of the spray in reacting conditions in order to compare it to the non-reacting case. The RMS image is shown in Fig.5.7.

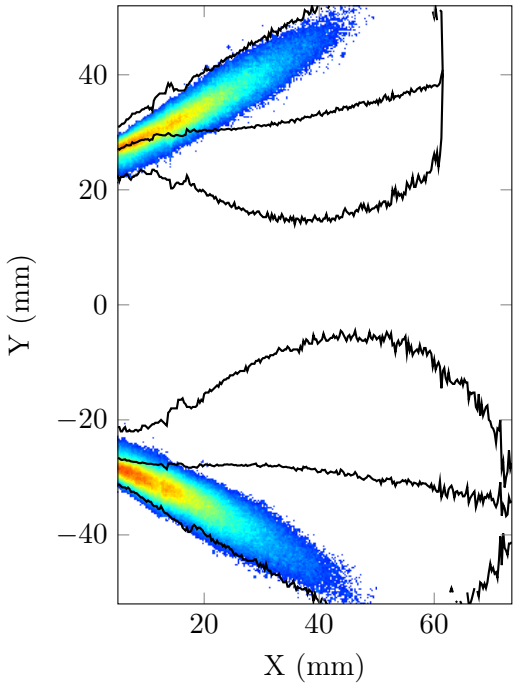

Figure 5.7 – *RMS image of Mie scattering intensity in the reacting case. A threshold has been set at 15% of the maximum value to highlight the shape of the spray. The black lines represent the spray limits extracted from the non-reacting Mie scattering RMS image (Fig.5.1).*

As already seen in chapter 4, the spray in reacting conditions is different from the one observed in non-reacting conditions. It is thin and does not spread towards the center of the chamber.
The spray has a general shape that is very similar to the one seen in pilot-only reacting conditions (with a V-shaped flame). The same diverging behaviour can be retrieved. In the pilot-only conditions, this particular shape was attributed to an effect of the bigger droplets ballistic behaviour and on the presence of the flame inside the injector.
As shown by the present non-reacting study, mostly small droplets seem injected here. This can also be confirmed by the smaller penetration length of the spray in the present case because smaller droplets have lower momentum and, more importantly, evaporate quickly.
There must however still be an effect of the flame on the air flow and average

spray velocities obtained with PIV shown in Fig. 5.8 can help understand it.

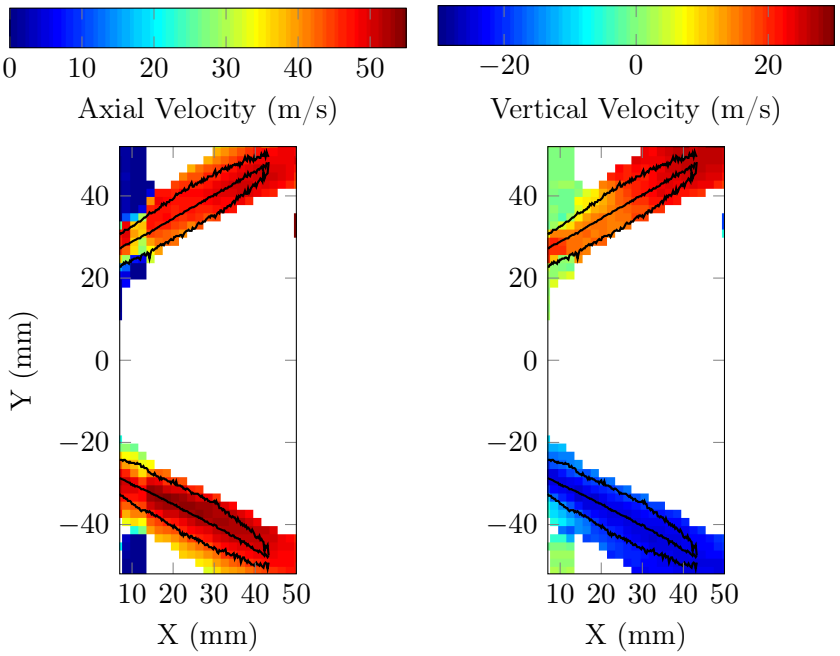

Figure 5.8 – *Mean axial (left) and vertical (right) spray velocities from the PIV treatment of the reacting Mie scattering fields. A threshold has been set at 2% of vector validation. The black lines represent the spray limits from the Mie scattering RMS image (Fig.5.7).*

The Mie scattering images are treated with 20×20 pixels interrogation windows and 60% overlap. Once again, a thresholding at 2% of validated vectors is set up. The resulting average spray velocity fields are shown in Fig. 5.8.
The velocity fields look strikingly similar to the ones observed in the reacting pilot-only conditions with strongly diverging velocities. Once again, it seems to have almost nothing in common with the non-reacting conditions. Higher velocities are observed, due to the presence of the flame as for the pilot-only conditions.
Computing a correction based on the change in the operating point does not work as well as for the non-reacting conditions. Indeed the flame creates a strong change in the air flow and, since the equivalence ratio is not the same, the heat release from the flame has changed.
Most of the information coming from the spray analysis is thus clearly similar to the one associated with reacting pilot-only conditions and leading to a V-shaped flame, even though the droplet population has changed. The photography of the flame in Fig. 5.6 however does not really look like a V. To analyze the differences, the CH^* chemiluminescence data is used in Fig. 5.9.

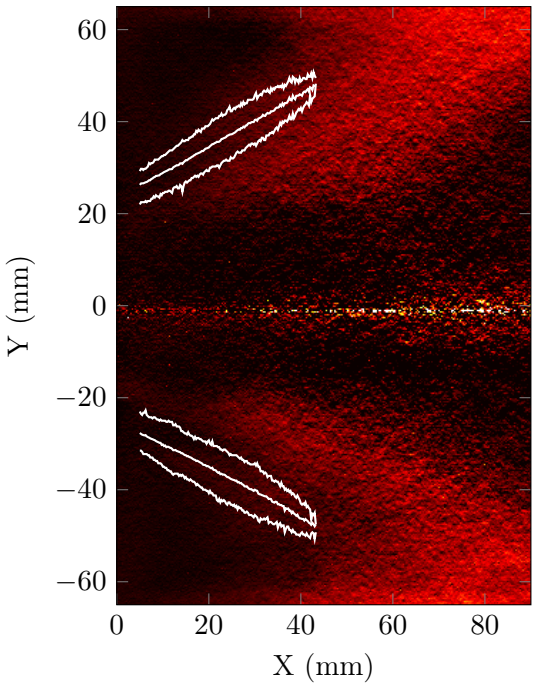

Figure 5.9 – *Abel-inverted mean CH* chemiluminescence image for the sV flame. The white lines represent the spray limits from the reacting Mie scattering RMS image (Fig.5.7).*

Figure 5.9, obtained after Abel deconvolution of the mean CH* chemiluminescence image, can be used to compare the respective positions and shapes of the flame and the spray. As stated before, the spray is extremely similar to the one obtained in pilot-only conditions but the flame looks different.
The first striking observation is the fact that the reaction zone is extended, leading to a quite diluted flame, hence the spread-V name for this flame. A second difference with the V flame is the fact that no reaction seems to occur in the upstream part of the flame and that it does not seem to be anchored inside the injector. In a sense, this flame can be seen as the complement for the V flame, still diverging and consuming the fuel from the inside but with strong reaction zones where the V flame does not burn. Finally, the beginning of the interactions with the top and bottom walls can be seen as if the flame was flowing back towards the upstream regions, consuming the remaining fuel from both sides.
The sV flame thus shows strong similarities with the V flame that seem mostly related to the similar shapes of the fuel sprays and air flow. In order to go further in the comparison with the pilot-only conditions, a dynamical analysis of the present regime can be performed with the same tools as in chapter 4.

5.2.2 Dynamical features of the operating point

Because of its similarity with the V flame, the dynamical features of the sV flame are expected to be close to what was observed in pilot-only conditions. The presence of a Precessing Vortex Core should impact the spray and the flame. A major difference may however be observed here because the fuel injection is staged and the PVC seemed to act only on the pilot injection which now represents just 15 % of the fuel injection. Dynamical features of the reacting spray can be seen in Fig. 5.10.

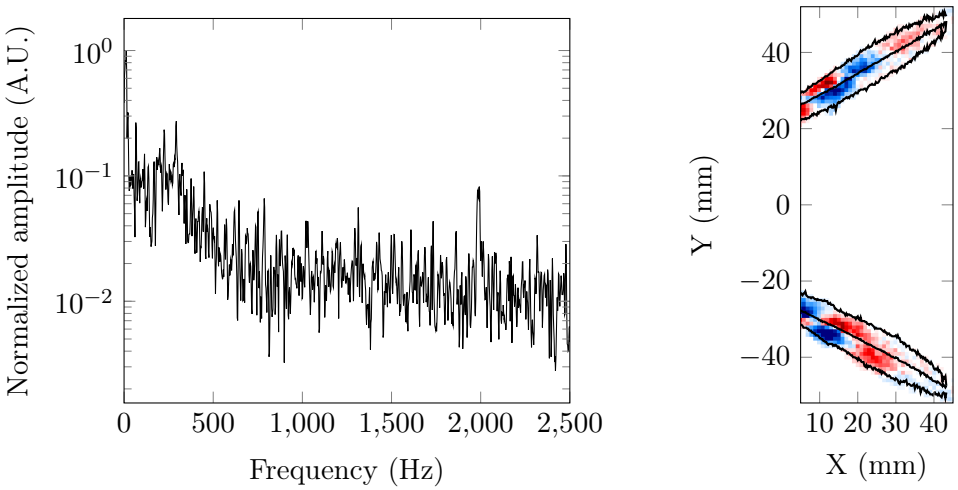

Figure 5.10 – *Power spectral density from a region of interest in the Mie scattering images (left) and DMD mode at the peak frequency (right). Positive Mie scattering fluctuations are in red and negative ones in blue. The black lines represent the spray limits from the Mie scattering RMS image (Fig.5.7).*

On the left of Fig. 5.10, a PSD of the signal from the usual 30×30 pixels window can be found. Although it is not very dominant comparatively to the noise level, a peak can be identified around 2000 Hz which is once again the trace of the PVC. The DMD mode at the same frequency can be seen on the right of Fig. 5.10.
The trace of the PVC on the spray, as extracted by DMD, seems less noisy than in the non reacting conditions, with a clear antisymmetrical modulation of the spray. This can be explained by the fact that, as for the V flame, the spray is much more confined and the smaller droplets coming from the multipoint injector (and which are thus not exposed to the PVC) have vaporised more than in non-reacting conditions. The shape of the small Mie scattering structures is also interesting. Indeed, for a given axial position, the internal and external parts of a given spray arm seem to be in opposite phases (see around X=15 mm, for example). This can be explained by the fact that the PVC induces a global precession of the fuel cone coming from the pilot nozzle. If the fuel cone is thin

enough, the resulting fluctuations have the typical trace found on the right of Fig. 5.10. This particular shape can also explain why the peak observed in the PSD is not very high even though the mode seems strongly marked. Indeed, in the averaging window used to obtain the temporal signal, positive and negative fluctuations can coexist and cancel each other out during the averaging operation.
Even though the fluctuations created by the PVC are marked on the fuel spray, they do not necessarily have a strong impact on the flame since a lot of fuel seems to be present in the vapor phase. Some information on the dynamical features of the sV flame can be seen in Fig. 5.11.

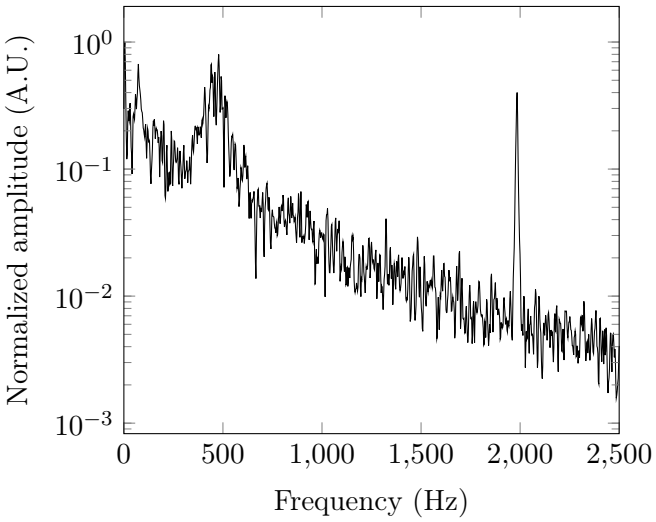

Figure 5.11 – *Power spectral density from a region of interest in the CH* chemiluminescence images of the sV flame.*

As usual, a 30×30 pixels region of interest is used to trace a spectrum of the chemiluminescence signal at X=5 mm and Y=20 mm which is really close to the chamber inlet. A strong peak can be detected around the PVC frequency meaning that the flame at this point seems to react quite well to the fluctuations created by the PVC. The particular location of the region of interest must however be emphasized since it corresponds to a region with a low mean level of CH* chemiluminescence signal (see Fig. 5.9). Furthermore, a Dynamic Mode Decomposition performed on the whole extent of the chemiluminescence image does not yield any specific mode at the PVC frequency.
The fact that the PVC can be detected on the chemiluminescence signal close to the injection region but is absent downstream leads to think that a flame exists inside the injector even though it cannot be properly detected from measurements inside the chamber. This flame is somehow anchored inside the injector because of the pilot injection which explains why a trace of the PVC can be

found close to its exit. The main reaction zone of the sV flame occurs however downstream in the chamber and is mainly fueled by the multipoint injection of the take-off stage. It is composed of small droplets and is probably well vaporised and mixed.
Complements on the PVC for the sV flame as well as for the other conditions can be found in the last section of the present chapter.

5.3 Lifted flame stabilization and behaviour

The sV flame, studied previously is the typical flame stabilisation when the current operating point is reached coming from high values of the staging parameter (that is, by reducing the pilot injection and increasing the multipoint injection). When the exact same operating point is reached from low values of α, the flame shape is completely different, as shown by the photography in Fig. 5.12. Precisions on the conditions leading to each flame stabilization are given in chapter 6.

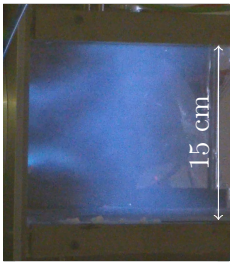

Figure 5.12 – *Photography of the lifted flame. Flow from left to right.*

Even though the previously highlighted sV flame could be related to the V flame obtained in pilot-only conditions, this flame seems far from what has already been studied in the scope of this work. Because of the position of the main reaction zone downstream in the chamber, this flame is called the lifted flame and is studied from an average as well as dynamical point of view in the present section.

5.3.1 Presentation of the flame and the spray

As usual, the same workflow is used to study this particular flame to allow for easier and faster comparisons with the other regimes. An average spray image based on the RMS of the Mie scattering data can thus be seen in Fig. 5.13.

From the image in Fig. 5.13, the lifted flame can seemingly be associated with a strong change in the spray shape. This change is however different from what was observed in the pilot-only conditions in chapter 4 or for the sV flame in the previous section.
First, it can be seen that the spray does not show the strongly defined external position the sV flame spray has. In the beginning of the chamber, for instance, it has the same thickness as the non-reacting spray whereas the sV flame spray is thinner. Another striking result is the low penetration of this spray in the

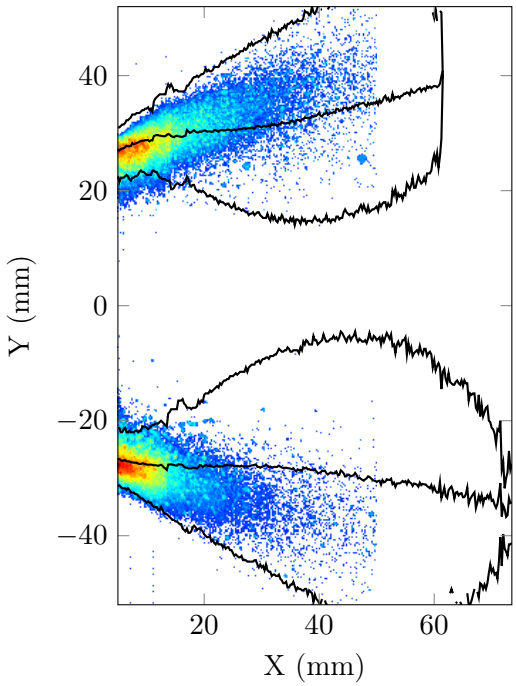

Figure 5.13 – *RMS image of Mie scattering intensity in the reacting case. A threshold has been set at 15% of the maximum value to highlight the shape of the spray. The black lines represent the spray limits from the non-reacting Mie scattering RMS image (Fig.5.1).*

chamber and its spread. Indeed, all the reacting point studied until here are characterised by confined air flows that shape the spray in a diverging fashion whereas it seems a lot more free here. In fact, the present spray is really similar to the non-reacting one, the strong differences between the two shapes arising from the lack of penetration in the reacting case. Indeed, since the operating point with a strong multipoint injection is characterised by small droplets, they are really sensitive to vaporization and the presence of a flame can thus cause a drastic reduction of the spray length. This is confirmed by reducing the thresholding value for the reacting Mie scattering RMS images. The lifted flame spray then becomes really close to the non-reacting spray (even though it does not converge as much towards the center) whereas the sV flame spray keeps its diverging behaviour.
To confirm the similarities between the non-reacting spray and the lifted flame spray, PIV results are presented in Fig. 5.14.

The usual 20×20 pixels interrogation windows with 60% overlap are used to obtain the fuel spray mean velocity components shown in Fig. 5.14. A 2% of vector validation thresholding is also used.
The velocity fields can be compared to the others obtained for the same operat-

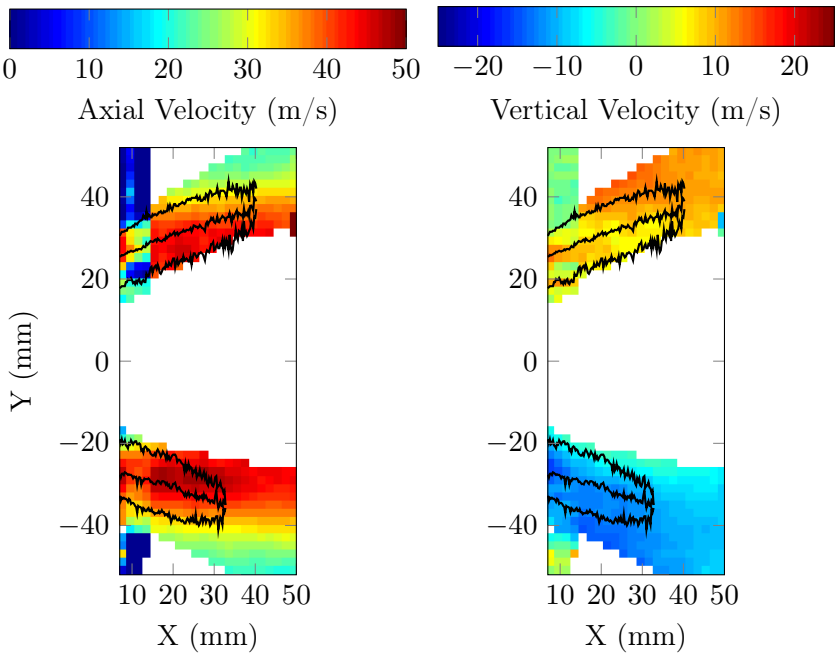

Figure 5.14 – *Mean axial (left) and vertical (right) spray velocities from the PIV treatment of the reacting Mie scattering fields. A threshold has been set at 2% of vector validation. The black lines represent the spray limits from the Mie scattering RMS image (Fig.5.13).*

ing point: in non-reacting conditions (Fig. 5.2) and for the sV flame (Fig. 5.8). A first look at the velocity range shows that the lifted flame fuel spray is globally faster than in non reacting conditions but less than the sV flame spray. The difference with the non reacting spray can be explained by the heat release from the flame that increases the temperature but the difference with the sV flame spray needs further investigation. This supplemental information can come from the vertical velocity field which shows that the lifted flame spray is much less divergent than the sV flame one. This further supports the theory of the confinement of the air flow on a diverging trajectory in the sV case due to the presence of an internal flame which would be absent here. This point will be further discussed in the last section of this chapter and in chapter 6.
A look at the axial velocity field also brings insight on the lifted flame spray shape. Indeed, the high axial velocity region (in red) apparently becomes almost horizontal as it progresses inside the chamber. This is strongly reminding of the cold air flow (chapter 4, Fig. 4.3) in the burner. All the clues thus seem to point out the fact that the lifted flame is characterized by a spray that is on average unchanged by the combustion, faster vaporization aside.
For further analysis of the lifted flame state, the usual workflow is carried on and the flame and spray relative positions can be seen in Fig. 5.15.

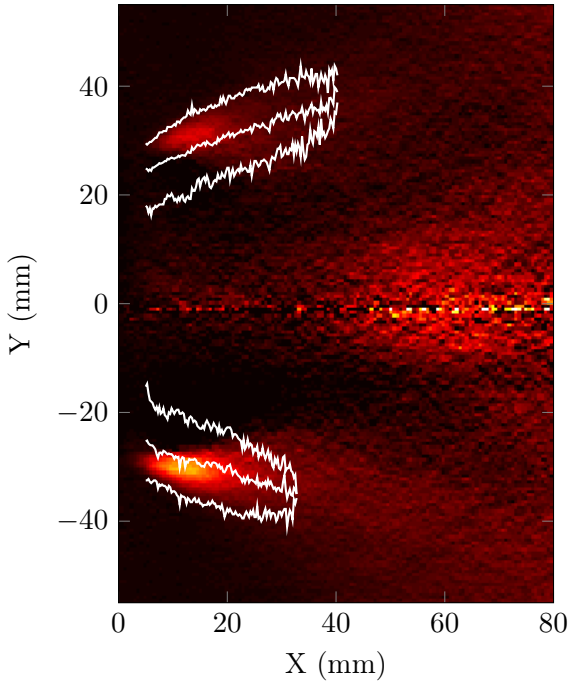

Figure 5.15 – *Abel-inverted mean CH* chemiluminescence image for the lifted flame. The white lines represent the spray limits from the reacting Mie scattering RMS image (Fig.5.13).*

Similarly to Fig. 5.9, an Abel deconvolution is performed on the mean CH* chemiluminescence image and contours of the spray from Fig. 5.13 are superimposed to yield the image in Fig. 5.15.
What can first be seen is the position of the main reaction zone downstream in the chamber, with a quite spread shape (some signal can even be found close to the center). Despite this downstream position and spreading, the flame remains very different from the sV case which was expected from the photographies in Fig. 5.6 and 5.12.
Where liquid fuel spray can be detected, it seems mostly consumed from the outside by the flame, which is the opposite of all the previously studied flames. A reaction zone can only be found on the inside after X=40 mm and nothing seems to happen upstream in the center, as the study of the spray has led to believe.
An interesting region to study however exists before X=30 mm for Y$\approx \pm$30 mm. Indeed, a superposition of liquid fuel and flame exists here and can come from only two phenomena. The first possible explanation is the presence of big droplets that did not have enough time to vaporise before the flame. This possibility is however contradicted by the PDA data in non-reacting conditions (Fig. 5.4) showing a dominance of small, quickly evaporating droplets. The most probable reason is thus an artifact coming from the use of average images and

the following study of the dynamics of the lifted flame should provide insight on this.

5.3.2 Dynamical behaviour and thermo-acoustic instability

As stated before, studying the dynamics of the lifted flame can explain the flame and liquid spray apparent superposition seen in Fig. 5.15. Indeed, alternating high values of Mie scattering and chemiluminescence at the same point can lead to such a superposition. For this purpose, information on the spray dynamics can be found in Fig. 5.16.

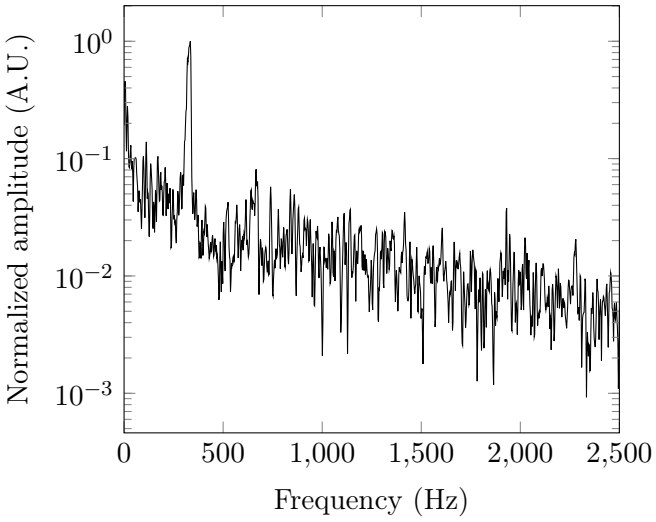

Figure 5.16 – *Power spectral density from a region of interest in the Mie scattering images.*

The usual 30×30 pixels averaging region placed at X=5 mm and Y=-25 mm is used to obtain the spectrum in Fig. 5.16.
Until now, the only dynamical structure encountered is the trace of the Precessing Vortex Core coming from the modulation of the pilot injection. It corresponds to generally high frequencies, over 1900 Hz for the currently studied bistable operating point. This trace is however not clearly detectable in the present case. A strong dynamical phenomenon can nevertheless be highlighted with a dominant peak around 330 Hz.
In Providakis (2013), a lifted flame is highlighted and it triggers a strong thermo-acoustic instability based on the quarter wave mode of the chamber which corresponds roughly to 330 Hz. The same phenomenon is occurring here even though the operating point is different. Further precisions on the burner eigenfrequencies that generate this thermo-acoustic instability require a specific acoustic study (Lamraoui et al. 2011) which is not within the scope of this work.

On the contrary to the PVC, the frequency of this peak is quite low which leads to new difficulties for the proper representation of the associated DMD mode. Indeed, in the PVC trace case, the frequency is high compared to the characteristic velocity and size of the spray, meaning that more than one PVC oscillation cycle can be seen in an image of the DMD mode, regardless of its phase. The oscillation can thus be studied in its entirety. This is the case in Fig. 5.10 for example and also the reason why no image can be seen alongside the spectrum in Fig. 5.16. Indeed, the average axial velocity of the spray is around 40 m/s (from Fig. 5.14) and it does not extend over more than 40 mm. This means that a perturbation is convected in about 1 ms from the beginning of the spray to its end. The fluctuation period being 3 ms for a 330 Hz frequency, it is thus impossible to obtain more than one third of a cycle on a given fixed phase image. This is the reason why it is necessary to look at several phases of the DMD mode, as shown in Fig. 5.17.

Dynamic Mode Decomposition is performed on 500 samples of the Mie scattering data and six phases of the mode at 330 Hz can be seen in Fig. 5.17.
As expected from the previous analysis based on the mode frequency and the convective time for a perturbation, it can be seen that the mode is characterized by a bulk effect on the spray with alternating periods of positive and negative fluctuations. The fluctuation cycle seems however to start from the external part of the spray, meaning that the effect on the liquid fuel is not fully axial. This seems similar to what was seen for the siren-induced modulations in chapter 4 where the oscillations were created before the swirlers, leading to axial and radial fluctuations. A comparable phenomenon must thus not be excluded here. From this diagnostic, it can be seen that the spray is subjected to strong modulations at a frequency of 330 Hz which is the beginning of an explanation for the spray/flame superposition in Fig. 5.15. A second step in the analysis must thus be taken by looking at the flame dynamical behaviour in Fig. 5.18.

The spectrum on the left of Fig. 5.18 is computed from the usual averaging window on CH^* chemiluminescence images. As expected from the spray dynamical behaviour, a strong peak can be seen at 330 Hz (representing the thermoacoustic instability) and no clear coherent signal can be identified around 1900 Hz. For a deeper analysis, the DMD mode (based on 500 chemiluminescence images) at 330 Hz is also represented on the right of Fig. 5.18. Because of the bigger spatial extent of the flame compared to the spray, one image at a given phase is enough to capture more than half of the oscillation so that the representation of the full cycle is unnecessary.
The mode shows alternating vertical regions of positive and negative oscillations, corresponding to a globally axial perturbation. As the cycle evolves, the fluctuations progress downstream. The superposition region thus sees alternating strong and weak flame signal. This is a second step towards the explanation of the flame and spray average superposition. Since it was shown that the spray

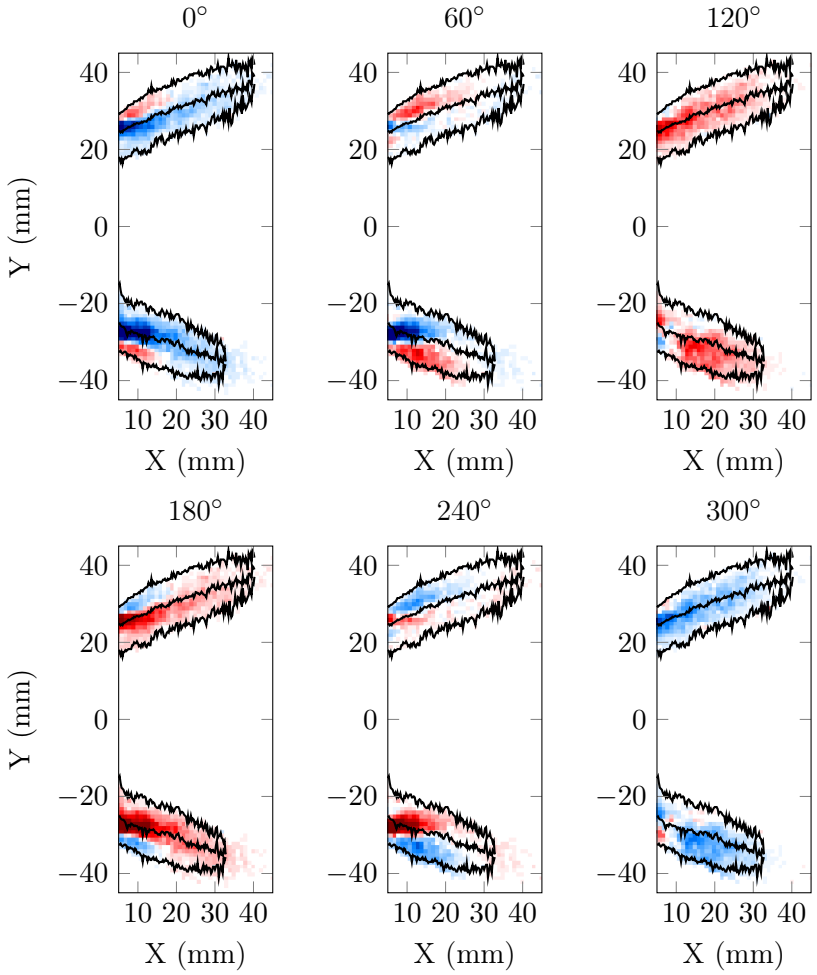

Figure 5.17 – *Evolution of the mode at the acoustic frequency from a DMD on the Mie scattering data. The blue (resp. red) color represents negative (resp. positive) fluctuations relatively to the mean. The black lines represent the spray limits from the reacting Mie scattering RMS image (Fig.5.13).*

was also submitted to modulations, what is now needed is the phase difference between the spray and flame oscillations to confirm or infirm the averaging artefact theory.

The Mie scattering and the CH* chemiluminescence recordings have not been performed simultaneously. To synchronize them, a common signal thus needs to be used. This synchronizing signal must present a response to the dynamical features one is interested in (here the thermo-acoustic oscillation). The signal from the microphone placed at the half length of the chamber is thus a good candidate for this purpose.
A common technique consists in performing a phase averaging of the two diag-

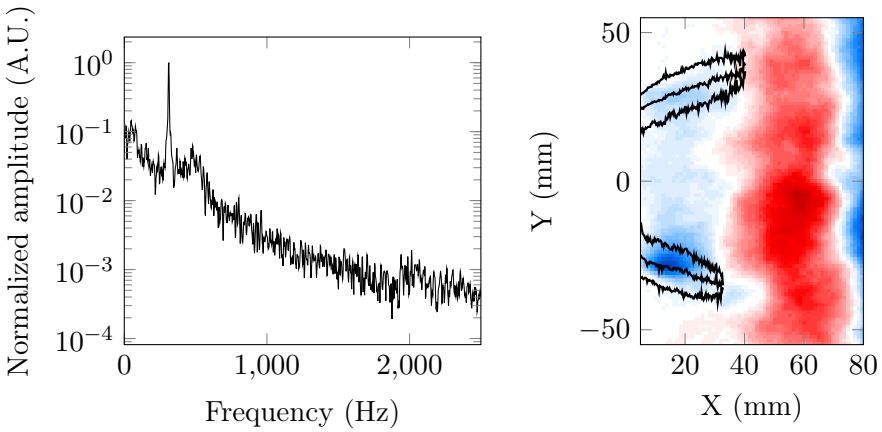

Figure 5.18 – *Power spectral density from a region of interest in the CH* chemiluminescence images (left) and DMD mode at the peak frequency (right). Positive CH* fluctuations are in red and negative ones in blue. The black lines represent the spray limits from the Mie scattering RMS image (Fig.5.13).*

nostics to synchronize based on the acoustic cycle detected by the microphone. Namely, because the microphone signal is often noisy, a filtering operation is first needed and then a Hilbert transform can be used to compute the instantaneous phase. A phase binning is chosen based on a trade-off between fine cycle description and signal-to-noise ratio and, furthermore, higher harmonics cannot easily be filtered out of the reconstructed cycle. Finally, the quality of the reconstruction is strongly dependent on the response of the synchronizing signal to the studied cycle and on the amount of data used for the averaging in each phase bin. This process, even though it is the only available one when the data is not time-resolved, thus requires a lot of user input. Another synchronization method is proposed in the following, making use of the high acquisition speed of the diagnostics.

In Richecoeur et al. (2012), it is shown that Dynamic Mode Decomposition can be performed with a mix of several diagnostics. This capability is used here by treating the microphone signal, recorded simultaneously with one optical diagnostic (such as Mie scattering for instance), like an additional spatial data point. This simply corresponds to appending it at the bottom of the snapshot matrix. The DMD is then carried out and provides modes based on the dynamical features of the optical diagnostic (and also a bit on the dynamics of the microphone signal). The process can thus be seen as an "intelligent" filtering of the microphone signal based on the dynamics of the associated optical diagnostic with an extremely thin frequency bandwidth since the result is a sinusoid.
Performing one DMD with microphone for the Mie scattering diagnostic and the chemiluminescence diagnostic thus determines the phase difference between

the two diagnostics from the phase difference between the two DMD-filtered microphone signals. It then easy to synchronize the two diagnostics. The method thus only requires a limited user input and a synchronizing signal that reacts to the probed phenomenon even though not necessarily strongly since a filtering is performed based on the dynamics of each diagnostic themselves.
This synchronisation process based on DMD with the microphone signals in the present case can be seen in Fig. 5.19.

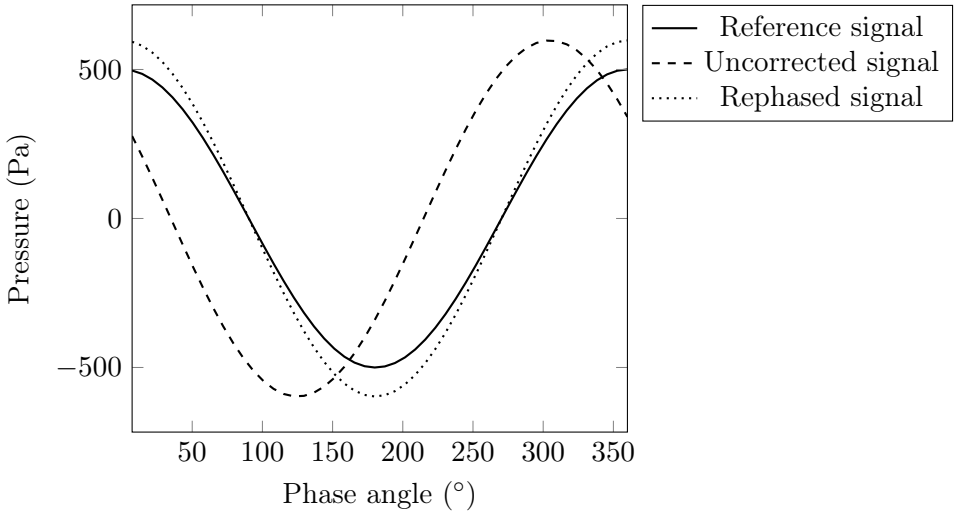

Figure 5.19 – *Microphone signals from DMD treatments of the Mie scattering and CH* chemiluminescence data. The reference signal corresponds to the microphone signal recorded simultaneously with the Mie scattering diagnostic. The rephased signal corresponds to the change of the phase origin of the uncorrected signal coming from the microphone part of the DMD on the chemiluminescence data.*

In the present study, it is arbitrarily decided (since phase is only relative) that the phase reference for synchronization is given by the microphone signal recorded at the same time as the Mie scattering measurements. A DMD based on 500 samples of the Mie scattering data with the additional line for the microphone is performed. The mode around 330 Hz, corresponding to the thermo-acoustic instability, is selected and the part of this mode corresponding to the microphone signal is plotted as a function of the phase angle of the cycle. The curve can be seen in Fig. 5.19 under the label "Reference signal".
A DMD based on 500 samples of the CH* chemiluminescence data with the additional line for the simultaneously recorded microphone signal is then performed. This DMD also gives a valid mode around 330 Hz since the flame responds to the thermo-acoustic instability (see Fig. 5.18). There is however no reason that this mode has the same phase reference as the Mie scattering mode. This can be seen in Fig. 5.19 by the "Uncorrected signal" curve which represents the microphone part of the chemiluminescence DMD mode.

The two curves being just different recordings of the same thermo-acoustic instability (even though not the same day), they should be almost identical. Here, this can be told by their similar amplitudes with peaks around 500 Pa. This amplitude corresponds to a Sound Pressure Level value of 145 dB as measured directly by the microphone. The DMD filtering has thus no strong deterrent effect on the signal amplitude. At this point, the potential quality of the synchronization can be assessed. Indeed, if the synchronizing signal does not react well to the probed phenomenon or if the two recordings one tries to synchronize are not really sensitive to the same phenomenon, the amplitudes of the synchronizing signals filtered by the DMD have no reason to be comparable. Since it is not the case here, it is possible to go on with the synchronization process.
As stated above, the phase reference for the two signals is not the same. However, since a DMD mode is a set of complex values, it is easy to compute the phase difference between the two filtered synchronizing signals by substracting their arguments. The phase correction can then be applied to the chemiluminescence microphone to yield the "Rephased signal" curve in Fig. 5.19 which almost overlaps with the reference signal coming from the Mie scattering microphone.
With this phase correction, the two diagnostics can thus have a common phase reference and the synchronization is performed here by correcting the chemiluminescence DMD mode. The superposition of the synchronised Mie scattering and chemiluminescence modes can be seen in Fig. 5.20.

To properly monitor the flame position instead of just looking at signal fluctuations, the DMD mode for the chemiluminescence signal is added to the average image and shown in shades of red and yellow in Fig. 5.20. The spray fluctuations are shown with contours colored in blue for negative fluctuations and in red for positive fluctuations.
From 0 to 180° phase angle, it can be seen that the spray fluctuations are mostly positive, meaning that more liquid fuel is introduced inside the chamber. On the contrary, the second part of the cycle is characterized by a lower presence of liquid fuel. The flame motion, especially regarding its presence in the upstream part of the chamber, seems complementary. Indeed, the cycle begins by the flame disappearing from the upstream part and the second part corresponds to an increase of the chemiluminescence signal.
This synchronization results thus clearly show that the fluctuations of the spray and flame do not occur at the same time. This finally explains the superposition of the mean Mie scattering and mean CH^* chemiluminescence signal seen in Fig. 5.15.
The increase in flame heat release is caused by an increase of the fuel supply brought by the spray. The two fluctuations are however clearly not simultaneous and analyzing the phase difference between the signals can bring insight on the reasons leading to this shift. For this purpose an image of the local phase

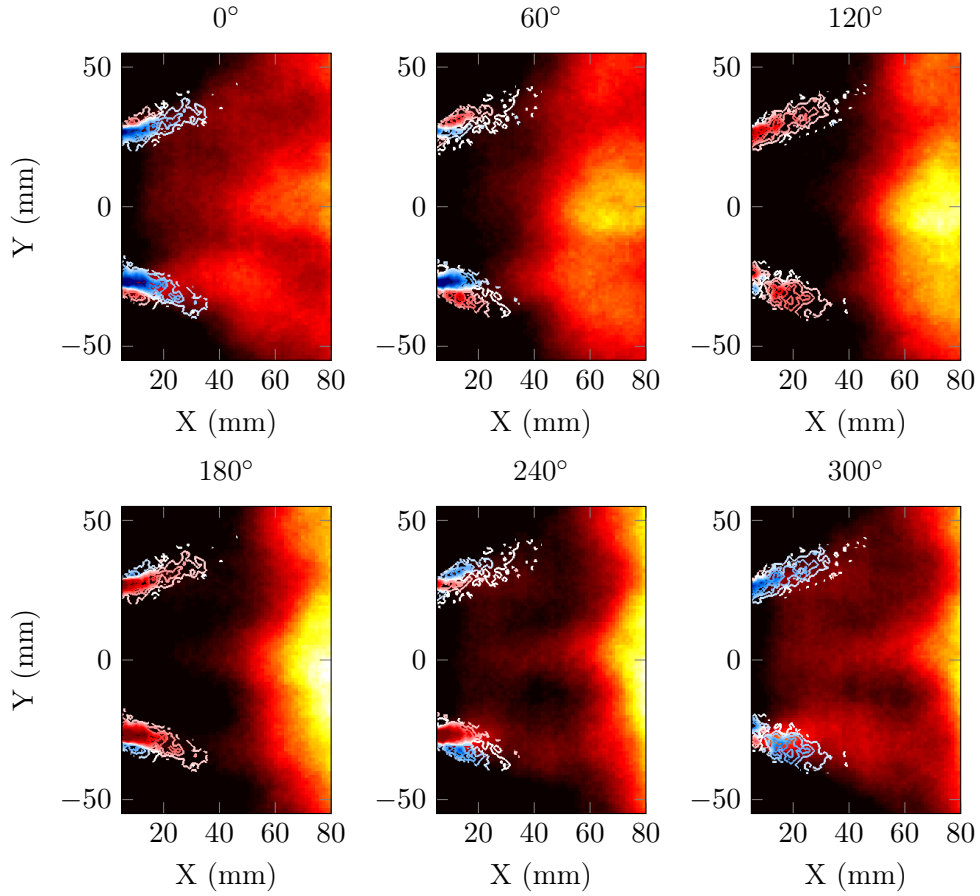

Figure 5.20 – *Synchronized evolutions of the DMD modes at the thermo-acoustic instability frequency from the Mie scattering and CH* chemiluminescence data. The blue (resp. red) color represents negative (resp. positive) Mie scattering fluctuations relatively to the mean. The red and yellow colormap represents the addition of the average chemiluminescence signal and the DMD mode.*

difference can be seen in Fig. 5.21.

Since DMD modes are sets of complex numbers, each spatial point is associated with a phase value. Because both diagnostics now have a common phase reference, local phase differences between the modes can be computed. No deterrent effect is expected from the line of sight integration of the chemiluminescence data for two reasons. First, the position of the analysis corresponds to the overlap between the average flame and spray, that is relatively far from the center where most of the line of sight integration effect occurs. Secondly, as can be seen in Fig. 5.18, the acoustic mode corresponds to a planar wave, meaning that, for a given axial position, all the points of the flame can be considered in phase. The resolution from the Mie scattering and chemiluminescence camera

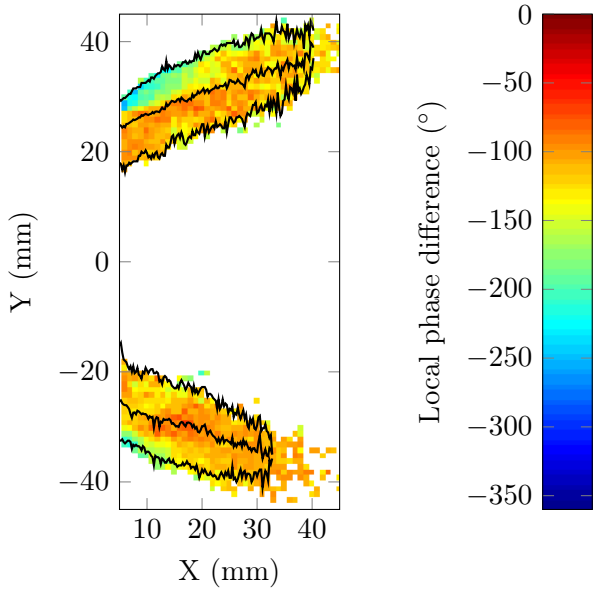

Figure 5.21 – *Local phase difference between the Mie scattering and CH* chemiluminescence DMD modes. The black lines represent the spray limits from the Mie scattering RMS image (Fig.4.2).*

are however different so a linear interpolation of the Mie scattering data on the coarser chemiluminescence mesh is performed before the local phase differences are computed. The results can be seen in Fig. 5.21.
The phase differences represent the delay between the Mie scattering and chemiluminescence signals for each spatial position. Negative values represent the fact that the chemiluminescence peak happens after the liquid fuel peak represented by the Mie scattering data. The most striking result here is the fact that the local difference is roughly constant over the whole spatial extent of the spray. The delay between liquid fuel and heat release must thus be piloted by a common process.
Because of the spatial uniformity of the local phase difference, one can look only at a spatial average value. To increase the confidence in the result, 10 DMD are performed for each diagnostic. Performing synchronizations yields a sample of 100 spatially averaged phase differences. The estimated mean value of the distribution is -125° with a 95% confidence interval of ±4°. This corresponds to a time delay of 1.04±0.03 ms.
This time delay value can also be compared to the vaporization time of the droplets because what effectively burns is the fuel vapour and chemical timescales can be supposed small compared to vaporization delay. Indeed, data extracted from Franzelli et al. (2010) show an ignition delay time for kerosene under 0.3 ms with conservative assumptions for the temperature (1200 K, which corresponds to the combustor outlet temperature) and, in the present case, burnt

gases recirculation speeds up the combustion initialization.
For the current operating point, the PDA data yield a mass median diameter of 23 µm for the spray. This means that half the liquid fuel mass is composed of smaller droplets and half of bigger droplets. This value thus seems a good indicator for the delay created by spray vaporization to fuel the flame. In a preheated atmosphere (at 160°C), the vaporization time of a 23 µm dodecane droplet is over 2 ms (based on data found in Perrin et al. 2014). Similarly, at 1800 K (roughly the adiabatic dodecane/air flame temperature for an equivalence ratio of 0.6), the vaporization time for the same droplet is around 0.5 ms (based on data extrapolated from Ghassemi et al. 2006, assuming that kerosene and dodecane have similar vaporization behaviours).
The time delay obtained experimentally is thus in-between the two extreme vaporization times for the droplet, meaning that vaporization must indeed be the dominant phenomenon leading to the delay between the peak of Mie scattering and the peak of chemiluminescence signal.

5.4 Comparison of the responses to the PVC

Even though it is not strong, a trace of the PVC can still be detected for this operating point when performing a DMD on Mie scattering images, regardless of the flame shape. It is thus interesting to compare the strength of the PVC trace in the non-reacting, sV flame and lifted flame cases as it can bring information on the flame stabilization process. This is the purpose of Fig. 5.22.

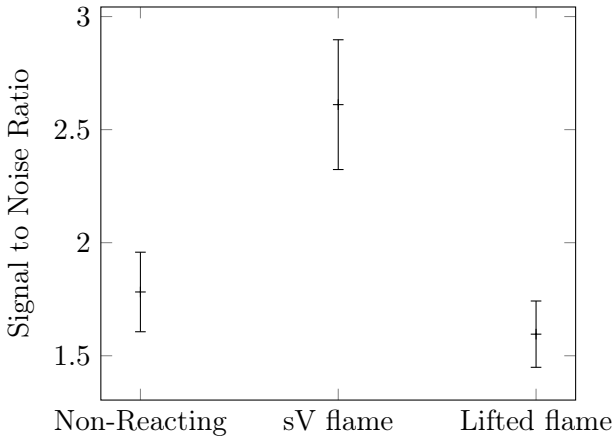

Figure 5.22 – *Mean signal-to-noise ratio of the amplitudes of the PVC modes for the Mie scattering data. The error bars represent the 95% confidence interval for the corresponding mean value.*

In chapter 4, a method is described to compare the effects of the PVC and the siren-induced modulations on the spray. It consists in computing a signal-

to-noise ratio for the peak of interest in the DMD spectrum. It used here on 30 DMD with 500 samples each using the non-reacting, the sV flame and the lifted flame Mie scattering recordings. The results of this treatment can be seen in Fig. 5.22.
In non-reacting conditions, the trace of the PVC is relatively weak with a mean signal-to-noise ratio around 1.8. In chapter 4, this is explained by the localization of the trace of the PVC compared to the extent of the spray. Here, the SNR is even lower than for the pilot-only conditions in chapter 4 (see Fig. 4.31 for CSR 0%, where the mean SNR is around 2.7). This difference is the effect of the weaker pilot injection in the present case which reduces the importance of the PVC trace on the global spray.
For the sV flame case, where the spray is similar to the reacting pilot-only case, the mean signal-to-noise ratio is higher than in non-reacting conditions. A similar evolution was observed in chapter 4 between the non-reacting conditions and the V flame case. This is explained by the reduction in the noise level due to the confinement of the spray created by the change in the air flow. The mean SNR in the present case is however lower than in the V flame case (chapter 4, Fig. 4.33). This can once again be explained by the staging of the fuel injection since the PVC acts on the spray at the pilot nozzle exit.
Even though it is also in reacting conditions, the situation for the lifted flame is really different from the sV flame case, with a mean SNR value around 1.6. Interestingly, the confidence interval overlaps with the non-reacting conditions one, adding to all the clues that link the lifted flame spray with the non-reacting one.
Further information can be obtained from the PVC strength if one manages to avoid the uncertainty added by the mixing and vaporization, that is by looking at the PVC effect at its root with the internal Mie scattering visualizations. They are used to provide the data in Fig. 5.23.

In the end of chapter 4 (Fig. 4.36), the internal Mie scattering visualizations are post-processed with a continuous wavelet transform to show the variability of the PVC frequency. The same method is used here between 1850 and 2100 Hz to generate the histograms in Fig. 5.23.
In the non-reacting case, the frequency of the PVC is centered around 1950 Hz and the frequency spread is noticeable but a peak can still be identified. The histogram for the sV flame shows a very different picture. First, the frequency is higher, around 2015 Hz, and seems really stable. Similarly to what was seen for the V flame, this difference can be attributed to heat release inside the injector and the change of the air flow in the sV flame case, leading to a more structured regime.
For the lifted flame, the situation is once again different from the sV flame one. The mean PVC frequency is around 1970 Hz and the frequency spread is large. This once again brings the lifted flame closer to the non-reacting case than the sV flame. The small frequency increase compared to the non reacting

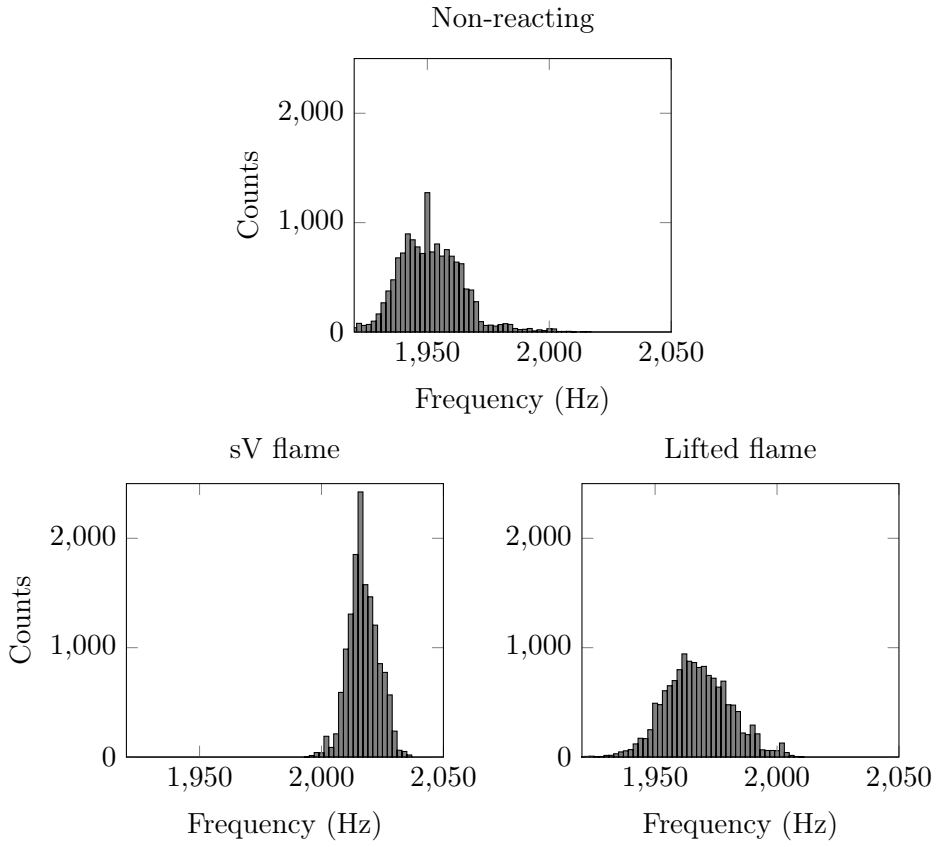

Figure 5.23 – *Histograms of the PVC frequency for the non-reacting and both reacting cases. The operating conditions are the same in the three cases.*

conditions can be attributed to an heat release effect (although weaker than for the sV flame). Keeping the comparison with the non-reacting conditions, no peak seems dominant for the lifted flame, leading to a slight increase in the frequency spread. This may be the effect of the thermo-acoustic instability which can weaken the PVC as the siren-induced modulations did in chapter 4.

Summary of the chapter

The operating point used in the study is characterized by a weak pilot injection and dominant multipoint one (α=15%). In reacting conditions, it also presents the peculiarity of enabling the stabilization of two different flames: the sV flame and the lifted flame, depending on the history of the burner.

In non-reacting conditions, the general shape of the spray from Mie scattering measurements is very similar to what was obtained in chapter 4 for the pilot-only injection even though the liquid fuel penetration in the chamber is reduced

and presents a higher spread. The major difference with the pilot-only injection lies however in the fuel droplets diameters which are much smaller in the present operating point since the multipoint injection is dominant and its purpose is to create smaller droplets for a fast mixing and vaporization. This impacts the velocity of the droplets, which does not show different behaviours depending on their size but rather follow the air flow quite well. From a dynamical point of view, the PVC trace on the spray can still be detected even though it is weaker than for the pilot-only injection, since the PVC has its root at the pilot nozzle. The PVC frequency is furthermore subjected to variability, probably because of the turbulent nature of the flow.

In reacting conditions, when the operating point is reached from high values of the staging parameter, that is by decreasing the pilot fuel flow rate and increasing the multipoint injection, the flame stabilizes in a particular shape called the sV flame. It is characterized by a reaction zone that roughly keeps a V shape but is spread and thus not well defined although it remains generally surrounded by the spray. The spray is however very similar to the spray associated with the V-shaped flame and the air flow shows the same change to a strongly diverging behaviour. From the combustion chamber point of view, the PVC trace can still be detected in the spray and in some very upstream parts of the flame only, probably because of the dominance of the multipoint injection, which barely interacts with the PVC. At its root, the PVC frequency is however well defined and higher than in non reacting conditions. This leads to suspect the presence of an internal flame inside the injector.

If the operating point is reached with a staging parameter increasing from low values, the flame shows a completely different topology called the lifted flame. In this case, the reaction is located downstream in the chamber and has no strongly defined shape. The spray is not as confined as in the sV flame case and seems very similar to the non-reacting case. The analysis of the PVC frequency inside the injector reveals that the air flow is also probably comparable to one associated with the non-reacting case. From an average point of view, regions where flame and liquid fuel coexist are highlighted. A dynamical analysis shows that this is the result of a strong thermo-acoustic instability that occurs when the burner presents this lifted flame shape. The fluctuations are coupled with fuel supply oscillations that create a flame motion after a delay caused by the vaporization of the droplets.

Part III

Transient operation

Chapter 6

Hysteresis phenomenon and stabilization mechanisms

In the present chapter, the fuel staging is varied while all the other operating point parameters are kept constant. A hysteresis cycle is highlighted and transitions between different combustion regimes can be observed. Small variations of the operating parameters enable to better understand the mechanisms leading to the particular flame stabilizations as well as some transitions between them.

In chapter 5, a particular operating point was chosen with a staging parameter α=15%. This operating point showed two possible flame shapes: the sV flame and the lifted flame. Here, the same air flow rate, power and preheating temperature are used but the fuel staging is slowly changed between 0 (full multipoint injection) and 50%. This can correspond to a potential evolution during the use of a real aeroengine from a low power pilot-only operating point (as in chapter 4) to high power fully staged operation. The parameters used for this particular operating point are reported in table 6.1.

Table 6.1 – *Hysteresis operating point definition.*

Global Parameters				
$\dot{m}_{air}$	T_{air}	$\dot{m}_{fuel}$	P	ϕ
($g.s^{-1}$)	(K)	($g.s^{-1}$)	(kW)	(-)
43.1	433	1.64	72	0.6
Staging				
α	$\dot{m}_{fuel,pilot}$	ϕ_{pilot}	$\dot{m}_{fuel,takeoff}$	$\phi_{takeoff}$
(%)	($g.s^{-1}$)	(-)	($g.s^{-1}$)	(-)
0 - 50	0 - 0.82	0 - 2.22	0.82 - 1.64	0.35 - 0.69

6.1 Response of the burner to fuel staging

As briefly mentioned in chapter 5, the ignition procedure is performed at a low-power pilot-only operating point (10 g/s of air with a global equivalence ratio of 0.7). The air flow and the pilot fuel are then increased while retaining a target value of 0.6 for the global equivalence ratio until the air flow rate is 30 g/s, corresponding to almost the maximum achievable flow rate for the pilot nozzle. In order to keep increasing the power, the multipoint injection is then switched on and a further increase to the present operating point global parameters is performed at a fixed equivalence ratio of 0.6. This procedure leads to a staging of 80%. Since high staging values do not present much interest for this operating range, the staging parameter is then decreased to 50%, reaching the higher limit of the staging study performed here.
Starting from this staging value, the sound pressure level in the chamber is monitored while the staging is slowly decreased (keeping all the other parameters constant) to 0% and then increased back to 50%. A microphone placed at half the length of the chamber is used to continuously record the pressure variations inside the chamber as the fuel staging is changed. The resulting curve can be seen in Fig. 6.1.

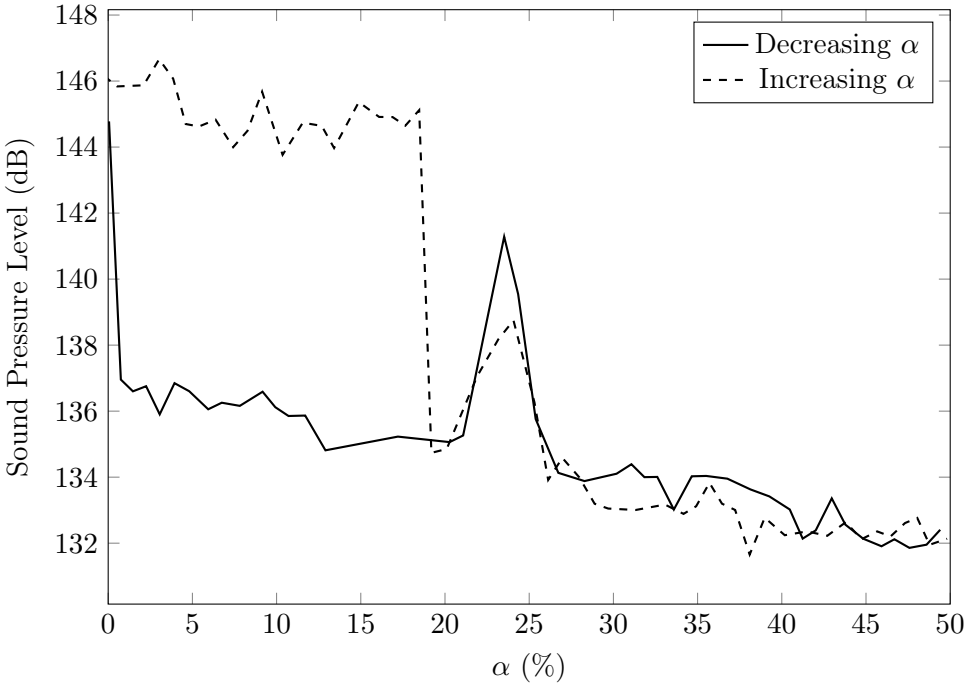

Figure 6.1 – *Sound Pressure Level in the chamber as a function of the fuel staging parameter. Only the fuel repartition is changed, all the other controlling parameters are kept constant.*

From one second long windows, the RMS value of the pressure is computed and converted into decibels using the classical 20 μPa reference pressure. The value of the staging parameter α is also recorded and its mean value over each window is used as the coordinate for the x axis. It must be noted that, since the fuel staging variations are voluntarily performed slowly, α does not change much inside the one second long windows (by 0.1 point at most). This means that the behaviour of the burner in the present case is quasi-stationary.
Starting from 50%, decreasing the fuel staging leads to a moderate sound pressure level in the chamber until α reaches a region between 20 and 26% where higher values are encountered. Further information on this first peak is provided all along the chapter. After this peak, the sound pressure level retains the previous values until a staging of almost 0% is reached, meaning that almost all the fuel is injected through the multipoint injector. At this point, a sudden increase of about 10 dB can be witnessed, highlighting a drastic change in the burner behaviour. A side note must however be made on the validity of this 0% staging. Indeed around this point, the precision of the pilot fuel coriolis flow meter becomes poor and staging parameter values below 5% must thus be treated with care.
As α start to increase back from 0%, the sound pressure level remains high. This corresponds to a clear hysteretic behaviour, leading to two different burner behaviours for the exact same operating point. As it will be confirmed later, one can already feel it is related to the bistable flames studied in chapter 5. As the staging parameter keeps increasing, another sudden change is encountered around 20% where the sound pressure level quickly drops to moderate values corresponding to the range obtained while decreasing α. Finally, further increases in the pilot fuel proportion lead to a path very similar to the one taken in the opposite direction.
The curves in Fig. 6.1 thus show a closed hysteresis cycle leading to two different potential burner behaviours for a range of staging values. This phenomenon happens for low values of α, that is for a dominant multipoint injection. From a real engine point of view, these values of the staging would be the operating point of choice since the multipoint injection is here to improve fuel mixing and thus reduce the pollutant emissions. Not being able to know the burner behaviour is thus an important drawback, especially when one of the states shows a strong noise production which is probably related to a thermo-acoustic instability. Further information can be obtained by looking at the dominant acoustic frequency as the staging parameter is varied in Fig. 6.2.

The microphone signal also contains the spectral signature of the pressure and it can be retrieved by computing a PSD. As for Fig. 6.1, one second long windows are used and the frequency of the PSD peak (0.25 s long Hamming windows with 50% overlap) is retrieved and plotted as a function of the staging parameter in Fig. 6.2. The staging parameter limits are slightly different from the ones used for Fig. 6.1 since the data come from another experiment where

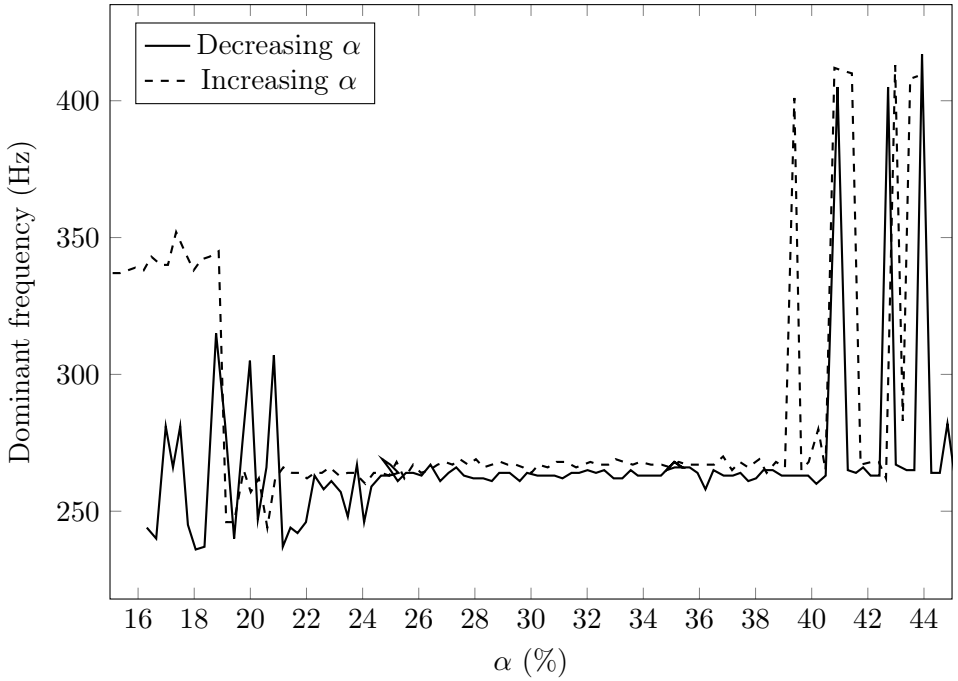

Figure 6.2 – *Dominant frequency of the microphone signal as a function of the fuel staging parameter.*

the change in the burner behaviour at low staging is artificially triggered at α=15% instead of naturally occurring for lower staging values. Several other experiments have shown that this has no impact on the global burner behaviour. Starting from high values of α down to around 40%, two frequencies seem to compete. The lower one around 260/270 Hz and the higher one over 400 Hz. This competition however happens at moderate sound pressure levels, meaning that it is not really noticeable when operating the burner. A slight change in the burner sound can however be heard when exiting this region. As α keeps decreasing, the lower frequency seems to win and dominate the pressure signal spectrum but it is once again not noticeable by hear, meaning that the signal-to-noise ratio of the peak must be relatively low. As the staging parameter reaches 25% and under, another change in the dominant frequency behaviour can be highlighted since it is not as stable as before. This limit can be associated with the peak in the sound pressure level shown in Fig.6.1 between 20 and 25%. Finally as α keeps decreasing, no dominant frequency can be retrieved and the data seems to correspond to a spread between roughly 250 and 300 Hz. The entrance in this region is also noticeable by hear, as the sound of the burner seems to show more broadband, low-frequency noises.
After the change in the burner behaviour and as α starts to increase back from 15%, a hysteresis phenomenon can once again be observed with a stable frequency around 340 Hz. Associated with the high sound pressure level, this

effect leads to suspect a strong thermo-acoustic instability occurring at this regime. This frequency can indeed be clearly heard when operating the burner. This particular behaviour stops when the staging parameter reaches around 19%, as in Fig. 6.1, and the dominant frequency moves back to previously observed values. As α keeps increasing, the behaviour in the stable frequency region is similar to what is observed when α decreases even though the frequency is slightly higher. Despite the efforts to reach thermal stability, this might be the consequence of a small thermal effect on the burner since the increase of α in the region occurs a few minutes after the decrease. A higher temperature indeed leads to a higher speed of sound and thus higher frequencies. Another reason can be an effect of the different response times of the fuel flowmeters that might slightly bias the burner global equivalence ratio towards a bit richer or leaner conditions during transient operation. Finally, as the staging parameter has increased back to around 40%, the frequency competition starts again, as expected.
Another global way of monitoring the burner behaviour during the operation is to look at the flame chemiluminescence signal using the photomultiplier tube presented in chapter 2. The frequency content of the signal as α is changed can be seen in Fig. 6.3.

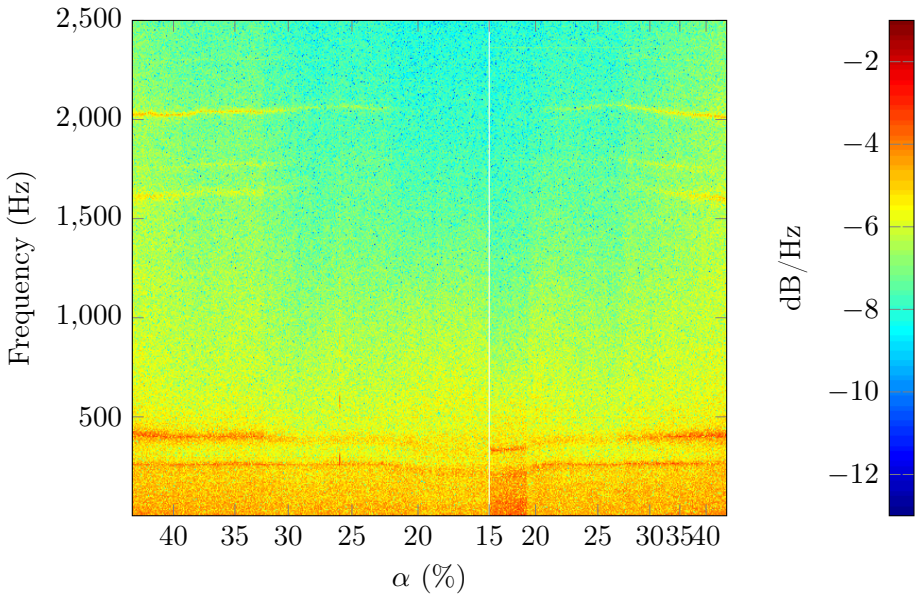

Figure 6.3 – *Power spectral density of the photomultiplier signal as a function of the fuel staging parameter.*

Similarly to what was performed for Fig. 6.1 and 6.2, one second long windows of the photomultiplier signal are treated separately and a PSD (0.25 s long Hamming windows with 50% overlap) is computed for each of them. The

results are shown as a function of time in Fig. 6.3, yielding a figure similar to a spectrogram. However, since a value of the staging parameter can be associated with each time instant, the x axis labels correspond to values of α. A white line at α=15% can be seen. It corresponds to a stop in the recording for the artificial triggering of the burner change of state. This is also the limit between decreasing and increasing values of α. Even though the right part of the graph is smaller, the changes in α are still performed at a very low speed. For illustration, the increase from 35 to 40% corresponds to 56 seconds, meaning an average increase of 0.1 point per second in this region which is the fastest of the whole recordings. The quasi-stationary assumption can thus be applied. The photomultiplier is equipped with a 431±10 nm filter to record mostly the CH^* emission. It is placed so that it records the light coming from regions close to the injector and does not collect all the light from the flame in order to potentially detect antisymmetrical phenomena such as the trace of the Precessing Vortex Core (PVC) on the flame (see Moeck et al. 2012, for instance).
As α is decreasing, two frequency regions can be observed for high values of the fuel staging. The low frequency region, under 500 Hz, can be associated with the acoustic activity of the flame. Indeed, the two frequencies around 260 and 400 Hz previously observed in Fig. 6.2 can be retrieved here. Interesting information however comes from a bit above 2000 Hz where a coherent trace can be observed. This is the effect of the PVC on the flame for this operating point. Interactions between the PVC and acoustic modulations of the chemiluminescence signal can also be seen between 1500 and 2000 Hz. As α keeps decreasing, it can be seen in the low frequency region that, as for the microphone signal, the lower frequency seems to win the competition, namely because the higher one disappears. A further decrease in the fuel staging leads to the progressive disappearance of the PVC trace between 25 and 20%, corresponding to the peak seen in Fig. 6.1. The remaining decrease of α shows no particular frequency structure, as it could already be expected from the microphone signal frequency in Fig. 6.2.
After the change in the burner behaviour at α=15%, the staging parameter is increased and, as expected, the state of the burner remains different from what was observed for decreasing values of α. A strong low frequency activity can be detected at this point, with a clearly defined frequency below 350 Hz as expected from Fig.6.1 and 6.2 which highlighted a thermo-acoustic instability. Once it is over, namely when α gets higher than 20%, the image is almost symmetric with respect to the white line, meaning that the burner keeps the same behaviour as for decreasing values of α.

When the staging parameter is changed while keeping all the other operating point parameters constant, different behaviours of the burner can thus be observed from an acoustic as well as chemiluminescence point of view. These behaviours can be associated with different types of flames and this correspondence can be seen in Fig. 6.4.

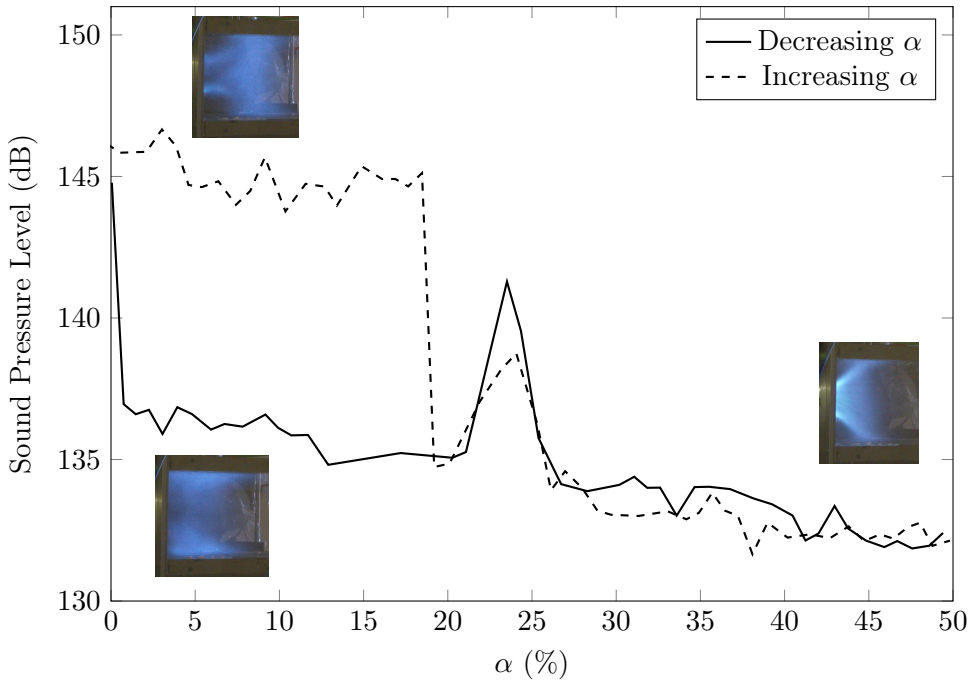

Figure 6.4 – *Sound Pressure Level in the chamber as a function of the fuel staging parameter with photographies of typical flame shapes.*

Using the sound pressure level plot of Fig. 6.1, the flame shapes studied in chapter 4 and 5 can be associated to three particular regions in Fig. 6.4.
First, for high values of α, a flame with similar properties as the one studied in pilot-only conditions in chapter 4 can be observed. As already mentioned, this flame is characterized by a strong anchoring inside the injector and a noticeable response to the PVC. This can in particular be seen in Fig. 6.3. The fact that this flame is detected for high staging values confirms the fact that its stabilization is related to a strong pilot injection.
For decreasing values of α, below the peak observed between 25 and 20%, the flame shows a shape studied in chapter 5: it is the sV flame. While it was studied for a staging value of 15%, its properties remain roughly constant over its whole existence domain. The flame is spread and this probably leads to the absence of a well defined dominant frequency in Fig. 6.2. The fact that it seems more free to move may however explain the small increase in the sound pressure level inside the chamber. It can already be noted here that the limit between the V and sV flame is not well defined. Phenomena involved in this transition region are described further in the present chapter.
Finally, the third flame shape that can be observed is the lifted flame, described in chapter 5. It was shown in that chapter that this particular flame shape triggers a strong thermo-acoustic instability around 330 Hz. This corresponds to the observations made in Fig. 6.1, 6.2 and 6.3.

The study of the present operating point for different staging values has thus enabled to extract three different flame stabilization modes leading to different behaviours of the burner from a global point of view. In order to gather more information on the reasons leading to these particular phenomena, two studies will be made in the remaining parts of the present chapter. First, the effect of slightly different operating conditions on the three flame shapes will be monitored in order to evaluate their robustness and sensitivity to changes. Then the transition regions from V to sV and sV to lifted will be studied. The third transition, between the lifted flame and the sV flame, is kept for a more detailed analysis in chapter 7.

6.2 Effect of operating conditions on the steady states

Fuel staging aside, three operating parameters can be defined: the air flow rate, the total fuel flow rate (which can also be expressed as the burner power) and the preheating temperature. In the present chapter, the studied operating point has values of 43 g/s, 72 kW and 160 °C for these three parameters respectively. The effects of small variations on these parameters with two more values for each of them is now investigated.
Three parameters with three possible values lead to an experimental matrix of 27 different experiments which is costly and time-consuming. In order to reduce the number of experiments to perform and since the objective is the response to small variations near the base point, a Box-Behnken experimental design method is chosen to reduce the number of experiments. Further information on this particular choice were given in chapter 3.
A total of 15 experiments have thus been performed and the choice of parameters for them is reported in table 6.2. These 15 experiments have led to the consumption of 46 litres of dodecane for around 12 hours of operation. Without any imaging recording, 11 GB of data have been generated from time-resolved sensors signals, clearly proving the interest of the design method.

Because of the large amount of generated data, particular post-processing methods have to be used in order to extract relevant information. First, indicators have to be defined to represent particular phenomena occurring at different positions in the burner during operation. For this purpose, five values have been chosen for their capability to give an overview of the burner state for the three studied flames.
The first chosen indicator is the temperature inside the injector obtained from a thermocouple placed on the lip of the separation between the pilot and take-off stages. This gives a quick overview on what is happening before the flame.
The second indicator is the temperature in the corner of the chamber. It is given by a thermocouple placed at 1 cm of the bottom, side and injector walls of the chamber. This gives information on the temperature of the Outer Recirculation

Table 6.2 – *Definition of the carried out experiments. In order to ease the understanding of the table, three sub-columns are used inside each parameter column.*

Experiment #	Air flow (g/s)	Power (kW)	Temperature (°C)
1	43	72	160
2	43	70	145
3	43	70	175
4	48	72	175
5	38	72	175
6	38	70	160
7	38	75	160
8	43	72	160
9	48	75	160
10	43	75	145
11	38	72	145
12	48	70	160
13	43	75	175
14	43	72	160
15	48	72	145

Zone and helps in monitoring the flame position.
The third indicator is the temperature at the chamber outlet thanks to another thermocouple. It provides information on the general combustion behaviour and the heat losses inside the chamber.
The fourth indicator is not a temperature value but the pressure fluctuations in the chamber measured by the RMS value of the microphone signal. This provides a clear monitoring of the acoustic activity of the studied point.
Finally, the fifth indicator is the RMS of the photomultiplier signal and provides an indication of the changes of flame close to the injector.
In the following subsections, these five indicators (respectively called Ti, Tc, To, Mic and PM) are computed for the three flame stabilizations for each experiment shown in table 6.2 and the effects of the changes in the operating conditions are determined using principal component analysis.

6.2.1 V flame

As stated, there are 5 indicators retained and 15 experiments. They therefore cannot be analyzed independently and the dimensionality of the data needs to be reduced. A principal component analysis (as described in chapter 3) is thus performed on the matrix composed of the five indicators (the variables) for each of the 15 experiments (the individuals). This matrix can be seen as the coordinates of the 15 experiments in the 5-dimensional space of the variables, creating a data cloud. The Principal Component Analysis (PCA) consists in computing a new axis system (the principal directions) oriented so that the axes

are orthogonal to each other and maximize the variance (visually, the inertia) of the data cloud along them. With this descriptive technique, only the first axes thus need to be looked at to explain the relationship between the variables and between the experiments.
Practically, in the present study, the PCA results are presented with two plots: the variable plot and the individual plot. The variable plot shows the correlation between the variables (shown as arrows) and the principal directions in order to explain how the axes are built. The individual plot shows the coordinates of the data points in the basis created by the principal direction. It enables to analyze which individuals have the most weight on the principal directions and can also be a useful tool to eliminate outliers.
A third set of particular variables are used. They are the one reported in table 6.2 (air flow rate, power and preheating temperature) plus a global equivalence ratio computed from the air flow rate and power values. These variables are called explanatory variables, meaning that they do not play any role in the computation of the principal directions. They are however *a posteriori* projected onto the new basis to help explain the meaning of the principal directions. They are thus shown on the variable plot with dashed arrows and their respective names are Air, P, Tp and ϕ.
For the sV flame case, the variables and individuals plots for the first two principal directions can be seen in Fig. 6.5.

For the present case, the indicators are computed as averages for decreasing values of α between 38 and 42%. In this region, all the experiments show a V flame that is similar to the one observed in pilot-only conditions. There are however differences between the experiments that can be highlighted with PCA. In order to assess whether what is observed is a valid effect or just naturally occurring variability, one can use the fact that the experiments 1,8 and 14 are performed at the exact same conditions. Ideally, they should therefore be undistinguishable from each other in the individuals plot. Their grouping can thus be seen as a clue about the effects detected by the principal directions. For example, in Fig. 6.5, experiments 8 and 14 are almost superimposed and experiment 1 is not far from them along the first axis and almost at the same position on the second axis. The effects detected here are thus not entirely due to intrinsic variability.
Since there are five variables, the principal component analysis provides five principal directions which are ordered according to the amount of the data variance they represent. In the present case, the first two principal directions are enough to explain about 83% of the variance. The first principal direction accounts for 66% and the second for 17% of it. This is the reason why the variables and individuals plots for these two directions only are represented in Fig. 6.5.

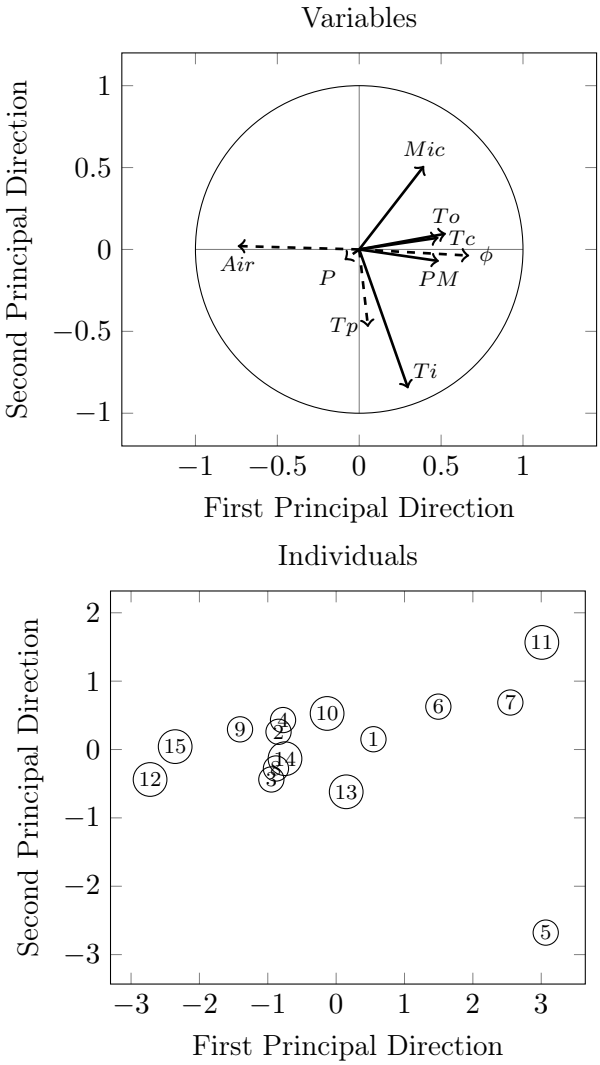

Figure 6.5 – *Variables (top) and individuals (bottom) plots for the first two principal directions of the PCA performed in the V flame state.*

On the top of Fig 6.5, it can be seen on the variables plot that all the variables seem to point in the same direction of the first principal component. This particular grouping is called a size effect and it means that all the variables are at least partly positively correlated. The correlation between the variables can be observed by the angle between them in the variables plot. A small angle represents a positive correlation, a right angle an independence and a wider angle a negative correlation. Here, it can for example be seen that Tc and To (the corner and outlet temperature respectively) seem strongly related to each other but not really with Ti (the injection temperature). Such a quick angle-based correlation analysis must however be performed with care since

the variables plot represents only the projection of the variables on the plane created by the first two principal directions when the variables are actually evolving on a 5-dimension hypersphere of unitary radius. The quality of the variable projection can be assessed by the size of the arrow in the variables plot. The closer it is to the unity circle, the more accurate the representation. As an illustration, one can look at the relative positions and sizes of the explanatory variables Air, P and Tp. They are by essence orthogonal since their values are independently changed between the 15 experiments (see Fig. 6.2). This orthogonality is roughly respected between Air and Tp since they are quite accurately projected on the analysed plane but not with P because its projection quality is poor.

In Fig. 6.5, it can be seen on the variables plot that the first principal direction is characterized by increasing values of Tc, To, PM and, to a lesser extent, Mic. On the individuals plot, this axis is structured by the opposition between the experiment couples (12-15) and (5-11). Looking at the parameters associated with these experiments in Fig. 6.2, this corresponds to extreme values for the air flow (high for 12-15 and low for 5-11). This is confirmed by the Air explanatory variable on the variables plot which is strongly negatively correlated with this axis. The first principal direction is thus associated with the changes in the air flow between some of the experiments. It must be reminded that the explanatory variables have no impact on the creation of the principal directions and this highlighting of the air effect only comes from the data contained in the five original indicators.
The effect of the air on the data can be better understood through its effect on the equivalence ratio which is also strongly correlated with the first principal direction but in the positive direction. An increase in the equivalence ratio indeed generates a stronger combustion (since the burner remains globally lean) which in turns lead to a higher heat release (explaining the positive tendencies of Tc and To) and thus a higher flame activity (explaining PM and Mic).

The second principal direction, which is less important than the first one, is strongly related to the value of Ti. This is reinforced by the very good projection of Ti on the plane. From the individuals plot on the bottom of Fig. 6.5, this axis seems built around the opposition between 11 and 5 and, to a lesser extent, 10 and 13. These particular experiments can be linked with opposite extreme values of the preheating temperature. The correlation between Tp and the second principal axis confirms this observation.
The second principal direction thus represents what is happening inside the injector through the injector temperature. The fact that it is independent from the first one shows that what happens upstream in the V flame case is roughly independent of the downstream part behaviour. Further information on the particular behaviour of the thermocouple used for this indicator are given later in the chapter and can explain its strong variability here.

From the values of the five indicators for the 15 experiments, the principal component analysis has thus enabled to retrieve the effect of changes in the equivalence ratio on the burner temperature and the flame activity as well as to highlight the independence between the temperature measured by the thermocouple placed inside the injector and the rest of the monitored elements. This second point was less expected and clearly shows the interest of the methodology. However, as the burner staging changes, the flame shape changes as well and the effects of the global operating parameter have no reason to remain the same.

6.2.2 sV flame

As shown in Fig. 6.4, when the staging parameter is decreased and reaches low values (roughly under 25%), the flame shape can be associated with the sV flame studied in chapter 5. Despite the proximity with the V flame, the sV flame has different properties that can lead to different responses to the global operating parameters and thus needs to be studied as well.
For this purpose, the five indicators are now computed for values of decreasing α between 21 and 19% when all the experiments are expected to show a sV flame. A PCA is performed in a similar fashion as for the V flame and the resulting individual plot can be seen in Fig. 6.6.

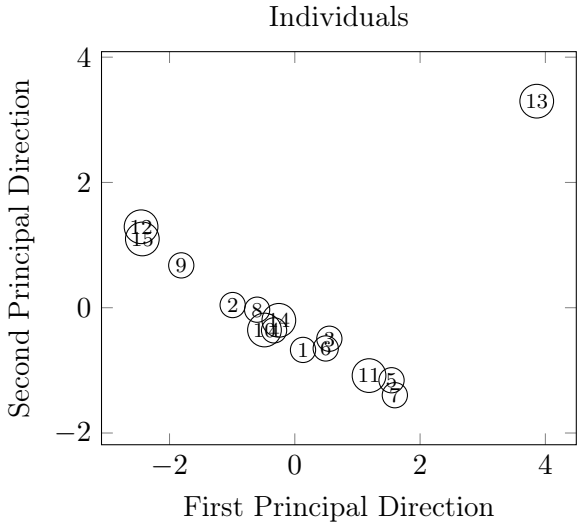

Figure 6.6 – *Individuals plot for the first two principal directions of the PCA performed in the sV flame state.*

The graph in Fig. 6.6 shows a very different aspect than the individuals plot in Fig. 6.5. Indeed, it can clearly be seen that experiment 13 has a very different behaviour compared to the others and is probably not in a proper

sV flame state. This highlights the capability of PCA to detect an outlier in the measurements. Here, this particular point has a clear deterrent effect on the computation of the principal directions. Indeed, all the other data points seem to be roughly spread along a (9-12-15)/(5-7-11) axis and, because it is so different, point 13 prevents PCA from detecting this tendency.
What happens to this particular point is explained further in the chapter. Here, in order to properly analyse the response of the sV flame to small changes in the global operating parameters, experiment 13 is removed from the data set and PCA is performed on the remaining 14 experiments. The results can be seen in Fig. 6.7.

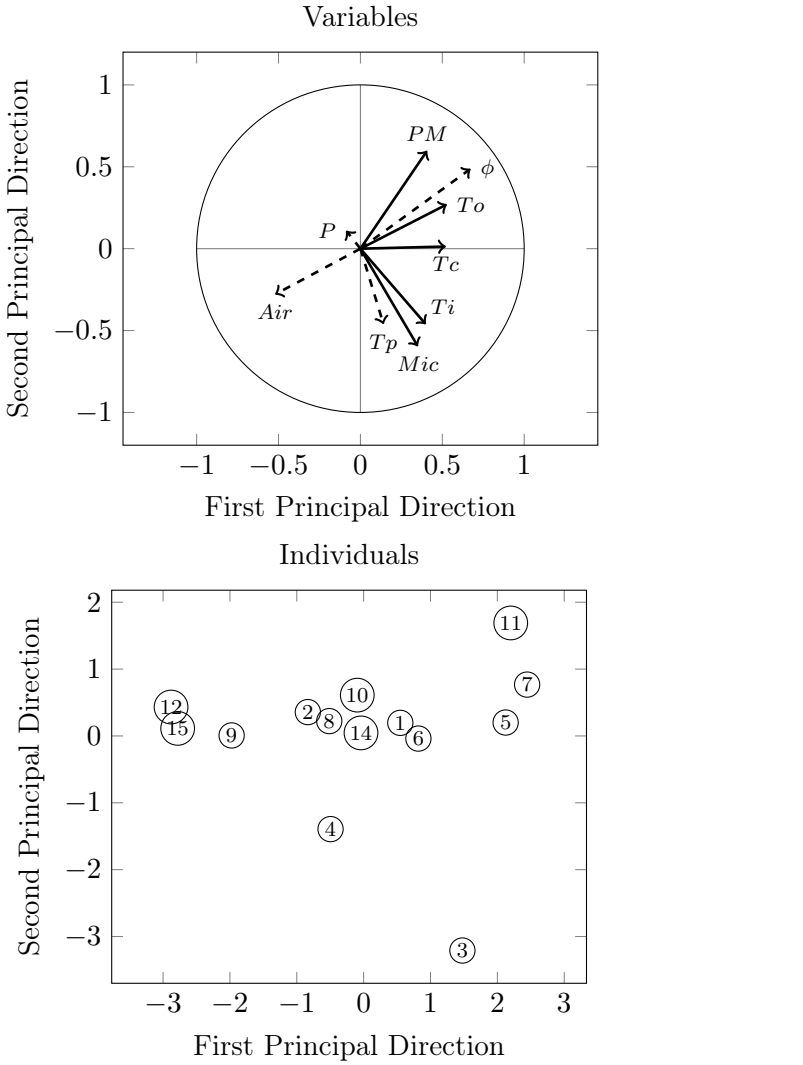

Figure 6.7 – *Variables (top) and individuals (bottom) plots for the first two principal directions of the PCA performed in the sV flame state after removal of the outlier.*

In the present case, the first principal direction accounts for 61% of the data variance and the second one for 25% of it, meaning that 86% of the variance is represented in Fig. 6.7. This variability furthermore seems to come from more than just intrinsic noise since the points 1, 8 and 14 are positioned near the center of the individuals plot.
As already seen in Fig. 6.5, a size effect can be witnessed in the variables plot of Fig. 6.7 where all the variables show components along the first principal direction. This principal direction is structured by the opposition between (9-12-15) and (5-7-11) which are respectively characterized by high and low air flow rate values. The direction of Air in the variables plot confirms the analysis, as well as the good projection of ϕ with a strong component along the first principal direction. This axis is similar to what was seen for the V flame in Fig. 6.5, representing the effect of changes in the equivalence ratio on the general flame behaviour.

The second principal direction represents more variability than for the V flame case and shows a different aspect. Indeed, it is constructed on the opposition between 3 and 11 as well as a contribution of 4 and no definite trend can be extracted from them apart from a contribution of the preheating temperature. Similarly, in the variables plot, opposite contributions of Mic and PM can be witnessed as well as opposite tendencies between ϕ and Tp, from the explanatory variables point of view.
This particular axis thus seems to show, from the opposition between PM and Mic, that an increase in the global equivalence ratio and a decrease in preheating temperature lead to a higher chemiluminescence activity detected by the photomultiplier as well as a lower acoustic activity which seems at first opposite. This issue can be resolved by looking at the particular photomultiplier position: it is set up to look at the flame close to the injector. This observation must be added to the particularity of the sV flame of having a strong signal downstream in the chamber but also a reaction happening inside the injector that can sometime be seen close to the chamber inlet. Further information on this dual flame behaviour are given in the last section of the present chapter.
The second principal direction thus highlights differences between flames that have a strong anchoring (leading to high PM values and low Mic values since they cannot move as freely as the others) and flames where the downstream spread aspect of the sV flame is more dominant (where the chemiluminescence signal is not recorded by the photomultiplier and where the flame is more free to move and generate noise). The anchoring is promoted by the equivalence ratio since it leads to more fuel to burn inside the injector and thus more signal that can be detected from the inlet of the chamber. The deterrent effect of the preheating temperature is however trickier. This, as well as the similar direction for Ti, may be explained by the fact that a higher preheating temperature improves fuel vaporization. From the internal flame point of view, it can lead to a flame burning earlier (in other words further inside) that is thus less

prone to be seen by the photomultiplier. Similarly, the improvement of the fuel vaporization reduces the thermal and mechanical inertia from the liquid spray and can lead to a less restrained flame generating more noise.

For the sV flame, PCA has highlighted the existence of an outlier which probably cannot be related to the sV state and, after removal of the outlier, two main effects of the global parameters. First, similarly to what was seen for the V flame, an increase in equivalence ratio leads to more activity from the flame in general. Secondly, because of the particular dual flame behaviour of the sV flame, combined effects of the temperature and the equivalence ratio can be extracted, leading to a more or less anchored flame.

6.2.3 Lifted flame

The third flame shape that needs to be studied is the lifted flame. In the set of studies performed with the Box-Behnken design, the transition from the sV flame to the lifted flame is most of the time artificially triggered at α=15%. For experiments 5 and 7, this triggering could not happen until α was reduced below 9% and for experiments 12 and 13, the transition occurred naturally. The indicators are computed at a stable staging parameter of 15% except for the experiment 7 where the lifted flame could only be maintained until α=12% and the indicators have thus been computed at this staging. The individuals plot from the PCA of the lifted flame data can be seen in Fig. 6.8.

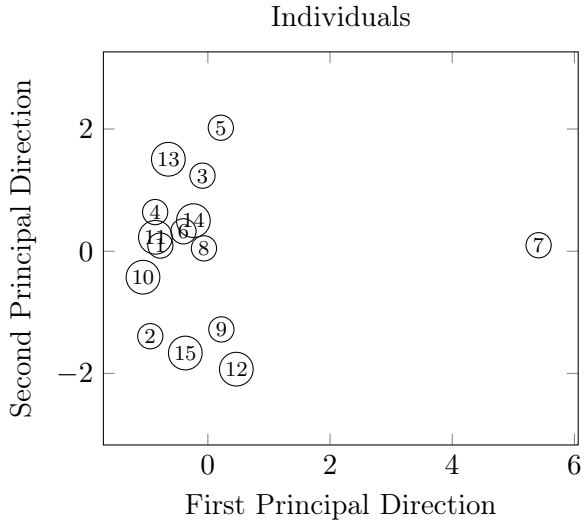

Figure 6.8 – *Individuals plot for the first two principal directions of the PCA performed in the sV flame state.*

The position of the individuals in Fig. 6.8 is here again different from what was seen in the previous PCA. Experiment 7 is an outlier that can clearly be identified, as in Fig. 6.6 for the sV flame. The situation here is somewhat different in the sense that the outlier does not perturb the two first principal directions but only the first one. The second principal direction, built along 5 and 12, is independent from experiment 7.
Experiment 7 is characterized by the extreme values of air flow rate and power which lead to the maximum equivalence ratio. As stated before, it also has a particular response to the staging variations and the indicators are thus computed at α=12%. These particularities can explain why it is very different compared to the other experiments. Indeed, the first principal direction here (which characterizes experiment 7) is well correlated with Mic and PM. It means that this experiment has a much stronger thermo-acoustic activity than the others, probably because of the higher equivalence ratio value.
Because of the very different behaviour of experiment 7, it is removed from the data and the PCA results on the 14 remaining experiments can be seen in Fig. 6.9.

Once experiment 7 is removed, the first two principal directions account for only 66% of the data variance. The first axis corresponds to 46% and the second one to 20% of the variance. These values are quite low and looking at other axes thus seems also important at first.
An interesting feature can however be seen in the individuals plot. As shown in table 6.2, experiments 1,8 and 14 are performed at the exact same conditions and should thus appear at the same position in the individuals plot. Here, experiment 1 is separated from experiments 8 and 14, especially along the second principal axis. This means that the variability represented by this axis is intrinsic and is not an effect of the modified operating conditions. Looking at other axes is thus not adequate for the present study as the effect they would highlight would anyway be less important than intrinsic variability for the same operating conditions.

The top of Fig. 6.9 shows the variables plot. The first axis once again highlights a size effect concerning Ti, To, PM and Mic. It is structured by the opposition between (2-12-15) and 5. Experiment 2 aside, this corresponds to a change in the air flow, similar to what was seen previously. The case of experiment 2, which has a low power and a low preheating temperature but a normal air flow, highlights changes in the potential heat released by the flame. Indeed, a lower preheating temperature means that more energy needs to be taken from the flame to vaporize the fuel and a lower equivalence ratio directly means a lower heat release. These observations are confirmed by the variables plot and the correlation of Air with the first principal direction.

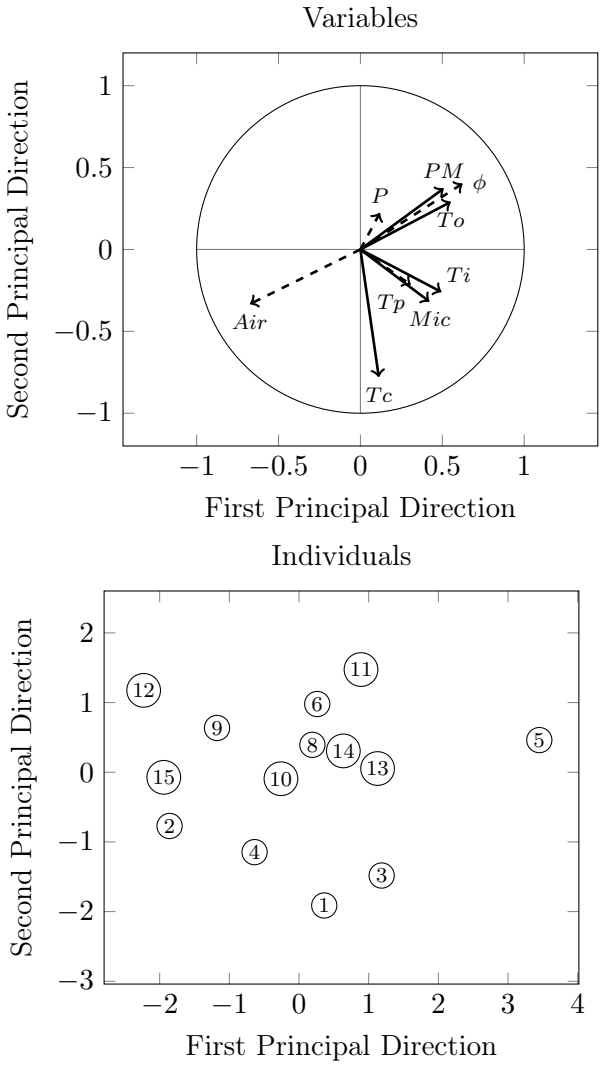

Figure 6.9 – *Variables (top) and individuals (bottom) plots for the first two principal directions of the PCA performed in the lifted flame state after removal of the outlier.*

The second principal direction is also interesting. Indeed, it was previously said that, along this axis, the experiments with the same conditions have different coordinates. The individuals plot thus cannot bring supplemental information.

From the variables plot on the top of Fig. 6.9, it can be seen that the second principal axis is strongly correlated with Tc and less with the explanatory variables. It means that, in the lifted flame state, the corner recirculation zone temperature is roughly independent of the operating point parameters. This probably indicates that the recirculating burnt gases in the ORZ in the lifted state have had time to be subjected to heat exchanges with the environment

before reaching the thermocouple placed in the corner of the chamber.

Even though it seems less fruitful than the two previous ones, the PCA on the lifted flame has provided interesting information on the studied regime. First, it has shown that the dominant source of variability of the five computed indicators comes from the changes in equivalence ratio and to a lesser extent preheating temperature, highlighting modifications of the flame heat release. Using these indicators, this is the only effect of the changes in the operating conditions that is dominant compared to the intrinsic variability of the burner, coming especially from the Outer Recirculation Zone temperature.

6.3 Study of two transition regions

As shown in Fig. 6.4, particular flame shapes can be associated with extreme staging values and their sensitivity to operating conditions have been studied in the previous section but nothing has yet been detailed about what happens for intermediate regions and when the stabilization regime changes. This is the purpose of the present section.
At the baseline operating point (43 g/s of air, 72 kW and 160 °C preheating), three main transitions can be highlighted. For α around 40%, the flame has a V shape and for α around 20% it has an sV shape. This transition can be witnessed in both directions and is called the intermediate staging values transition. The second noticeable transition is the one happening for very low decreasing values of α in Fig. 6.1, highlighting the switch from the sV flame to the lifted flame. It is referred to as the lift of the flame. The third transition is the opposite of the previous one, occurring slightly before α=20% in the increasing direction. It is called the attachment of the flame as it shows the change from the lifted flame to the sV flame.
In the present section, only the first two transitions are studied, the third one being the subject of chapter 7.

6.3.1 Intermediate staging values: V-sV flames

Because marked differences cannot be extracted between the V and sV flames, except from their shapes, defining a transition instant is tricky. Two candidates for indicators of this transition can however be found.
The first one comes from Fig. 6.2 and corresponds to the existence of a dominant frequency in the microphone signal. Such an indicator can however only give a region of interest, namely around 20 and 25% of staging and cannot be summed up into a boolean value for the stabilization regime.
The second one is extracted from Fig. 6.3 and represents the detectability of the PVC from the photomultiplier data. This indicator is however not consistent either since it highly depends on the PM position and no proper threshold can be set.

Furthermore, other phenomena may happen when α is between 20 and 40%. From Fig. 6.2, a switch between one and two dominant frequencies in the microphone signal can be observed. Similarly, a transition zone marked by the disappearance of the interactions between acoustics and the PVC in the photomultiplier signal in Fig. 6.3 can be detected. These two phenomena seem however to happen while the flame still looks more like a V flame and do not denote strong changes either.
The transition between the V and sV flames thus looks really progressive and not as marked as the other two transitions which can be clearly defined by the change in sound pressure level in the chamber. It is thus necessary to study the changes undergone by the burner when α varies between 20 and 40%. This task is complicated by supplemental variability in this region, as it can be seen in Fig. 6.10.

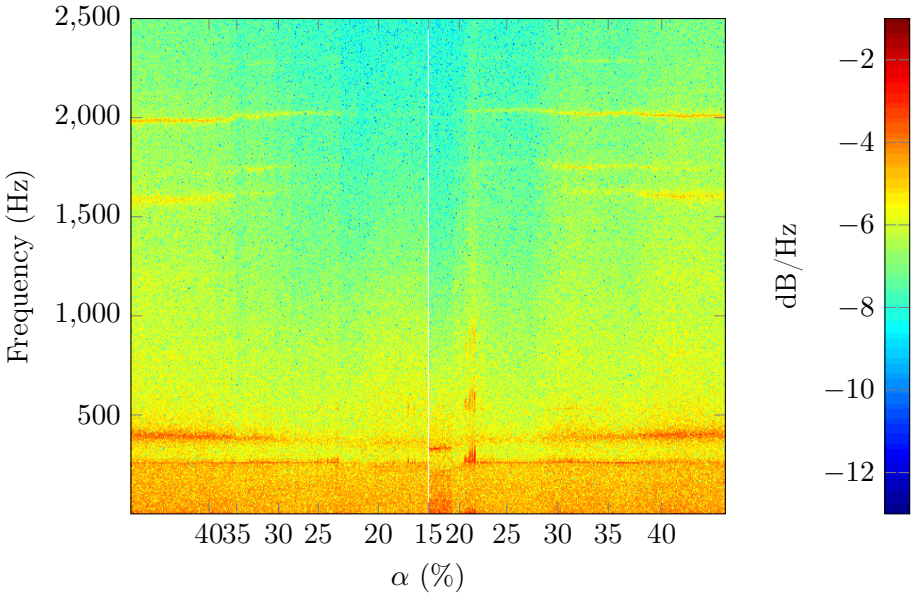

Figure 6.10 – *Power spectral density of the photomultiplier signal as a function of the fuel staging parameter.*

As shown in table 6.2, three experiments have been performed in the same operating conditions. The data shown in Fig. 6.2 and 6.3 come from experiment 14. The exact same process used to generate Fig. 6.3 from the photomultiplier measurements is used here again but on the data provided by experiment 1 and the result is Fig. 6.10.
At first sight, it seems very similar to Fig. 6.3, especially for the extreme values of α. At high α, the characteristic signature of the V flame can be retrieved and for α increasing starting from 15%, the lifted flame region is present. From a global point of view, it thus looks like the burner behaves as expected.

Values of α between 15 and 25% show however a different picture, especially in the increasing region. The chemiluminescence activity indeed seems increased after α=20% with a strong signal around 260 Hz and easily detectable harmonics. The first one of these harmonics can also be detected for decreasing values of α a bit below 25% and above 15%. This corresponds to the trace of a very strong thermo-acoustic instability (leading to pressure fluctuations that can reach 160 dB) which, in the present case happened for several seconds in the increasing staging region and intermittently when α was decreasing. Such a phenomenon is responsible for the fact that experiment 13 is an outlier in the sV flame analysis. For this experiment, no stable sV flame can indeed be identified as the burner is strongly unstable until the lift of the flame occurs.
The conditions of appearance of such an instability remains not fully understood, mostly because the high level of fluctuations prevents safe experimental analysis of the phenomenon. Indeed, this particular instability can lead to cracks in the silica windows and can also disturb the Coriolis flowmeters with the vibrations. Experiment 13 and other data however seem to indicate that increases in equivalence ratio and temperature tend to raise the likelihood of this kind of instability. The role of air flow yet remains to be fully understood. It must however be noted that in Providakis (2013), a similar thermo-acoustic instability is always encountered around α=40% for an operating point at 54 g/s of air and 200°C preheating with the same global equivalence ratio as in the present study.
This particular instability can also lead to variations in the flame lift as it will be shown later. In the present case, it further highlights the fact that several complex phenomena seem to happen to the burner in the intermediate staging values region. Another interesting indicator of this complexity is the behaviour of the injector thermocouple, plotted in Fig. 6.11.

Similarly to what was done for Fig. 6.1 and 6.2, one second long windows are used to compute the average value of the injector thermocouple as the staging parameter is varied. The data comes from experiment 14 and the lifted flame part is removed to highlight only what happens in the V and sV states. The result can be seen in Fig. 6.11.
On this graph, two distinct behaviours can be highlighted, independently of the variation direction of the staging parameter. For high values of α, the temperature indicated by the injector thermocouple is low (around 105 °C) and seems stable with variations below ±2 °C. On the contrary, for low values of α (below 26%), the injector temperature is around 130 °C and shows variations up to ±10 °C. In between these two extreme behaviours the situation corresponds to a transition (α roughly between 26 and 32%) with a possible memory effect depending on the increasing or decreasing direction. Interestingly, the injector thermocouple temperature is always below the preheating temperature of 160 °C in Fig. 6.11. It must however be noted that, for high values of α when almost all the fuel injection is performed through the pilot nozzle, the indicated

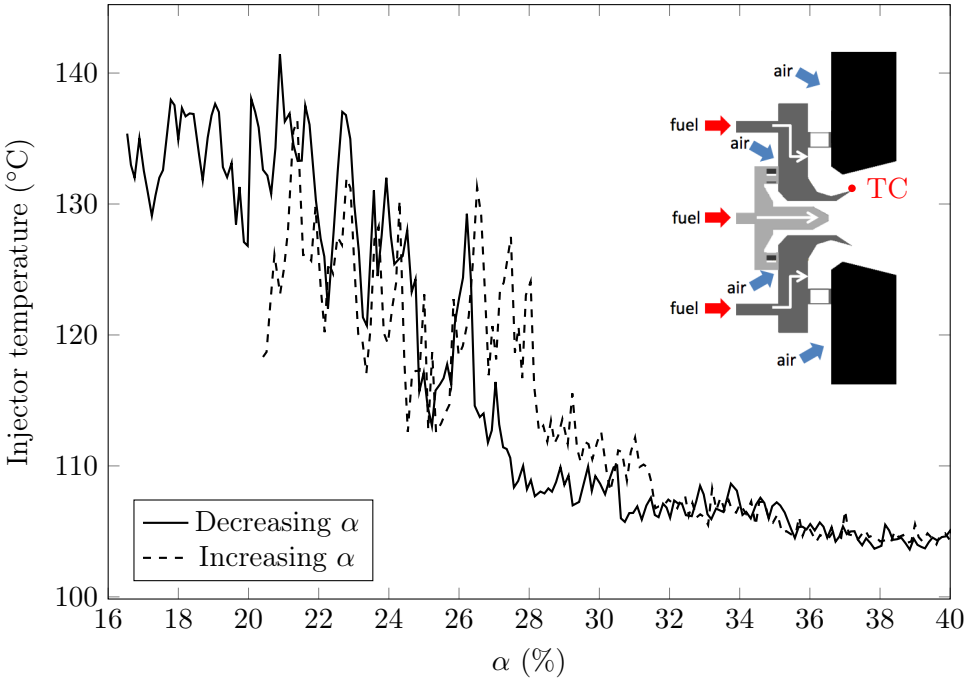

Figure 6.11 – *Injector thermocouple temperature as a function of the staging parameter in decreasing and increasing directions. The thermocouple position relative to the injection device is marked as TC on the schematics.*

temperature does reach 160 °C.

To understand what is seen in Fig. 6.11, one must look at the position of the thermocouple inside the injector. It is placed on the lip of the separation between the pilot and take-off stages on the side of the take-off stage. The fuel injection through the multipoint holes is also placed on the same wall as the thermocouple even though the orientations are different (see the tip of the white arrows in Fig. 6.11).
Simple calculations of the take-off liquid fuel injection temperature (based on heating through the fuel ducts in the plenum) show that it does not go over 100 °C, even with conservative hypotheses. The low temperature measured by the thermocouple is thus likely to be related to the multipoint liquid fuel injection. The increase in temperature with decreasing α seems however at first to counter this hypothesis. Indeed, as α decreases, the fuel flow rate through the take-off stage increases and, since the fuel thus spends less time in the plenum, it has less time to heat up and is injected at a lower temperature. There must thus be a change in the injection conditions that can explain the behaviour of the injector thermocouple.

As stated in chapter 1, the multipoint injection works as a fuel jet in an air crossflow created by the swirler vanes. A key parameter governing this kind of injections is the fuel-to-air momentum ratio defined as:

$$J = \frac{\rho_{fuel} V_{fuel}^2}{\rho_{air} V_{air}^2} \tag{6.1}$$

or sometimes:

$$r = \sqrt{J} \tag{6.2}$$

where ρ represents the density and V the velocity.
As the momentum ratio increases the jet can penetrate further into the crossflow, enhancing the atomization (Stenzler et al. 2006). In Schlüter and Schönfeld (2000), it is stated that for values of r under unity, the fuel jet may not penetrate further than the boundary layer and in Rachner et al. (2002), an image of a kerosene jet in crossflow for J=2 shows contact of the liquid fuel with the wall on the injection side.
In the present case, for α=20%, the value of J is 2.7 while it is only 1.5 when α=40%. The latter low value leads to suspect that the fuel injection is not well realised and results in the air flow pushing the liquid fuel along the wall, eventually reaching the thermocouple. The same mechanism is proposed in a very similar configuration in Apeloig et al. (2015) to explain the varying liquid fuel injection behaviour during a thermo-acoustic instability cycle.

When α is high, the liquid fuel momentum is not high enough to penetrate the cross flow and flows along the wall until it reaches the tip of the stages separation where the thermocouple is placed. The thermocouple is therefore surrounded by liquid fuel which was injected at a low temperature and has not had much time to heat up, resulting in a low temperature value. This hypothesis is supported by the low variability of the temperature which can be linked to the high thermal inertia of the fuel in the liquid state.
For low values of α, the fuel injection momentum is higher and the liquid fuel can be properly atomized by the cross flow. The thermocouple is then in contact with the air and not drowned into liquid fuel. The higher variability of the temperature reading supports this proposition as air has a lower thermal inertia and is characterized by higher levels of turbulence. The fact that the thermocouple temperature remains under the preheating temperature can be explained by spray cooling due to the mist of evaporating liquid fuel droplets.
The present theory can also explain two more observations. First, the memory effect seen between α=26% and α=32% can probably be associated with the time needed to remove the remaining liquid fuel around the thermocouple in the decreasing direction. In the increasing direction, it can similarly correspond to the time required to build up the liquid fuel "bubble" around the thermocouple. The second observation that can be explained is the particular second

principal axis of the PCA of the V flame (Fig. 6.5) which highlights the relative independence of the injector temperature. The fact that, for such high values of α, the thermocouple is covered by liquid fuel enables to understand its relative insensitivity to the operating conditions, preheating temperature aside.

Such a modification in the multipoint fuel injection leads to drastic changes on the atomization behaviour. Indeed, it was seen in chapter 5 that the take-off stage is built to perform a good droplet atomization and mixing but this can happen only when the jet in crossflow configuration is fully realized. In the case where the liquid fuel sticks to the wall, it can be expected that the mode of fuel atomization switches to a film-like atomization, most likely with a poor efficiency since nothing in the injector is designed for its promotion.
This phenomenon can help explain the switch from a ballistic dominated V flame to the sV flame associated with a greater importance of the air flow. Indeed, big droplets produced by the poor atomization will tend to have a similar ballistic behaviour as the big droplets produced by the pilot whereas smaller droplets tend to follow the air flow. This change in the atomization is however not the only phenomenon happening in the intermediate staging transition region and the changes in the pilot and take-off stages local equivalence ratio are reported in table 6.3.

Table 6.3 – *Local equivalence ratio between α=40% and α=20%.*

α (%)	ϕ_{pilot} (-)	$\phi_{takeoff}$ (-)	α (%)	ϕ_{pilot} (-)	$\phi_{takeoff}$ (-)
40	1.78	0.42	30	1.33	0.49
38	1.69	0.43	28	1.24	0.50
36	1.60	0.44	26	1.16	0.51
34	1.51	0.46	24	1.07	0.53
32	1.42	0.47	22	0.98	0.54
30	1.33	0.49	20	0.89	0.55

With the knowledge of the global equivalence ratio and of the air split between the pilot and take-off stages computed in chapter 1, it is possible to compute a (theoretical) local equivalence ratio for each of the stages depending on the value of the staging parameter. For the present global equivalence ratio of 0.6 and values of α between 20 and 40%, the local pilot and take-off equivalence ratios can be read in table 6.3.
For the take-off injection, the equivalence ratio increases from 0.42 to 0.55 as the staging parameter decreases from 40% to 20%. The safety data for dodecane (Coward and Jones 1952) indicate a lower flammability limit of the vapour around 0.6% in volume in air. This limit is relevant here since the already present pilot-fueled flame acts as a permanent igniter. This proportion corresponds to an equivalence ratio of 0.11, which is below what is witnessed

in table 6.3. There should thus be no strong change from the take-off injection point of view in the intermediate staging region but it must be kept in mind that the increase in equivalence ratio still promotes combustion.
The pilot injection local equivalence ratio contains more interesting information. Indeed, it starts at 1.78 for α=40% and reaches 0.89 for α=20%. This means that the pilot injection crosses the stoichiometry line around α=23% which is in the region where changes in the burner behaviour seem to happen (see Fig. 6.1, 6.2 and 6.3). A local equivalence ratio below one means that the pilot-injected fuel can potentially burn independently of the take-off injection in the sense that the consumption of part of the take-off air flow is not a requirement as it is when the pilot local equivalence ratio is over one. Such a difference can be related to the hints of the existence of an independent inner flame in the sV case studied in chapter 5.

To sum up, as shown by Fig. 6.10 and 6.11 and by table 6.3, the transition between the V and sV flames is complex to study. First, no strong criterion for the switch into one or the other state can be defined and the transition seems progressive rather than abrupt. It is furthermore complicated by the fact that, sometimes, the transition region is associated with a very strong thermo-acoustic instability leading to potential safety issues. Finally, changes in the droplet atomization and in the local equivalence ratios happen at the same time, leading to uncertainties about the phenomena that may control the transition.

6.3.2 Lift of the flame

Detecting the lift of the flame is easier than detecting the transition between the V and sV flames since it is always accompanied by a fast and strong increase in the chamber sound pressure level as well as the appearance of a fixed dominant frequency because of the triggering of the thermo-acoustic instability by the lifted flame. The fact that it is well defined does not however mean that this transition is straightforward to study.
For the moment, three ways of lifting the flame have been mentioned. The first one consists in decreasing the staging parameter to low values with uncertainty issues coming along. The second one was just defined as "artificially triggered" at α=15%. The third one comes from the statement, during the PCA study of the lifted flame, that for experiments 12 and 13 the transition had occurred naturally before α had decreased to 15%.
In order to first study this natural transition, the sound pressure level in the chamber as a function of decreasing staging values associated with a different operating point studied in Providakis (2013) is presented in Fig. 6.12.

In Providakis (2013), an air flow rate of 54 g/s with a global equivalence ratio of 0.6 and 200 °C preheating is used. Even though the operating point

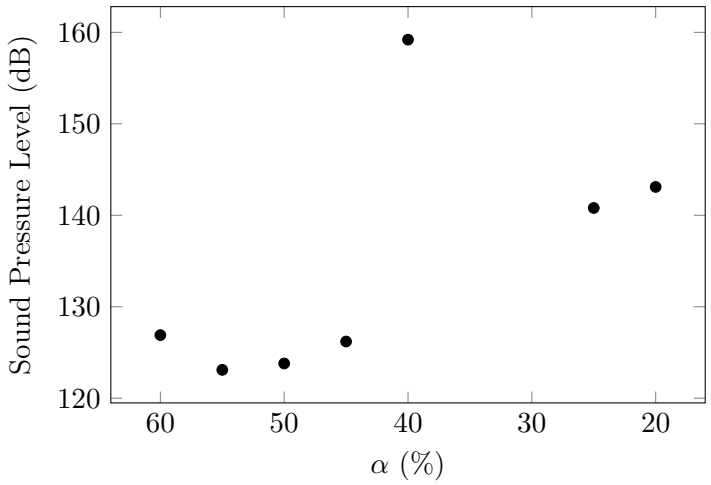

Figure 6.12 – *Sound Pressure Level in the chamber as a function of decreasing staging parameter. Taken from Providakis (2013).*

is different from the one studied here, it provides a similar response to staging changes with the beginning of a hysteresis cycle (that unfortunately cannot be closed) and a very strong thermo-acoustic instability around α=40% as already stated. The data is used in Fig. 6.12 to highlight the comparable burner response as well as to provide information on the flame lift.
Similarly to Fig. 6.1, the idea is to monitor the Sound Pressure Level in the chamber for different decreasing staging values. However, instead of doing it in a continuous fashion, particular values of α are chosen to realize a measure of the SPL. It is first interesting to look at the similarities between Fig. 6.12 and Fig.6.1. For high values of α, moderate sound pressure level is encountered and, even though it is not shown here, the flame presents a V shape. For low values of α, the SPL is higher and the flame stabilizes in the lifted state. Such a qualitative agreement is interesting since it means that the same stabilization mechanisms are involved.
There are however strong differences, mostly when one looks at the values of α. Indeed, it is shown that the lifted flame can appear for relatively high values of α (over 20% and in fact it can be observed at higher staging since the attachment back to a V flame never occurs) and in the decreasing direction. The first observation will be explained in chapter 7 while the second one is to be treated now.
For α=40%, the Sound Pressure Level in the chamber reaches an extreme value of almost 160 dB. This very strong thermo-acoustic instability was already encountered in the transition region between the V and sV flames and was also said to be responsible for the fact that experiment 13 never shows the sV flame state. As stated before, experiment 13 is also a case where the lift of the flame occurred naturally. In Fig. 6.12, the natural lift of the flame is also associated

with the occurrence of a strong thermo-acoustic instability, meaning that this particular instability has the capability of triggering the flame lift. This explains why lifted flames can, in particular cases, be encountered for decreasing values of α.

The goal of the present study is to gather information on the lift of the flame and, for this purpose, a controlled setup for this transition needs to be found. As stated before, going through the lower values of α creates major uncertainty problem, namely because the pilot fuel keeps flowing with a very low rate until it is manually closed and this action also seems to trigger the lift.
A second option would be to count on the fact that the naturally occurring thermo-acoustic instability can trigger the transition at higher values of α. Safety issues aside, such an option is not compatible with repeatable experiments since the occurrence of this thermo-acoustic instability is not fully under control.
The third option, which is the chosen one, consists in taking advantage of the presence of the siren in the air feeding line. With the proper settings, it can in some way simulate the air flow modulations encountered during a strong thermo-acoustic instability and act in a similar fashion on the flame. Since the particular value of α=15% is already thoroughly studied in chapter 5, it is a well suited candidate for the artificially triggered lift experiments. Data extracted from the chamber microphone during such experiments can be seen in Fig. 6.13.

In Fig. 6.1, the lift of the flame is simply detected by looking at the instant when the sound pressure level in the chamber undergoes an abrupt increase. In the present case, such a technique cannot be used since the siren generates additional noise. In chapter 4, a 14 dB increase due to the siren is indeed measured and this value is over the expected increase associated with the flame lift read in Fig. 6.1. Another detection technique must thus be used and it is provided by the observations made in Fig. 6.2 where the lift is associated with the appearance of the thermo-acoustic instability frequency above 300 Hz.
To trigger the transition, the siren wheel, rotating at a stable 290 Hz frequency, is progressively introduced inside the flow to generate increasing fluctuations until the flame gets lifted. During this operation, a spectrogram is computed on 0.2 s long windows (with 50% overlap) of the chamber microphone signal and two values are extracted. First, since the frequency of the siren is extremely stable, most of its energy lands into only one of the 5 Hz-wide frequency bins. Reading the SPL value associated with this frequency thus gives an indication of the amplitude of the siren-induced modulations. It is traced as a function of time at the top of Fig. 6.13. In parallel, the dominant frequency is extracted from the same data, after the 290 Hz bin is removed to avoid the deterrent influence of the siren. This frequency is reported as a function of time at the bottom of Fig. 6.13.

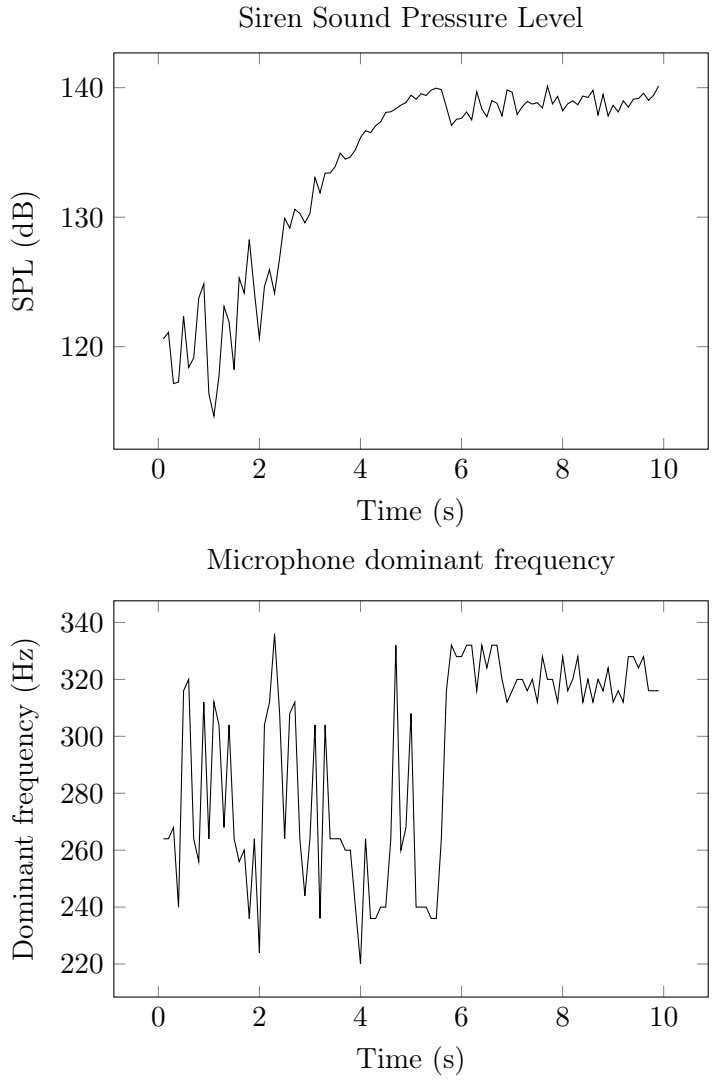

Figure 6.13 – *Siren sound pressure level at 290 Hz (top) and chamber microphone dominant frequency (bottom) as a function of time during a triggered lift of the flame at α=15%.*

At the top of Fig. 6.13, it can be seen that the siren SPL increases with time as expected since the toothed wheel is progressively introduced inside the air flow. The data show variability in the beginning but the curve becomes smoother when the siren becomes dominant. As it reaches its maximum value, a small decrease in the siren SPL can be witnessed (slightly before 6 s) and the value then becomes relatively stable since the toothed wheel is now fully inserted inside the flow.
At the bottom of Fig. 6.13, one can observe the behaviour of the expected dominant frequency that was already described in Fig. 6.2. Indeed, in the beginning

of the experiment, no dominant frequency is clearly defined and the curve oscillates between roughly 240 and 300 Hz. In Fig. 6.2, this was associated with the behaviour of the sV flame and it is expected to find the same response here. However, slightly before t=6 s, an abrupt change in the dominant frequency behaviour can be witnessed as it stabilizes around 320 Hz. This can clearly be associated with the lifted flame, meaning that the introduction of the siren has indeed triggered the transition of the sV flame to a lifted flame. Coming back to the siren SPL plot, this lift is associated with the small reduction in the siren SPL. This comes from the fact that the microphone placed in the chamber records the sound contributions of the siren as well as of the flame and, as the lift occurs, the flame changes its shape and does not react as well to the siren induced modulations, thus generating less noise at 290 Hz.
As hinted before, at the beginning of the lifted flame PCA study, the triggering of the lift with the siren is not always possible at α=15% and seems to be harder with increased equivalence ratio and preheating temperature. These particular cases are however not within the scope of the study since it focuses on the lift progress. For this purpose, other diagnostics can be used like the internal Mie scattering visualizations to gather more information on what happens inside the injector. Some results recorded simultaneously with the data in Fig. 6.13 can be seen in Fig. 6.14.

In chapters 4 and 5, a 30×30 pixels region of interest is used to compute the PVC frequency from the internal Mie scattering data. The same window is used here and the resulting signal is not used to compute a histogram of the PVC frequency but traced in a time-frequency plane using a reassigned spectrogram method. Because of the relatively high computational cost of this post-processing technique, focus is put on the instant of the lift itself as defined in Fig. 6.13. Preliminary tests on synthetic signals have shown that the expected temporal precision is around ±0.2 s. The resulting time-frequency map around the PVC frequency can be seen at the top of Fig. 6.14.
For low time values, a trace can be seen slightly above 2000 Hz and the color seems to highlight a strong structure. This can be put in parallel with Fig.5.23 in chapter 5 where the sV flame shows a well defined peak around 2015 Hz in the histogram of the PVC frequency. The trace of the PVC frequency is then progressively disturbed at 5.64 s until it gets no longer detectable around 5.67 s. This window probably corresponds to the start of the transition itself. About 20 ms later, another frequency can be detected below 2000 Hz and it seems less stable than previously. This can once again be related to the results in Fig. 5.23 where the PVC frequency for the lifted flame is spread around 1970 Hz. The decrease in frequency is an effect of reduced velocity, maybe because of a decrease in temperature and the slight spread in frequency may be associated with a less confined structure.
From the PVC frequency point of view, which can be related to changes in the air flow, the transition thus occurs around 5.68 s. This value must be compared

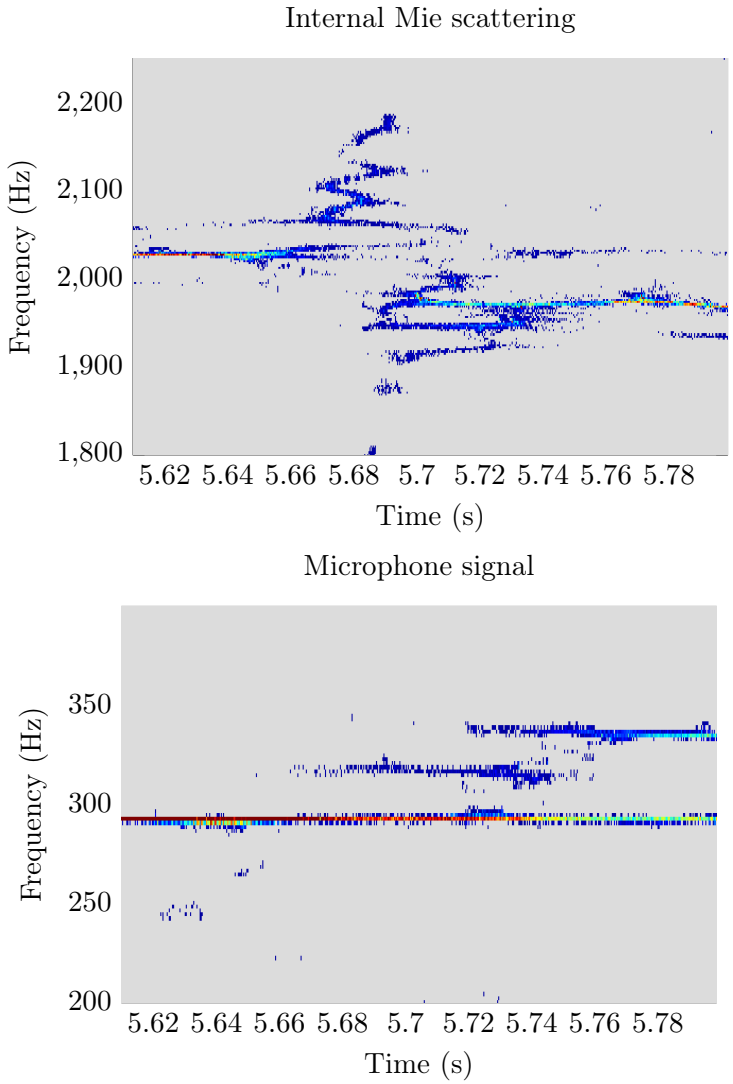

Figure 6.14 – *Reassigned spectrograms of the internal Mie scattering signal (top) and the microphone signal (bottom) during an artificially triggered lift at α=15%. For visualization purposes, the colormap corresponds to a linear scale and the values below 1% of the maximum are associated with gray.*

to a similar one obtained from another diagnostic to be able to reconstruct the chain of events.

For this purpose, the microphone signal is traced on a time-frequency plane using the same post-processing method. Here again, the observation is focused on the transition instant and the frequency axis is limited to the region where the thermo-acoustic instability frequency is present. The result can be seen at the bottom of Fig. 6.14.

First, a clear horizontal line that spans the whole time window can be observed. It is the trace of the siren at 290 Hz. Between the beginning and the end of the recording, its intensity decreases which can be related to the small change in the siren SPL highlighted in Fig. 6.13 at the transition instant. A more interesting information provided by the present time-frequency plane is the appearance of the thermo-acoustic frequency after 5.73 s when the PVC frequency changes around 5.68 s. It means that the lift of the flame from an acoustic point of view is detected after the lift from the aerodynamic point of view.
It must at this point be noted that the chamber microphone is not close to the flame but placed at half the length of the chamber, that is 250 mm from the inlet. With a conservative sound velocity of 340 m/s (knowing that because of the flame heat release, the real value is higher), this leads to a delay below 1 ms which is not enough to explain the difference seen in Fig. 6.14.
The present analysis thus leads to consider that the lift of the flame occurs because of the change in the air flow inside the injector which in turn triggers the new flame stabilization and thus the thermo-acoustic instability. This change in the air flow is itself piloted by strong oscillations (whether naturally occurring or induced by the siren) or by the fact that the fuel staging gets low.

6.4 Changes in the stabilization mechanisms

In chapters 4 and 5, several phenomena have been witnessed about the three different flame shapes. These information have been completed by data obtained in the beginning of the present chapter either by changing the fuel staging or the other operating point parameters. The purpose of this section is to organise all the observations in order to extract potential mechanisms explaining the behaviour of the burner.

6.4.1 V flame

From the pilot-only conditions studied in chapter 4 and data gathered during the study of the hysteresis cycle operating point, it is possible to sum up the observations on the V flame to a few key points. In order to be considered, a stabilization mechanism must fulfil all these observations without relying on too many assumptions. Table 6.4 regroups all the key observations on the V flame as well as the related diagnostic and reference figure leading to the observation.

In the case of the V flame, 8 key elements can be extracted and they are related to three main categories: the air flow (observations 6, 7 and 8), the spray (1, 2, 3 and 4) and the flame (observation 5). As it has been seen before, these three categories show strong interplay meaning that none of them alone can explain the other two.

Table 6.4 – *Key observations on the V flame*

#	Observation	Diagnostic	Figure
1	Strong or moderate pilot injection	Photography	4.16 and 6.4
2	Spray mostly composed of big droplets	PDA	4.6
3	Big droplets segregated outwards	PDA	4.6
4	Outer spray limit not related to air jet	Mie and PIV	4.3
5	Diverging flame inside the spray	CH^*	4.18
6	High PVC frequency	Mie	4.22
7	Stable PVC frequency	Internal Mie	4.36
8	Diverging reacting air flow	PDA	4.20

From all these key observations, the dominant one is the diverging shape of the flame (observation 5) since it is the one that gives its name to the V flame. Assuming a fully premixed behaviour, the flame should stabilize in the Inner Shear Layer (ISL). However, in non-reacting conditions, the ISL is not clearly diverging like the flame. There must thus be a mechanism that leads the flame to open.
Observation 4 highlights the fact that, in non-reacting conditions, the liquid fuel spray does not behave like the underlying air flow and it can be explained by observation 3. Indeed, because of their ballistic behaviour and large mass, the bigger fuel droplets tend to be expelled towards the external parts of the spray by the strong swirling motion of the air flow. Since the fuel spray is mostly composed of big droplets (observation 2), the previous effect is dominant in the fuel spray and, furthermore, the biggest droplets are the one carrying most of the fuel mass (since the mass is proportional to the cube of the droplet diameter). Observations 2, 3 and 4 combined thus lead to think that the fuel distribution is biased towards the external parts of the spray. Observation 1 however states that this fuel stratification effect may not be always the same since V flames for moderate staging values (α=30%) can be observed.
From observation 8, it can be deduced that the flame has an impact on the air flow since it becomes different compared to the one associated with non-reacting conditions and shows a diverging trajectory. This impact of the flame on the flow can also be detected by two changes in the PVC frequency: it is higher than in non-reacting conditions (observation 6) and also shows less variability (observation 7). These two observations tend to point to a hotter and more confined internal air flow.
All these observations and their consequences lead to propose a two-step mechanism for the flame stabilization into a V-shape. Schematics for these two steps are shown in Fig. 6.15.

The first step of the stabilization mechanism is represented on the left of Fig. 6.15. It enables to explain observation 5 on the flame shape while taking

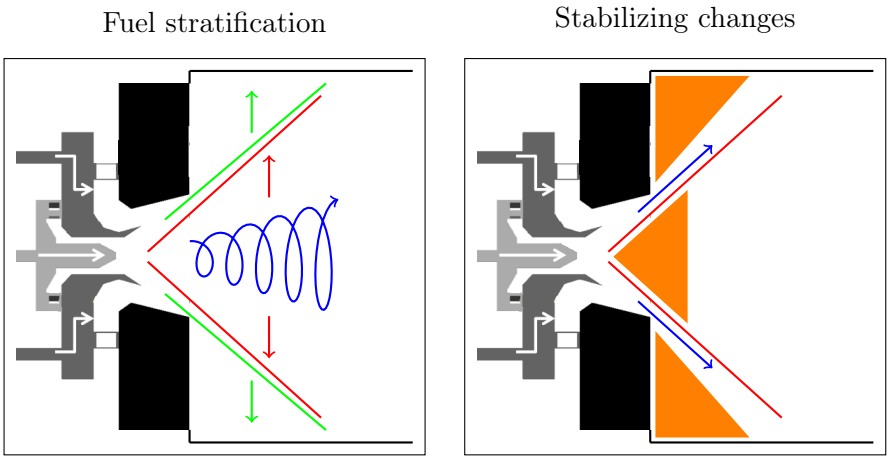

Figure 6.15 – *Stabilization mechanisms for the V flame. The blue color corresponds to the air flow, green to the fuel, red to the flame front and orange to hot combustion products.*

support on observations 2, 3 and 4 about the fuel stratification. Because of the swirling flow, the fuel mass tends to concentrate towards the outer parts of the spray and this is supposed to be the reason of the flame opening. Additional clues, exposed in chapter 7, are supporting this theory.
This explanation is however not sufficient to fulfil observation 1 since, as stated previously, the stratification effect is not necessarily always the same. A supplemental advantage of this mechanism is nevertheless the fact that it also explains why the flame takes a V shape when the burner is ignited with a pilot-only injection and not with a multipoint-only injection in Providakis (2013).
The second step of the mechanism, shown on the right of Fig. 6.15, can explain why the flame remains in the V shape and is proposed thanks to the observations on the air flow (6, 7 and 8). The main idea behind it consists in the fact that, once it takes a V shape, the flame creates the conditions for its own stabilization into this particular shape. This is performed thanks to two effects: the modification of the air flow structure and the creation of hot regions.
The changes in the PVC and the diverging behaviour of the air flow can be explained by the fact that combustion happens inside the injector and blocks the path of air, forcing it to a diverging trajectory. This change means that not only the bigger droplets but all of the fuel is carried on the same trajectory, helping the flame to keep this particular shape.
This change in the air flow is accompanied by the creation of hot burnt gases regions, notably one in the Inner Recirculation Zone that helps to maintain the combustion reaction inside the injector. The Outer Recirculation Zone can also be associated with hot recirculation thanks to the data obtained with the thermocouple placed in the corner of the chamber. This is the reason why its temperature value is well correlated with the equivalence ratio in the PCA of

the V flame (Fig. 6.5).

In a nutshell, the V flame can be considered as resulting from a two step stabilization mechanism. First, because of the fuel stratification created by the swirling flow and the dominance of big droplets, the flame is attracted towards the external parts of the spray even though it may not be its preferred stabilization mode in perfectly premixed conditions. This step only needs to occur once, during the ignition for example, the rest of the stabilization being explained by the second step. Indeed, once the flame has reached a V shape through the first mechanism, it imparts changes onto the air flow setting it into a diverging trajectory and also generates stabilizing regions filled with hot products. This enables the flame to keep a V shape even though the strength of the fuel stratification mechanism changes as the staging is varied.

6.4.2 sV flame

Similarly to the previous study on the V flame, the key observations made during the study of the sV flame in chapter 5 as well as in the present chapter are reported in table 6.5.

Table 6.5 – *Key observations on the sV flame*

#	Observation	Diagnostic	Figure
1	Weak pilot injection	Photography	6.4
2	Spray mostly composed of small droplets	PDA	5.4
3	Spread diverging flame	CH^*	5.9
4	High PVC frequency	Mie	5.10
5	Stable PVC frequency	Internal Mie	5.23
6	Diverging reacting air flow	Spray PIV	5.8
7	Local pilot equivalence ratio under 1	-	Tab. 6.3
8	Killed by very low staging	Microphone	6.1
9	Killed by strong air fluctuations	Microphone	6.13

Here again, the key elements can be grouped. The first three previously mentioned categories can be found: observation 3 represents the flame, observations 4, 5 and 6 are related to the air flow and finally 1, 2 and 7 highlight the spray and fuel injection conditions. A new category corresponding to the conditions leading to the end of the sV state can also be highlighted and is represented by observations 8 and 9.
The spread aspect of the flame (3) may be linked to observation 2. Indeed, since the spray is mostly composed of small droplets, they tend to vaporize and mix quickly with the air, leading to a well premixed combustion. Associated with

the high level of turbulence created by the swirled air flow, this may be the reason for the flame's diluted appearance from an average point of view.
An interesting feature is that some observations are similar to what was seen in the V flame case in table 6.4, namely 4, 5 and 6, while others are opposite (1 and 2). This corresponds to the fact that, between the V flame and the sV flame, the air flow is similar but the liquid fuel injection is completely different. The fuel stratification mechanism previously highlighted can thus not be invoked here to explain the diverging part of observation 3. The diverging air flow is on the contrary a good lead since it is the reason why the V flame keeps its diverging shape independently of the staging when it is high enough. It however requires the existence of a flame inside the injector to maintain it.
The fact that the PVC frequency is still higher than in non-reacting conditions is a clue for the idea that a flame indeed exists inside the injector near the pilot and leads to higher temperatures and thus higher velocities there. This idea is supported by observations 8 and 9 that can be linked with the extinction of this internal flame, either by blowing it (9) or by cutting the pilot fuel supply (8).
All these observations lead to propose a mechanism for the stabilization of the sV flame that is summed up by the schematics in Fig. 6.16.

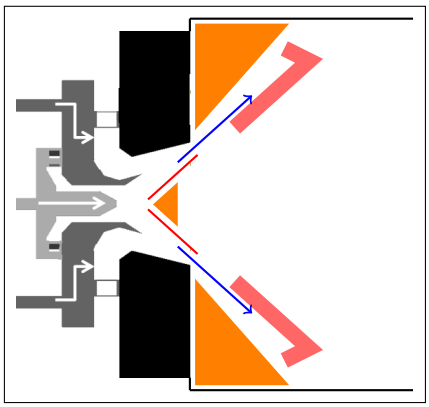

Figure 6.16 – *Stabilization mechanisms for the sV flame. The blue color corresponds to the air flow, red to the flame front and orange to hot combustion products.*

The stabilization mechanism considered here relies mostly on the similarity of the air flow with the V flame. Indeed, it is really similar to the second step of the mechanism exposed in Fig. 6.15 and relies on the presence of a pilot flame inside the injector which keeps the shape of the air flow and thus the fuel distribution in a diverging fashion.
The main drawback of this theory is that the existence of an internal flame cannot be directly witnessed since it is not possible to have a direct look inside the injector. There are however several clues that hint at its existence. The strongest ones were exposed previously, coming namely from observation 4 (on

the PVC) and observations 8 and 9 (on the ways of ending the sV flame stabilization). The possibility to detect a small signature of the PVC from a region of interest close to the injector in the CH^* images in Fig. 5.11 (chapter 5) is one more. Finally, in the PCA of the sV flame, the second principal axis (see Fig. 6.7) can be justified by the existence of an internal flame.
The impossibility to see the internal flame from the chamber can be explained by observation 7 since it means that most of the pilot fuel can burn with the pilot air only and thus does not need to wait for mixing with the take-off air. The flame can thus be really concentrated close to the pilot nozzle which also explains why it can remain on down to really low staging values (and thus low local pilot equivalence ratio). Indeed, in Cavaliere et al. (2013), a spray flame keeps burning at an equivalence ratio under 0.2 since the liquid fuel distribution is such that relatively high local fuel concentrations can be found.

The stabilization mechanism of the sV flame is thus characteristic of a dual flame behaviour. Thanks to the previous stabilization as a V flame, an internal flame can be found close to the pilot nozzle and helps in shaping the air flow into its particular trajectory. This enables the small fuel droplets generated by the multipoint injector to mix and vaporize while following the air flow, leading to a spread flame that keeps a diverging shape.
This particular behaviour is probably the most wanted from an industrial point of view. Indeed, the low intensity pilot flame is here to stabilize the system and prevent the lift of the flame (and thus the occurrence of a thermo-acoustic instability) while most of the power is provided by the well mixed downstream flame, probably leading to reduced pollutant emissions. The main issue with this regime is that its operating range is limited and that it is sensitive to perturbations, as shown by the siren-triggered lift.

With the help of the stabilization mechanisms in Fig. 6.15 and 6.16, it is now possible to further understand the progressive transition from the V to the sV flame.
Working with decreasing values of α, the first phenomenon that can be witnessed is the change in the atomization quality of the multipoint injection (detected by the change in the injector thermocouple in Fig. 6.11). For high values of α, the big droplets created by the multipoint injector reinforce the fuel stratification which is the first step of the V flame mechanism. Even if this step is not the most important, the promotion of the V flame is reduced anyway when the multipoint atomization becomes better.
As α keeps decreasing, the local equivalence ratio of the pilot stage falls below one and this is probably around this region that the internal flame gets no longer visible. The appearance of the strong thermo-acoustic instability near this region might come from a competition for the air between the two stages or from extinction and reignition of the internal flame.

6.4.3 Lifted flame

The third stabilization mechanism to study is the one leading to the lifted flame which was thoroughly studied in chapter 5. As before, key observations are reported in table 6.6.

Table 6.6 – *Key observations on the lifted flame*

#	Observation	Diagnostic	Figure
1	Weak pilot injection	Photography	6.4
2	Spray mostly composed of small droplets	PDA	5.4
3	Spread detached flame	CH^*	5.15
4	Undetectable PVC trace on the flame	CH^*	5.18
5	Low PVC frequency	Internal Mie	5.23
6	Spread PVC frequency	Internal Mie	5.23
7	Air flow not changed	Spray PIV	5.14

As defined previously, three categories can be used to group the observations: the flame (3 and 4), the air flow (5, 6 and 7) and the spray (1 and 2). The analysis of these data is however more straightforward than for the two complex previous cases.
Starting with the air flow observations, they all fit with the fact that the air flow for the lifted flame is really similar to the non reacting flow whether it is seen from the chamber (observation 7) or analyzed through derived means inside the injector (observations 5 and 6). Adding these observations with the droplet size (2) leads to think that the burner behaviour is probably close to one that can be obtained in well premixed gaseous conditions.
Observations 3 and 4 highlight the fact that most of the combustion reaction happens downstream in the chamber and that no anchoring or internal pilot flame can be suspected. This gives even more time for the already small droplets to mix and evaporate before reaching the reaction regions.
Using these observations, a simple stabilization mechanism is proposed in Fig. 6.17.

As stated before, because of the efficient multipoint injection, most of the fuel is well mixed with air and the burner can be considered as working in premixed conditions. These observations can also be made in Large Eddy Simulations based on the operating point studied in Providakis (2013).
In the same reference, it is shown that the measured swirl number inside the chamber is really low, close to 0.3. Using a variable swirler in perfectly premixed gaseous conditions, it is shown in Durox et al. (2013) that for such low values of the swirl number, the flame stabilizes downstream of the injector while it progresses upstream for higher values. Even though the conditions are different,

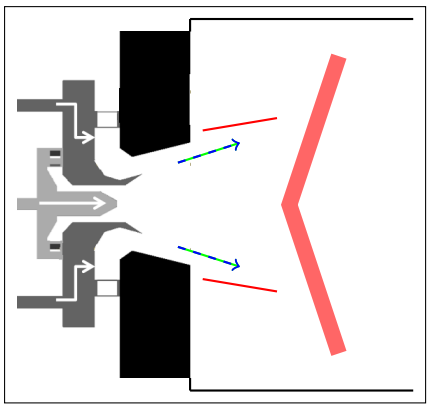

Figure 6.17 – *Stabilization mechanisms for the lifted flame. The blue color corresponds to the air flow, green to the fuel and red to the flame front.*

this provides support to the proposed idea that the lifted flame is close to a classical well premixed flame in relatively low swirl conditions.
The two flame arms that can be seen on the outer parts of the spray must be the result of the thermo-acoustic instability, as shown in Fig. 5.20. They do not seem to play a great role in the flame stabilization. Neither does the ORZ since, in the PCA of the lifted flame, it was shown that its temperature was more related to intrinsic variability than to changes in the operating parameters.

Summary of the chapter

In the present chapter, several phenomena are highlighted, all related to the changes in the burner behaviour as the fuel staging is changed while keeping the other parameters constant.
For high values of α, moderate values of sound pressure level in the chamber are recorded and the flame shows a trace of the PVC in its spontaneous emission. This case is associated with a V flame shape similar to the one studied in pilot-only conditions.
For low values of α in the decreasing direction, the SPL in the chamber remains moderate and no dominant frequency can be extracted from the microphone signal. The trace of the PVC in the flame emission has disappeared and the flame stabilizes with a sV shape. This state remains until α gets really low where an abrupt increase in the chamber SPL can be seen.
When α increases back from almost 0%, the sound pressure level remains high with a well-defined frequency around 330 Hz, showing the existence of a thermo-acoustic instability. The flame presents a lifted shape and its particularity is that it can exist for the same staging values as the sV flame. If however α keeps increasing, the stabilization finally switches back to the sV flame.

The effect of small changes in the global operating point parameters on the three previously highlighted flame stabilization regimes are then studied using Principal Component Analysis based on five representative indicators. All the analyses show the same global effect of changing the equivalence ratio but have also highlighted other phenomena.
For the V flame, the apparent insensitivity of the injector thermocouple to changes in the air flow or power has led to further analysis of its behaviour in the transition region between the sV and V flames.
In the sV flame case, opposite weights along the second axis for the microphone and photomultiplier fluctuations highlight differences in the internal flame behaviour based on equivalence ratio and preheating temperature.
The last PCA, performed on the lifted flame data shows a lot of intrinsic variability, notably coming from the ORZ temperature leading to think that it does not play a great role in the flame stabilization.

Three main transition are observed during the modification of the fuel staging. First, an undefined region corresponds to the switch between the V and sV flames. The second one, being the lift from the sV flame to the lifted flame is well defined by the abrupt increase in the chamber SPL. The third one, the attachment of the flame from the lifted flame back to an sV flame is left for chapter 7.
The transition between the sV and V flames is hard to detect since it is not accompanied by sudden changes. It can however be accompanied by the occurrence of a very strong thermo-acoustic instability that can eventually lead to the flame lift. In stable conditions, the transition corresponds more or less to a continuum that can be related to two major injection modifications. In the decreasing α direction, the multipoint injection first switches from wall dripping to proper jet in crossflow, probably leading to smaller, more easily mixed and vaporized droplets. The second modification that then occurs is the decrease of the local pilot equivalence ratio under the stoichiometry, enabling the internal pilot flame to potentially completely burn independently of the take-off air.
The lift of the flame can be related to the extinction of the internal flame, whether because the pilot fuel injection is reduced to almost zero or because of strong air flow fluctuations (Hardalupas et al. 2000). Using the siren to generate these fluctuations, it is possible to study the transition on time-frequency planes and results show that the modification of the air flow induced by the extinction of the internal flame occurs before the appearance of the lifted flame thermo-acoustic instability.

Finally, from all the data gathered until now, it is possible to propose stabilization mechanisms for the three flame shapes.
The V flame stabilization depends on two step. First, the fuel stratification induced by the centrifugation of the big droplets leads the flame to open. This

diverging shape is then stabilized with the help of changes in the air flow induced by the flame, mostly inside the injector.
The stabilization of the sV flame is based on the same principle but without any fuel stratification. It takes advantage of an already existing flame inside the injector that keeps the air flow on a diverging trajectory. The rest of the fuel can then burn in a well mixed fashion downstream.
To finish, the stabilization process for the lifted flame is much more straightforward and can be related to a well premixed regime with a relatively low swirl, leading to a detached flame.

Chapter 7

Attachment of the flame

The present chapter can be seen as a complement to the previous one. Indeed, its aim is to provide information on the not yet studied transition form the lifted flame to the sV flame in order to close the hysteresis cycle. For this purpose, effects of varying operating point parameters on the transition instant are studied before focusing on the transition event itself, highlighting a particular new flame stabilization. Mechanisms leading to the flame attachment are finally proposed based on global as well as time-resolved data.

In chapter 6, the effects of slowly changing the staging parameter α while keeping other parameters constant were highlighted. A hysteresis cycle with a bistable behaviour between the sV and lifted flames was shown and the transition from the former to the latter flame shapes was studied. It was related to the extinction of an internal flame, leading to the lift of the main flame. It was also shown that, for higher values of the staging parameter, the inverse transition happens and the flame can reattach to the injector. For the design point (43 g/s of air, 72 kW, 160 °C preheating), this attachment seemed to happen around α=20%. This region is thus under scrutiny in the present chapter and the associated parameters are reported in table 7.1.

Table 7.1 – *Attachment operating point definition.*

Global Parameters				
$\dot{m}_{air}$	T_{air}	$\dot{m}_{fuel}$	P	ϕ
($g.s^{-1}$)	(K)	($g.s^{-1}$)	(kW)	(-)
43.1	433	1.64	72	0.6
Staging				
α	$\dot{m}_{fuel,pilot}$	ϕ_{pilot}	$\dot{m}_{fuel,takeoff}$	$\phi_{takeoff}$
(%)	($g.s^{-1}$)	(-)	($g.s^{-1}$)	(-)
≈20	≈0.33	≈0.89	≈1.31	≈0.56

7.1 Transition instant and global observations

To properly study the transition instant, a criterion must be defined. Fortunately, this transition, like the lift of the flame, corresponds to an abrupt change in the chamber sound pressure level (see Fig. 6.1). The transition time can thus be well defined with a precision that can be estimated below ±0.5 s. Because of the small variation of the fuel flow rates during such a time interval, it is possible to associate a particular value of α to this transition instant, called α_t. The precision of the flowmeters (0.2% of the reading) leads to an uncertainty on α_t of ±0.06 points in the present case.

7.1.1 Effect of operating conditions on the attachment instant

During preliminary experiments, it was observed that changes in the global operating point parameters could lead to different behaviours concerning the instant of the flame attachment. Supplemental questions were also raised by the observations made in Providakis (2013) where, as shown before, the behaviour of the burner at a different operating point is similar to the one witnessed in chapter 6 except that no flame attachment ever occurs. All these observations lead to focus on the response of α_t to changes in the global operating point parameters which are the air flow rate, the power and the preheating temperature.
In table 6.2, the parameters for 15 experiments following a Box-Behnken design are presented. The exact same experiments are used here except that no principal component analysis is performed since only one variable is studied: the value of α at the attachment instant, α_t. The goal of the present analysis is to study the changes of α_t near the design point when the global parameters are slightly changed.

For the present purpose, the idea is to obtain a model that can link the variations of α_t to the variations of the three global operating point parameters relatively to their values at the design point shown in table 7.1. With the chosen set of experiments, it is possible to obtain a model for α_t that takes into account some interactions between the parameters as well as quadratic terms. The equation for the model is the following:

$$\begin{aligned}\alpha_t = & \, Constant \\ & + k_1 * \frac{\Delta air}{air_d} + k_2 * \frac{\Delta P}{P_d} + k_3 * \frac{\Delta T}{T_d} \\ & + k_4 * \frac{\Delta air}{air_d}\frac{\Delta P}{P_d} + k_5 * \frac{\Delta air}{air_d}\frac{\Delta T}{T_d} + k_6 * \frac{\Delta P}{P_d}\frac{\Delta T}{T_d} \\ & + k_7 * \left(\frac{\Delta air}{air_d}\right)^2 + k_8 * \left(\frac{\Delta P}{P_d}\right)^2 + k_9 * \left(\frac{\Delta T}{T_d}\right)^2\end{aligned} \tag{7.1}$$

The air flow rate is represented by the variable air, the power by P and the preheating temperature by T. The subscript d stands for the design values.
For such a model, ten values are thus to be determined: the constant and the 9 coefficients k_1 to k_9. As an aside, it can be noted that the value of the constant corresponds to the value of α_t at the design point. In order to determine the ten values, multiple linear regression is used.

A linear regression aims at explaining a set of observations or measurements Y with a predictor variable X. It must be noted here that the two variables do not have the same status: Y is a set of observations and thus of random variables while the values of X are fixed. The goal is to determine the best values for the coefficients a and b such that $Y \approx a + b * X$. The most common way for this is through the least square method which consists in finding the values of a and b that minimize the sum of the squared residuals between Y and $a+b*X$. However, as stated before, each element of Y is a random variable and the computed values for a and b may just come from a sampling effect. This corresponds to a problem of statistical estimation and a measure of confidence thus needs to be obtained.
For this purpose, an hypothesis is made on the probability law of the observations Y_i that make the set Y. Each of them is supposed to come from the drawing of one sample from a normal law of expectation $a + b * X_i$ and of variance σ^2 that is the same for all the Y_i. This is equivalent to saying that the residuals follow a normal law of expectation 0 and variance σ^2. It is possible to estimate σ^2 from the dataset and, thanks to the normal law assumption, to obtain the probability laws for the estimators of a and b. It is then straightforward to compute 95% confidence intervals for the linear regression coefficients.
In the present case, where several predictor variables are used, the calculations are more complex but the original idea is the same and further information can be found in Draper and Smith (1981). The linear regression coefficients for the present model can be found in Fig. 7.1.

The values of the coefficients k_1 to k_9 are scaled down to be represented on the same graph as the constant in Fig. 7.1. This scaling is performed so that the values represented on the graph correspond to the changes in α_t observed when the variables $\frac{\Delta air}{air_d}$, $\frac{\Delta P}{P_d}$ and $\frac{\Delta T}{T_d}$ see a 10% change. The graph can thus directly be used to quickly compute values of α_t as will be shown later.
At the design point, the value of α_t corresponds to the constant which, in the present case, has a value of 18.9% with a confidence interval corresponding to $\pm$5.6 points. This value is coherent with the observations in chapter 6, where the attachment of the flame was seen to happen around α=19%.
As stated, quick computations of α_t for 10% deviations from the design point can be directly performed using the values in Fig. 7.1. For example, a 10% increase in the air flow rate while keeping the other two parameters constant lead to a value of α_t that can be computed by adding the constant, the value

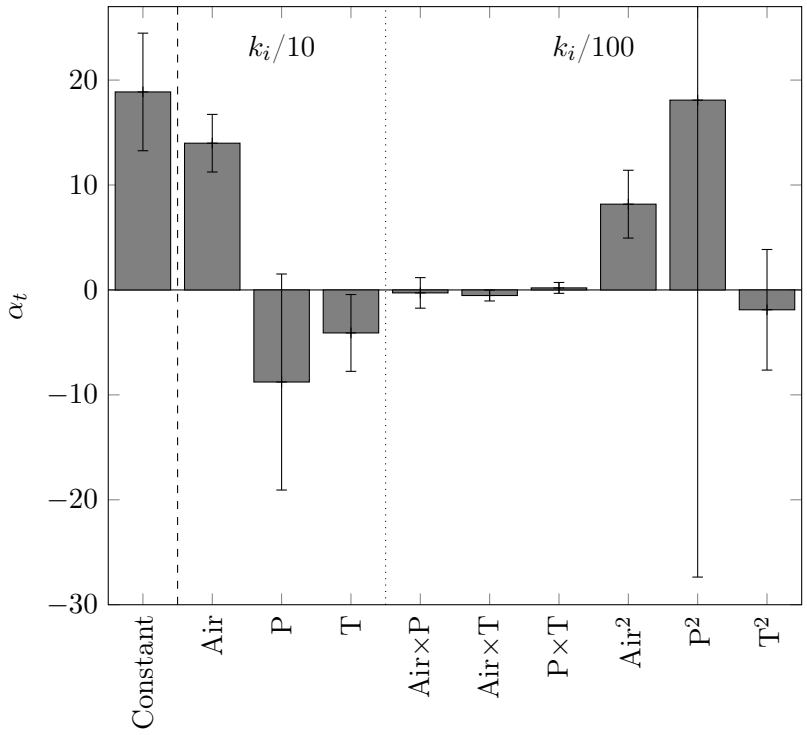

Figure 7.1 – *Coefficients for the model in equation 7.1. The horizontal axis labels show the name of the variable each coefficient is related to. Except for the constant, the values have been scaled down to fit in the same graph and correspond to a 10% variation of the variables.*

with the label Air and the value with the label Air^2. The estimation for α_t from this reading gives a result of 41%. Similarly, the value for a reduction of 10% in the air flow is obtained by adding the constant and the value for Air^2 while removing the value for Air and gives an estimation of $\alpha_t \approx$13%. Knowing that the value of α_t at the design point is around 19%, this highlights the fact that the effect of changes in the air flow rate seems to be strongly non linear.

The previous quick computations rely only on the estimated values of the correlation coefficients. The trust one can put in the results however depends on the size of the confidence intervals. Since it can be seen that they can get very wide, a quantitative study is complicated but the analysis of the signs of the coefficients can still provide interesting insight. The large size of the confidence intervals comes from the trade-off between the number of experiments and the expected precision made when choosing the Box-Behnken experimental design instead of heavier matrices like a factorial design.
For changes in the air flow rate, the confidence intervals of the associated coefficients do not cross 0 and are quite narrow, meaning that the signs of the coefficients can be trusted as well as the values, to a certain extent. The results

of the quick computations performed previously thus seem valid.
The situation is different for the coefficients associated with changes in the power of the burner. Indeed, all the confidence intervals cross 0 so no sure information on the sign of the coefficients can be extracted. This is an effect of the narrow limits for the experiments, where the variations of the power relatively to the design point are smaller than the ones of the air flow rate or the temperature. These limitations were provided by safety concerns (high power) and lean blow-off limits (low power) so they could not be avoided. However, since the upper limit of the confidence interval for the linear effect of $\frac{\Delta P}{P_d}$ is quite close to 0, it can be considered likely that the associated coefficient is negative but with a lower confidence than 95%.
From the preheating temperature point of view, the linear effect is negative but lower in intensity than the linear effect of the air flow. The quadratic effect is small and the associated confidence interval is such that it is likely less important than the quadratic effect of the air. From these data, it seems that increasing the preheating temperature compared to the design point leads to an earlier attachment of the flame, with an almost linear negative effect on α_t.
Finally, the values of the coefficients for the linear interaction terms are also interesting. They are really small compared to the quadratic effect of the air and with very narrow confidence intervals. The only confidence interval that does not cross 0 is the one associated with the interaction between the air flow rate and the preheating temperature. This seems to indicate a small but real effect. However, its amplitude is so small that it can be considered almost negligible, especially in front of the quadratic effect of the air (which is 16 times higher).

When studying combustion phenomena, the equivalence ratio is often a parameter of choice and the variations of α_t observed here for the changes of the air flow rate or the power (which is proportional to the fuel flow rate) may just result from changes in the equivalence ratio.
Indeed, the global equivalence ratio is proportional to the ratio of power over air and, in Fig. 7.1, equal and opposite values for the linear effects of power and air cannot be ruled out because of the sizes of the confidence intervals. In order to go further into this analysis, it is needed to check how variations of the equivalence ratio ϕ can be translated into variations of air flow rate and power. For this purpose, the quantity $\frac{\Delta\phi}{\phi_d}$ can be written as a function of $\frac{\Delta air}{air_d}$ and $\frac{\Delta P}{P_d}$. Since only variations near the design point are required, a Taylor expansion is used to link the expression with the model presented in equation 7.1. It yields:

$$\frac{\Delta\phi}{\phi_d} = -\frac{\Delta air}{air_d} + \frac{\Delta P}{P_d} - \frac{\Delta air}{air_d}\frac{\Delta P}{P_d} + \left(\frac{\Delta air}{air_d}\right)^2 + O\left(\left(\frac{\Delta air}{air_d}\right)^3\right) \quad (7.2)$$

From this equation, it can be seen that an impact of the equivalence ratio would translate into impacts of the linear terms for the air flow rate and the power, of the interaction term and of the quadratic term for the air flow rate. A linear

effect of ϕ would thus be detected by equivalent values for all the previously cited coefficients. This is not the case in Fig. 7.1 and furthermore, the signs of the linear and quadratic terms for the air flow rate are not different. This does not allow to dismiss any effect of the global equivalence ratio on α_t but it shows at least that the changes in the air flow rate also have their own effect on the attachment instant.

The model used here has thus enabled to gain insight on the effect the global operating point parameters can have on the transition instant. Its results will also be used later when studying the mechanisms for this transition.
As an illustration, it can be interesting to compute the value of α_t predicted by the model for the operating point used in Providakis (2013): 54 g/s of air, 90 kW and 200°C of preheating. This of course corresponds to an extrapolation of the model and leads to a huge uncertainty that cannot give any beginning of trust to the result. Nevertheless, the predicted value would be α_t=170% which is coherent with the fact that no attachment of the flame is observed in these conditions. Once again, no credit can be given to this observation and it is just presented here for illustrative purposes.

7.1.2 Observations on the flame shape

As stated previously, the instant of the transition is defined as the moment when the sound pressure level in the chamber brutally decays. To perform a study on the attachment event, 37 experiments at this particular region of the design point have been performed. They all show values for α_t between 17.2% and 21.5% which is well inside the confidence interval for the constant in Fig. 7.1. It must furthermore be noted that, since the preheating temperature is not controlled in a closed-loop fashion, it slightly depends on the original air temperature. The 37 experiments having been performed over 8 months, they show preheating temperature values between 157 and 164°C.
Thanks to a monitoring video camera, the flame shape can be observed before and after the transition instant. The images are shown in Fig. 7.2.

Half a second before the transition is detected by the chamber microphone, it can be seen in Fig. 7.2 that the flame is in the lifted state. This is expected from the analysis in chapter 6. Similarly, a few seconds after the drop in the chamber sound pressure level (on the right of Fig. 7.2), the flame takes the expected sV shape.
The situation becomes however more complicated if one looks at the flame shape relatively closely to the transition event (in the middle of Fig. 7.2). It can indeed be seen that the flame can exist in two states. The expected sV flame can be recognized at the bottom while a new flame shape can be identified at the top. Because of its shape, it is called the tulip flame and it is thoroughly

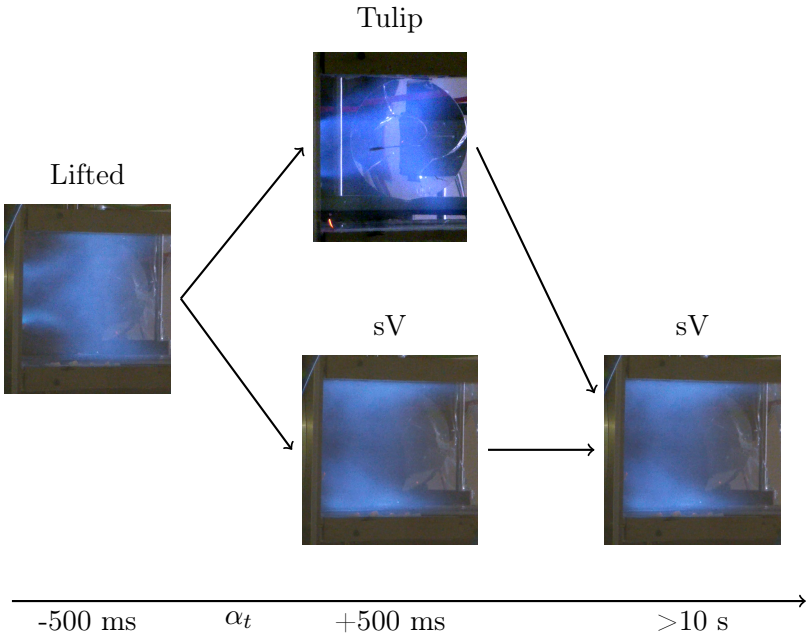

Figure 7.2 – *Visualizations of the flame before and at two instants after the transition.*

studied in the next section of this chapter. This tulip flame does not however live for a long time and ends up switching to a sV flame in just a few seconds. In the 37 realised experiments, the tulip shape has been witnessed 17 times while the remaining 20 experiments showed the sV flame shortly after the transition. This gives a measured proportion of 46% of tulip flames. This proportion can also be seen as an estimation of the tulip flame appearance probability computed from 37 samples. It is thus possible to compute a 95% confidence interval for this proportion using the normal distribution since the sample can be considered big enough (Poinsot 2004). The result is that one can expect the probability of appearance of a tulip flame to be between 30 and 62% in the present conditions.
The remaining parts of the chapter focus on these observations, first by studying the tulip flame itself and then by looking in details into the progress of the transition event.

7.2 Study of the tulip flame

As shown in Fig. 7.2, the flame can take a tulip shape just after the transition event. The purpose of this section is to study this particular stabilization with the same processes used for the study of the steady states in chapters 4 and 5. Similar diagnostics are thus used but they are limited by the randomness and the transient nature of the tulip state. This for example prevents the use of

the PDA since about 10 s are required for each measurement point. The Mie scattering and CH* chemiluminescence imaging techniques can however still be used because of their high speed characteristics. The tulip flame is recorded for 550 ms. This is long enough to obtain well converged statistics.

7.2.1 Mean behaviour

In this section, the global behaviour of the spray and the flame in the tulip shape is presented, leaving the dynamical features aside. It follows the same workflow as in chapters 4 and 5 to allow for easier comparisons. There are however some small variations on the diagnostics (field of view, frame rate) because they were also used to study the transient event that is the flame attachment. The acquisition parameters for the Mie scattering recording of the tulip state studied here are reported in table 7.2.

Table 7.2 – *Acquisition parameters for the tomographic Mie scattering measurements.*

Acquisition frequency (kHz)	2×10
Delay between laser pulses (µs)	20
Image size (pixels)	704×520
Equivalent field of view (mm)	112×83
Number of images	11000
Recording length (s)	0.55

As stated above, the parameters are set primarily to focus on the transition event but the recording duration (over 1.5 s for the whole transition event) allows to gather information on a steady tulip flame for more than half a second. The recording mode is set so that the operator indicates the end of the recording rather than its beginning. It is thus possible to stop the acquisition once the change in the chamber sound pressure level is heard. Because of the delay mainly induced by the human reaction time, the images near the end of the recording correspond to an attached flame (either tulip or sV). The Mie scattering data used in the present case are taken from the longest sequence with a tulip flame. After removing the uncertainty region just after the transition, this gives a recording duration of 550 ms.
Using these data, the RMS image of the Mie scattering signal is first presented in Fig. 7.3.

As explained in chapter 4, using a RMS image is well suited to highlight the average spray shape from Mie scattering recordings. Usually, interesting information can be drawn from the comparison between the non-reacting and reacting sprays. Here however, since the staging at the transition instant is not fixed, no clear correspondence can be made. Still, since α_t at the design point is

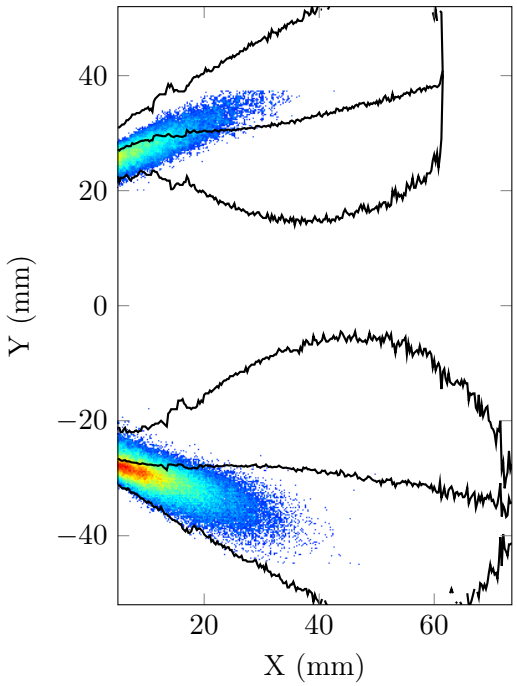

Figure 7.3 – *RMS image of Mie scattering intensity in the tulip flame case. A threshold has been set at 15% of the maximum value to highlight the shape of the spray. The black lines represent the spray limits from the non-reacting Mie scattering RMS image (Fig.5.1).*

roughly under 20%, the non-reacting spray from the measurements of chapter 5 at α=15% is used here for comparison.
It can be seen in Fig. 7.3 that the spray in reacting conditions appears similar to the non-reacting one close to the injector but does not propagate as much in the chamber (around X=30 mm) and doest not spread. This is an effect of the improved vaporization of the droplets due to the flame. Fruitful comparisons can also be drawn with Fig. 5.7 and 5.13 in chapter 5. Indeed, since the attachment region corresponds to the potential existence of the lifted flame and the sV flame also, it is interesting to compare their respective sprays with the tulip one.
In Fig. 5.7, the spray for the sV flame is shown and is characterized by a thin diverging shape (along the external limits of the non-reacting spray) with a relatively strong penetration (up to X=40 mm). The spray shown in Fig. 7.3 seems however only slightly diverging and disappears quite quickly. There is thus no obvious link between the sV and the tulip spray shapes.
The situation is rather different when comparing with the lifted flame spray in Fig. 5.13. This image indeed shows a not really diverging spray and, even though some signal can be detected past X=40 mm, the bulk signal stops before X=35 mm. This seems similar to the present image in Fig. 7.3 even

though one strong discrepancy remains: the lifted flame spray seems broader than the tulip one. This can probably be associated with the thermo-acoustic instability occurring in the lifted state that smears the average data as explained in chapter 5.
The spray average shapes seem to link the tulip flame with the lifted one but further information is needed to validate this. For this purpose, the average velocity fields obtained from spray PIV are shown in Fig. 7.4.

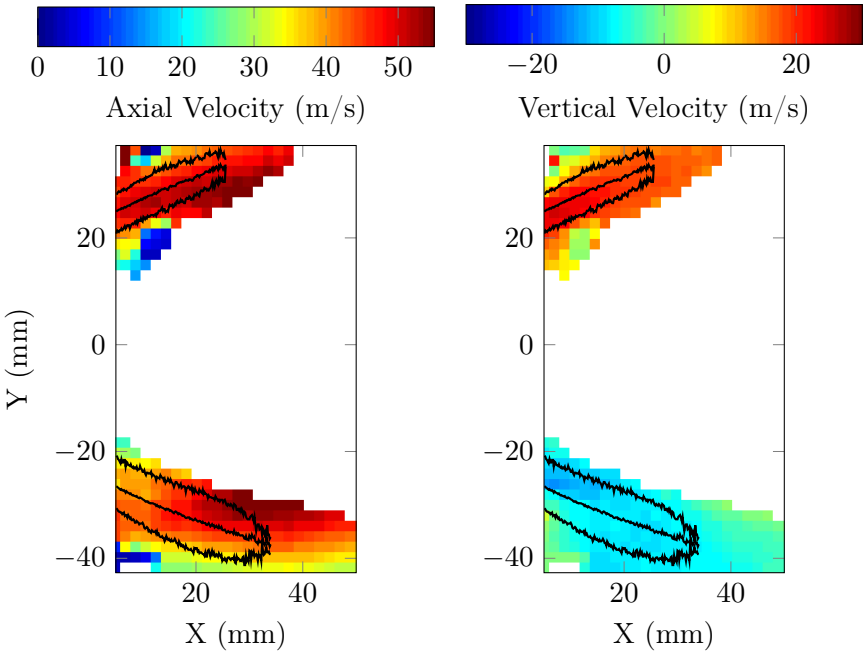

Figure 7.4 – *Mean axial (left) and vertical (right) spray velocities from the PIV treatment of the tulip Mie scattering fields. A threshold has been set at 2% of vector validation. The black lines represent the spray limits from the Mie scattering RMS image (Fig.7.3).*

In the previous studies, the velocity fields are computed using 20×20 pixels interrogation windows with 60% overlap. Here, because of the slightly different parameters used for the acquisition, the pixel pitch is not the same. The choice is made to keep the physical size of the interrogation windows constant over all the PIV treatments and thus keep a comparable number of droplets in the windows. In the present case, this corresponds to using 31×31 pixels interrogation windows with 60% overlap and the usual 2% validation threshold is used.
The PIV results are here again interesting to compare with the sV and lifted flame cases in Fig. 5.8 and 5.14 respectively. First the comparison with the sV flame shows that the general behaviour in the tulip state is not as divergent, with vertical velocities slightly over ±15 m/s rather than ±25 m/s. This

seems to provide further ground to what was seen from the spray images. The comparison with the lifted flame velocity fields shows that the velocity fields are very similar from the vertical velocity point of view. In the axial direction, the velocity component seems a bit higher in the tulip case but an interesting information on the jet shape can be obtained from the bottom part of the axial velocity field for the tulip shape in Fig. 7.4. It seems to show that the jet has almost no divergent behaviour and it is really similar to the shape observed in the lifted flame axial velocity field.
The analysis of the average spray velocity fields (which can be considered close to the air flow velocity fields because of the small average droplet size for the low staging values) confirms that the tulip flame can be linked to the lifted flame from this point of view. The main difference lies in the thermo-acoustic instability which is not present here. In Fig. 7.2, it however looks like the lifted flame and the tulip flame shapes are finally different. For flame observation, CH^* chemiluminescence is used in the previous chapters. Here, the parameters for this diagnostic are also different because of the need to observe the transition event. They are reported in table 7.3.

Table 7.3 – *Acquisition parameters for the CH^* chemiluminescence measurements.*

Acquisition frequency (kHz)	20
Image size (pixels)	640×640
Equivalent field of view (mm)	149×149
Number of images	11000
Recording length (s)	0.55

The same causes being responsible for the same effects, only the last parts of the chemiluminescence recordings can be used. In the present case, CH^* chemiluminescence is recorded simultaneously to Mie scattering and the data used here thus come from the same experiment that gave Fig. 7.3 and 7.4. This leads to the same 550 ms recording length in the tulip state. The most noticeable difference with the CH^* chemiluminescence setup used in chapters 4 and 5 is the increase of the acquisition frequency to 20 kHz. This allows for a better temporal resolution of the transition phenomenon but does not impact the rest of the treatments and the signal-to-noise ratio of the instantaneous images remains high enough thanks to the intensifier.
Using these parameters, the shape of the tulip flame can be more closely monitored and is presented in Fig. 7.5.

The background signal of the CH^* chemiluminescence images is removed from the instantaneous snapshot which are then averaged before being deconvoluted with an inverse Abel transform to get rid of the line of sight integration. The contours of the spray are superimposed to the resulting image in Fig. 7.5.

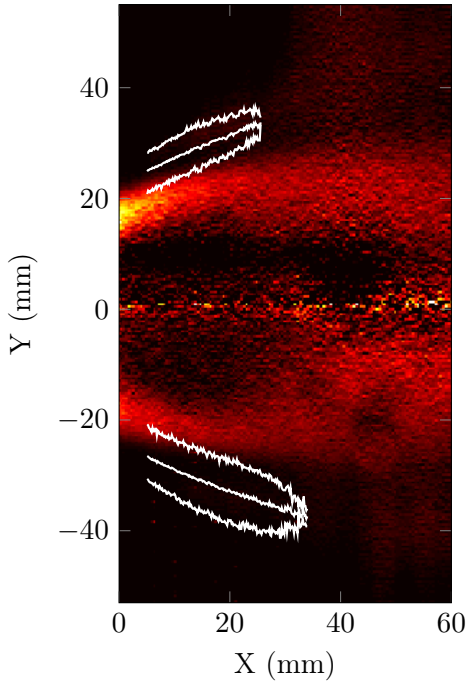

Figure 7.5 – *Abel-inverted mean CH* chemiluminescence image for the tulip flame. The white lines represent the spray limits from the Mie scattering RMS image (Fig.7.3).*

From the study of the spray, it is shown that the tulip flame can be related to the lifted state. The information provided by the chemiluminescence average image is however very different. Indeed, the flame is placed inside the spray and seems anchored inside the injector, two characteristics that can be associated with the sV and V flames. There is however a visible discrepancy with these flames: the tulip flame does not open up downstream and keeps its non-diverging behaviour.
The study of the average states of the spray and the flame thus bring seemingly contradictory information. From the air flow and spray point of view, the tulip flame corresponds to the lifted state (thermo-acoustic instability aside) whereas considering the flame itself, a parallel can be drawn with the attached states. Studying the dynamics of this particular state can bring more information on this apparent opposition.

7.2.2 Dynamics of the tulip spray and flame

Keeping the same procedures used in chapters 4 and 5, it is possible to study the dynamics of the tulip state. As usual, focus will be put on the trace of the PVC. The results for Mie scattering can be seen in Fig. 7.6.

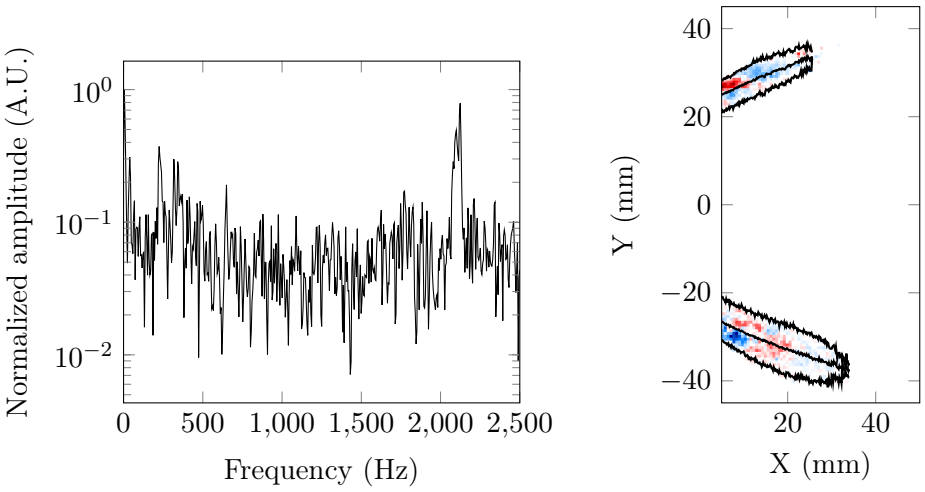

Figure 7.6 – *Power spectral density from a region of interest in the Mie scattering images (left) and DMD mode at the peak frequency (right) for the tulip flame. Positive Mie scattering fluctuations are in red and negative ones in blue. The black lines represent the spray limits from the Mie scattering RMS image (Fig.7.3).*

In the previous chapters, the dynamics of the spray are first studied using a 30×30 pixels averaging window placed at X=5 mm and Y=-25 mm and computing a spectrum for the obtained signal. Here, as mentioned before the PIV processing of the Mie scattering images, the pixel pitch is not the same so the physical size of the averaging window is conserved and a 46×46 pixels window is used. The signal is then processed as usual with a Welch's periodogram method based on 0.25 s long Hamming windows with 50% overlap. The resulting spectrum is shown on the left of Fig. 7.6.

From an average point of view, it was shown that the tulip flame spray could be associated with the lifted flame one. Here, no trace of a thermo-acoustic instability can be highlighted, on the contrary to Fig. 5.16 which represents the dynamics of the lifted flame spray. A peak can however be seen slightly after 2000 Hz, corresponding to the trace of the PVC. This is similar to the sV flame case in Fig. 5.10, even though the two states are different from an average point of view. The DMD mode associated with the peak frequency can be seen on the right of Fig. 7.6.

Following the previously established methods, a DMD is performed on 500 images of the Mie scattering recording to obtain the represented mode. The mode corresponds to the expected antisymmetrical response of the spray to the PVC but the structure seems quite noisy. At first, one would like to relate this to the weak pilot injection. In Fig. 5.10, in the sV flame case, the pilot injection is even weaker but the structure is more marked. This difference can probably be explained by the average observations. Indeed, in the sV flame case, the spray is more confined than in the tulip case and, because of this, the PVC trace may

be less damped.
The fluctuations of the flame spray can have an impact on the flame dynamics and, to verify this, dynamical features extracted from the CH* chemiluminescence data are shown in Fig. 7.7.

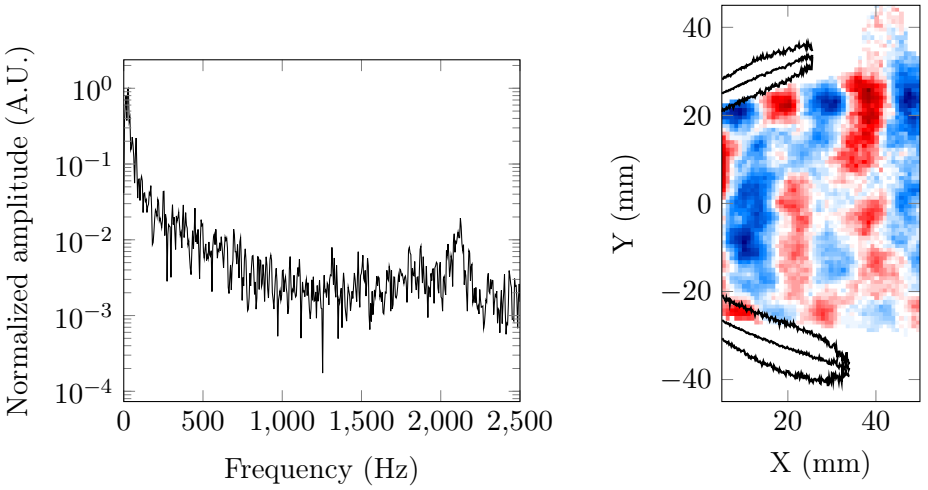

Figure 7.7 – *Power spectral density from a region of interest in the CH* chemiluminescence images (left) and DMD mode at the peak frequency (right) in the tulip flame case. Positive CH* fluctuations are in red and negative ones in blue. The black lines represent the spray limits from the Mie scattering RMS image (Fig.7.3).*

For the CH* chemiluminescence images, no change in the averaging window is needed and the usual 30×30 pixels region placed at X=5 mm and Y=20 mm is used to compute the spectrum shown on the left of Fig. 7.7. A peak region can be seen above 2000 Hz but it does not seem well defined, especially when comparing the spectrum to the sV flame one in Fig. 5.11.
The DMD mode (based on 500 samples) traced on the right of Fig. 7.7 shows however a clear structure at the PVC frequency. Such a structure could not be identified in the sV flame case, probably because of its dual flame characteristic. Indeed, the main flame in the sV case is fueled by the multipoint injection while the internal flame uses the pilot fuel. This explains why no trace of the PVC can be detected in the main flame but only close to the injection in the sV case. For the present tulip flame, the fact that a trace of the PVC can be detected in the global flame chemiluminescence means that both the multipoint and the pilot injections probably participate in its feeding.
In chapters 4 and 5, a third way of analysing the dynamics with the help of internal Mie scattering visualizations is used. It allows to monitor the PVC frequency and its spread in each state. This provides information on the air flow inside the injector which is not accessible by other means. Histograms of the PVC frequency can be seen in Fig. 7.8.

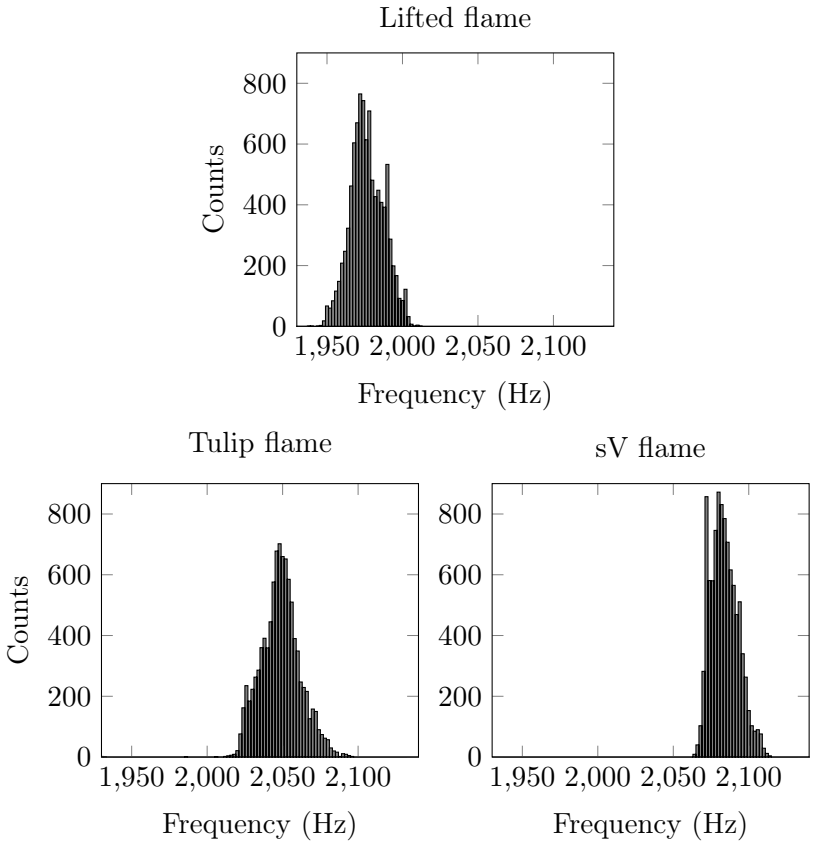

Figure 7.8 – *Histograms of the PVC frequency before (top) and after the transition (bottom).*

A few flame attachment experiments have been performed while recording the internal Mie scattering signal with the parameters defined in chapter 4. After averaging through a 30×30 pixels interrogation window, continuous wavelet analysis is performed on the resulting signal and histograms of the PVC frequency can be traced. The full processing procedure is explained at the end of chapter 4. In the present case, a few modifications are to be highlighted because the recordings come from the transition event and are thus not steady.
Since the main interest of the processing comes from precise comparisons between the states, it is preferable to obtain data in conditions that are as similar as possible. Using the data obtained in chapter 5 again is thus not recommended. It is fortunately possible to use the parts recorded just before and after the transition as it is done for the study of the tulip flame. This way, the data for the lifted flame (just before the transition) and the sV and the tulip flame (just after the transition) are recorded under similar conditions. They however cannot come from the exact same experiment since, just after the transition, the flame is either a sV or a tulip.

The histograms obtained from these three parts correspond to 9709 frequency values each. For the lifted and sV flames, the results have been compared with other similar recordings (4 for the lifted flame and 3 for the sV) to verify that no reproducibility issue happens but, because of its random nature, only one of the transitions recorded with the internal visualization led to a tulip flame and it is the one presented here. In spite of these precautions, it is thus necessary to remain careful about the conclusions of this analysis.

It is first interesting to compare the lifted and sV flame results presented here to the ones obtained in perfectly steady conditions in Fig. 5.23. For the lifted flame, a good agreement can be observed both in terms of average frequency (around 1975 Hz) and in spread. For the sV flame case, while the average frequency is higher (above 2075 Hz), the frequency distribution is similar.
This increase in the frequency of a few percents can be explained by the fact that, during the transient operation leading to the transition, the pilot and take-off fuel flowmeters do not exactly respond with the same delay. More precisely, the pilot fuel controller is faster to increase than the take-off one is to decrease. This leads to a power during transient operation that is slightly higher than in steady conditions (less than 2% higher). Since the increase in the PVC frequency in the injector in the sV case compared to the lifted case is probably due to the heating created by the internal flame, a similar phenomenon can explain why the PVC frequency in the post-transition sV flame (with a higher power and so a higher flame heat release) is slightly higher than in the steady sV flame case. This effect remains however low and does not seem to play a great role in the global study.
From the tulip flame point of view, it is interesting to see that its situation seems to be in between the two previously studied cases. From the sV flame, the tulip retains the higher average frequency whereas the lifted flame seems to give it the spread aspect. This remains coherent with the observations made in the present section where the tulip flame shows the average flow characteristics of the lifted flame with the dynamics of the sV flame. Indeed, the increase in PVC frequency can be explained by the fact that the tulip flame is anchored and that there is thus a reaction zone inside the injector, heating the air and increasing the PVC frequency. On the opposite side, the spread of the frequency links the tulip shape to an undisturbed flow field, as the one observed in the lifted flame case.

Since several observations have been made on the tulip state, it is better to sum them up before going on. The tulip flame is anchored inside the injector but does not show a divergent shape like the other attached states (sV and V flames). This particular shape can probably be linked to the average flow field which seems really close to the lifted (and by extension non-reacting) one. Interestingly, the observations made on the PVC lead to think that a reaction zone is actually installed inside the injector but it does not lead to the flow

widening and spray confinement associated with the other two attached states. Everything thus looks like the tulip is a kind of transitional state and this proposition seems confirmed by the fact that all the tulip flames eventually widen into sV flames.

7.3 Progress of the transition event

Since the steady (or quasi steady) flame stabilization modes before and after the transition are well defined, it is now possible to look into the flame attachment itself. For this purpose, the evolution of the flame shape during the transition is first presented and the phenomena piloting this evolution are then thoroughly detailed.

7.3.1 Flame shape during the transition

In the previous sections, the transition instant is detected by the abrupt decrease of the sound pressure level in the chamber. As stated before this however leads to a temporal uncertainty which is low compared to the flowmeters reaction time (hence its use to compute α_t) but high when compared to the flow time scales. A better precision is thus needed to properly detect the transition instant.
For this purpose, and since the attachment is strongly linked with drastic changes in the flame shape, the use of the available time-resolved CH^* recordings seems well suited. A way to associate the instantaneous flame shape with one of the three previously highlighted states is thus needed and the transition instant then corresponds to the switch between two states. For the association purpose, the idea is to compute a 2D correlation value between an instantaneous flame image and the average images for each of the state. The instantaneous flame shape is then associated to the state it correlates the best with.
As explained previously, when a transition is recorded, the beginning and the end of the film correspond to quasi steady states of the lifted (for the beginning) and tulip or sV flames (for the end). The average images for the three states are computed using these parts of the recordings for all the transitions recorded with the CH^* chemiluminescence camera (9 transitions, 5 leading to a tulip and 4 to a sV flame). The average images that are used as references for the correlation operation are thus in fact averages (along the experiments) of temporal averages. This way, they represent the most canonical versions of their respective states.
The correlation operation is then performed on all the transition recordings. For all the transitions leading to a tulip flame, the transition detection works well and no particular issue is noticeable. The situation is however different when one looks at the correlation coefficients for a transition leading to a sV flame. A typical graph for this kind of transition is presented in Fig. 7.9.

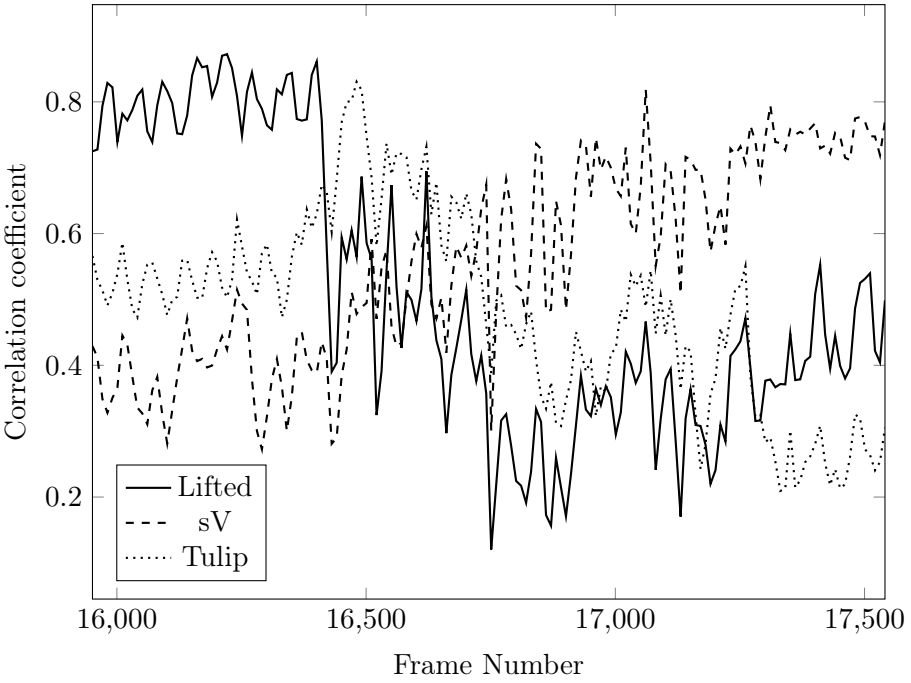

Figure 7.9 – *Value of the three correlation coefficients during a transition leading to a sV flame. The frame rate is 20 kHz.*

The frame rate for the chemiluminescence measurements is 20 kHz so the horizontal axis in Fig. 7.9 can be directly linked to time values and the data shown here thus spans 80 ms. The vertical axis corresponds to the value of the correlation coefficient with the three average images representing the three steady states.
In the beginning of the graph, for frame numbers around 16000, the correlation coefficient of each instantaneous frame with the lifted flame is higher than with the other two states. This means that the transition has not occurred yet and the flame is indeed in the lifted state. As an aside, it is interesting to note that the oscillations observed in the blue curve correspond roughly to the thermo-acoustic instability period.
In the other side of the graph, for frame numbers between 17000 and 17500, the instantaneous flame image correlates the best with the sV flame. It is expected since this particular transition ends with a sV flame.
The most interesting part of Fig. 7.9 actually lies in the middle of the graph. While it is expected that the transition can be detected by a fast switch between the lifted flame and the sV flame, it can be seen that the instantaneous flame image shows a good correlation with the tulip flame in between. This means that even when the attachment ends with a sV flame, it briefly goes through a tulip state.

The previous observation provides a new way of looking at the transition. Instead of seeing two different events, one leading to a sV flame and the other to a tulip one that eventually widens, what is witnessed is actually a two-step event. First, from the lifted state, the flame systematically attaches itself inside the injector with a tulip shape. It is this first step that can be associated with the decrease in the burner sound pressure level. Then, from this tulip state, the flame widens into a sV flame more or less rapidly. It is the variability of the time scales for this second step that creates the illusion of seeing two different phenomena. The rest of this section aims at studying these two steps, starting with the first one.

7.3.2 First step of the transition: anchoring

The first step of the transition corresponds to the anchoring of the flame with a tulip shape. It can be detected by the switch from the dominant solid curve to the dominant dotted curve in Fig. 7.9. In this graph, this seems to happen in the order of a few milliseconds. It is interesting to note that this first step can be studied independently of the second one. Indeed, whether the tulip flame then widens quickly or slowly into a sV flame, the flame anchoring is always the same. For its study, the high-speed of the chemiluminescence recording is required since it enables to freeze the flame motion. It is then possible to understand the phenomena leading to the flame anchoring by looking at the instantaneous images. Some of them are presented in Fig. 7.10.

For visualization purposes, the instantaneous chemiluminescence images are inverted meaning that black corresponds to high intensities and white to no signal with shades of gray in between. Time stamps with an arbitrary origin are added above the images to monitor the duration of the phenomena.
The first and the last images can be easily explained. The first one is clearly related to the lifted flame with no reaction occurring in the beginning of the chamber and most of the combustion located after X=60 mm. The last image seems a bit more complex at first since the downstream reaction zone remaining from the lifted flame is still present. The key element is however the fact that the flame is also present in the upstream part of the chamber and that it seems to propagate downstream without diverging. The instantaneous image can thus be related to the tulip flame, as expected.
The top row of Fig. 7.10 corresponds to the propagation of the flame from the main reaction zone to the injector. Indeed, in the center of the chamber for images 2 to 4, a finger-like structure moving upstream can be observed. This corresponds to a flashback, probably happening inside the IRZ. Indeed, between the second and the third image, it can be seen that the tip of the structure gains roughly 10 mm towards the injector. Knowing that the two images are separated by 0.5 ms, this gives a propagation velocity around 20 m/s which corresponds to the order of magnitude of the reverse axial velocities in the IRZ (Fig. 5.3).

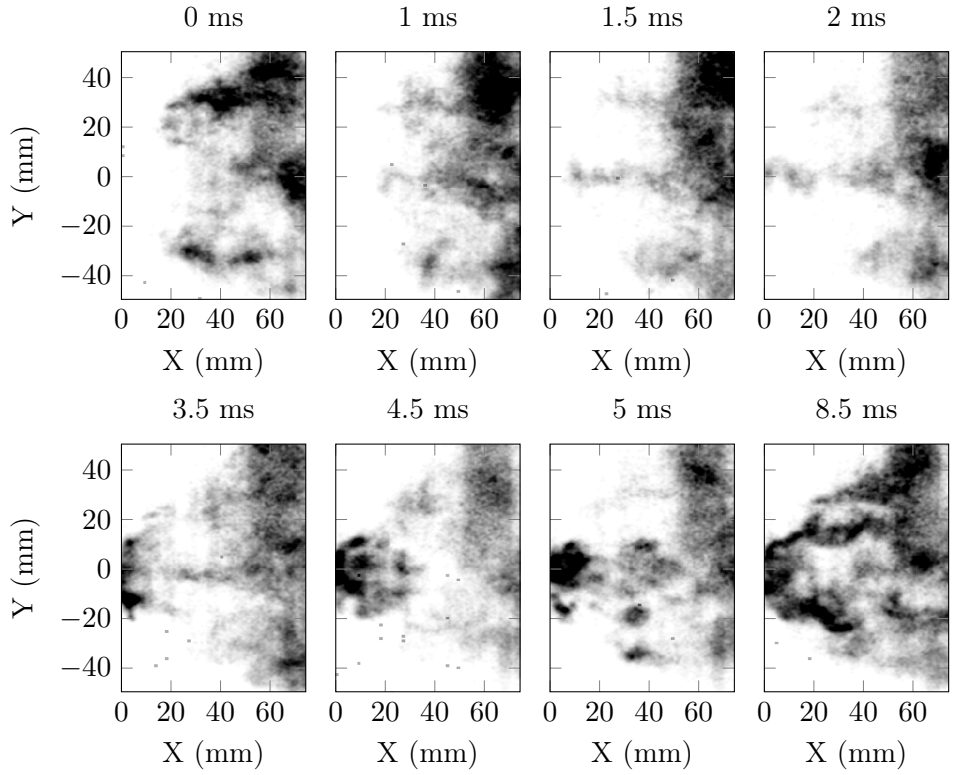

Figure 7.10 – *Instantaneous CH* chemiluminescence images at different instants during the first step of the transition, between lifted and tulip shapes.*

After this flashback step, the flame has reached the inside of the injector. Then nothing seems to happen for about 1 ms and the images look like the first one showing a lifted flame. During this period, things are however probably happening inside the injector, namely the internal flame ignition and anchoring. Interestingly this period can result in a failure of the transition and nothing happens until another flashback occurs. Key mechanisms are thus probably at stake inside the injector but are unfortunately hidden.
Finally, if this hidden step is successful, what is seen is shown on the bottom row of Fig. 7.10. The flame appears from the inside of the injector in the beginning of the chamber as shown on the fifth image. It then propagates downstream, corresponding to the new possibility for the flame to consume the fuel spray from the inside. This motion ends up giving the expected tulip flame and the first step of the transition is over.

This first step is thus strongly dependent on two phenomena: a flashback to bring the flame in the injector and the success of the ignition inside the injector. As explained in the introduction, flashback can have multiple causes. In lean premixed cases, the combustion induced vortex breakdown (Kröner et al. 2007)

is a dominant cause of flashback. This is however not what happens here since the IRZ already exists and is not created by the flame as it propagates. This particular flashback thus seems to correspond to a classical flame propagation in a reverse velocity zone.
For this flame propagation to happen, a combustible mixture needs to be found in the recirculation zone. It is probably provided by the increase in the pilot fuel injection. In Fig. 7.1, it is seen that small increases in the burner power and preheating temperature tend to decrease the value of α_t meaning that the transition happens earlier than for the design point. This can be linked to the propensity towards flashback. Indeed, an increase in the burner power means more fuel to burn and an increase in the preheating temperature means that the liquid fuel is more easily vaporised and that the flame speed is increased. These effects are obvious promoters for the flashback.
From the observations, it is however remarked that another strong cause of the non-occurrence of the transition is the failure of the ignition inside the injector even though the flashback has happened. This step is unfortunately impossible to monitor but interesting information can be drawn from the study of α_t in Fig. 7.1. Indeed, the effect of air is clearly non-linear and increasing the air flow prevents the transition from happening. In ignition studies, it is often seen that increasing the turbulence or the stretch rate is deterrent to the flame ignition probability (Griskey and Archer 1965; Ahmed 2014). A similar effect can be suspected here, where the increase of the air flow prevents the appearance of a flame inside the injector.

7.3.3 Second step of the transition: flame widening

In Fig. 7.2, a distinction is made between the transitions based on the flame shape after 500 ms. Even though it now seems artificial, this separation has practical roots. Indeed, 500 ms corresponds roughly to the duration of the camera recordings after the transition. It is thus impossible to clearly monitor the flame shape afterwards. The transitions giving a sV flame before 500 ms are called "early widening" while the rest is called "late widening". Out of the 37 performed experiments, there are thus 20 early widening cases and 17 late widening cases.

A key point to understand the second step of the transition lies in measuring the delay between the first step and the widening. This corresponds to the lifetime of the flame in the tulip shape.
The way of measuring this lifetime depends on the studied population. For the early widening, the flame shape during the experiments is filmed, either with the previously presented CH^* chemiluminescence setup or with a high-speed camera at 5 kHz without any filter. In the CH^* case, Fig. 7.9 shows that it is possible to monitor the flame shape with a precision below a few milliseconds by taking the highest correlation coefficient. For the other cases of early widening,

the same procedure is used and the flame shape can be defined with a similar precision. The tulip lifetime can thus be relatively accurately monitored for the 20 early widening cases.
The situation is however very different for the late widening population. Indeed, no recording of the flame shape exists after 500 ms and it is thus impossible to use the correlation technique. To overcome this drawback, the correlation idea is kept but is performed without relying on the camera data but rather on the pressure fluctuations in the chamber recorded by the microphone. This method is based on the shape of the spectrum for each of the flames, shown in Fig. 7.11.

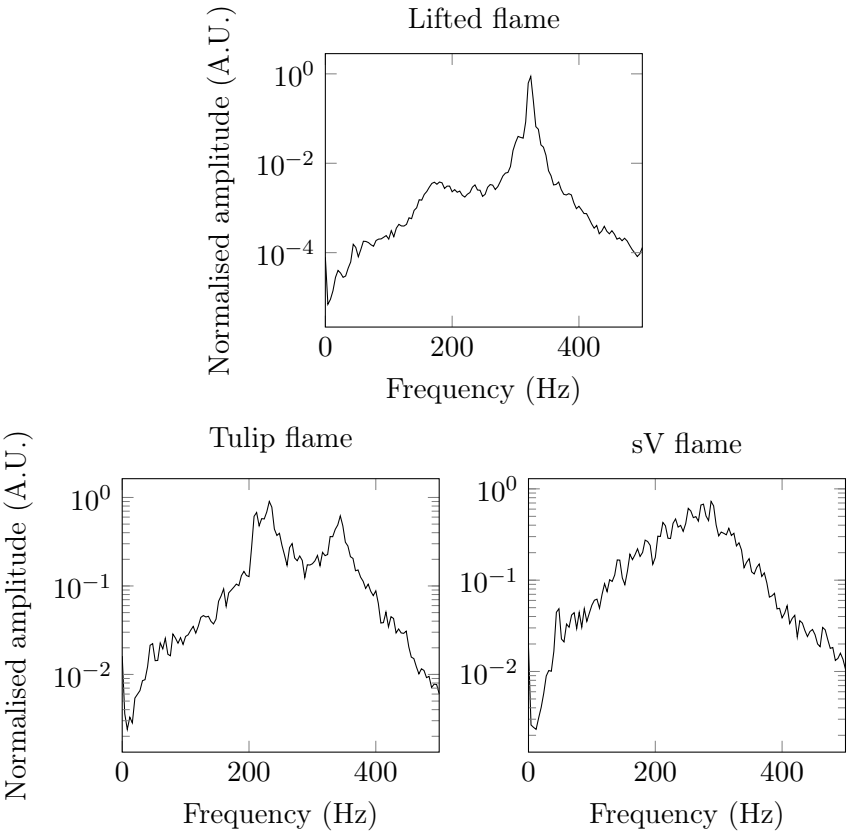

Figure 7.11 – *Spectral signatures of the three states based on the chamber pressure fluctuations signal recorded by the microphone for the lifted, tulip and sV flames.*

The spectra between 0 and 500 Hz are computed (0.25 s Hamming windows) using the microphone signal in the parts where the flame shape is clearly identified thanks to the optical diagnostics. They are normalized and then averaged between the experiments to obtain the canonical spectral footprint for each state similarly to what was done for the average images leading to Fig. 7.9.

For the lifted flame on the top of Fig. 7.11, the peak of the thermo-acoustic instability around 330 Hz can be identified and is clearly dominant compared to the noise level. For the two other flames, no strong dominant frequency emerges but the tulip flame presents two particular peaks while the sV flame spectrum is more spread.
Using these three different spectral signatures, it is thus possible to compute a correlation coefficient between the spectrum of any part of the microphone signal and these references. The determination of the state of the burner can thus be continued after the end of the camera recording. Of course, since at least a 0.25 s long window is required to compute a spectrum, the temporal precision is relatively poor.
In order to assess the reliability of this method, its capability of giving a good estimation of the first step instant (within its inherent uncertainty) has been first tested and gave satisfactory results. Furthermore, the values of the tulip lifetimes obtained through this method are consistent with the naked eye observations made during the experiments. It must however be noted that in some cases (in the event of a strong thermo-acoustic instability as defined in chapter 6 for example), the correlation coefficients are too low (below 0.5) or too close to each other to be trusted. The tulip lifetime has thus been measured for only 10 of the 17 late widening cases.
The distributions of the tulip lifetime values computed by flame image correlation for the early widening case and by spectral footprint correlation for the late widening case are shown in Fig. 7.12.

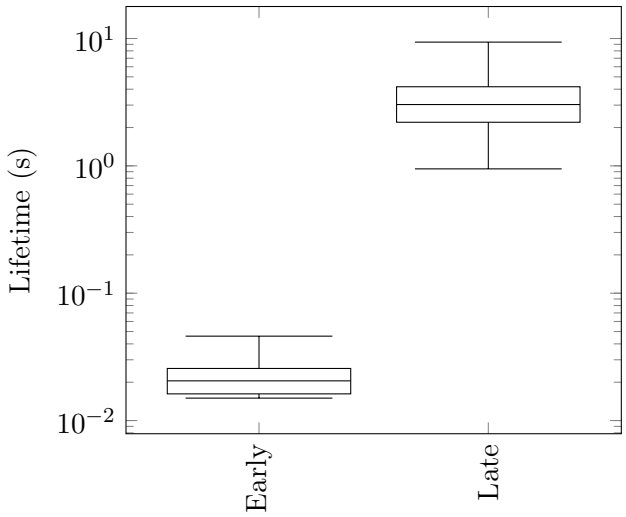

Figure 7.12 – *Box plot of the five-number summary (minimum, first quartile, median, third quartile and maximum) for the tulip lifetime distribution in the two populations (early and late widening). The early population is composed of 20 samples and the late one of 10 samples.*

To represent the position and the spread of the tulip lifetime distributions in the early and late widening cases, a five-number summary is used. The idea is to represent the location of the distribution with the median, its spread with the quartiles and its range with the extreme values.
For the early widening population, the tulip is short-lived and the widening occurs between 15 and 50 ms after the first step of the transition with a median value of 21 ms. The situation is not the same for the late widening population where the median is at 3 s and the tulip lifetime's values extend between 0.9 and 10 s.
The data shown in Fig. 7.12 thus highlights the fact that the separation of the populations between early and late widening is not as arbitrary as it previously seemed. Indeed, the lifetime ranges of the two populations do not overlap and are even separated by more than one order of magnitude. It must be reminded here that no difference between the two populations could be detected in the data before the transition.

If the widening step is a random process with a more or less uniform probability to happen at a given time after the first step, such a strong difference between the two populations should not be seen. The gap between the two sets of data must thus come from a change triggered by the flame itself, meaning that if the widening does not happen quickly, the fact that the flame stabilizes with a tulip shape prevents it from widening for a longer duration. It is thus necessary to study the late widening population to check what can trigger this widening.
The tulip lifetimes for the late widening population are of the order of a few seconds. Not that many phenomena occurring in the combustor have such large timescales. The flow field, vaporization and chemical characteristic times are indeed all well below this order of magnitude. The only two candidates that seem to remain are thermal effects (heat transfer in a solid part for example) and changes in the fuel staging (since the studied case corresponds to a transient operation). The former cannot be thoroughly studied without supplemental experiments and furthermore all the available measurements show no difference on this point. On the contrary, further information can be obtained on the latter since the fuel flow rates are recorded all along the experiment.
To perform this study, the change in the staging parameter during the tulip lifetime in the late widening case is more precisely analysed in Fig. 7.13.

During the transition, the fuel flow rates are changing slowly. In the previous studies, the staging parameter is considered constant since all the recordings are performed over relatively short time scales. Here, the tulip lifetimes are of the order of a few seconds and the staging cannot be considered constant anymore. To monitor the evolution of the staging during the tulip phase, the staging parameter at the anchoring instant (the previously defined α_t) is subtracted to the staging parameter at the widening instant to give the value called $\Delta\alpha$.

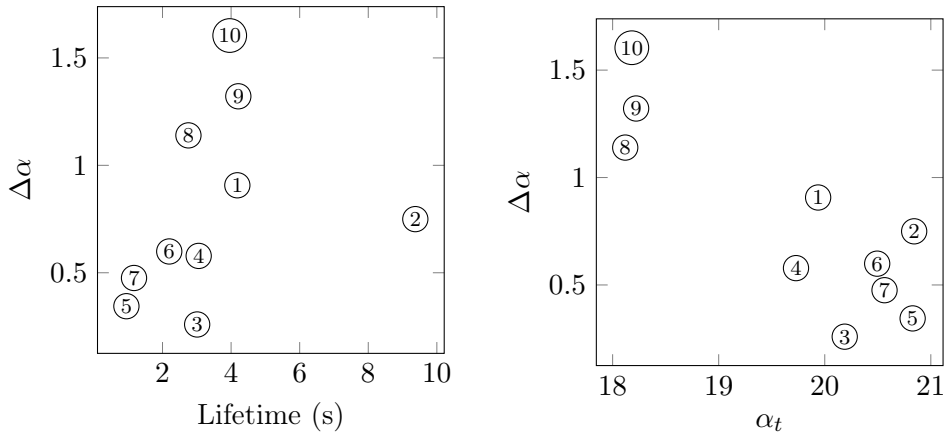

Figure 7.13 – *Variation ($\Delta\alpha$) of the staging parameter during the tulip phase as a function of the tulip lifetime (left) and of the staging value at the transition instant (right). Each number represent one experiment out of the 10 that make the late widening population.*

Before working with this value, it is necessary to verify that it is not too much dependent on the lifetime of the tulip. Indeed, $\Delta\alpha$ is the variation of the staging parameter during the tulip shape. If the rate of change of α is the same for all the experiments, looking at $\Delta\alpha$ would be useless since it is then well correlated with the tulip lifetime. There would thus be no way to discriminate between an effect of the modification of the fuel staging and an effect of the duration in the tulip state. The goal of the graph on the left of Fig. 7.13 is to check this potential dependency between $\Delta\alpha$ and the tulip lifetime.
Fortunately, this graph shows that no strong link can be made between the tulip lifetime and $\Delta\alpha$. Indeed, the correlation coefficient is only 0.3, meaning that only 9% of the variance of $\Delta\alpha$ can be explained by the tulip lifetime. This can be felt by looking at the difference between experiments 6 and 2 where $\Delta\alpha$ does not change much whereas the lifetime does or at the difference between experiments 3 and 10 which shows the inverse situation. These results mean that the rate of change of the staging parameter is not constant for all the experiments and it is important since it enables to decouple the effect of the lifetime from the results observed on $\Delta\alpha$.

To go further in the analysis of the staging, the value of $\Delta\alpha$ is plotted versus the value of the staging parameter at the anchoring instant (α_t) on the right of Fig. 7.13. In this case, the situation is very different from the previous graph and the correlation coefficient between the two variables is -0.86 (95% confidence interval: [-0.97,-0.49]), meaning that 73% of the variance of $\Delta\alpha$ can be explained by α_t. Even if the number of samples is low, this coefficient is high enough to be considered significant with a 5% risk (Saporta 2011).
This link between the two variables means that when α_t is low, more change

in the staging parameter is needed before widening that when it is high. Once again, it must be said that this effect is independent of the duration itself between the anchoring and the widening. These data highlight the fact that the changes in the fuel flow rate are actually triggering the widening of the flame, probably because of an undefined threshold to reach. A mechanism fitting with this behaviour is thus needed to explain the widening step.

In chapter 6, the stabilization process for the V flame is explained with the help of a two-step mechanism (Fig. 6.15). The first step corresponds to setting the flame into its diverging shape thanks to the fuel stratification created by the bigger droplets. This step can indeed be compared with the widening observed here. Unfortunately, no PDA measurements can be used in the present case to analyze the droplet size spatial distribution so other clues must be used.
The staging parameter α represents the proportion of fuel injected through the pilot stage. Since the multipoint injector generates smaller droplets, α can also be considered as a qualitative indicator of the amount of big droplets in the spray. In Fig. 7.13, it is shown that, if the anchoring happens at a low staging parameter, a bigger increase in α is needed than when it happens at a higher staging parameter. This could be linked to the fact that the proportion of big droplets needs to reach a certain threshold to trigger the flame widening.
The existence of the two different widening populations can also be explained by this mechanism. Indeed, if the proportion of fuel droplets is high enough just after the first step of the transition, the widening happens then almost instantly (early widening) and the stabilizing changes described in the second step of Fig. 6.15 get into play to maintain the flame into its sV shape. On the contrary, if there are not enough big droplets to trigger the widening of the flame, the flame remains in the tulip state (corresponding to an anchored flame with a non-diverging airflow). Because of its anchoring inside the injector, the tulip flame increases the vaporization rate of the droplets which reduces their size and thus the stratification effect. It is then needed to wait for a sensible increase of the staging parameter to obtain enough big droplets for the widening which explains the gap in the tulip lifetimes between the two populations.
Because of the experimental difficulties when dealing with such transient events and small variations in the fuel flow rates, the proposed mechanism cannot be further backed up. Its main advantage lies in the fact that it enables to explain what is observed without adding too much complexity.

Summary of the chapter

This chapter focuses on the phenomena happening in the burner when the staging parameter is increased and the flame switches from the lifted state with a thermo-acoustic instability to the quieter sV state.

The effect of the global operating parameters on the value of the staging parameter when the sound pressure level in the chamber drops is studied first. Fifteen experiments following a Box-Behnken design are used to set up a quadratic model with the first interaction terms. This model shows that increasing the air flow rate has a strong non-linear deterrent effect on the transition. On the contrary, despite a relatively large uncertainty, it seems that increasing the power and the temperature are favourable to earlier transitions. Finally, no strong interaction between the parameters can be detected compared to the effect of the parameters variation alone.

Looking at the flame shape half a second after the SPL drop shows two possible shapes for the flame: the expected sV flame and a new one called the tulip flame. The properties of the tulip flame are studied with the tools used for the other flame shapes.
From an average point of view, the spray and the air flow seem closer to the lifted/non-reacting ones than to the sV flame ones. The flame shape is however peculiar in the sense that it is anchored but not diverging.
The dynamics of the tulip state seem to be closer to the attached states with a discernible presence of the PVC trace in the spray and the flame. A study of the PVC frequency from internal visualizations confirms the fact that the flame is anchored inside the injector but that the air flow remains almost undisturbed. The tulip flame can thus clearly be described as an in between state, showing properties of both the lifted and the sV flames.

The transition itself is finally studied in a time-resolved fashion. The observation of the flame instantaneous images shows that it actually happens in two steps: first from a lifted flame to a tulip flame and then from this tulip state to the sV flame.
The first step corresponds to a propagation of the flame in the IRZ which can be assimilated to a flashback because of the negative axial velocities there. This is triggered by the increase of the pilot fuel flow rate during the evolution of the staging. Once the flame reaches the inside of the injector, it ignites the mixture there and anchors. The occurrence of this particular phenomenon is the key for the success of the transition and a large air flow rate can prevent it. If it is successful, the flame stabilizes with a tulip shape.
The second step corresponds to the widening of the tulip into a sV flame. Observations on the evolution of the staging parameter during the transition seem to indicate that this step is triggered by the fuel stratification created by the fuel droplets. If this stratification is present just after the first step, the flame widens almost instantly otherwise it must wait for an increase in the staging parameter, that is an increase of the part of the pilot fuel injection.

Conclusion & Perspectives

In the present work, mechanisms piloting the flame stabilization and the transient behaviour of a swirled liquid-fueled burner have been studied with the help of several diagnostics and post-processing methods. Three main different flame shapes with different properties have been highlighted as well as the phenomena leading to transitions between these shapes.
This complex behaviour comes from the intricate interactions between the gaseous flow, the liquid fuel droplets and the flame itself which have been promoted by the use of a staged injection enabling to change the fuel spatial distribution. The capability of this technique to stabilize a quiet flame in close to LPP conditions has also been observed.
All the observations made during this study can be summed up by three flame stabilization mechanisms and their relative importance depending on the operating point.

Pilot-driven stabilization

The pilot stage consists in a swirled air injection (13.5% of the total mass flow rate, S_{geom}=0.6) coupled with a pressurized nozzle that creates a hollow cone of droplets. PDA measurements for pilot-only conditions tend to indicate that the size of the generated droplets is relatively high, giving them a strong ballistic behaviour as well as a sensitivity to centrifugal effects created by the swirling flow. This creates a stratification of the fuel distribution and, in non-reacting conditions, it can be observed that the spray does not follow well the swirling air jet.
When the flame is ignited, the particular fuel distribution makes it open up to take a clear V shape. As this happens, the presence of the flame inside the injector triggers a bifurcation of the air flow and sets it onto a diverging trajectory that deviates from the non-reacting conditions. This bifurcations is accompanied by an increase the PVC frequency inside the injector and more importantly by a diminution of its variability, meaning that the air flow becomes more confined. This change in the air flow as well as the presence of hot combustion products in particular regions help maintain the flame in this place. Air flow rate modulations performed with the help of a siren device show that this particular state is especially robust. It is shown that these air flow rate

modulations can reduce the trace of the PVC on the spray by reducing the coherence of the structure but, even for very high amplitude modulations, the flame does not seem much disturbed, in particular no non-linear effects are observed.

This particular flame stabilization can be observed even when a dominant part of the fuel injection is made through the take-off stage (86.5% of air, S_{geom}=1) thanks to the associated multipoint injection. However, as the staging gets more and more in favour of the take-off stage, the stabilization switches to a history-driven one.

History-driven stabilization

The history-driven stabilization corresponds to a stabilization that can only occur if the burner went through particular previous states. It is observed for relatively low staging values, when the multipoint injection is dominant. In this case, PDA data show that the spray is mostly composed of small droplets that follow the air flow well because of their low Stokes number. This also leads to a good mixing between the fuel and the air and explains why the flame looks diluted and takes a spread-V (sV) shape.
Despite the fact that the fuel stratification does not occur anymore, the flame shape remains globally divergent and the data on the PVC frequency indicate that a flame is still present inside the injector. Measurements of the air flow also show that it remains on a diverging trajectory. These observations lead to associate the stabilization with the presence of the internal flame that maintains the air flow on a diverging trajectory followed by the fuel spray. Since the internal flame can only exist because the previous flame was already attached, this is why this particular stabilization is driven by the history of the burner.

This state can exist in parallel to the flow driven stabilization (see next paragraph) and has shown a relatively poor resistance to perturbations. It can indeed trigger a very strong thermo-acoustic instability when some conditions are reunited. A study of these conditions is however difficult because of safety reasons. More importantly, this particular stabilization mechanism can be destroyed by strong air flow rate modulations.
It must however be noted that the history-driven state is a good illustration of the capability of the staging strategy to stabilize a flame with interesting properties. Indeed, this regime shows moderate acoustic fluctuation levels while most of the injection is performed through the take-off stage. Good performances in terms of mixing and vaporization can be expected and this is thus interesting for the reduction of pollutant emissions. When compared with the flow-driven stabilization that can also be observed for the same conditions, this stabilization process should be preferred.

Flow-driven stabilization

The third observed dominant stabilization mechanism is the flow driven one. It occurs when the fuel injection is dominated by the multipoint stage. As stated previously, this corresponds to a majority of small droplets which leads to a good mixing between the fuel and the air as well as a quick vaporization of the droplets. This is particularly highlighted by the small penetration length of the spray in this state.
Because of this good mixing, a parallel can be drawn between the behaviour of the burner and a premixed gaseous one. The flame indeed shows a diluted shape detached from the injector as it is expected for relatively low swirl values. The air flows also looks like the non-reacting one which is confirmed by the measurement of the PVC frequency inside the injector. The flame stabilization is thus neither dependent on the liquid fuel nor on the history of the burner.

While the two previous stabilization mechanisms lead to relatively quiet flames (probably because of their anchoring), the flow-driven stabilization gives a loud lifted flame. This comes from the fact that the flame triggers a thermo-acoustic instability based on the quarter-wave mode of the chamber. The feedback mechanism giving rise to this instability is given by the response of the fuel droplets to the oscillations and it is shown that a delay due to vaporization exists between the fuel spray and the flame fluctuations.
A way of tackling this thermo-acoustic instability issue could consist in changing the fuel staging to allow the flame to anchor again and thus switch to one of the two previous states. The phenomena triggering such changes have also been studied.

Transition between the states

Since the ignition of the burner is always performed with a pilot-only injection, the starting flame shape is a V, stabilized by the pilot-driven mechanism. As the staging is reduced, two phenomena happen. First, the multipoint injection starts providing smaller droplets thanks to a good atomization instead of just dripping when the fuel flow rate is too low. Then the local equivalence ratio of the pilot stage falls below one meaning that an internal flame can burn completely, independently of the take-off stage. These two observations are considered to be responsible for the switch to a sV flame and thus a history-driven stabilization. It must however be noted that this particular transition is hard to define since it corresponds more to a continuum than to an abrupt change.

When the flame shows a sV shape, it is possible to switch to the lifted flame, characteristic of a flow-driven stabilization. In some cases, this even happens naturally because of the previously stated strong thermo-acoustic instability.

It is also possible to trigger the transition by moving to low staging values with almost no residual pilot fuel injection or by creating strong air flow rate modulations. These two possibilities have to be linked with the existence of an internal flame in the history-driven stabilization mechanism. Blowing this flame off indeed prevents the air flow from remaining in its diverging state and it thus returns to its non-reacting behaviour which makes the flame stabilize with a lifted shape.

The last transition, from the lifted flame with a flow-driven stabilization to the sV flame, is particular since it shows the existence of an intermediate state. The change consists in two separate steps. First, the increase of the pilot fuel injection provides a combustible mixture inside the inner recirculation zone which makes a flame finger flashback towards the injector. If favourable conditions are present, a reaction zone is started inside the injector and the flame takes a new shape called the tulip. If the proportion of big fuel droplets is high enough, this flame almost instantly widens, following the pilot-driven stabilization mechanism. It otherwise remains in the tulip state until the staging gets high enough to trigger the widening.

Key implications

All the previous observations have implications on the approach used when dealing with liquid fuel combustion.
From an experimental point of view, the use of liquid fuel adds two major complex phenomena. First, the distribution of the fuel is strongly dependent on the quality of its atomization and thus the droplet size. Secondly, the vaporization time adds a delay that is also dependent on the atomization quality. These two phenomena strengthen the link between the air flow and the fuel distribution and, more importantly, they add a new dependency by enabling the flame to act on the fuel distribution itself through changes in the vaporization properties. All these interdependencies thus makes it illusory to expect understanding liquid fuel combustion processes from gaseous fuel observations, except in very particular cases like the lifted flame here for example. Moreover, changes in the liquid fuel properties (viscosity or vaporization propensity for example) may also lead to very different responses.
From a simulation point of view, it seems that the description of the liquid phase remains a key issue. Indeed, depending on the distribution of the droplets sizes and on their particular trajectories, the results can also strongly change. Obviously, the observations made from the experimental point of view are also valid here and this highlights the necessity of knowing fine properties for the fuel vaporization and the chemical mechanisms.

Perspectives

The perspectives opened by this work are mostly twofold and rely on the use of specific tools to observe what could not be observed in the present study.

The use of numerical simulations provides two main advantages. First, physical quantities can be obtained in a time-resolved fashion at any point of the computational domain. This means that it is then easy to probe what is happening inside the injector. The present study has indeed highlighted that the behaviour of the burner seems strongly dependent on the presence or absence of a flame inside the injector but only indirect traces of such a flame have been obtained. Performing numerical simulations on the operating points studied in the present work could thus bring two main advances. A good way of describing the liquid phase (maybe with a lagrangian framework) could be set up by comparison with the experimental results since, especially for the pilot-driven stabilization, these results seem to depend strongly on a liquid fuel spray effect. Then, the stabilization mechanisms proposed in the present work could be validated or rejected by performing similar numerical experiments.
A second strong advantage of simulation is that numerical experiments are safe. The conditions leading to the natural lift of the sV flame through the strong thermo-acoustic instability could be analysed without any risk for the experimentalist or the setup. This would once again help in giving credit to the stabilization mechanisms proposed here.

A key element that could not be measured in the present study is the fuel vapour phase. This corresponds to the missing link between the spray and the flame and it would provide precious information on the flame stabilization. The most promising way for this is the use of laser-induced fluorescence on tracers added to the fuel but two main drawbacks have to be tackled.
The first one is the fact that, when a tracer is highly concentrated in the droplets, it gives a much stronger signal than in the vapour phase. The fluorescence from the fuel droplets must thus be removed from the signal from the vapour phase. The use of exciplex techniques (Desantes et al. 2005) enable this by changing the fluorescence wavelength between the liquid and the vapour phase but, because of strong oxygen quenching, they are limited to nitrogen atmospheres. Another method relies on the post-processing of images to create a mask hiding the droplets (Orain et al. 2005). This method is widely used but care must be taken regarding the dynamic range of the camera.
The second drawback comes from the choice of an effective tracer. For dodecane, aromatics (and especially naphtalene) are good candidates since they are soluble and have a close vaporization temperature (Kaiser and Long 2005; Orain et al. 2011). A key issue however concerns the quenching of their fluorescence by O_2. Indeed, quantitative measurements require the knowledge of the oxygen partial pressure (Koban et al. 2005; Orain et al. 2014) or the assumption of a

closure relationship for the species (Orain et al. 2009). In the present burner, numerical simulations have shown the presence of hot mixing regions where fuel mixes with burnt gases. The oxygen concentration is unknown there and quantitative measurements thus become non straightforward. They however remain a key element for the study of flame stabilization and their realization must be pursued.

Appendix A

Choice of the cross-correlation algorithm

The present study aims at comparing different algorithms for the cross-correlation step that enables to obtain an estimation of the fuel spray velocity from PIV post-processing. Three different algorithms are used.
The first algorithm (A) performs a one step cross-correlation with Fourier transform and is based on 16×16 pixels analysis windows. It uses the proprietary Dantec Dynamic Studio software with "black box" routines.
The second algorithm (B) corresponds to an adaptive correlation method (also with Fourier transform) where two passes are performed: one with 32×32 pixels windows and then 16×16 pixels. This algorithm also requires the Dantec Dynamic Studio routines.
Finally, the third algorithm (C) uses a direct cross-correlation method on 16×16 pixels windows with the open-source PIVLab software, working with Matlab. The subpixel estimator is based on a 2D Gauss interpolation.
All the algorithms work with a 50% overlap between the windows and a range validation of the vectors is performed based on the minimal and maximal velocity values recorded by the PDA. If less than 2% of the vectors at a given point are validated, the associated average value is not computed but set to zero to avoid the deterrent effect of non-converged statistics.

The study is performed on data coming from an operating point representing the "worst case scenario" in terms of seeding. The raw images come from a reacting pilot-only case with a global equivalent ratio of 0.5, thoroughly described in chapter 4. In this case, not many droplets are present. They furthermore tend to regroup in two thin arms, as shown in Fig. A.1.

The computations are performed on 7818 image pairs, separated by 25 µs. Since four pixels of the image represent 1 mm, a displacement of 1 pixel corresponds to 10 m/s. For the validation step, the extreme values recorded by the

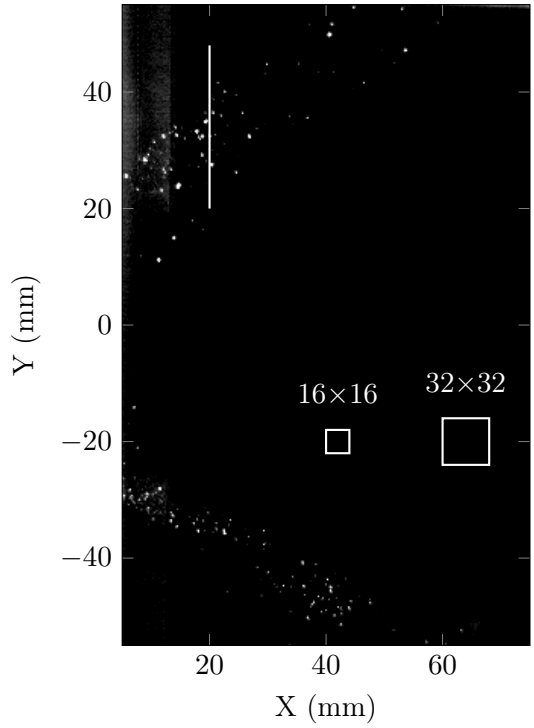

Figure A.1 – *Instantaneous Mie scattering image from the chosen operating point. An artificial saturation is performed to allow for a better visualization of the spray. The white line represents the profile used for the comparison between the algorithms. The squares show the sizes of the interrogation windows.*

PDA are [-30;123] m/s for the axial velocity and [-47;48] m/s for the vertical velocity.
In the best case, only around 50% of the computed vectors for one point are validated, about half of the time because the SNR of the correlation peak is too low and the other half of the time because of an out of range value. This highlights the difficulty of performing PIV on a fuel spray in reacting conditions. A comparison of the mean axial velocity profiles for an arm of the spray can be seen in Fig. A.2.

First, it can be seen that no cross-correlation algorithm can reach the PDA-computed velocities. This phenomenon can have two origins. First, as explained previously, PDA measurements are biased towards high velocities and even though a weighting method is applied, it might not completely correct the bias. Secondly, it must be kept in mind that the measured velocities are not the same: the PDA measures the velocity of individual droplets while PIV yields the most probable displacement of the droplets inside a given window. Individual high velocity droplets in a slower environment are thus not detected in PIV but contribute to the PDA average.

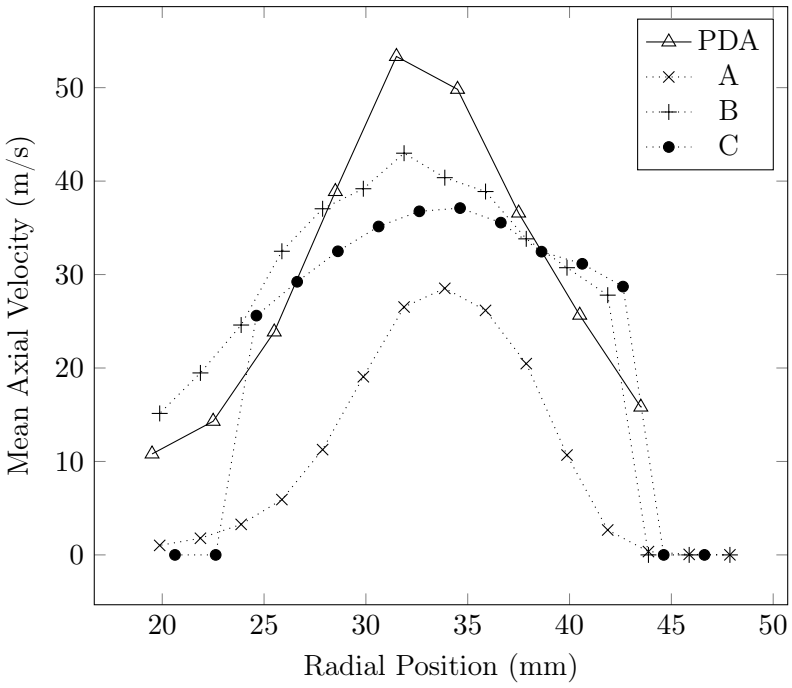

Figure A.2 – *Mean axial velocity profiles for an arm of the spray computed with different methods. The position of the profile is marked in Fig. A.1. The line corresponds to PDA data. Algorithm A is the one pass Fourier correlation, B the adaptive Fourier correlation and C the direct cross-correlation.*

The second striking result is the impossibility for the one step Fourier cross-correlation algorithm (algorithm A) to retrieve the same values as the other PIV algorithms. This is a result of aliasing which prevents the method from finding high velocities (the aliasing occurs at 80 m/s) that increase the average. The direct cross-correlation algorithm (C) which is immune to aliasing indeed shows higher results. Algorithm B (using an adaptive procedure, which is the classical mean of tackling the aliasing issue) also provides better velocity values but seems to broaden the spray width (under 25 mm). This phenomenon comes from the fact that the original 32×32 pixels window corresponds roughly to the spray width as seen in Fig. A.1. The original velocity estimates are thus too coarse compared to the seeding non-uniformity. This drawback can however be countered by using a mask based on the raw Mie scattering images to define the spray limits.

The choice of the PIV algorithm thus has to be made between algorithms B and C which both yield similar results. The adaptive-correlation algorithm has a slightly better validation rate (at best 51% versus 48%) but the direct-cross correlation one is much faster. Indeed, even though FFT-based cross-correlation is inherently faster, several passes are needed in the adaptive correlation case.

As a result, the processing time for the 7818 image pairs on a dedicated personal computer rises from around 2 hours with algorithm C to nearly 5 hours with algorithm B.
The direct cross-correlation method also has one advantage that proves particularly useful for the present study. Using Fourier based method, the size of the interrogation windows is limited to powers of two whereas no such limitation is imposed by direct cross-correlation. Because of the non uniform seeding in fuel spray applications, there is a trade-off between the number of droplets in each window and the number of windows inside the spray. The ability to precisely tailor the size of the interrogation window is thus of paramount importance.
For all the previously exposed reasons, the algorithm used in the present work is based on a direct cross-correlation technique. The size of the interrogation window is chosen based on the raw images to process.

Appendix B

Simulation of the PDA signal

This appendix presents the simple model simulating the droplets arrival time for the analysis of the time-intervals in chapter 4. It is based on the modulation of the detection probability of the droplets.

For the pilot-only operating point in non-reacting conditions, the histogram of the interval time between the big droplets for a probing point at X=10 mm and Y=-30 mm has a particular shape with peaks a bit below 600 µs as shown in Fig. B.1.

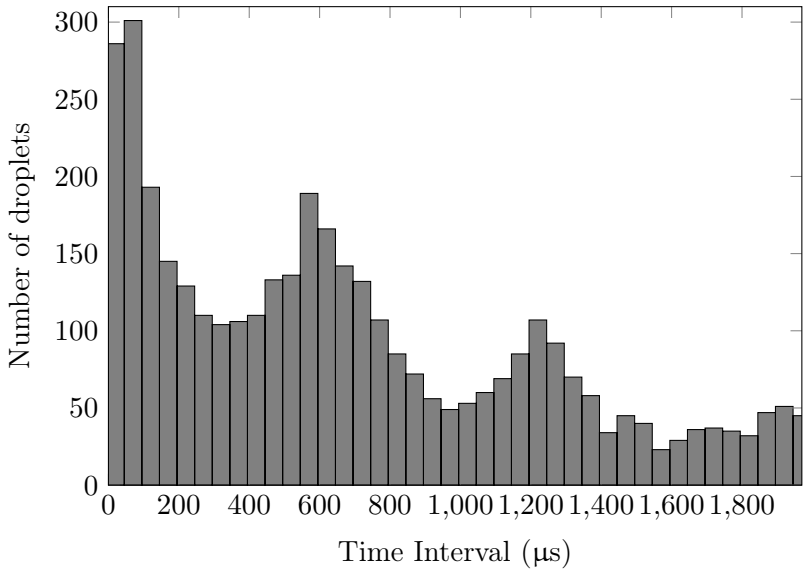

Figure B.1 – *Histogram of the time intervals for big droplets (D>30 µm) at X=10 mm and Y=-30 mm.*

A simple model simulating the arrival time of particles is used to understand the meaning of the histogram. Its goal is to approach the experimental dataset.

For this purpose, the duration of the recording is divided into 1 µs time steps. An average probability of droplet detection is computed based on the total number of droplets detected in the original signal divided by the total number of time steps. First, this probability is uniformly associated to each time step. The core of the model consists in a random drawing at each time step defining if a particle is detected or not. If a particle is detected, its arrival time is stored and time intervals are then computed by the difference in the arrival times.
The average arrival probability for the experimental signal is 0.0012 droplet per microsecond. With this uniform probability for each time step, the resulting histogram can be seen in Fig. B.2.

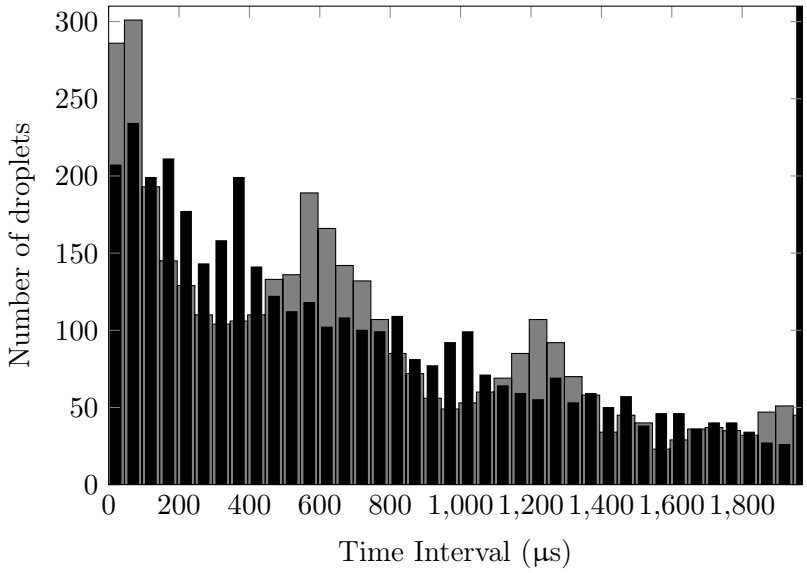

Figure B.2 – *Simulated histogram of the time intervals for a uniform probability arrival time.*

It is clear that the histogram does not correspond to the recorded experimental data. It shows, as one can expect, a globally linear decreasing trend because, since the detection probability is uniform, long time intervals between two consecutive droplets become increasingly less probable. This corresponds to a constant droplet density.
Because the Precessing Vortex Core is suspected to be responsible for the particular shape of the experimental histogram, its effect is simulated with a simple model. Since the PVC is expected to disturb the droplet density, the detection probability for the droplets is modulated by a sine wave at the PVC frequency (around 1580 Hz, which corresponds to a period of 633 µs). The amplitude of the sine wave is fixed at 95% of the average detection probability following an iterative study. A realisation of the histogram with the arrival probability modulation can be seen in Fig. B.3.

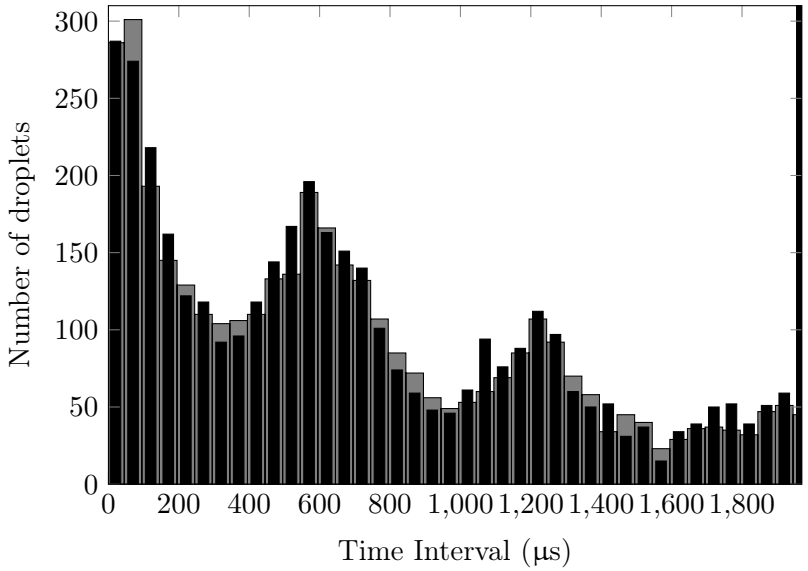

Figure B.3 – *Simulated histogram of the time intervals for a uniform probability arrival time.*

The agreement between the two histograms is now very satisfying. The experimental signal has thus been retrieved using a very simple model which can provide useful information. First, the presence of the two peaks mean that no droplets are detected for some PVC cycles and it is thus needed to wait until the next cycle to detect a droplet. This is characteristic of a very low average seeding density. The amplitude of the modulation is also well defined. Indeed, an amplitude of 90% of the average detection probability tends to smooth out the peaks and a value of 100% of the average detection probability does not provide enough detected droplets in the lower part of the cycle.
In a nutshell, this very simple analysis enables to highlight the fact that, for this particular point, the PVC acts on the spray by modulating the droplets density with almost zero droplets during the low phases of its cycle.

References

Adrian, R. J. (1991). Particle-Imaging Techniques for Experimental Fluid Mechanics. *Annual Review of Fluid Mechanics 23*(1), 261–304. *(p. 48)*

Agarwal, T. and L. Zimmer (2012). Two dimensional Laser Induced Plasma Spectroscopy for the measurements of local composition in gaseous flow and sprays. In *16th Int Symp on Applications of Laser Techniques to Fluid Mechanics*, Lisbon, Portugal. *(p. 104)*

Ahmed, S. F. (2014). The probabilistic nature of ignition of turbulent highly-strained lean premixed methane-air flames for low-emission engines. *Fuel 134*, 97–106. *(p. 189)*

Albrecht, H. E., N. Damaschke, M. Borys, and C. Tropea (2013). *Laser Doppler and Phase Doppler Measurement Techniques*. Springer Berlin Heidelberg. *(p. 34, 46, 47)*

Alekseenko, S. V., V. M. Dulin, Y. S. Kozorezov, and D. M. Markovich (2012). Effect of High-Amplitude Forcing on Turbulent Combustion Intensity and Vortex Core Precession in a Strongly Swirling Lifted Propane/Air Flame. *Combustion Science and Technology 184*(10-11), 1862–1890. *(p. 95)*

Apeloig, J. M., F.-X. d'Herbigny, F. Simon, P. Gajan, M. Orain, and S. Roux (2015). Liquid-Fuel Behavior in an Aeronautical Injector Submitted to Thermoacoustic Instabilities. *Journal of Propulsion and Power 31*(1), 309–319. *(p. 151)*

Auger, F., P. Flandrin, P. Gonçalvès, and O. Lemoine (1996). Time-frequency toolbox. *CNRS France-Rice University*. *(p. 46)*

Barbosa, S. (2008). *Etude expérimentale de la dynamique de combustion d'un injecteur multipoint étagé de turbine à gaz*. PhD thesis, Ecole Centrale Paris, Châtenay Malabry, France. *(p. 15, 19, 20, 22, 28)*

Barbosa, S., P. Scouflaire, and S. Ducruix (2009). Time resolved flowfield, flame structure and acoustic characterization of a staged multi-injection burner. *Proceedings of the Combustion Institute 32*(2), 2965–2972. *(p. 4, 58)*

Benedict, L. H., H. Nobach, and C. Tropea (2000). Estimation of turbulent velocity spectra from laser Doppler data. *Measurement Science and Technology 11*(8), 1089. *(p. 47)*

Berkooz, G., P. Holmes, and J. L. Lumley (1993). The proper orthogonal decomposition in the analysis of turbulent flows. *Annual Review of Fluid*

Mechanics 25(1), 539–575. *(p. 44)*

Bernier, D. (2001). *Contrôle actif des instabilités de combustion dans les turbines à gaz bas-Nox*. PhD thesis, Ecole Centrale Paris, Châtenay Malabry, France. *(p. 7)*

Bond, T. C., S. J. Doherty, D. W. Fahey, P. M. Forster, T. Berntsen, B. J. DeAngelo, M. G. Flanner, S. Ghan, B. Kärcher, D. Koch, S. Kinne, Y. Kondo, P. K. Quinn, M. C. Sarofim, M. G. Schultz, M. Schulz, C. Venkataraman, H. Zhang, S. Zhang, N. Bellouin, S. K. Guttikunda, P. K. Hopke, M. Z. Jacobson, J. W. Kaiser, Z. Klimont, U. Lohmann, J. P. Schwarz, D. Shindell, T. Storelvmo, S. G. Warren, and C. S. Zender (2013). Bounding the role of black carbon in the climate system: A scientific assessment. *Journal of Geophysical Research: Atmospheres 118*(11), 5380–5552. *(p. 2)*

Borghi, R. (1996). Background on droplets and sprays. *Lecture series-von Karman Institute for fluid dynamics 2*. *(p. 14)*

Boudy, F. (2012). *Nonlinear dynamics and control analysis of combustion instabilities based on the Flame Describing Function (FDF)*. PhD thesis, Ecole Centrale Paris, Châtenay Malabry, France. *(p. 9)*

Boxx, I., M. Stöhr, C. Carter, and W. Meier (2010). Temporally resolved planar measurements of transient phenomena in a partially pre-mixed swirl flame in a gas turbine model combustor. *Combustion and Flame 157*(8), 1510–1525. *(p. 86)*

Buchhave, P., W. K. George, and J. L. Lumley (1979). The Measurement of Turbulence with the Laser-Doppler Anemometer. *Annual Review of Fluid Mechanics 11*(1), 443–503. *(p. 46)*

Candel, S. (2002). Combustion dynamics and control: progress and challenges. *Proceedings of the Combustion Institute 29*(1), 1–28. *(p. 4)*

Candel, S., F. Lacas, N. Darabiha, and J.-C. Rolon (1999). Group combustion in spray flames. *Multiphase Science and Technology 11*(1). *(p. 14)*

Candel, S. M. (1992). Combustion instabilities coupled by pressure waves and their active control. In *Symposium (International) on Combustion*, Volume 24, pp. 1277–1296. Elsevier. *(p. 10)*

Cavaliere, D. E., J. Kariuki, and E. Mastorakos (2013). A Comparison of the Blow-Off Behaviour of Swirl-Stabilized Premixed, Non-Premixed and Spray Flames. *Flow, Turbulence and Combustion 91*(2), 347–372. *(p. 164)*

Chanaud, R. C. (1965). Observations of oscillatory motion in certain swirling flows. *Journal of Fluid Mechanics 21*(01), 111. *(p. xi, 7)*

Chigier, N. (1983). Group combustion models and laser diagnostic methods in sprays: A review. *Combustion and Flame 51*, 127–139. *(p. 14)*

Chigier, N. A. and J. M. Beér (1964). Velocity and Static-Pressure Distributions in Swirling Air Jets Issuing From Annular and Divergent Nozzles. *Journal of Basic Engineering 86*(4), 788. *(p. 5)*

Chiu, H. H., H. Y. Kim, and E. J. Croke (1982). Internal group combustion of

liquid droplets. In *Symposium (International) on Combustion*, Volume 19, pp. 971–980. Elsevier. *(p. 14)*

Chiu, H. H. and T. M. Liu (1977). Group Combustion of Liquid Droplets. *Combustion Science and Technology 17*(3-4), 127–142. *(p. xi, 14, 15)*

Correa, S. M. (1998). Power generation and aeropropulsion gas turbines: From combustion science to combustion technology. *Symposium (International) on Combustion 27*(2), 1793–1807. *(p. 4)*

Coward, H. and G. Jones (1952). *Limits of flammability of gas and vapors*, Volume 503. US Bureau of Mines. *(p. 152)*

Culick, F. E. (2006). Unsteady motions in combustion chambers for propulsion systems. Technical report, NATO Research And Technology Organization. *(p. 9)*

Delabroy, O., E. Haile, F. Lacas, S. Candel, A. Pollard, A. Sobiesiak, and H. A. Becker (1998). Passive and active control of NOx in industrial burners. *Experimental thermal and fluid science 16*(1), 64–75. *(p. 10)*

Desantes, J., J. Pastor, J. Pastor, and J. Juliá (2005). Limitations on the use of the planar laser induced exciplex fluorescence technique in diesel sprays. *Fuel 84*(18), 2301–2315. *(p. 201)*

DGAC (2012). Les émissions gazeuses liées au trafic aérien en France. Technical report. *(p. 1)*

Domann, R. and Y. Hardalupas (2003). Quantitative measurement of planar droplet Sauter mean diameter in sprays using planar droplet sizing. *Particle & Particle Systems Characterization 20*(3), 209–218. *(p. 29, 33)*

Dowling, A. P. and Y. Mahmoudi (2015). Combustion noise. *Proceedings of the Combustion Institute 35*(1), 65–100. *(p. 85)*

Draper, N. R. and H. Smith (1981). *Applied Regression Analysis*. Wiley. *(p. 171)*

Druault, P., P. Guibert, and F. Alizon (2005). Use of proper orthogonal decomposition for time interpolation from PIV data: Application to the cycle-to-cycle variation analysis of in-cylinder engine flows. *Experiments in Fluids 39*(6), 1009–1023. *(p. 45)*

Durox, D., J. P. Moeck, J.-F. Bourgouin, P. Morenton, M. Viallon, T. Schuller, and S. Candel (2013). Flame Dynamics of a Variable Swirl Number System and Instability Control. *Combustion and Flame*. *(p. xi, 11, 165)*

Escudier, M. P. (1984). Observations of the flow produced in a cylindrical container by a rotating endwall. *Experiments in fluids 2*(4), 189–196. *(p. 5)*

Everson, R. and L. Sirovich (1995). Karhunen–Loève procedure for gappy data. *Journal of the Optical Society of America A 12*(8), 1657. *(p. 45)*

Fenimore, C. P. (1971). Formation of nitric oxide in premixed hydrocarbon flames. In *Symposium (International) on Combustion*, Volume 13, pp. 373–380. Elsevier. *(p. 3)*

Franzelli, B., E. Riber, M. Sanjosé, and T. Poinsot (2010). A two-step

chemical scheme for kerosene–air premixed flames. *Combustion and Flame 157*(7), 1364–1373. *(p. 121)*

Fritz, J., M. Kröner, and T. Sattelmayer (2004). Flashback in a Swirl Burner With Cylindrical Premixing Zone. *Journal of Engineering for Gas Turbines and Power 126*(2), 276. *(p. 4, 8)*

Galley, D., S. Ducruix, F. Lacas, and D. Veynante (2011). Mixing and stabilization study of a partially premixed swirling flame using laser induced fluorescence. *Combustion and Flame 158*(1), 155–171. *(p. xi, 4, 7, 8, 73)*

Ghassemi, H., S. W. Baek, and Q. S. Khan (2006). Experimental study on evaporation of kerosene droplets at elevated pressures and temperatures. *Combustion Science and Technology 178*(9), 1669–1684. *(p. 14, 122)*

Giuliani, F., P. Gajan, O. Diers, and M. Ledoux (2002). Influence of pulsed entries on a spray generated by an air-blast injection device: An experimental analysis on combustion instability processes in aeroengines. *Proceedings of the Combustion Institute 29*(1), 91–98. *(p. 25)*

Giuliani, F., A. Lang, K. J. Gradl, P. Siebenhofer, and J. Fritzer (2012). Air Flow Modulation for Refined Control of the Combustion Dynamics Using a Novel Actuator. *Journal of Engineering for Gas Turbines and Power 134*. *(p. 26)*

Griskey, R. G. and D. H. Archer (1965). Ignition criterion for turbulent high velocity, combustible gases with pilot-stabilized flames. *Applied Scientific Research 14*(1), 309–320. *(p. 189)*

Guéniat, F. (2013). *Détection de Structures Cohérentes dans des Ecoulements Fluides et Interfaces Homme-Machine pour l'Exploration et la Visualisation Interactive de Données Scientifiques*. PhD thesis, Université Paris-Sud, Orsay. *(p. 51)*

Guiberti, T. (2015). *Analysis of the topology of premixed swirl-stabilized confined flames*. PhD thesis, Ecole Centrale Paris, Châtenay Malabry, France. *(p. xi, 10)*

Guin, C. and P. Trichet (2004). Optimisation of a two-head lean prevaporised premixed combustor. *Aerospace Science and Technology 8*(1), 35–46. *(p. 9)*

Hall, M. G. (1972). Vortex Breakdown. *Annual Review of Fluid Mechanics 4*(1), 195–218. *(p. 5)*

Hardalupas, Y., A. Selbach, and J. H. Whitelaw (2000). Liquid-fuelled flames with imposed air oscillations. In *Laser techniques applied to fluid mechanics*, pp. 403–416. Springer. *(p. 167)*

Higgins, B., M. Q. McQuay, F. Lacas, J.-C. Rolon, N. Darabiha, and S. Candel (2001). Systematic measurements of OH chemiluminescence for fuel-lean, high-pressure, premixed, laminar flames. *Fuel 80*(1), 67–74. *(p. 32)*

Hinze, J. O. (1955). Fundamentals of the hydrodynamic mechanism of splitting in dispersion processes. *AIChE Journal 1*(3), 289–295. *(p. 13)*

Huang, Y. and V. Yang (2004). Bifurcation of flame structure in a lean-premixed swirl-stabilized combustor: transition from stable to unstable

flame. *Combustion and Flame 136*(3), 383–389. *(p. xi, 11, 12)*

IARC (1985). Soots, Summary of Data Reported and Evaluation. *International Agency for Reasearch on Cancer - Summaries and Evaluations 35*, 219. *(p. 2)*

International Civil Aviation Organization (Ed.) (2011). *Airport air quality manual* (1. ed ed.). Number 9889. Montréal: International Civil Aviation Organization. *(p. 1)*

International Energy Agency (2014). Key World Energy Statistics 2014. Technical report. *(p. 1)*

Iudiciani, P. and C. Duwig (2011). Large Eddy Simulation of the Sensitivity of Vortex Breakdown and Flame Stabilisation to Axial Forcing. *Flow, Turbulence and Combustion 86*(3-4), 639–666. *(p. 95)*

Jovanović, M. R., P. J. Schmid, and J. W. Nichols (2014). Sparsity-promoting dynamic mode decomposition. *Physics of Fluids 26*(2), 024103. *(p. 53)*

Kaiser, S. A. and M. B. Long (2005). Quantitative planar laser-induced fluorescence of naphthalenes as fuel tracers. *Proceedings of the Combustion Institute 30*(1), 1555–1563. *(p. 201)*

Keane, R. D. and R. J. Adrian (1992). Theory of cross-correlation analysis of PIV images. *Applied scientific research 49*(3), 191–215. *(p. 49)*

Kim, K. T., J. G. Lee, H. J. Lee, B. D. Quay, and D. A. Santavicca (2010). Characterization of Forced Flame Response of Swirl-Stabilized Turbulent Lean-Premixed Flames in a Gas Turbine Combustor. *Journal of Engineering for Gas Turbines and Power 132*(4), 041502. *(p. 11)*

Koban, W., J. Koch, V. Sick, N. Wermuth, R. Hanson, and C. Schulz (2005). Predicting LIF signal strength for toluene and 3-pentanone under engine-related temperature and pressure conditions. *Proceedings of the Combustion Institute 30*(1), 1545–1553. *(p. 201)*

Kröner, M., T. Sattelmayer, J. Fritz, F. Kiesewetter, and C. Hirsch (2007). Flame Propagation in Swirling Flows—Effect of Local Extinction on the Combustion Induced Vortex Breakdown. *Combustion Science and Technology 179*(7), 1385–1416. *(p. 188)*

Lacour, C., D. Durox, S. Ducruix, and M. Massot (2011). Interaction of a polydisperse spray with vortices. *Experiments in Fluids 51*(2), 295–311. *(p. 71)*

Lamraoui, A., F. Richecoeur, T. Schuller, and S. Ducruix (2011). A Methodology for On the Fly Acoustic Characterization of the Feeding Line Impedances in a Turbulent Swirled Combustor. *Journal of Engineering for Gas Turbines and Power 133*(1), 011504. *(p. 114)*

Law, C. (1982). Recent advances in droplet vaporization and combustion. *Progress in Energy and Combustion Science 8*(3), 171–201. *(p. 14)*

Lefebvre, A. H. (1989a). *Atomization and sprays*. Combustion. Taylor & Francis. *(p. 104)*

Lefebvre, A. H. (1989b). Properties of sprays. *Particle & Particle Systems Characterization 6*(1-4), 176–186. *(p. 104)*

Lefebvre, A. H. (1995). The Role of Fuel Preparation in Low-Emission Combustion. *Journal of Engineering for Gas Turbines and Power 117*(4), 617–654. *(p. 2)*

Lefebvre, A. H. (2010). *Gas turbine combustion*. CRC Press. *(p. xi, 3)*

Leibovich, S. (1978). The Structure of Vortex Breakdown. *Annual Review of Fluid Mechanics 10*(1), 221–246. *(p. 5)*

Liang, H. and T. Maxworthy (2005). An experimental investigation of swirling jets. *Journal of Fluid Mechanics 525*, 115–159. *(p. 6)*

Lieuwen, T. and B. T. Zinn (1998). The role of equivalence ratio oscillations in driving combustion instabilities in low NOx gas turbines. *Symposium (International) on Combustion 27*(2), 1809–1816. *(p. 9)*

Lieuwen, T. C. and V. Yang (2005). Combustion instabilities in gas turbine engines(operational experience, fundamental mechanisms and modeling). *Progress in astronautics and aeronautics*. *(p. 4, 9)*

Lucca-Negro, O. and T. O'Doherty (2001). Vortex breakdown: a review. *Progress in Energy and Combustion Science 27*, 431–481. *(p. 5)*

Lusseyran, F., F. Guéniat, J. Basley, C. L. Douay, L. R. Pastur, T. M. Faure, and P. J. Schmid (2011). Flow coherent structures and frequency signature: application of the dynamic modes decomposition to open cavity flow. *Journal of Physics: Conference Series 318*(4), 042036. *(p. 50)*

McDougall, T. J. (1980). Bias correction for individual realisation LDA measurements. *Journal of Physics E: Scientific Instruments 13*(1), 53. *(p. 46)*

McKinley, G. H. and M. Renardy (2011). Wolfgang von Ohnesorge. *Physics of Fluids 23*(12), 127101. *(p. 13)*

Mellor, A. M. (2000). Predicting Effectiveness of HO Injection for NO Reduction in Stationary Gas Turbines. *Journal of Propulsion and Power 16*(6), 988–993. *(p. 3)*

Mirat, C. (2015). *Analyse des instabilités de combustion dans des foyers de centrale thermique fonctionnant au fioul lourd*. PhD thesis, Ecole Centrale Paris, Châtenay Malabry, France. *(p. 9)*

Moeck, J. P., J.-F. Bourgouin, D. Durox, T. Schuller, and S. Candel (2012). Nonlinear interaction between a precessing vortex core and acoustic oscillations in a turbulent swirling flame. *Combustion and Flame 159*(8), 2650–2668. *(p. 7, 86, 134)*

Moeck, J. P., J.-F. Bourgouin, D. Durox, T. Schuller, and S. Candel (2013). Tomographic reconstruction of heat release rate perturbations induced by helical modes in turbulent swirl flames. *Experiments in Fluids 54*(4). *(p. 82)*

Motheau, E., Y. Mery, F. Nicoud, and T. Poinsot (2013). Analysis and Modeling of Entropy Modes in a Realistic Aeronautical Gas Turbine. *Journal of Engineering for Gas Turbines and Power 135*(9), 092602. *(p. 85)*

Mounaïm-Rousselle, C. and O. Pajot (1999). Droplet Sizing by Mie Scattering Interferometry in a Spark Ignition Engine. *Particle & Particle Systems Characterization 16*(4), 160–168. *(p. 33)*

Mugele, R. A. and H. D. Evans (1951). Droplet Size Distribution in Sprays. *Industrial & Engineering Chemistry 43*(6), 1317–1324. *(p. 13)*

Nicol, D. G., P. C. Malte, and R. C. Steele (1994). Simplified Models for NOx Production Rates in Lean-Premixed Combustion. In *ASME 1994 International Gas Turbine and Aeroengine Congress and Exposition*, pp. V003T06A037–V003T06A037. American Society of Mechanical Engineers. *(p. 3)*

Noiray, N. (2007). *Linear and nonlinear stability analysis of acoustic-combustion instabilities, application to multipoint injection systems and passive control strategies.* PhD thesis, Ecole Centrale Paris, Châtenay Malabry, France. *(p. 9)*

Novick, A. and D. Troth (1981). Low NOx Heavy Fuel Combustor Concept Program. Technical report, NASA. *(p. 4)*

Oberleithner, K., M. Stöhr, S. H. Im, C. M. Arndt, and A. M. Steinberg (2015). Formation and flame-induced suppression of the precessing vortex core in a swirl combustor: Experiments and linear stability analysis. *Combustion and Flame 162*(8), 3100–3114. *(p. 7)*

Ohnesorge, W. v. (1936). Formation of drops by nozzles and the breakup of liquid jets. *Z. Angew. Math. Mech 16*(4), 355–358. *(p. 12)*

Orain, M., P. Baranger, C. Ledier, J. Apeloig, and F. Grisch (2014). Fluorescence spectroscopy of kerosene vapour at high temperatures and pressures: potential for gas turbines measurements. *Applied Physics B 116*(3), 729–745. *(p. 201)*

Orain, M., P. Baranger, B. Rossow, and F. Grisch (2011). Fluorescence spectroscopy of naphthalene at high temperatures and pressures: implications for fuel-concentration measurements. *Applied Physics B 102*(1), 163–172. *(p. 201)*

Orain, M., F. Grisch, E. Jourdanneau, B. Rossow, C. Guin, and B. Trétout (2009). Simultaneous measurements of equivalence ratio and flame structure in multipoint injectors using PLIF. *Comptes Rendus Mécanique 337*(6-7), 373–384. *(p. 202)*

Orain, M., X. Mercier, and F. Grisch (2005). PLIF imaging of fuel-vapor spatial distribution around a monodisperse stream of acetone droplets: comparison with modeling. *Combustion Science and Technology 177*(2), 249–278. *(p. 201)*

Palies, P., T. Schuller, D. Durox, and S. Candel (2011). Modeling of premixed swirling flames transfer functions. *Proceedings of the Combustion Institute 33*(2), 2967–2974. *(p. 10)*

Paschereit, C. O., E. Gutmark, and W. Weisenstein (1999). Coherent structures in swirling flows and their role in acoustic combustion control. *Physics of Fluids 11*(9), 2667–2678. *(p. 9)*

Pearson, K. (1901). On lines and planes of closest fit to systems of points in space. *Philosophical Magazine Series 6 2*(11), 559–572. *(p. 44)*

Perrin, L., G. Castanet, and F. Lemoine (2014). Etude expérimentale de

l'évaporation de gouttelettes de combustible à haute température par utilisation de techniques optiques combinées. Influence de la volatilité du combustible. In *Congrès Francophone de Techniques Laser*, Marseille. *(p. 122)*

Pilch, M. and C. Erdman (1987). Use of breakup time data and velocity history data to predict the maximum size of stable fragments for acceleration-induced breakup of a liquid drop. *International Journal of Multiphase Flow 13*(6), 741–757. *(p. 13)*

Poinsot, D. (2004). Statistiques pour statophobes. *(p. 175)*

Poinsot, T. and D. Veynante (2005). *Theoretical and numerical combustion*. RT Edwards, Inc. *(p. 8)*

Poinsot, T. J., A. C. Trouve, D. P. Veynante, S. M. Candel, and E. J. Esposito (1987). Vortex-driven acoustically coupled combustion instabilities. *Journal of Fluid Mechanics 177*(-1), 265. *(p. 9)*

Providakis, T. (2013). *Compétition entre Structures Aérodynamiques et Modes Acoustiques dans une Flamme Swirlée: Influence de la Répartition de Carburant*. Ph. D. thesis, Ecole Centrale Paris, Châtenay Malabry, France. *(p. ix, xviii, 15, 19, 23, 27, 28, 58, 68, 104, 114, 149, 153, 154, 161, 165, 170, 174)*

Rachner, M., J. Becker, C. Hassa, and T. Doerr (2002). Modelling of the atomization of a plain liquid fuel jet in crossflow at gas turbine conditions. *Aerospace Science and Technology* (6), 496–506. *(p. 151)*

Raffel, M., C. E. Willert, and J. Kompenhans (1998). *Particle Image Velocimetry: A Practical Guide; with 24 Tables*. Springer Science & Business Media. *(p. 48)*

Rayleigh, L. (1878). The Explanation of Certain Acoustical Phenomena. *Nature 18*(455), 319–321. *(p. 9)*

Reveillon, J. and F.-X. Demoulin (2007). Effects of the preferential segregation of droplets on evaporation and turbulent mixing. *Journal of Fluid Mechanics 583*, 273. *(p. 14)*

Reveillon, J. and L. Vervisch (2005). Analysis of weakly turbulent dilute-spray flames and spray combustion regimes. *Journal of Fluid Mechanics 537*, 317. *(p. 14)*

Richecoeur, F., L. Hakim, A. Renaud, and L. Zimmer (2012). DMD algorithms for experimental data processing in combustion. In *Proceedings of the Summer Program*, pp. 459. *(p. 50, 117)*

Rink, K. K. and A. H. Lefebvre (1986). Influence of Fuel Drop Size and Combustor Operating Conditions on Pollutant Emissions. *(p. 2)*

Rizk, N. and H. Mongia (1991). Low NOx rich-lean combustion concept application. American Institute of Aeronautics and Astronautics. *(p. 4)*

Roudnitzky, S., P. Druault, and P. Guibert (2006). Proper orthogonal decomposition of in-cylinder engine flow into mean component, coherent structures and random Gaussian fluctuations. *Journal of Turbulence 7*, N70. *(p. 44)*

Sahu, S., Y. Hardalupas, and A. M. K. P. Taylor (2014). Simultaneous droplet and vapour-phase measurements in an evaporative spray by combined ILIDS and PLIF techniques. *Experiments in Fluids 55*(2). *(p. 33)*

Saporta, G. (2011). *Probabilités, analyse des données et statistique*. Editions Technip. *(p. 193)*

Sarpkaya, T. (1971). On stationary and travelling vortex breakdowns. *Journal of Fluid Mechanics 45*(03), 545. *(p. 5)*

Scarano, F. and M. L. Riethmuller (1999). Iterative multigrid approach in PIV image processing with discrete window offset. *Experiments in Fluids 26*(6), 513–523. *(p. 48)*

Scarpato, A. (2014). *Linear and nonlinear analysis of the acoustic response of perforated plates traversed by a bias flow*. PhD thesis, Ecole Centrale Paris, Châtenay Malabry, France. *(p. 10)*

Schlüter, J. U. and T. Schönfeld (2000). LES of jets in cross flow and its application to a gas turbine burner. *Flow, Turbulence and Combustion 65*(2), 177–203. *(p. 151)*

Schmid, P. J. (2010). Dynamic mode decomposition of numerical and experimental data. *Journal of Fluid Mechanics 656*, 5–28. *(p. 49)*

Schmid, P. J., L. Li, M. P. Juniper, and O. Pust (2011). Applications of the dynamic mode decomposition. *Theoretical and Computational Fluid Dynamics 25*(1-4), 249–259. *(p. 51)*

Schmitt, P., T. Poinsot, B. Schuermans, and K. P. Geigle (2007). Large-eddy simulation and experimental study of heat transfer, nitric oxide emissions and combustion instability in a swirled turbulent high-pressure burner. *Journal of Fluid Mechanics 570*, 17–46. *(p. 12)*

Schuller, T., D. Durox, and S. Candel (2002). Dynamics of and noise radiated by a perturbed impinging premixed jet flame. *Combustion and Flame 128*(1), 88–110. *(p. 32)*

Sengissen, A., A. Giauque, G. Staffelbach, M. Porta, W. Krebs, P. Kaufmann, and T. Poinsot (2007). Large eddy simulation of piloting effects on turbulent swirling flames. *Proceedings of the Combustion Institute 31*(2), 1729–1736. *(p. 4)*

Seo, S. (1999). *Parametric study of lean premixed combustion instability in a pressurized model gas turbine combustor*. PhD thesis, Pennsylvania State University. *(p. 11)*

Sommerer, Y., D. Galley, T. Poinsot, S. Ducruix, F. Lacas, and D. Veynante (2004). Large eddy simulation and experimental study of flashback and blow-off in a lean partially premixed swirled burner. *Journal of Turbulence 5*. *(p. 4, 8)*

Spalding, D. B. (1953). The combustion of liquid fuels. In *Symposium (international) on combustion*, Volume 4, pp. 847–864. Elsevier. *(p. 14)*

Stenzler, J. N., J. G. Lee, D. A. Santavicca, and W. Lee (2006). Penetration of liquid jets in a cross-flow. *Atomization and Sprays 16*(8). *(p. 151)*

Syred, N. (2006). A review of oscillation mechanisms and the role of the

precessing vortex core (PVC) in swirl combustion systems. *Progress in Energy and Combustion Science 32*(2), 93–161. *(p. xi, 6)*

Syred, N., W. Fick, T. O'Doherty, and A. J. Griffiths (1997). The Effect of the Precessing Vortex Core on Combustion in a Swirl Burner. *Combustion Science and Technology 125*(1-6), 139–157. *(p. 6)*

Tacina, R. R. (1990). Low NOx potential of gas turbine engines. *AIAA Aerospace Sciences Meeting and Exhibit 90. (p. 4)*

Tarnogrodzki, A. (1993). Theoretical prediction of the critical Weber number. *International journal of multiphase flow 19*(2), 329–336. *(p. 13)*

Thielicke, W. and E. J. Stamhuis (2014). PIVlab – Towards User-friendly, Affordable and Accurate Digital Particle Image Velocimetry in MATLAB. *Journal of Open Research Software 2. (p. 49)*

Weigand, P., W. Meier, X. Duan, W. Stricker, and M. Aigner (2006). Investigations of swirl flames in a gas turbine model combustor. *Combustion and Flame 144*(1-2), 205–224. *(p. 73)*

Welch, P. D. (1967). The use of fast Fourier transform for the estimation of power spectra: A method based on time averaging over short, modified periodograms. *IEEE Transactions on audio and electroacoustics 15*(2), 70–73. *(p. 45)*

Zeldovich, Y. A., D. Frank-Kamenetskii, and P. Sadovnikov (1947). *Oxidation of nitrogen in combustion*. Publishing House of the Academy of Sciences of USSR. *(p. 2)*

Zimmer, L., R. Domann, Y. Hardalupas, and Y. Ikeda (2003). Simultaneous Laser-Induced Fluorescence and Mie Scattering for Droplet Cluster Measurements. *AIAA Journal 41*(11), 2170–2178. *(p. 14)*

Titre : Etude de la stabilisation des flammes et des comportements transitoires dans un brûleur étagé à combustible liquide à l'aide de diagnostics rapides.

Mots clés : combustion turbulente, LPP, injection multipoint, hystérésis, DMD

Résumé: La combustion prévaporisée prémélangée pauvre est une piste de choix pour réduire les émissions polluantes des moteurs d'avions mais peut conduire à l'apparition d'instabilités thermo-acoustiques. Afin d'améliorer la stabilité de telles flammes, l'étagement du combustible consiste à contrôler la distribution spatiale du carburant. Une telle procédure s'accompagne cependant d'une complexité accrue du système pouvant déboucher sur des phénomènes inattendus. Un brûleur à l'échelle de laboratoire alimenté par du dodécane liquide est utilisé dans cette thèse. Le combustible est injecté dans deux étages séparés, permettant ainsi de contrôler sa distribution. Cette particularité permet l'observation de différentes formes de flammes et notamment de points bistables pour lesquels deux flammes différentes peuvent exister malgré des conditions opératoires identiques.

L'utilisation de diagnostics optiques à haute cadence (diffusion de Mie des gouttes de combustible et émission spontanée de la flamme) est couplée à des méthodes de post-traitement avancées comme la Décomposition en Modes Dynamiques. Ainsi, des mécanismes pilotant la stabilisation des flammes ainsi que leurs changements de forme sont proposés. Ils mettent notamment en lumière les interactions entre l'écoulement gazeux, les gouttes de combustible et la flamme.

Title : High-speed diagnostics for the study of flame stabilization and transient behaviour in a swirled burner with variable liquid-fuel distribution.

Keywords : turbulent combustion, LPP, multipoint injection, hysteresis, DMD

Abstract : A promising way to reduce jet engines pollutant emissions is the use of lean premixed prevaporized combustion but it tends to trigger thermo-acoustic instabilities. To improve the stability of these flames, a procedure called staging consists in splitting the fuel injection to control its spatial distribution. This however leads to an increased complexity and unexpected phenomena can occur. In the present work, a model gas turbine combustor fed with liquid dodecane is used. It is equipped with two fuel injection stages to control the fuel distribution in the burner. Different flame stabilizations can be observed and a bistable case where two flame shapes can exist for the same operating conditions is highlighted. High-speed optical diagnostics (fuel droplets Mie scattering and chemiluminescence measurements) are coupled with advanced post-processing methods like Dynamic Mode Decomposition. The results enable to propose mechanisms leading to flame stabilization and flame shape transitions. They show a strong interplay between the gaseous flow, the fuel droplets and the flame itself.

Université Paris-Saclay
Espace Technologique / Immeuble Discovery
Route de l'Orme aux Merisiers RD 128 / 91190 Saint-Aubin, France